EXPERIMENTAL AND ANALYTICAL INVESTIGATION ON IMPACT BEHAVIOR OF CONVENTIONAL AND STEEL FIBER REINFORCED CONCRETE BEAMS

A DOCTOR OF PHILOSOPHY THESIS

IN

MODELING AND DESIGN OF ENGINEERING SYSTEMS

(MODES)

(MAIN FIELD OF STUDY: CIVIL ENGINEERING)

ATILIM UNIVERSITY

BY

AZDEEN SALEH NAJAH

JUNE 2018

EXPERIMENTAL AND ANALYTICAL INVESTIGATION ON IMPACT BEHAVIOR OF CONVENTIONAL AND STEEL FIBER REINFORCED CONCRETE BEAMS

A THESIS SUBMITTED TO
THE GRADUATE SCHOOL OF NATURAL AND APPLIED SCIENCES
MODELING AND DESIGN OF ENGINEERING SYSTEMS
OF
ATILIM UNIVERSITY
BY

AZDEEN SALEH NAJAH

IN PARTIAL FULFILLMENT OF THE REQUIREMENTS FOR
THE DEGREE OF
DOCTOR OF PHILOSOPHY
IN
MODELING AND DESIGN OF ENGINEERING SYSTEMS
(MAIN FIELD OF STUDY: CIVIL ENGINEERING)

JUNE 2018

Approval of the Graduate School of Natural and Applied Sciences, Atılım University.

_____

Prof. Dr. Ali Kara
Director

I certify that this thesis satisfies all the requirements as a thesis for the degree of Doctor of Philosophy.

_____

Assoc. Prof. Dr. Ender Keskinkılıç
Head of Department

This is to certify that we have read the thesis "Experimental and Analytical Investigation on Impact Behavior of Conventional and Steel Fiber Reinforced Concrete Beams" submitted by Azdeen Saleh Najah that in our opinion it is fully adequate, in scope and quality, as a thesis for the degree of Doctor of Philosophy.

_____	_____
Prof. Dr. Kağan Tuncay	Assist. Prof. Dr. Halit Cenan Mertol
Co-Supervisor	Supervisor

Examining Committee Members

Prof. Dr. Tolga Akış	_____
Assoc. Prof. Dr. Burcu Burak Bakır	_____
Assoc. Prof. Dr. Eray Baran	_____
Assist. Prof. Dr. Saeid Kazemzadeh Azad	_____
Assist. Prof. Dr. Halit Cenan Mertol	_____

Date: 22nd of June, 2018

I declare and guarantee that all data, knowledge and information in this document has been obtained, processed and presented in accordance with academic rules and ethical conduct. Based on these rules and conduct, I have fully cited and referenced all material and results that are not original to this work.

Name, Last name: Azdeen Saleh Najah

Signature:

ABSTRACT

EXPERIMENTAL AND ANALYTICAL INVESTIGATION ON IMPACT BEHAVIOR OF CONVENTIONAL AND STEEL FIBER REINFORCED CONCRETE BEAMS

Azdeen Saleh Najah

Ph. D., Modeling and Design of Engineering Systems (MODES)

Main Field of Study: Civil Engineering

Supervisor: Assist. Prof. Dr. Halit Cenan Mertol

Co-Supervisor: Prof. Dr. Kağan Tuncay

June 2018, 157 pages

This research investigated the experimental and analytical behavior of unreinforced and reinforced concrete beams cast using conventional concrete (CC) and steel fiber reinforced concrete (SFRC) under impact loading. Dramix ZP-305 type steel fibers were used for SFRC. Half of the beam specimens were unreinforced and the others were reinforced using one 8 mm diameter steel reinforcement fixed at center of specimen cross section. Cylinder concrete compressive strengths used in this study were 12 and 26 MPa for CC specimens and 35 MPa for SFRC specimens. Beam specimens had 60×60×500, 100×100×500, and 150×150×500 mm dimensions. The specimens were tested under impact loading using a drop-hammer testing apparatus having a weight of 58.5 N. This weight was dropped from various heights (1.20, 2.00, and 2.95 m for unreinforced specimens and 2.95, 3.00, and 3.04 m for reinforced specimens) based on specimen sizes. The slow motion videos of the tested specimens were recorded using a high-speed camera having a frame rate of 2000 fps. Experimental velocity-time relationships for hammer were obtained by analyzing of recorded impact videos using the TEMA Motion Analysis Software. Beams, hammer, and supports were modeled in ANSYS Finite Element Analysis Program and parameters related to modeling were calibrated based on the test results. Riedel, Hiermaier, and Thoma (RHT) Concrete Model was used in ANSYS Dynamic Explicit AUTODYN solver. The results were compared to the experimental studies on CC and SFRC in this research and input parameters of the model were modified. Comparisons of the experimental and modeling results indicated that velocity-time

relationships of hammer showed very good agreement for various concrete compressive strengths and dimensions of specimens. It can be concluded that the calibrated concrete model presented in this study could provide some general guidelines for predicting the behavior of reinforced and unreinforced CC and SFRC under impact loading.

Keywords: Drop-hammer testing apparatus, impact loading, ANSYS, RHT Concrete Model, steel fiber reinforced concrete, high-speed camera, TEMA Motion Analysis Software, velocity-time relationships.

ÖZ

NORMAL VE ÇELİK LİFLİ BETON KULLANILAN BETONARME KİRİŞLERİN DARBE ETKİSİ ALTINDAKİ DAVRANIŞININ DENEYSEL VE ANALİTİK OLARAK İNCELENMESİ

Azdeen Saleh Najah
Doktora, Mühendislik Sistemlerinin Modellenmesi ve Tasarımı (MODES)
Ana Çalışma Alanı: İnşaat Mühendisliği ABD
Tez Yöneticisi: Dr. Öğretim Üyesi Halit Cenan Mertol
Ortak Tez Yöneticisi: Prof. Dr. Kağan Tuncay
Haziran 2018, 157 sayfa

Bu çalışmada donatılı ve donatısız geleneksel beton (GB) ve çelik lifli beton (ÇLB) kullanılan kirişlerin darbe yüklemesi altındaki deneysel ve analitik davranışları araştırılmıştır. ÇLB için Dramix ZP-305 tipi çelik lifler kullanılmıştır. Kirişlerin yarısında donatı kullanılmamış, diğer yarısında ise elemanların tam ortasında bir adet 8 mm çapında çelik donatı kullanılmıştır. Bu çalışmadaki beton silindir basınç dayanımları, GB için 12 ve 26 MPa, ÇLB için 35 MPa olarak ölçülmüştür. Kiriş numuneler 60×60×500, 100×100×500 ve 150×150×500 mm boyutlarındaydı. Numunelerin darbe yüküne maruz bırakılması için 58.5 N ağırlığında çekice sahip, düşen çekiç test düzeneği kullanılmıştır. Bu çekiç ağırlığı deney numunesi boyutlarına göre farklı yüksekliklerden bırakılmıştır (donatısız elemanlar için 1.20, 2.00 ve 2.95 m, donatılı elemanlar için 2.95, 3.00 ve 3.04 m). Deney sırasında 2000 kare hızına sahip yüksek hızlı fotoğraf makinası kullanılarak numunelerin yavaş çekim videoları kaydedilmiştir. Kaydedilen videolar TEMA Hareket Analiz Programı kullanılarak analiz edilmiş ve çekiç için deneysel hız-zaman ilişkileri elde edilmiştir. Kiriş, çekiç ve mesnetler ANSYS Sonlu Elemanlar Analiz Programı kullanılarak modellenmiş ve modelleme parametreleri deney sonuçlarına göre kalibre edilmiştir. ANSYS Dynamic Explicit AUTODYN çözümünde Riedel, Hiermaier ve Thoma (RHT) Beton Modeli kullanılmıştır. Sonuçlar bu çalışmadaki deney sonuçları ile karşılaştırılmış ve kullanılan beton modeli parametreleri bu sonuca göre

değiştirilmiştir. Deney ve modelleme sonuçlarının karşılaştırılması ile çekiç için oluşturulan hız-zaman ilişkilerinin farklı beton basınç dayanımları ve farklı kesit boyutları için çok iyi uyum içinde olduğu saptanmıştır. Bu araştırma sonucunda kalibre edilmiş modeller kullanılması durumunda, donatısız ve donatılı GB ve ÇLB kullanılan elemanların darbe etkisi altındaki davranışları iyi bir şekilde tahmin edilebilmektedir.

Anahtar Kelimeler: Düşen çekiç test düzeneği, darbe yüklemesi, ANSYS, RHT Beton Modeli, çelik lifli beton, yüksek hızlı fotoğraf makinesi, TEMA Hareket Analiz Programı, hız-zaman ilişkileri.

DEDICATION

I wish to dedicate this thesis to my late Mother, Yeza. She taught me to persevere and prepared me to face the challenges with faith and humility. She was constant source of inspiration to my life. Although she is not here to give me strength and support, I always feel her presence that used to urge me to strive to achieve my goals in life.

To my Father, Saleh, who always had confidence in me and offered me encouragement and support in all my endeavors.

ACKNOWLEDGMENTS

Firstly, I would like to express my sincere gratitude to my advisor, Dr. Halit Cenan Mertol, for his continuous support of my Ph. D. study and related research, for his patience, motivation, and immense knowledge. His guidance helped me in all the time of the research and during the thesis write-up. I could not have imagined having a better advisor and mentor for my Ph. D. study.

Besides my advisor, I would like to thank my co-advisor, Dr. Kağan Tuncay, and the rest of my thesis committee: Dr. Tolga Akış, Dr. Burcu Burak Bakır, Dr. Eray Baran, and Dr. Saeid Kazemzadeh Azad for their insightful comments and encouragement, but also for the challenging questions which motivated me to improve my research in various perspectives.

My sincere thanks also goes to Atilim University Civil Engineering Department's Structural Mechanics Laboratory staff, Doğan Tok and Muhammed Sağlam, for their assistance during experimental study and Atilim University Mechatronic Engineering Department's staff, Ph. D. Candidate Cahit Gürel, for his technical support and esteemed efforts in video recording using the high-speed camera and analyzing the recorded videos.

I would like to thank my family; to my late mother, my father, my brothers, and sisters for supporting me spiritually throughout my life in general.

To my daughter Hager and my sons Asem, Alhareth, Albara, and Qusay for the sleepless nights during late-night studies before deadlines and during the five years of Ph. D. study.

And finally, the person who has made all this possible has been my wife, Maryem. She has been a constant source of support and encouragement and has made an untold number of sacrifices for the entire family, and specifically for me to continue my education. She is a great inspiration to me. Hence, great appreciation and

enormous thanks are due to her. Without her understanding, I am sure this thesis would never be completed. I thank you all.

TABLE OF CONTENTS

ABSTRACT ..... **i**

ÖZ ..... **iii**

DEDICATION ..... **v**

ACKNOWLEDGMENTS ..... **vi**

TABLE OF CONTENTS ..... **viii**

LIST OF FIGURES ..... **xi**

LIST OF TABLES ..... **xxi**

1. INTRODUCTION **1**

1.1 GENERAL 1

1.2 MOTIVATION 1

1.3 OBJECTIVES AND SCOPE 2

1.4 THESIS ORGANIZATION 2

2. BACKGROUND **4**

2.1 DROP-HAMMER TESTING APPARATUS 4

2.1.1 Banthia et al. (1989) 4

2.1.2 Bindiganavile (2003) 5

2.1.3 Ravindrarajah and Lyte (2007) 6

2.1.4 Zhang et al. (2008) 6

2.1.5 Rao et al. (2011) 8

2.1.6 Kantar et al. (2011) 9

2.2 IMPACT LOADING ON CC AND SFRC 12

2.2.1 Mohammadi et al. (2009) 12

2.2.2 Weidner et al. (2012) 13

2.2.3 Wang and Wang (2013) 13

2.3 MATERIAL MODELS 14

2.3.1 CC in Compression 14

2.3.2 SFRC in Compression 14

2.3.3 SFRC in Tension 15

2.3.4 Riedel, Hiermaier, and Thoma (RHT) Concrete Model in ANSYS (Riedel et al. 1999) 17

2.4 MODELING IMPACT BEHAVIOR OF CC AND SFRC 26

2.4.1 Leppänen (2006) 26

2.4.2 Kantar et al. (2011) 27

2.4.3 Nyström and Gylltoft (2011) 27

2.4.4 Haido and Musa, (2013) 27

2.4.5 Subramani et. al. (2014) 27

2.4.6 Yılmaz et al. (2014) 28

2.4.7 Galuta and Regig (2017) 28

2.4.8 Hokes et al. (2006) 28

2.4.9 Badiger and Malipatil (2014) 29

2.4.10 Vaiciunas et al. (2011) 29

2.4.11 Vasudevan et al. (2013) 29

2.5 HIGH-PERFORMANCE FIBER REINFORCED CEMENTITIOUS COMPOSITES (HPFRCC) 29
3. EXPERIMENTAL PROGRAM 32
3.1 GENERAL 32
3.2 TEST SPECIMENS 32
3.3 MATERIALS 34
3.3.1 Concrete 34
3.3.2 Steel Fibers 35
3.3.3 Reinforcement 36
3.4 SPECIMEN PREPARATION 36
3.4.1 Molds, Formworks, and Reinforcement 36
3.4.2 Concrete Mixing 39
3.4.3 Casting and Curing 40
3.4.4 Test Set-Ups and Procedures 44
4. RESULTS AND DISCUSSIONS 57
4.1 GENERAL 57
4.2 COMPRESSIVE STRENGTH TEST RESULTS 57
4.3 FLEXURAL TENSILE STRENGTH TEST RESULTS 60
4.4 IMPACT BEHAVIOR TEST RESULTS 62
5. ANALYTICAL WORK 79
5.1 GENERAL 79
5.1.1 Finite Element Modeling 79
5.1.2 Geometry 79
5.1.3 Material Properties 81
5.1.4 Analysis Settings 83
5.2 MODIFICATIONS TO RHT CONCRETE MODEL 89
5.2.1 Density (Unit Weight) 93
5.2.2 Compressive Strength 94
5.2.3 Tensile Strength 95
5.2.4 Stress-Strain Relationship 95
5.2.5 Compressive Strain Rate Exponent 102
5.2.6 Tensile Strain Rate Exponent δ input variables 102
5.3 STEEL MODEL 103
5.4 ANALYSIS RESULTS AND COMPARISONS 103
5.4.1 General 103
5.5 COMPARISON OF VELOCITY-TIME RELATIONSHIPS OF HAMMER USING DEFAULT AND MODIFIED RHT CONCRETE MODEL FOR LSC AND NSC SPECIMENS 113
5.6 COMPARISON OF VELOCITY-TIME RELATIONSHIPS OF HAMMER USING DEFAULT AND MODIFIED RHT CONCRETE MODEL FOR SFRC SPECIMENS 121
5.7 COMPARISON OF PREDICTED VELOCITY-TIME RELATIONSHIPS ... 126
5.7.1 Effect of Specimen Size 126
5.7.2 Effect of Concrete Strength 129
5.7.3 Effect of Reinforcement 133

5.7.4 Energy Absorption Capacity 138
5.8 PARAMETRIC STUDY ON REINFORCEMENT 140
6. SUMMARY, CONCLUSIONS, AND RECOMMENDATIONS 143
6.1 SUMMARY 143
6.2 CONCLUSIONS 143
6.3 RECOMMENDATIONS 146
7. REFERENCES 148
8. APPENDICES A1

LIST OF FIGURES

Figure 2-1 – Schematic view of the drop-hammer testing apparatus (Zhang et al., 2008).....7
Figure 2-2 – Geometry of tested specimens and locations of accelerometers (Zhang et al., 2008).....7
Figure 2-3 – Experimental load-displacement relationships (Zhang et al., 2008).....8
Figure 2-4 – Schematic view of drop-hammer testing apparatus (Rao et al., 2011).....9
Figure 2-5 – Experimental and analytical acceleration-time relationships obtained by Kantar et al. (2011).....10
Figure 2-6 – Typical failure mode of specimens obtained by Kantar et al. (2011).....11
Figure 2-7 – Modeling of specimens by Kantar et al. (2011).....11
Figure 2-8 – Idealized tensile stress-strain relationship of SFRC (Soranakom et al., 2008).....16
Figure 2-9 – RHT representation of compressive meridian (Riedel et al., 1999).....18
Figure 2-10 – The third invariant dependence (R_3) (Riedel et al., 1999).....19
Figure 2-11 – Bilinear strain hardening function in uniaxial compression case (Riedel et al., 1999).....20
Figure 2-12 – RHT elastic, fracture, and residual failure surfaces (Riedel et al., 1999).....22
Figure 2-13 – Tensile crack softening failure and Fracture energy G_f (Riedel et al., 1999).....26
Figure 2-14 – Tensile stress-strain relationships of plain concrete, FRC, and HPFRCC (Naaman and Reinhardt, 1996).....30
Figure 2-15 – Details of the regions in the tensile stress-strain relationship of (a) FRC and (b) HPFRCC (Naaman and Reinhardt, 1996).....31
Figure 3-1 – General and cross-sectional views of the specimens.....34
Figure 3-2 – Materials proportioning.....35
Figure 3-3 – Steel fibers at the mixing stage.....36
Figure 3-4 – Cylinder and prism molds.....37
Figure 3-5 – Preparations of formworks for 60×60×500, 100×100×500, and 150×150×500 mm beam specimens.....38

Figure 3-6 – Formworks for 60×60×500, 100×100×500, and 150×150×500 mm beam specimens before casting....38
Figure 3-7 – Mixing of materials....39
Figure 3-8 – Slump test....40
Figure 3-9 – Placing concrete into molds and formworks....41
Figure 3-10 – Casting of specimens - Batch 1 (CC)....42
Figure 3-11 – Casting of specimens - Batch 2 (CC)....42
Figure 3-12 – Casting of specimens – Batch 3 (SFRC)....43
Figure 3-13 – Curing of specimens....44
Figure 3-14 – Compressive strength tests....45
Figure 3-15 – Compressive strength tests of specimens of Batch 1 (CC)....46
Figure 3-16 – Compressive strength tests of specimens of Batch 2 (CC)....46
Figure 3-17 – Compressive strength tests of specimens of Batch 3 (SFRC)....47
Figure 3-18 – Flexural strength tests (four-point bending)....48
Figure 3-19 – Schematic view of the drop-hammer testing apparatus used in this research....49
Figure 3-20 – Construction process of the drop-hammer testing apparatus....50
Figure 3-21 – Steel hammer used in this research....50
Figure 3-22 – Cameras used in trial tests....51
Figure 3-23 – Drop-hammer testing apparatus at different locations (indoors and outdoors)....52
Figure 3-24 – Recording of test videos using high-speed camera....52
Figure 3-25 – Analysis of test videos using TEMA Motion Software....53
Figure 3-26 – Dropping heights for various specimens....54
Figure 3-27 – Impact behavior tests - Batch 1....55
Figure 3-28 – Impact behavior tests - Batch 2....56
Figure 3-29 – Impact behavior tests - Batch 3....56
Figure 4-1 – Typical failure mode of CC cylinders under compression....58
Figure 4-2 – Typical failure mode of SFRC cylinders under compression....59
Figure 4-3 – Typical failure mode of CC prisms under flexure 1....60
Figure 4-4 – Typical failure mode of CC prisms under flexure 2....61
Figure 4-5 – Typical failure mode of SFRC prisms under flexure....61

Figure 4-6 – Failure modes of Batch 1 LSC unreinforced specimens (Groups 1, 3, and 5).....63
Figure 4-7 – Failure modes of Batch 2 NSC unreinforced specimens (Groups 2, 4, and 6).....64
Figure 4-8 – Failure modes of Batch 3 SFRC unreinforced specimens (Groups 13, 15, and 17).....65
Figure 4-9 – Failure modes of Batch 1 LSC reinforced specimens (Groups 7, 9, and 11).....66
Figure 4-10 – Failure modes of Batch 2 NSC reinforced specimens (Groups 8, 10, and 12).....67
Figure 4-11 – Failure modes of Batch 3 SFRC reinforced specimens (Groups 14, 16, and 18).....68
Figure 4-12 – Experimental velocity-time relationships of hammer for 60×60×500 mm unreinforced LSC specimens.....70
Figure 4-13 – Experimental velocity-time relationships of hammer for 60×60×500 mm unreinforced NSC specimens.....70
Figure 4-14 – Experimental velocity-time relationships of hammer for 60×60×500 mm unreinforced SFRC specimens.....71
Figure 4-15 – Experimental velocity-time relationships of hammer for 100×100×500 mm unreinforced LSC specimens.....71
Figure 4-16 – Experimental velocity-time relationships of hammer for 100×100×500 mm unreinforced NSC specimens.....72
Figure 4-17 – Experimental velocity-time relationships of hammer for 100×100×500 mm unreinforced SFRC specimens.....72
Figure 4-18 – Experimental velocity-time relationships of hammer for 150×150×500 mm unreinforced LSC specimens.....73
Figure 4-19 – Experimental velocity-time relationships of hammer for 150×150×500 mm unreinforced NSC specimens.....73
Figure 4-20 – Experimental velocity-time relationships of hammer for 150×150×500 mm unreinforced SFRC specimens.....74
Figure 4-21 – Experimental velocity-time relationships of hammer for 60×60×500 mm reinforced LSC specimens.....74

Figure 4-22 – Experimental velocity-time relationships of hammer for 60×60×500 mm reinforced NSC specimens 75
Figure 4-23 – Experimental velocity-time relationships of hammer for 60×60×500 mm reinforced SFRC specimens 75
Figure 4-24 – Experimental velocity-time relationships of hammer for 100×100×500 mm reinforced LSC specimens.....76
Figure 4-25 – Experimental velocity-time relationships of hammer for 100×100×500 mm reinforced NSC specimens 76
Figure 4-26 – Experimental velocity-time relationships of hammer for 100×100×500 mm reinforced SFRC specimens 77
Figure 4-27 – Experimental velocity-time relationships of hammer for 150×150×500 mm reinforced LSC specimens.....77
Figure 4-28 – Experimental velocity-time relationships of hammer for 150×150×500 mm reinforced NSC specimens 78
Figure 4-29 – Experimental velocity-time relationships of hammer for 150×150×500 mm reinforced SFRC specimens 78
Figure 5-1 – General view of model.....80
Figure 5-2 – Number of elements used for convergence study for unreinforced specimen having 60×60×500 mm dimensions 84
Figure 5-3 – Number of elements used for convergence study for reinforced specimen having 60×60×500 mm dimensions 85
Figure 5-4 – Results of the convergence study for unreinforced specimen having 60×60×500 mm dimensions 85
Figure 5-5 – Results of the convergence study for reinforced specimen having 60×60×500 mm dimensions 85
Figure 5-6 – Final meshed model for unreinforced specimen having 60×60×500 mm dimensions.....86
Figure 5-7 – Final meshed model for reinforced specimen having 60×60×500 mm dimensions.....86
Figure 5-8 – Average velocity of hammer used in ANSYS modeling for Group 1 specimens.....88
Figure 5-9 – Measurement of specimens weight at laboratory to determine its density 93

Figure 5-10 – Typical elastic, failure, and residual branches of stress–strain relationship of RHT concrete model in compression.....96
Figure 5-11 – Comparison of default and modified RHT Concrete Models to Popovics (1973) Concrete Model for 35 MPa concrete compressive strength ..97
Figure 5-12 – Comparison of default and modified RHT Concrete Models to Popovics (1973) CC Model for 14.1 MPa concrete compressive strength 98
Figure 5-13 – Comparison of default and modified RHT Concrete Models to Popovics (1973) CC Model for 30.6 MPa concrete compressive strength 98
Figure 5-14 – Comparison of default and modified RHT Concrete Models to Ezeldin and Balaguru (1990) SFRC Model for 41.1 MPa concrete compressive strength 99
Figure 5-15 – Tensile stress-strain relationships for SFRC proposed by Soranakom et al. (2008) for 3.543 MPa tensile strength and various μ values (0.25, 0.5, and 0.75).....100
Figure 5-16 – Post-failure stress–fracture energy curve applied in the non- linear model.....101
Figure 5-17 – Typical failure modes of various specimens 104
Figure 5-18 – Comparison of the motions for various times after impact obtained from the impact tests and the analyzed model for 60C12-1 105
Figure 5-19 – Comparison of the motions for various times after impact obtained from the impact tests and the analyzed model for 100C26-1 106
Figure 5-20 – Comparison of the motions for various times after impact obtained from the impact tests and the analyzed model for 150C12-3 107
Figure 5-21 – Comparison of the motions for various times after impact obtained from the impact tests and the analyzed model for 60C12R-2 108
Figure 5-22 – Comparison of the motions for various times after impact obtained from the impact tests and the analyzed model for 100C26R-3 109
Figure 5-23 – Comparison of the motions for various times after impact obtained from the impact tests and the analyzed model for 150C12R-2 110
Figure 5-24 – Comparison of the motions for various times after impact obtained from the impact tests and the analyzed model for 60SFRC35-3 111
Figure 5-25 – Comparison of the motions for various times after impact obtained from the impact tests and the analyzed model for 100SFRC35R-1.....112

Figure 5-26 – Comparison of the motions for various times after impact obtained from the impact tests and the analyzed model for 150SFRC35-2 113
Figure 5-27 – Experimental and analytical velocity-time relationships of hammer using default and modified RHT Concrete Model for Group 1 specimens..... 114
Figure 5-28 – Experimental and analytical velocity-time relationships of hammer using default and modified RHT Concrete Model for Group 2 specimens..... 115
Figure 5-29 – Experimental and analytical velocity-time relationships of hammer using default and modified RHT Concrete Model for Group 3 specimens..... 115
Figure 5-30 – Experimental and analytical velocity-time relationships of hammer using default and modified RHT Concrete Model for Group 4 specimens..... 116
Figure 5-31 – Experimental and analytical velocity-time relationships of hammer using default and modified RHT Concrete Model for Group 5 specimens..... 116
Figure 5-32 – Experimental and analytical velocity-time relationships of hammer using default and modified RHT Concrete Model for Group 6 specimens..... 117
Figure 5-33 – Experimental and analytical velocity-time relationships of hammer using default and modified RHT Concrete Model for Group 7 specimens..... 117
Figure 5-34 – Experimental and analytical velocity-time relationships of hammer using default and modified RHT Concrete Model for Group 8 specimens..... 118
Figure 5-35 – Experimental and analytical velocity-time relationships of hammer using default and modified RHT Concrete Model for Group 9 specimens..... 118
Figure 5-36 – Experimental and analytical velocity-time relationships of hammer using default and modified RHT Concrete Model for Group 10 specimens.... 119
Figure 5-37 – Experimental and analytical velocity-time relationships of hammer using default and modified RHT Concrete Model for Group 11 specimens.... 119
Figure 5-38 – Experimental and analytical velocity-time relationships of hammer using default and modified RHT Concrete Model for Group 12 specimens.... 120
Figure 5-39 – Experimental and analytical velocity-time relationships of hammer using default and modified RHT Concrete Model for Group 13-a specimens for various G_f..... 122
Figure 5-40 – Experimental and analytical velocity-time relationships of hammer using default and modified RHT Concrete Model for Group 13-b specimens for various G_f..... 122

Figure 5-41 – Experimental and analytical velocity-time relationships of hammer using default and modified RHT Concrete Model for Group 14 specimens for various G_f.....123
Figure 5-42 – Experimental and analytical velocity-time relationships of hammer using default and modified RHT Concrete Model for Group 15 specimens for various G_f.....123
Figure 5-43 – Experimental and analytical velocity-time relationships of hammer using default and modified RHT Concrete Model for Group 16 specimens for various G_f.....124
Figure 5-44 – Experimental and analytical velocity-time relationships of hammer using default and modified RHT Concrete Model for Group 17 specimens for various G_f.....124
Figure 5-45 – Experimental and analytical velocity-time relationships of hammer using default and modified RHT Concrete Model for Group 18 specimens for various G_f.....125
Figure 5-46 – Predicted velocity-time relationships for LSC unreinforced specimens (Group 1: 60×60 mm, Group 3: 100×100 mm, and Group 5: 150×150 mm) ..127
Figure 5-47 – Predicted velocity-time relationships for NSC unreinforced specimens 127
Figure 5-48 – Predicted velocity-time relationships for SFRC unreinforced specimens (Group 13: 60×60 mm, Group 15: 100×100 mm, and Group 17: 150×150 mm).....128
Figure 5-49 – Predicted velocity-time relationships for LSC reinforced specimens (Group 7: 60×60 mm, Group 9: 100×100 mm, and Group 11: 150×150 mm).128
Figure 5-50 – Predicted velocity-time relationships for NSC reinforced specimens (Group 8: 60×60 mm, Group 10: 100×100 mm, and Group 12: 150×150 mm) 129
Figure 5-51 – Predicted velocity-time relationships for SFRC reinforced specimens (Group 14: 60×60 mm, Group 16: 100×100 mm, and Group 18: 150×150 mm) 129
Figure 5-52 – Predicted velocity-time relationships for 60×60 mm unreinforced specimens (Group 1: LSC, Group 2: NSC, and Group 13a, 13b: SFRC) 130

Figure 5-53 – Predicted velocity-time relationships for 100×100 mm unreinforced specimens (Group 3: LSC, Group 4: NSC, and Group 15: SFRC).....130
Figure 5-54 – Predicted velocity-time relationships for 150×150 mm unreinforced specimens (Group 5: LSC, Group 6: NSC, and Group 17: SFRC).....131
Figure 5-55 – Predicted velocity-time relationships for 60×60 mm reinforced specimens (Group 7: LSC, Group 8: NSC, and Group 14: SFRC).....131
Figure 5-56 – Predicted velocity-time relationships for 100×100 mm reinforced specimens (Group 9: LSC, Group 10: NSC, and Group 16: SFRC).....132
Figure 5-57 – Predicted velocity-time relationships for 150×150 mm reinforced specimens (Group 11: LSC, Group 12: NSC, and Group 18: SFRC).....132
Figure 5-58 – Predicted velocity-time relationships for 60×60 mm LSC specimens (Group 1: unreinforced and Group 7: reinforced).....133
Figure 5-59 – Predicted velocity-time relationships for 60×60 mm NSC specimens (Group 2: unreinforced and Group 8: reinforced).....134
Figure 5-60 – Predicted velocity-time relationships for 60×60 mm SFRC specimens (Group 13a, 13b: unreinforced and Group 14: reinforced) 134
Figure 5-61 – Predicted velocity-time relationships for 100×100 mm LSC specimens (Group 3: unreinforced and Group 9: reinforced).....135
Figure 5-62 – Predicted velocity-time relationships for 100×100 mm NSC specimens (Group 4: unreinforced and Group 10: reinforced).....135
Figure 5-63 – Predicted velocity-time relationships for 100×100 mm SFRC specimens (Group 15: unreinforced and Group 16: reinforced).....136
Figure 5-64 – Predicted velocity-time relationships for 150×150 mm LSC specimens (Group 5: unreinforced and Group 11: reinforced).....136
Figure 5-65 – Predicted velocity-time relationships for 150×150 mm NSC specimens (Group 6: unreinforced and Group 12: reinforced).....137
Figure 5-66 – Predicted velocity-time relationships for 150×150 mm SFRC specimens (Group 17: unreinforced and Group 18: reinforced).....137
Figure 5-67 – Definitions for crack length and beam width 139
Figure 5-68 – Velocity-time relationships of hammer obtained from ANSYS for various reinforcement diameters for LSC specimens (Group 9 specimens) 141
Figure 5-69 – Velocity-time relationships of hammer obtained from ANSYS for various reinforcement diameters for NSC specimens (Group 10 specimens)..141

Figure 5-70 – Velocity-time relationships of hammer obtained from ANSYS for various reinforcement diameters for SFRC specimens (Group 16 specimens) 141
Figure A-1 – Specifications of high-speed camera 1 ..... A1
Figure A-2 – Specifications of high-speed camera 2 ..... A2
Figure A-3 – Comparison of the motions for various times after impact obtained from the impact tests and the analyzed model for 60C12-1 ..... A3
Figure A-4 – Comparison of the motions for various times after impact obtained from the impact tests and the analyzed model for 60C26-1 ..... A4
Figure A-5– Comparison of the motions for various times after impact obtained from the impact tests and the analyzed model for 100C12-2 ..... A5
Figure A-6– Comparison of the motions for various times after impact obtained from the impact tests and the analyzed model for 100C26-1 ..... A6
Figure A-7– Comparison of the motions for various times after impact obtained from the impact tests and the analyzed model for 150C12-3 ..... A7
Figure A-8– Comparison of the motions for various times after impact obtained from the impact tests and the analyzed model for 150C26-1 ..... A8
Figure A-9– Comparison of the motions for various times after impact obtained from the impact tests and the analyzed model for 60C12R-2 ..... A9
Figure A-10– Comparison of the motions for various times after impact obtained from the impact tests and the analyzed model for 60C26R-2 ..... A10
Figure A-11– Comparison of the motions for various times after impact obtained from the impact tests and the analyzed model for 100C12R-2 ..... A11
Figure A-12– Comparison of the motions for various times after impact obtained from the impact tests and the analyzed model for 100C26R-3 ..... A12
Figure A-13– Comparison of the motions for various times after impact obtained from the impact tests and the analyzed model for 150C12R-2 ..... A13
Figure A-14– Comparison of the motions for various times after impact obtained from the impact tests and the analyzed model for 150C26R-3 ..... A14
Figure A-15– Comparison of the motions for various times after impact obtained from the impact tests and the analyzed model for 60SFRC35-1 ..... A15
Figure A-16– Comparison of the motions for various times after impact obtained from the impact tests and the analyzed model for 60SFRC35-3 ..... A16

Figure A-17– Comparison of the motions for various times after impact obtained from the impact tests and the analyzed model for 60SFRC35R-1..... A17
Figure A-18– Comparison of the motions for various times after impact obtained from the impact tests and the analyzed model for 100SFRC35-1 ..... A18
Figure A-19– Comparison of the motions for various times after impact obtained from the impact tests and the analyzed model for 100SFRC35R-1..... A19
Figure A-20– Comparison of the motions for various times after impact obtained from the impact tests and the analyzed model for 150SFRC35-2 ..... A20
Figure A-21– Comparison of the motions for various times after impact obtained from the impact tests and the analyzed model for 150SFRC35R-3..... A21

LIST OF TABLES

Table 2-1 – Comparison of results of tested specimens and analytical modeling (Kantar et al., 2011) 12
Table 2-2 – RHT concrete parameters input data (Riedel et al., 1999) 24
Table 2-3 – Concrete EOS: p-α EOS input parameters (Riedel et al., 1999) 25
Table 2-4 – The input data for softening failure model (Riedel et al., 1999) 26
Table 3-1 – Details of the beam specimens (CC specimens) 33
Table 3-2 – Details of the beam specimens (SFRC specimens) 34
Table 3-3 – Concrete mixture proportions 35
Table 3-4 – Properties of steel fibers 36
Table 4-1 – Average measured concrete compressive strengths of batches 60
Table 4-2 – Average measured concrete flexural tensile strengths of batches 62
Table 5-1 – Details related to modeling of beams 80
Table 5-2 – Details related to modeling of hammer 80
Table 5-3 – Details related to modeling of supports 81
Table 5-4 – Material properties of concrete defined in modeling (RHT Concrete model) 82
Table 5-5 – Material properties of steel defined in modeling 82
Table 5-6 – Erosion option settings 83
Table 5-7 – Determination of mesh size according to convergence study 87
Table 5-8 – Experimental and ANSYS impact velocities 87
Table 5-9 – Modified analysis parameters of RHT Concrete Model for LSC (Batch 1) 90
Table 5-10 – Modified analysis parameters of RHT Concrete Model for NSC (Batch 2) 91
Table 5-11 – Modified analysis parameters of RHT Concrete Model for SFRC (Batch 3) 92
Table 5-12 – Details of calculation of unit weights of specimens 94
Table 5-13 – Material properties of steel 103
Table 5-14 – Velocities and calculated energies obtained from the predicted velocity-time relationships 139

1. INTRODUCTION

1.1 General

Concrete members in structural applications may be subjected to impact loads coming from various sources such as vehicles, dropping or flying objects, explosions, etc. Behavior of concrete subjected to such loading shall be understood very well to design impact resistant reinforced concrete structures. Research on impact loading is usually hard and expensive due to the nature of loading. Therefore, researchers used a set-up called drop-hammer testing apparatus to simulate various impact effects on scaled members and finite element models to predict the behavior of these scaled members. Later, these finite element models were used to estimate the behavior of full-scale structures.

The modeling of concrete under impact loading using finite element became very important in recent days due to its accurate results compared to the experimental investigations and because it is saving time and money. Steel fibers drew the researchers' attention due to its ability to improve the concrete strength, ductility, post-cracking behavior, and toughness. Therefore, researchers used various finite element software packages available in the market to simulate and estimate the behavior of full-scale structures. Many researchers have used ANSYS Finite Element Software Package to model and study the behavior of conventional concrete (CC) and steel fiber reinforced concrete (SFRC) under impact loading.

1.2 Motivation

Understanding the behavior of concrete under impact loading is very important to evaluate the behavior of structures under loadings such as explosions, car crash loads, etc. Once this behavior is understood, impact resistant structures can be designed with enough confidence. This research is performed to understand the impact behavior of CC and SFRC.

1.3 Objectives and Scope

This research investigated the experimental and analytical behavior of unreinforced and reinforced concrete beams constructed from CC and SFRC under impact loading. Dramix ZP-305 type steel fibers were used for SFRC. Half of beam specimens were unreinforced and the others were reinforced with one 8 mm diameter steel reinforcement fixed at center of specimen cross section. Concrete compressive strengths used in this study were 12 MPa and 26 MPa for CC specimens and 35 MPa for SFRC specimens. Beams specimens had 60×60×500 mm, 100×100×500 mm, and 150×150×500 mm dimensions. The specimens were tested under impact loading using a drop-hammer testing apparatus having a weight of 58.5 N. This weight was dropped from various heights (1.20, 2.00, and 2.95 m for unreinforced specimens and 2.95, 3.00, and 3.04 m for reinforced specimens) based on specimen sizes. The slow motion videos of the tested specimens were recorded using a high-speed camera having a frame rate of 2000 fps. Experimental velocity-time curves for hammer were obtained by analyzing of recorded impact videos using the TEMA Motion Analysis Software. Beams, hammer, and supports were modeled in ANSYS Finite Element Analysis Program and parameters related to modeling were calibrated based on the test results. Riedel, Hiermaier, and Thoma (RHT) Concrete Model used in ANSYS Dynamic Explicit AUTODYN solver was studied and compared to CC and SFRC previous studies and stress-strain parameters were modified.

The most important difference of this research compared to the studies in the literature was that the material properties of concrete and analysis options in modeling were determined based on the motion of the steel hammer.

1.4 Thesis Organization

General introduction related to the subject of this thesis is given in Chapter 1.

The literature review related to application of impact loading on CC and SFRC are presented in Chapter 2. The background related to the material models for CC and SFRC is also explained in this chapter.

Details related to the experimental work are explained in Chapter 3.

In Chapter 4, the test results and discussion are presented.

An analytical work carried out to predict the velocity-time relationships of hammer is explained in Chapter 5.

Conclusions obtained from the test results and analyses are presented in Chapter 6. This chapter also includes recommendations for the future work.

2. BACKGROUND

2.1 Drop-Hammer Testing Apparatus

Different types of tests have been conducted to study the behavior the concrete under impact loading. The ACI Committee 544 (1988) classified the impact tests according to impacting mechanism. The monitored parameters during impact loading were classified as follows:

1. Weighted pendulum Charpy-type impact test.
2. Drop-weight test (single or repeated impact).
3. Constant strain-rate test.
4. Projectile impact test.
5. Split-Hopkinson pressure bar (SHPB) test.
6. Explosive test.
7. Instrumented pendulum impact test.

The tests conducted for impact loading in the literature were various, such as some of these tests were difficult to conduct. Due to the lack of data and variation of the results, no standard impact test method was specified until 1988. ACI Committee 544 (1988) proposed a drop-hammer impact test set-up to evaluate the impact resistance of concrete. Because this test set-up was simple, economical, and easy to construct, thus, it became widely used afterwards.

2.1.1 Banthia et al. (1989)

The authors of this research described the details of a drop-hammer testing apparatus, its instrumentation, calibration, and correction of internal loading. The impact loading was applied on the specimens as compression, tension, and three-point bending loading. The specimens consisted of five groups according to its concrete mixture as following:

1. Normal strength plain concrete.
2. High strength plain concrete.
3. Normal strength polypropylene concrete.
4. Normal strength SFRC.
5. Conventional reinforced normal strength SFRC.

The materials with low strain at failure were associated as brittle materials. Concrete showed stress-rate sensitivity in all three loading cases, compression, tension and flexure. This indicated that statistically evaluated concrete properties in the laboratory may not be directly used to predict the behavior of concrete under various stress-rates of impact loading such as blast and earthquake. The authors concluded that the constructed and instrumented drop-hammer testing apparatus might be successfully used to test concrete under impact loading. This research indicated that concrete was sensitive to loading stress-rate loading. Generally, the concrete was stronger and had more absorption capacity when subjected to impact loading than static loading.

2.1.2 Bindiganavile (2003)

The drop-hammer testing apparatuses might be designed for various hammer mass systems, dropping heights, and release mechanism methods. The University of British Columbia where this research was performed, conducted tests on three such apparatuses for a wide range of impact loading possibilities. One of the aims for this study was to implement a parametric study of drop-hammer testing to study the influence of dropping height and mass of hammer on the impact response of plain concrete. It was found that drop-hammer testing apparatus clearly affected the apparent stress-rate sensitivity. For investigation of test energy, it was established that dropping height was the most critical and important parameter for comparison of test data for all the machines. The author emphasized that any future standard for impact loading tests for concrete materials should give special importance to dropping height, not to the mass of hammer.

2.1.3 Ravindrarajah and Lyte (2007)

In this research, two grades of concrete mixtures having compressive strengths of 30 and 45 MPa (normal concrete and polystyrene aggregate concrete) were tested under impact loading using a drop-hammer testing apparatus having a 75 kgf (735.5 N) hammer and 0.462 m dropping height. The load-time impact responses were monitored. The results were used to describe the impact responses of concrete. The maximum load and contact time were taken in consideration as significant measurable quantities to identify the energy absorption capacity of concrete. The results presented that polystyrene aggregate concrete yielded better behavior than the normal concrete under impact loading due to its better quality of energy absorption since polystyrene beads expanded in concrete specimens. Under the impact loading, test represented that polystyrene concrete showed 28% increase in contact time and 18% lower maximum load compared to that of normal concrete.

2.1.4 Zhang et al. (2008)

Zhang et al. (2008) showed the main characteristics of their specially designed drop hammer testing apparatus to study the dynamic behavior of concrete specimens under impact loading. The apparatus and tested specimens are shown Figure 2-1 and Figure 2-2. They found some difficulty to analyze the crack propagation, fracture, and loading with fast ratio. The machine had two main parts, the mechanical installed structure and the data collection system. The mechanical structure consisted of steel hammer moving down and guided by two parallel steel columns impacting the specimen at top center with energy of 7860 J. The data collection system consisted of piezoelectric force rate sensors, accelerometers, and fiber optic photoelectric sensors with signal and oscilloscope conditioners.

The authors presented the results of some preliminary tests that showed the sensitivity of specimens to the rate of loading. The results showed that the drop-hammer testing apparatus was successfully used to investigate the behavior of concrete structure under impact load. Based on the results, it was concluded that concrete had higher strength and more energy absorption capacity under impact loading than under static loading as shown in Figure 2-3.

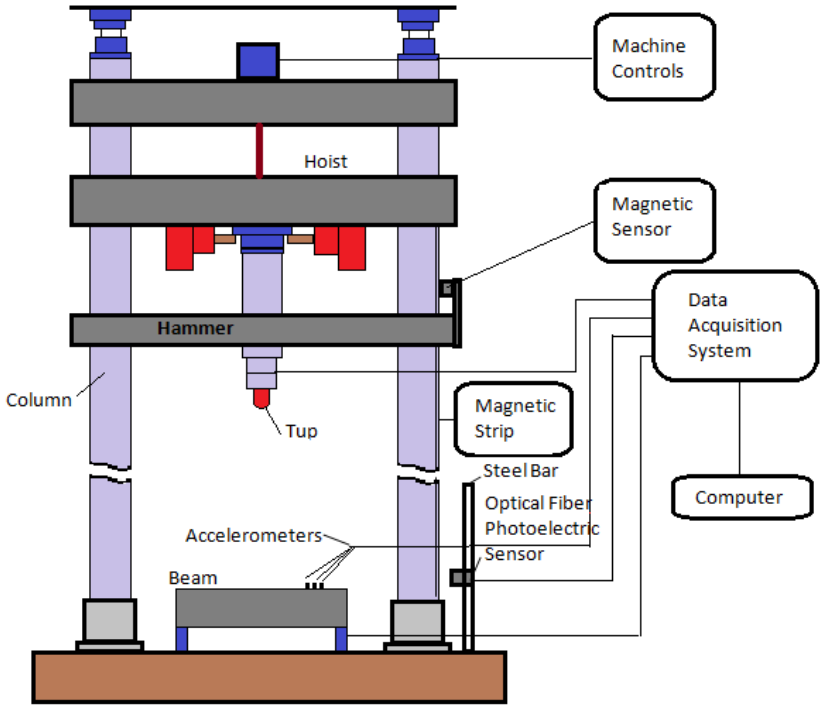

Figure 2-1 – Schematic view of the drop-hammer testing apparatus (Zhang et al., 2008)

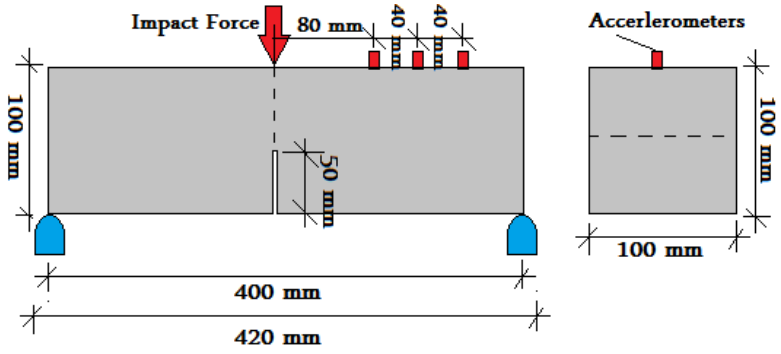

Figure 2-2 – Geometry of tested specimens and locations of accelerometers (Zhang et al., 2008)

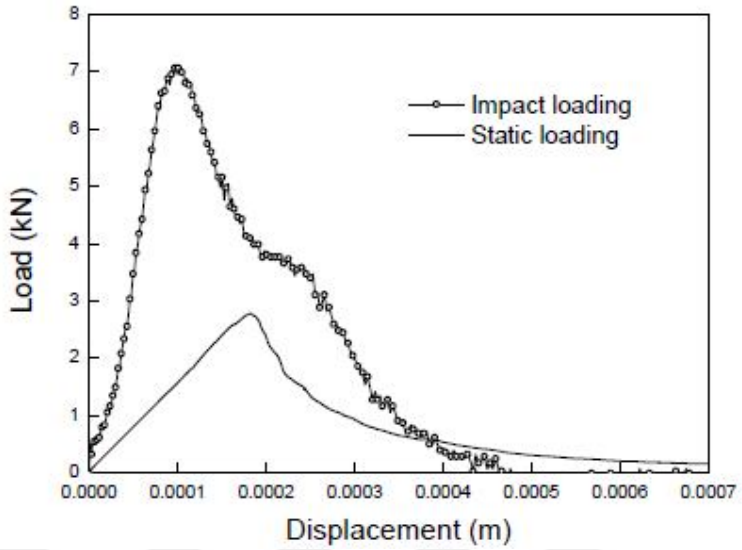

Figure 2-3 – Experimental load-displacement relationships (Zhang et al., 2008)

2.1.5 Rao et al. (2011)

Rao et al. used a drop-hammer testing apparatus shown in Figure 2-4. In this study concrete beam specimens having mixtures consisted of recycled coarse aggregate material (RCA) were subjected to impact loading with low velocity. The amounts of recycled aggregate concrete were the test variables. The RCA was supplied from demolition of reinforced concrete culverts. Four concrete mixtures having 0%, 25%, 50%, and 100% RCA were prepared. The impact loading was applied to the specimen having 100×150×1150 mm dimensions. The results indicated that the mixture having 25% RCA did not have any effect on concrete strength. It was stated that for the same impact energy, the mixtures having 100% and 50% RCA were significantly behaved better than the specimens having 25% RCA.

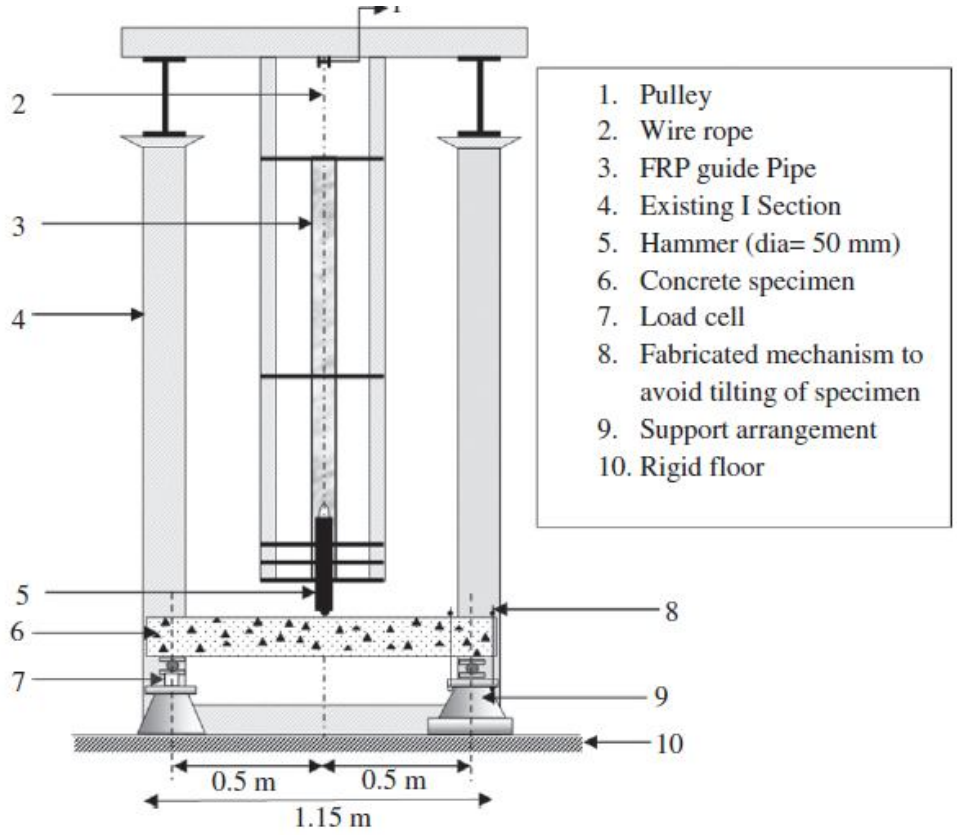

Figure 2-4 – Schematic view of drop-hammer testing apparatus (Rao et al., 2011)

2.1.6 Kantar et al. (2011)

Kantar et al. (2011) stated according to Kishi et al. (2002) and Barr and Baghli (1988) that there was no confirmed standards or systems for impact loading test set-up. But according to Siewert et al. (1999) (as cited in Kantar et al., 2011), ASTM E23 regulations improved the test set-up implementation safely and assigned good beginning points for the framework of impacts experiments.

In this research, total of ten specimens having 710×150×150 mm dimensions were tested under impact loading using a steel hammer dropping from various heights. Five of the specimens were cast using normal strength concrete without reinforcement and the remaining five had high-strength concrete mixture without reinforcement. The acceleration resulted from the impact load was measured wrt. time. For all the specimens, the velocity changes, displacement, and energy were calculated as shown in Figure 2-5. The modes of failure of normal- and high-strength

concrete specimens are shown in Figure 2-6. The researchers in this study used ABAQUS software package to model the behavior. The modeling yielded compatible output results with experimental specimens as shown in Figure 2-7 and Table 2-1. The results of the study stated that the generation of the model was very hard due to the lack of previously obtained experimental data and standard test procedure. It was found that the number of drops was a very important parameter for impact loading. It was seen that the observed value of number of drops for high compression strength specimens were significantly higher than that of specimens with normal compressive strength. The difference of value of number of drops between high and normal compressive strength specimens decreased when the dropping height is increased. The specimens with normal strength concrete had more ductility and more displacement than that of high-strength ones.

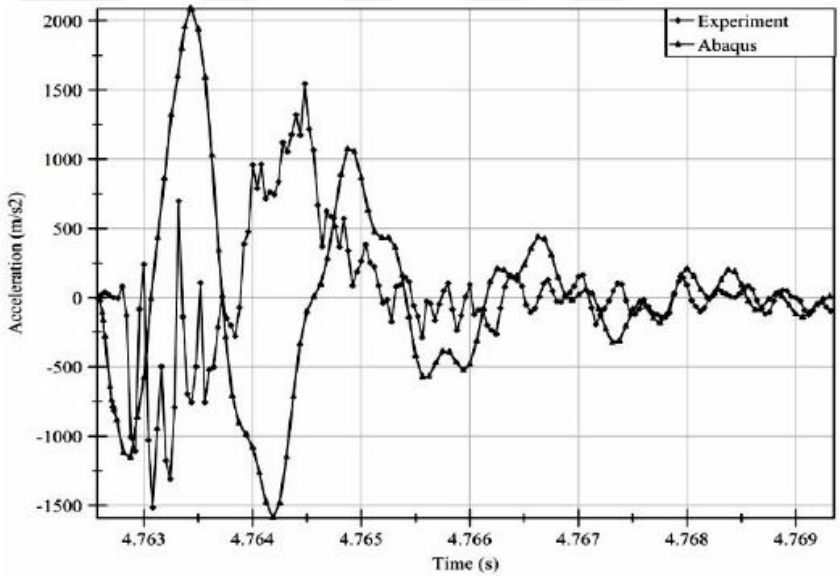

Figure 2-5 – Experimental and analytical acceleration-time relationships obtained by Kantar et al. (2011)

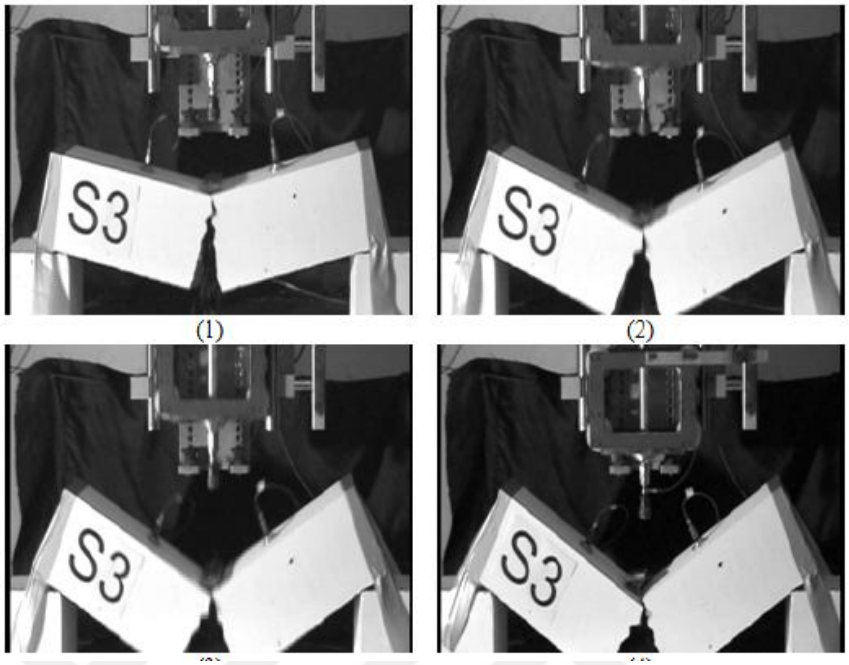

Figure 2-6 – Typical failure mode of specimens obtained by Kantar et al. (2011)

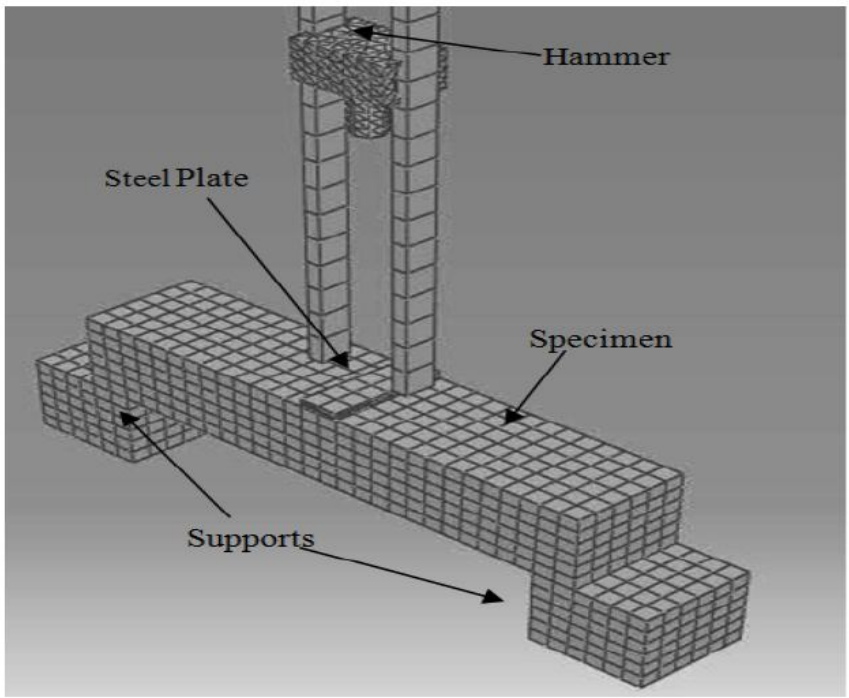

Figure 2-7 – Modeling of specimens by Kantar et al. (2011)

Table 2-1 – Comparison of results of tested specimens and analytical modeling (Kantar et al., 2011)

Experimental/ABAQUS Acceleration Ratio		Energy		Experimental/ABAQUS Energy Ratio
		Experimental	ABAQUS	
Min.	Max.			
1.45	1.89	1.346	3.741	0.36
0.67	0.91	1.769	4.232	0.42
0.74	0.95	2.649	4.826	0.55
0.86	1.17	1.742	5.649	0.31
0.68	1.46	3.159	6.221	0.51
0.90	1.06	1.295	3.288	0.39
1.09	1.18	1.689	3.702	0.46
0.89	1.22	2.090	4.293	0.49
0.73	1.27	2.219	5.142	0.43
0.65	1.75	1.797	5.510	0.33

2.2 Impact Loading on CC and SFRC

Since the early 1800's, concrete as a material was used for construction worldwide. It was known that concrete material was weak in tension. The failure of concrete under tensile stresses was a sudden failure without any warnings. This brittle behavior was due to its weakness under tensile forces. This behavior was clearly not desirable for such a construction material. Therefore, concrete required reinforcement against tensile forces to enhance its brittle behavior and to improve its tensile strength.

Through time, various materials have been added to concrete in order to enhance its properties especially in tension. The steel fiber was one of the materials that became widely used addition. This addition produced SFRC which improved many specific characteristics and properties of concrete such as compressive strength, flexural tensile strength, ductility, flexural toughness, crack resistance, and abrasion resistance. Lately, SFRC technology has received more attention from researchers and the concrete industry.

2.2.1 Mohammadi et al. (2009)

Mohammadi et al. (2009) investigated CC and SFRC specimens having various SFRC ratios impact loading. A total of 108 specimens having 100×100×500 mm dimensions were used. The specimens consists three volume fractions of corrugated steel fibers, i.e. 1.0%, 1.5%, and 2.0%. For each SFRC mix, two different steel fiber

sizes, 0.6×2.0×25 and 0.6×2.0×50 mm, were used. Number of blows of the falling hammer required to induce first visible crack and the failure of specimen were measured. The results showed that concrete containing long fibers with a 2.0% volume fraction was the most effective under impact loading.

2.2.2 Weidner et al. (2012)

Weidner et al. (2012) studied the performance of concrete cylinders subjected to impact loading using a drop-hammer testing apparatus. The apparatus consisted of a steel hammer falling from a height of 16 ft. (4.88 m). The dropping height was changed throughout the tests. 4×8 in. (101.6×203.2 mm) cylinder specimens were cast with and without steel fibers. They also performed tests at elevated temperatures. A data collection system was used to monitor the strains and load data. Two high-speed cameras were also used to record the impact videos.

2.2.3 Wang and Wang (2013)

Five groups of steel fiber light-weight concrete (SFLWC) with various steel fiber ratios of 0.0%, 0.5%, 1.0%, 1.5% and 2.0% were tested to study the influence of steel fibers on the mechanical properties under static and impact loading. The mechanical properties investigated under static loading were compressive strength, tensile strength, flexural strength for first crack, flexural strength, flexural toughness, etc. After implementation of series of drop-hammer tests, the impact resistance was also obtained for SFLWC specimens. The test results represented that addition of steel fiber can greatly enhance mechanical properties such as the splitting strength under tensile loading, strength under flexural loading, toughness under flexural loading and impact resistance. However, the influence of steel fibers on compressive strength was limited. The test results showed that there was a logarithmic relationship between flexural toughness energy of static flexural test and drop-hammer tests. Furthermore, the researchers suggested that the optimum volume ratio of steel fibers was 1 to 1.5%.

2.3 Material Models

2.3.1 CC in Compression

Based on the research performed by Bello (2014), Abdussalam (2015), Faeq (2015), and Abdelmola (2018), the best model to for CC in compression was determined as Popovics (1973). Therefore, Popovics (1973) model was used as the material model to study the compressive behavior of CC in this research. The non-linear equation for CC proposed by this model was as follows:

$$f_c = f_{ck}\frac{\frac{\varepsilon_c}{\varepsilon_{co}}\, n}{n - 1 + \left(\frac{\varepsilon_c}{\varepsilon_{co}}\right)^{nk}}$$ Equation 2-1

where, f_c is the stress at any point on the curve, f_{ck} is the concrete compressive strength obtained from the cylinder test, ε_c is the strain corresponding to the stress *fc*, and ε_{co} is the strain at peak stress.

The strain at peak stress, ε_{co}, constants *n* and *k*, and modulus of elasticity of concrete (E_c) is defined as follows:

Error! Reference source not found. Error! Reference source not found. Error! Reference source not found. Error! Reference source not found.

2.3.2 SFRC in Compression

Based on the research performed by Bello (2014), Abdussalam (2015), Faeq (2015), and Abdelmola (2018), the best model to for SFRC in compression was determined as Ezeldin and Balaguru (1992). Therefore, Ezeldin and Balaguru (1992) model was used as the material model to study the compressive behavior of SFRC in this research. The analytic expression, that was based on the one proposed by Carreira and Chu (1985) for uniaxial compression of conventional plain concrete, included a material parameter β, and it was the slope at the curve descending part. Ezeldin and Balaguru (1992) stated the following as model for compression stress-strain curve for SFRC:

$$\frac{\sigma_c}{f_{cf}} = \beta \frac{\left(\frac{\varepsilon}{\varepsilon_{pf}}\right)}{\beta - 1 + \left(\frac{\varepsilon}{\varepsilon_{pf}}\right)^{\beta}}$$ Equation 2-2

where, f_{cf} is the compressive strength of SFRC, ε is the strain, ε_{pf} is the strain at peak stress. β is the factor related to the effect of fiber on the descending part of the curve.

$$f_{cf} = f_c + 3.51\ (RI)$$ Equation 2-3

$$RI = W_{fc} x\ l_f / d_f$$ Equation 2-4

$$\varepsilon_{pf} = \varepsilon_{co} + 446x10^{-6}\ (RI)$$ Equation 2-5

$$\varepsilon_{co} = 0.002$$

$$\beta = 1.093 + 0.7132\ (RI)^{-0.926}$$ (For hooked end fibers) Equation 2-6

where, *RI* is the fiber reinforcement index by weight of straight fibers.

2.3.3 SFRC in Tension

Based on the research performed by Bello (2014), Abdussalam (2015), Faeq (2015), and Abdelmola (2018), the best model to for SFRC in tension was determined as Soranakom et al. (2008). Therefore, Soranakom et al. (2008) model was used as the material model to study the tensile behavior of SFRC in this research. The model included a linear stress-strain part up to the tensile strain point where the crack happened. After which the post-cracking behavior is characterized by a decaying stress-strain relationship. The contribution of fibers in the post-cracking response was represented by an average constant post-cracking tensile parameter, σ_p which is related to the fiber volume fraction and bond behavior of the matrix.

$$\sigma_{cr} = E_{cr} = 0.56\sqrt{f_c}\ (MPa)$$ Equation 2-7

$$E = 4733\sqrt{f_c}\ (MPa)$$ Equation 2-8

where, σ_{cr} is the cracking stress and f_c is the maximum uniaxial cylinder compression strength. The first crack tensile strain of the SFRC model was obtained assuming Hooke's Law as:

$$\varepsilon_{cr} = \frac{\sigma_{cr}}{E} = \frac{0.56\sqrt{f_c}}{4733\sqrt{f_c}} = \frac{6.7\sqrt{f_c}}{57{,}000\sqrt{f_c}} = 118 \text{ microstrain} \qquad \text{Equation 2-9}$$

$$\beta_{tu} = \frac{\varepsilon_{tu}}{\varepsilon_{cr}} = \frac{0.025}{118\times10^{-6}} \approx 212 \qquad \text{Equation 2-10}$$

$$\sigma_p = \mu E \varepsilon_{cr} : \mu(0 \le \mu \le 1) \qquad \text{Equation 2-11}$$

According to RILEM Model (2003):

$$\varepsilon_{tu} = 0.025 \qquad \text{Equation 2-12}$$

The parameter μ represent the post-cracking strength as a fraction of the cracking tensile strength, σ_{cr}. The idealized tension model proposed by Soranakom et al. (2008) is shown in Figure 2-8.

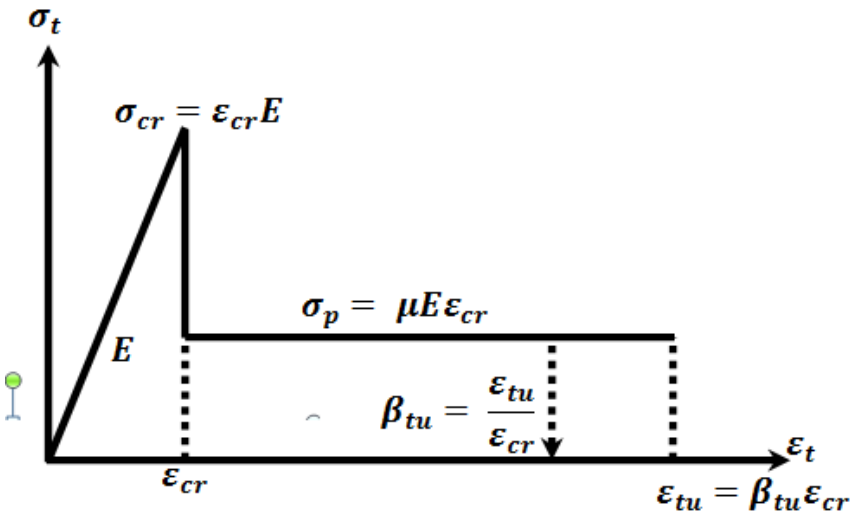

Figure 2-8 – Idealized tensile stress-strain relationship of SFRC (Soranakom et al., 2008)

2.3.4 Riedel, Hiermaier, and Thoma (RHT) Concrete Model in ANSYS (Riedel et al. 1999)

The RHT Concrete model is advanced plasticity model for brittle materials developed by Riedel et al. (1999). This model is readily available in ANSYS AUTHODYN with default values for concrete C35 and C135 only.

The RHT constitutive model is a combined model consisting plasticity and shear damage with deviatoric stress in the material which is limited by a generalized failure surface through.

$$f\left(P, \sigma_{eq}, \Theta, \dot{\varepsilon}\right) = \sigma_{eq} - Y_{TXC(P)} * F_{CAP(P)} * R_{3(\Theta)} * (F)_{RATE(\dot{\varepsilon})} \qquad \text{Equation 2-13}$$

This failure surface can be used to represent the aspects of the response of geological materials such as pressure hardening, strain hardening, strain rate hardening, strain softening, and third invariant dependence. In stress space, three pressure-dependent surfaces, elastic limit surface, failure surface, and residual surface.

2.3.4.1 Fracture Surface

The fracture surface is represented as follows:

$$Y_{TXC} = f_c^{'}\left[A_{Fail}\left(P^{*} - P^{*}_{spall} F_{RATE}\right)^{N_{Fail}}\right] \qquad \text{Equation 2-14}$$

where, $f_c^{'}$ is the cylinder strength, A_{Fail} and N_{Fail} are parameters defined by user, P^{*} is pressure normalized with respect to $f_c^{'}$, P^{*}_{spall} is the normalized hydrodynamic tensile limit, and F_{RATE} is a rate dependent enhancement factor.

There is an option to modify the fracture surface to fit through the experimentally observed points at low pressures, while detained the flexibility to match points at high pressures. This feature of fracture surface is described in Figure 2-9.

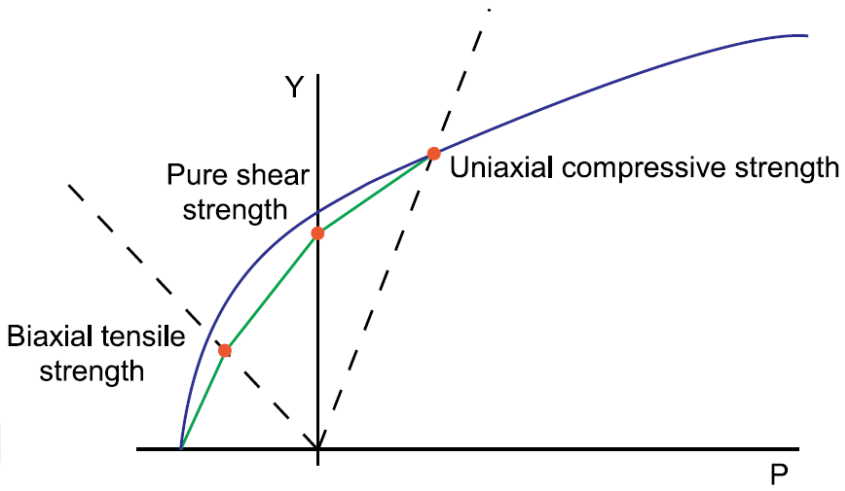

Figure 2-9 – RHT representation of compressive meridian (Riedel et al., 1999)

2.3.4.2 Tensile and Compressive Meridians

In RHT model the difference between compressive and tensile meridian are represented in terms of material strength through the term of third invariant dependence (R_3).

The third invariant dependence (R_3) can be used to represent the reduction in concrete strength that is observed under triaxial extension compared to triaxial compression. The term of third invariant dependence (R_3) is formulated according to the following expression:

$$R_3 = \frac{2\left(1-Q_2^2\right)\cos\theta+(2Q_2-1)\sqrt{4\left(1-Q_2^2\right)\cos^2\theta-4Q_2}}{4\left(1-Q_2^2\right)\cos^2\theta+(1-Q_2)^2} \qquad \text{Equation 2-15}$$

where,

$$\cos(3\theta) - \frac{3\sqrt{3}J_3}{2^{2/3}\sqrt{J_2}} \qquad \text{Equation 2-16}$$

$$Q_2 = Q_{2,0} + BQ.P^* \qquad \text{Equation 2-17}$$

and

$$0.5<Q_2<1, BQ = 0.0105$$ Equation 2-18

The input parameter $Q_{2.0}$ is defined as the strength ratio at zero value pressure and the coefficient term BQ which expresses the transition of fracture surface from brittle to ductile through transition from approximately triangular in from a circular with increasing pressure. The third invariant dependence (R_3) is shown in Figure 2-10.

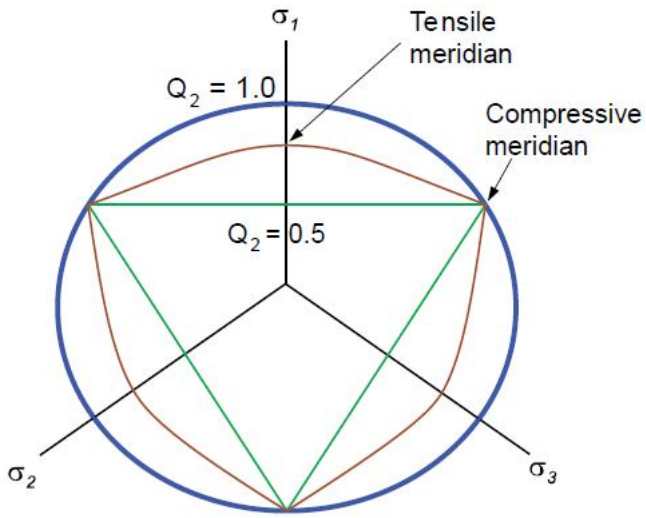

Figure 2-10 – The third invariant dependence (R_3) (Riedel et al., 1999)

2.3.4.3 Strain Hardening

Strain hardening is a bi-linear curve through defining the elastic limit surface and hardening slope. The user defines the (elastic strength/f_c) and (elastic strength/f_t) ratios by scaling the limit surfaces down from surface and hardening slope. Therefore, the pre-peak fracture surface is defined through interpolation between the fracture surfaces and elastic using the hardening slope, $(\frac{G_{plastic}}{G_{elastic}-G_{plastic}})$. Strain hardening according to:

$$Y^* = Y_{elastic} + \frac{\varepsilon_{pl}}{\varepsilon_{pl}(pre-softening)}(Y_{fail} - Y_{elastic})$$ Equation 2-19

where,

$$\varepsilon_{pl}(pre-softening) = \frac{Y_{fail} - Y_{elastic}}{3G} * (\frac{G_{elastic}}{G_{elastic} - G_{plastic}})$$ Equation 2-20

The bi-linear strain hardening function in uniaxial compression case is shown in Figure 2-11.

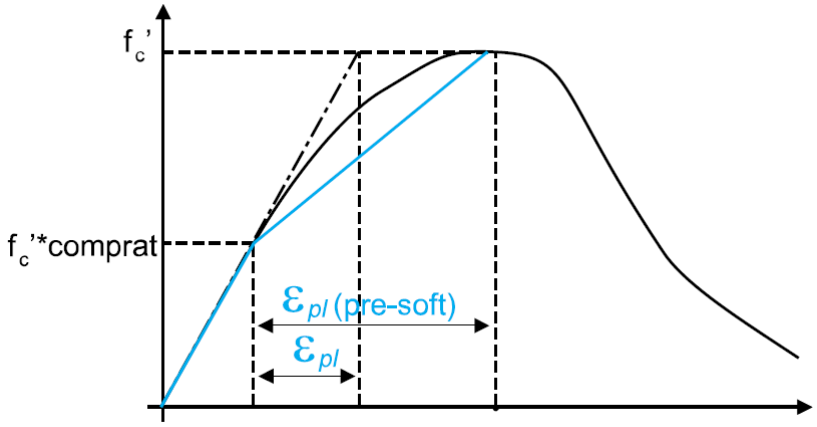

Figure 2-11 – Bilinear strain hardening function in uniaxial compression case (Riedel et al., 1999)

2.3.4.4 Shear Damage

Shear damage is supposed to increase due to inelastic deviatoric strains (shear cracking) using the following relationships:

$$D = \sum \frac{\Delta\varepsilon_{pl}}{\varepsilon_p^{failure}}$$ Equation 2-21

$$\varepsilon_p^{failure} = D_1(P^* - P^*_{small})^{D_2}$$ Equation 2-22

where D_1 and D_2 are material constants used to show the damage effective strain as a function of pressure. Accumulated damage can have two influences in the model; reduction in strength (strain softening) and reduction in shear stiffness.

2.3.4.5 Reduction in Strength (Strain Softening)

The present fracture surface for a specified level of damage is scaled down from the intact surface using the following expressions:

$$Y^*_{fractured} = (1 - D)Y^*_{failure} + DY^*_{residual}$$ Equation 2-23

where,

$$Y^*_{residual} = Min[B(P^*)^M, Y_{XTC} * SFMAX]$$ Equation 2-24

Y_{XTC}*SFMAX term is used to set the limits of maximum residual shear strength (for material that damaged completely) and maximum fracture strength ratio (SFMAX) of the present fracture strength.

2.3.4.6 Reduction in Shear Stiffness

The present shear modulus is defined through the following:

$$G_{fractured} = (1 - D)\,G_{elastic} + DG_{residual}$$ Equation 2-25

2.3.4.7 Porous Collapse Damage

This efficiently leads to the presumption that porous compaction results in a reduction in deviatoric strength.

Figure 2-12 shows the final combination of elastic, fracture and residual failure surfaces.

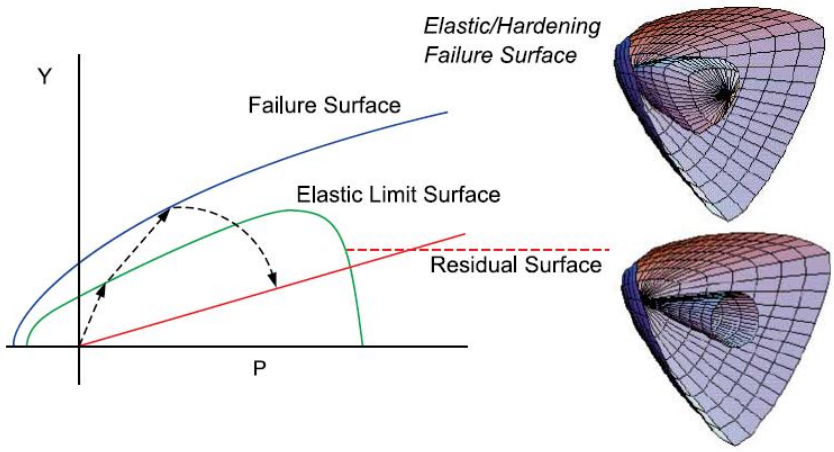

Figure 2-12 – RHT elastic, fracture, and residual failure surfaces (Riedel et al., 1999)

2.3.4.8 Strain Rate Effects

Strain rate effects are shown through reduction in fracture strength with plastic strain rate. Two various terms can be used for tensile and compression with linear interpolation that used in the mediate pressure regime.

$$F_{Rate}\begin{cases} 1+\left(\frac{\varepsilon}{\varepsilon_0}\right)^{\alpha} for\ P > 1/3f_c(compression) \\ 1+\left(\frac{\varepsilon}{\varepsilon_0}\right)^{\delta} for\ P > 1/3f_t(tensile) \end{cases}$$

Equation 2-26

where ε_0 = 0.000003 in tension and 0.00003 in compression.

2.3.4.9 Tensile Failure

Tensile failure is defined by default using a hydrodynamic tensile limit. The material maximum tensile pressure is limited to the following expression:

$$P = \max[(1-D) * P_{min}, P(\rho, e)]$$

Equation 2-27

By using this option, the user is not required to enter any other additional input value since the value of P_{min} is derived from f_t, which forms part of the input for the strength model.

The model data for concrete with cube strengths of 35 MPa and 140 MPa are already included in the distributed material library in ANSYS AUTODYN.

According to ANSYS Explicit Dynamics Analysis Guide, 2015; "The model is formulated such that input can be scaled with the cube strength, f_c i.e. you can retrieve one of the two concretes in the library, change its cube strength to match the concrete you want to model and the remaining terms will automatically scale proportionately. The resulting data set will be approximate and we recommend validation of the material data against experimental characterization tests in all cases."

The RHT concrete parameters input data are shown in Table 2-2.

Table 2-2 – RHT concrete parameters input data (Riedel et al., 1999)

Name	Symbol	Units	Notes
Shear Modulus	G	Stress	
Compressive Strength	f_c	Stress	
Tensile Strength	f_t/f_c	None	
Shear Strength	f_s/f_c	None	
Intact failure surface constant A	A_{FAIL}	None	
Intact failure surface constant N	N_{FAIL}	None	
Tens./Comp. Meridian ratio	$Q_{2.0}$	None	
Brittle to Ductile Transition	BQ	None	
Hardening Slope		None	$G_{ei}/(G_{ei}-G_{pi})$
Elastic Strength/fc		None	
Elastic Strength/ft		None	
Fracture Strength Constant	B	None	
Fracture Strength Exponent	m	None	
Compressive strain rate exponent	α	None	
Tensile strain rate exponent	δ	None	
Maximum fracture strength ratio	SFMAX	None	
Use cap on elastic surface		None	Option: Yes (default), No
Damage constant	D_1	None	
Damage constant	D_2	None	
Minimum strain to failure		None	
Residual Shear modulus fraction		None	
Tensile Failure		Hydro, Principal Stress	
Principal Tensile Failure		Stress	
Maximum Principal Stress Difference/2		Stress	
Crack softening		None	Option: Yes (default), No
Fracture energy	G_f	Energy/Area	
Flow Rule		None	Option List: Radial Return, No Bulking (Default), Bulking (Associative)
Erosion Strain / Instantaneous Geometric Strain		None	

Table 2-3 – Concrete EOS: p-α EOS input parameters (Riedel et al., 1999)

Name	Symbol	Units	Notes
Parameter A1	A1	Stress	Even equivalent to the material bulk modulus
Parameter A2	A2	Stress	
Parameter A3	A3	Stress	
Parameter B0	B0	Stress	
Parameter B1	B1	Stress	
Parameter T1	T1	Stress	This value will be automatically set to the material bulk modulus if entered as zero.
Parameter T2	T2	Stress	
Solid Density	ρ_s	Density	Density at pressure for fully compacted material
Porous Density	ρ_p	Density	
Porous Sound-speed		Velocity	
Initial compaction pressure	P_e	Stress	
Solid compaction pressure	P_s	Stress	
Compaction Exponent	N	None	

2.3.4.10 Crack Softening Failure

The tensile crack softening model is a damage model based on fracture energy that can be used with many various failure types for its initiation models to supply a gradual decrease in the ability of an element to carry on tensile tress. The model is initially used for study failure of brittle materials, but has been used to other materials to decrease the effects of mesh dependency. Failure initiation model is applicable base on any of the principal tensile failure models such as, Hydro, Principal Stress-Strain. A softening linear slope is defined then to decrease the ultimate possible main tensile stress in the material as a function of strain of crack. This softening linear slope is defined as a function of the element local size and the material parameter, the fracture energy, G_f. which represent the area under linear slope as shown in Figure 2-13.

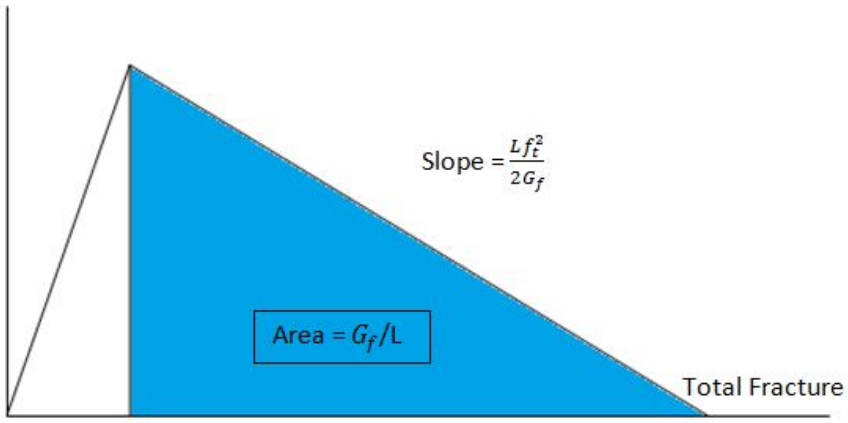

Figure 2-13 – Tensile crack softening failure and Fracture energy G_f (Riedel et al., 1999)

The algorithm of crack softening can be used only with solid elements. It can be used in combination with any solid equation of state, plasticity model or brittle strength model. The Table 2-4 shows the input data for softening failure model.

Table 2-4 – The input data for softening failure model (Riedel et al., 1999)

Name	Symbol	Units	Notes
Fracture Energy	G_f	Energy/Area	
Flow rule			Option List: Radial Return, No Bulking (Default), Bulking (Associative)

2.4 Modeling Impact Behavior of CC and SFRC

Many researchers have modeled the impact behavior of CC and SFRC using finite element software packages.

2.4.1 Leppänen (2006)

Leppänen (2006) achieved modeling of crack softening and strain rate dependency in tension using AUTODYN. The researcher implemented parametric studies and compared numerical analyses with conducted experiments in the literature. It was concluded that the penetration depth was mainly dependent on concrete compressive strength. For a correct model behavior, the importance of tensile strength, fracture

energy, and strain rate were emphasized. It was also stated that the accuracy of the results in the numerical analyses of concrete subjected to impact loading was improved by using the law of bilinear softening and the tension modified strain rate dependency.

2.4.2 Kantar et al. (2011)

Kantar et al. (2011) modeled the specimens subjected to drop-hammer loading. The tests results in terms of acceleration-time diagrams and stress distribution were compared to the results of the model constructed using ABAQUS software. They stated that ABAQUS software had critical assumptions and was very hard to model the behavior of beams due to its complexity.

2.4.3 Nyström and Gylltoft (2011)

Nyström and Gylltoft (2011) conducted numerical study and modeling of impact load applied on plain and SFRC using ANSYS. The researchers used RHT material model available in ANSYS Dynamic Explicit library with some modifications including turning off the strain-rate dependence for the ultimate tensile strength, using a principal-stress tensile-failure model instead of the hydrodynamic tensile failure model and using a bi-linear crack-softening relation instead of a linear one. It was concluded the model simulated the behavior of the specimens reasonably.

2.4.4 Haido and Musa, (2013)

Haido and Musa, (2013) performed modeling to investigate the cracking strength for SFRC shallow beams that subjected to impact loads using ANSYS Software. It was stated that fiber reinforced concrete (FRC) shallow beams were successfully modeled using tetrahedral elements with RHT nonlinear concrete model.

2.4.5 Subramani et. al. (2014)

Subramani et. al. (2014) conducted non-linear finite element modeling using ANSYS Software Package to investigate the behavior of reinforced concrete structures subjected to explosive loading. Researchers stated that performance of finite element

analysis combined with blast and impacts of fragments were very complex. The RHT model in AUTODYN showed good ability to predict both the blast penetration depth and the crater size in concrete under projectile impact. For the mesh dependency, the obtained results were in good agreement.

2.4.6 Yılmaz et al. (2014)

Yılmaz et al. (2014) conducted tests and modeling using ANSYS for unreinforced beam specimens under static and low-velocity impact loading. The experimental and ANSYS outputs including load-displacement relationships, energy dissipation capacities, stiffnesses, and failure modes were discussed and compared. It was concluded that the numerical results obtained from ANSYS modeling were in good agreement with the experimental results.

2.4.7 Galuta and Regig (2017)

Galuta and Regig (2017) implemented numerical modeling of reinforced concrete panels under high-velocity impact loading to study the effect of erosion input parameter in ANSYS RHT model. It was stated that the erosion strain value and mesh size had significant effects on the residual velocity of the impacting object and the depth of penetration of concrete panel.

2.4.8 Hokes et al. (2006)

Hokes et al. (2006) performed modeling using ANSYS Finite Element Software Package on experimental study that was conducted by Strauss et al. (2014). It was stated that the main problem faced with nonlinear material model was the existence of material parameters that was not known in advance. The model became complicated due to the difficulty of choice of the correct type of element and the correct bond between elements of meshes. Hokes et al. (2006) concluded that the solution for the above problem could be achieved by applying an optimization technique by comparing the model output curve with the experimental curve and minimizing the difference between them.

2.4.9 Badiger and Malipatil (2014)

Badiger and Malipatil (2014) conducted four point bending modeling and analysis using ANSYS for reinforced concrete beams. The researchers stated that modeling beam without steel plates at four points of loading and supports showed more cracks than the beam with steel plates. The researcher concluded that ANSYS Finite Element Software Package could be used successfully as modeler to analyze reinforced beams with accurate results.

2.4.10 Vaiciunas et al. (2011)

Vaiciunas et al. (2011) performed experimental study and modeling to investigate the behavior of reinforced concrete slab under impact loading. The researchers conducted drop-hammer tests using steel hammer with 80 kgf weight falling from 2 m height with a velocity of 6.3 m/s. The finite element modeling was performed by ANSYS Software Package. High-speed camera was used to record testing videos. The researchers concluded that comparison of experimental and finite element modeling outputs showed reasonable agreement.

2.4.11 Vasudevan et al. (2013)

Vasudevan et al. (2013) achieved experimental and non-linear finite element modeling to study the behavior of reinforced concrete beam under impact loading. The experimental work including drop-hammer tests on 250×200×2000 mm beam specimens. The non-linear finite element modeling performed by ANSYS Software Package. The researchers concluded that ANSYS results were in close agreement with the experimental results.

2.5 High-Performance Fiber Reinforced Cementitious Composites (HPFRCC)

FRC composites can be cateogrized into three groups:

- **Group 1:** FRC with low fiber volume fractions (<1%) which is mostly used to decrease shrinkage cracks, as stated by Balaguru and Shah (1992).

- **Group 2:** FRC with moderate fiber volume fractions (1% - 2%) which shows enhanced mechanical properties such as better fracture toughness, greater modulus of rupture (MOR), and enhanced impact resistance.
- **Group 3:** FRC with high fiber volume fractions (2%<) which has a different strain-hardening behavior than the first two groups.

FRC with high fiber volume fractions was first developed by Naaman and Reinhardt (1996) from a FRC matrix without coarse aggregates, and stated as fiber reinforced cement mixture or mortar. The most important advantages of this material that was called as HPFRCC compared to plain concrete and FRC was its high tensile ductility and the strain hardening response. The tensile stress-strain relationships of plain concrete, FRC, and HPFRCC are shown in Figure 2-14. Details of the regions in the tensile stress-strain relationship of FRC and HPFRCC are shown in Figure 2-15. The cracking behavior of plain concrete and FRC was similar since there was one crack in the tested specimens. However, in HPFRCC there were multi-crack throughout the length of the specimen.

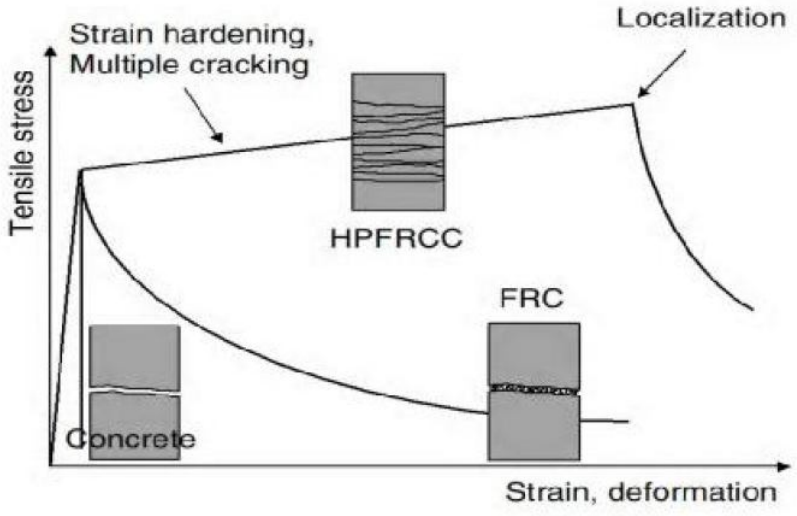

Figure 2-14 – Tensile stress-strain relationships of plain concrete, FRC, and HPFRCC (Naaman and Reinhardt, 1996)

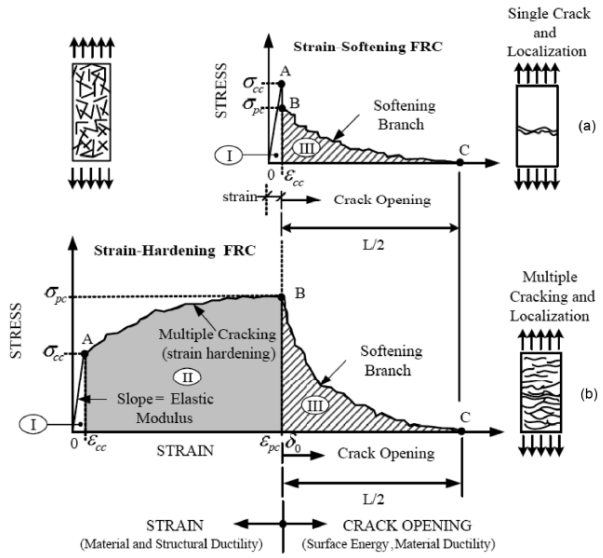

Figure 2-15 – Details of the regions in the tensile stress-strain relationship of (a) FRC and (b) HPFRCC (Naaman and Reinhardt, 1996)

Kim et al. (2009) implemented experimental study to investigate the behavior of HPFRCC and normal concrete and conventional FRC. The authors declared that the benefits of using HPFRCC included high load carrying capacity, better durability, enhanced ductility, and greater energy absorption. These advantages were especially preferred for structures subjected to special loading conditions such as earthquake, impact and blast.

The SFRC mixture used in this research was a Group 2 FRC having moderate steel fiber volume fraction. The behavior of this mixture in tension was completely different from HPFRCC. The tested specimens in this research had one significant crack as shown in Chapter 4.

3. EXPERIMENTAL PROGRAM

3.1 General

This chapter describes the experimental program to investigate impact loading on concrete beams. Test specimens, material properties, test set-ups, instrumentation, test procedures are summarized in the following sections.

3.2 Test Specimens

The main parameters related to the test specimens were beam dimensions, reinforcement, and type of concrete (low-strength concrete-LSC, normal-strength concrete-NSC, and SFRC). Three different concrete beam specimens having 60×60×500, 100×100×500, and 150×150×500 mm dimensions were used in this research. For each batch, half of the specimens were reinforced with one ϕ8 mm steel reinforcement located at geometric centroid of the cross-section of the beam specimen. Other half did not have any reinforcement. Three concrete batches were cast (namely C12, C26, SFRC35) in the scope of this research. The first batch having 12 MPa concrete target strength was simulating the LSC applications; the second batch having 26 MPa concrete target strength was simulating the NSC applications; and the third batch having 35 MPa concrete target strength was simulating the concrete applications having steel fibers. Minimum three cylinders having 150×300 mm dimensions and minimum three prismatic beams having 150×150×600 mm dimensions were cast for each batch to evaluate the material properties. The details of the testing program are shown in Table 3-1 and Table 3-2. The notation for the labels of the specimens first includes two or three digit number indicating the dimensions of the cross-section of the specimen, eg. 60 is for 60×60 specimen, etc. The letter/letters after these numbers indicate/indicates the concrete type, eg. C stands for CC and SFRC stands for SFRC. The numbers after concrete type indicate the concrete compressive strength in MPa, eg. 26 means 26 MPa. After concrete strength, if there is a letter “R” it shows that the specimen is reinforced. If no letter appears after the compressive strength, that means the specimens are unreinforced. The last numbers after “-” indicates the repeatation of the specimen for each group, eg. -1, -2, and -3. Batch 1 specimens were cast on 28/03/2017 and tested on 26/04/2017 (Group 1, 3, 5, 7, 9, and 11 specimens). Batch 2 specimens were cast on

21/08/2017 and tested on 20/09/2017 (Groups 2, 4, 6, 8, 10, and 12 specimens). Batch 3 specimens were cast on 23/08/2017 and tested on 21/09/2017 (Group 13 to 18 specimens). General views of the specimens are shown in Figure 3-1.

Table 3-1 – Details of the beam specimens (CC specimens)

Group No	Specimen ID	Concrete Compressive Strength (MPa)	Cross-Section (mm)	Length (mm)	Reinforcement	Dropping Height (m)
1	60C12-1	12.0 (Batch 1 - LSC)	60×60	500	Unreinforced	1.20
	60C12-2					
	60C12-3					
2	60C26-1	26.0 (Batch 2 - NSC)				
	60C26-2					
	60C26-3					
3	100C12-1	12.0 (Batch 1 - LSC)	100×100			2.00
	100C12-2					
	100C12-3					
4	100C26-1	26.0 (Batch 2 - NSC)				
	100C26-2					
	100C26-3					
5	150C12-1	12.0 (Batch 1 - LSC)	150×150			2.95
	150C12-2					
	150C12-3					
6	150C26-1	26.0 (Batch 2 - NSC)				
	150C26-2					
	150C26-3					
7	60C12R-1	12.0 (Batch 1 - LSC)	60×60		1ϕ8 mm	3.04
	60C12R-2					
	60C12R-3					
8	60C26R-1	26.0 (Batch 2 - NSC)				
	60C26R-2					
	60C26R-3					
9	100C12R-1	12.0 (Batch 1 - LSC)	100×100			3.00
	100C12R-2					
	100C12R-3					
10	100C26R-1	26.0 (Batch 2 - NSC)				
	100C26R-2					
	100C26R-3					
11	150C12R-1	12.0 (Batch 1 - LSC)	150×150			2.95
	150C12R-2					
	150C12R-3					
12	150C26R-1	26.0 (Batch 2 - NSC)				
	150C26R-2					
	150C26R-3					

Table 3-2 – Details of the beam specimens (SFRC specimens)

Group No	Specimen ID	Concrete Compressive Strength (MPa)	Cross-Section (mm)	Length (mm)	Reinforcement	Dropping Height (m)
13-a	60SFRC35-1	35.0 (Batch 3 - SFRC)	60×60	500	Unreinforced	3.04
	60SFRC35-2					
13-b	60SFRC35-3					1.20
14	60SFRC35R-1				1ϕ8 mm	3.04
	60SFRC35R-2					
	60SFRC35R-3					
15	100SFRC35-1		100×100		Unreinforced	2.00
	100SFRC35-2					
	100SFRC35-3					
16	100SFRC35R-1				1ϕ8 mm	3.00
	100SFRC35R-2					
	100SFRC35R-3					
17	150SFRC35-1		150×150		Unreinforced	2.95
	150SFRC35-2					
	150SFRC35-3					
18	150SFRC35R-1				1ϕ8 mm	2.95
	150SFRC35R-2					
	150SFRC35R-3					

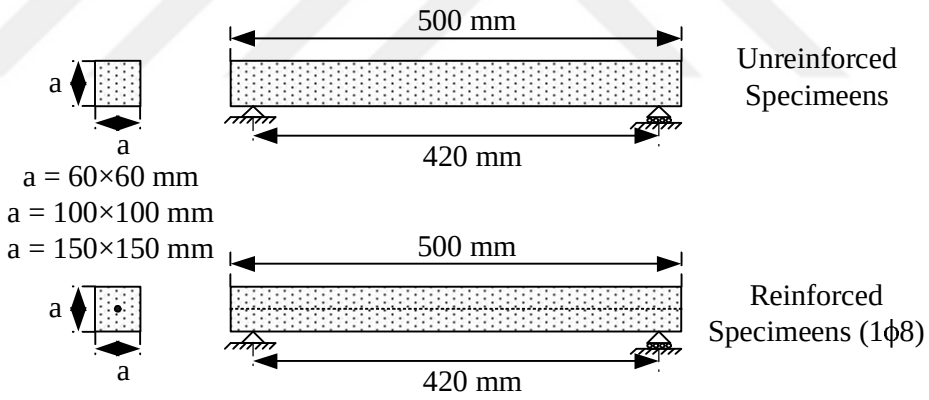

Figure 3-1 – General and cross-sectional views of the specimens

3.3 Materials

3.3.1 Concrete

The all the mixtures, materials that regularly used in concrete mixtures including ordinary Portland Cement (CC 32.5), clean tap water, river sand having sizes between 0 and 4 mm, fine aggregate having sizes between 4 and 16 mm, coarse aggregate having sizes between 15 to 25 mm were used in this research. Glenium ACE 450 superplasticizer was also used to adjust the mixture fluidity of the mixture.

For SFRC mixtures, steel fibers were added 1% by volume (3% by weight) to the mixture. The concrete mixture proportions used in this research are shown in Table 3-3. Proportioning of materials was performed using a calibrated digital weighing scale where quantity of each material was measured before mixing is shown in Figure 3-2.

Table 3-3 – Concrete mixture proportions

Materials	Quantity (kgf)		
	Batch 1 - LSC	Batch 2 - NSC	Batch 3 - SFRC
Cement	392	392	392
Sand	883	883	883
Fine aggregate	432	432	432
Coarse aggregate	569	569	569
Steel fiber	-	-	75.5
Water	392	196	143
Superplastisizer	-	-	0.98

Figure 3-2 – Materials proportioning

3.3.2 Steel Fibers

Based on the literature review results, hooked end steel fiber was the most effective to enhance the properties of bonding to hold the crack, increase the ductility and absorb the energy under impact loading. Therefore, the hooked ended Dramix ZP 305 type steel fibers were used in the composite concrete mixture for the SFRC

specimens. Mechanical properties of the steel fibers provided by the manufacturer are shown in Table 3-4. A photograph of the steel fibers at the mixing stage is shown in Figure 3-3.

Table 3-4 – Properties of steel fibers

Effective Length (mm)	Equivalent Diameter (mm)	Aspect Ratio	Young's Modulus (MPa)	Tensile Strength (MPa)	Density (kgf/m^3)
30	0.55	55	210000	1345	7850

Figure 3-3 – Steel fibers at the mixing stage

3.3.3 Reinforcement

Deformed reinforcing steel bars having a minimum yield strength of 420 MPa were used to reinforce the reinforced concrete specimens.

3.4 Specimen Preparation

3.4.1 Molds, Formworks, and Reinforcement

Steel cylinder molds having 150×300 mm and steel prisms having 150×150×600 mm dimensions were used to determine the material properties (compressive strength and modulus of rupture of the specimens) for each batch as shown in Figure 3-4.

Formwork for beam specimens were constructed using plywood for three sizes, 60×60×500, 100×100×500, and 150×150×500 mm. These formworks were used for both the reinforced and unreinforced specimens. For reinforced specimens, a hole was drilled at the geometric centroid of the cross-section and reinforcement was located to the necessary location. Preparations of the formworks are shown in Figure 3-5. Typical formworks for unreinforced and reinforced beam specimens are shown in Figure 3-6.

Figure 3-4 – Cylinder and prism molds

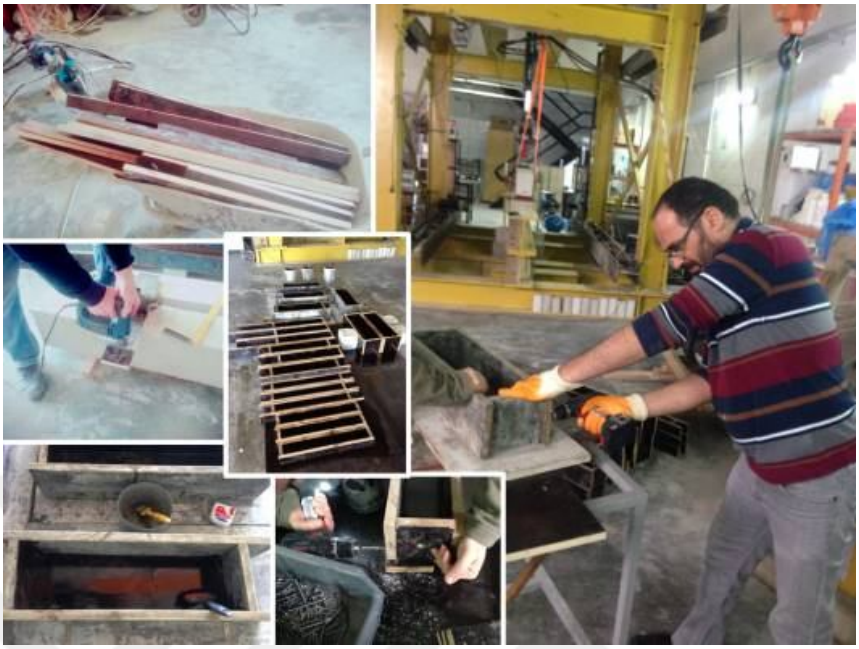

Figure 3-5 – Preparations of formworks for 60×60×500, 100×100×500, and 150×150×500 mm beam specimens

Figure 3-6 – Formworks for 60×60×500, 100×100×500, and 150×150×500 mm beam specimens before casting

3.4.2 Concrete Mixing

A stationary tilting drum mixer was used to mix the concrete mixtures. The mixer bucket had the ability to revolve in clockwise and counterclockwise directions to avoid segregation, mortar balling, and hard workability. Sand, fine, and coarse aggregates and portland cement were placed into the mixer bucket and mixed approximately for three minutes. For the SFRC mixtures, steel fibers were added to the mixing bucket while the mixer was revolving. For SFRC mixtures, the mixture was mixed for three more minutes after the fibers are added. After the materials are mixed enough in dry condition, 80% of required water was added into mixing bucket during. The mixture was mixed for 5 minutes before the superplasticizer and the remaining water (20% of required) were added. The mixture was mixed approximately for another 10 minutes or until the desired workability was obtained. The mixing time was a little longer for SFRC mixtures compared to others. A photograph of the mixing of materials is showed in Figure 3-7. Slump tests based on ASTM C143 was performed to evaluate the workability of the mixture. The target slump used in this research was approximately 60 mm which indicated to slump with medium workability as shown in Figure 3-8.

Figure 3-7 – Mixing of materials

Figure 3-8 – Slump test

3.4.3 Casting and Curing

For each concrete batch, minimum three 150×300 mm cylindrical and three 150×150×600 mm prismatic concrete specimens were cast along with the 18 beam specimens. Each group of specimens had a repeatability of three. Therefore a total of 18 beam specimens consisting of three different cross-sections and presence of reinforcement or not were cast for each batch.

Before casting, all molds and formworks were cleaned and form release was applied on their inner surfaces for removal of specimens easily. During casting, the concrete in molds and formworks were compacted using a tamping rod and plastic hammer according to ASTM C192. Photographs related to casting are shown in Figure 3-9 to Figure 3-12.

Figure 3-9 – Placing concrete into molds and formworks

Figure 3-10 – Casting of specimens - Batch 1 (CC)

Figure 3-11 – Casting of specimens - Batch 2 (CC)

Figure 3-12 – Casting of specimens – Batch 3 (SFRC)

After casting, the concrete specimens were set to dry and kept in molds and formworks during the first twenty four hours. Wet burlap was used to cover the specimens to minimize loss of moisture content due to evaporation. Appropriate curing was performed by making the specimens sufficiently wet using the water spray on the specimens covered with wet burlap as shown in Figure 3-13. Similar curing procedure was performed for cylinders, prisms, and beam specimens of the same batch.

Figure 3-13 – Curing of specimens

3.4.4 Test Set-Ups and Procedures

Three types of tests were conducted in the scope of this research. Compression tests were performed to determine the test day concrete compressive strength of cylinders. Three-point bending tests were performed to investigate the flexural tensile strength prism specimens. Drop-hammer tests were conducted to evaluate the behavior of beam specimens under impact loading.

3.4.4.1 Compressive Strength Tests

Cylinders having 150×300 mm dimensions were tested under compression to evaluate the compressive strength based on ASTM C39 as shown in Figure 3-14 to Figure 3-17. These tests were performed on the day when or one day before the beam

specimens were tested under impact loading. The tests were performed using a hydraulic compression testing machine having a 1500 kN capacity. Before testing, the top and bottom surfaces of cylinder specimens were cut and smoothed using a concrete cutter machine. This helped the specimens achieving a smooth contact with the testing machine plates and uniformly distributing the compressive forces on the cylinder. For cylinders size 150×300 mm, the compression load cell is used in compressive strength test machine to collect the load values. Load was applied at the rate of 0.25 MPa/sec approximately by control the setting lever that was attached to the testing machine. Compressive load was applied to each cylinder until failure occurred. The maximum and average values of the compressive strength evaluated and obtained from cylinder compressive load values for each tested cylinder divided by the initial area of tested cylinder cross section.

Figure 3-14 – Compressive strength tests

Figure 3-15 – Compressive strength tests of specimens of Batch 1 (CC)

Figure 3-16 – Compressive strength tests of specimens of Batch 2 (CC)

Figure 3-17 – Compressive strength tests of specimens of Batch 3 (SFRC)

3.4.4.2 Flexural Tensile Strength Tests

Prisms having 150×150×600 mm dimensions were tested under four-point loading to evaluate the flexural tensile according to ASTM C78 as shown in Figure 3-18. These tests were performed on the day when or one day before the beam specimens were tested under impact loading. The tests were performed using a hydraulic compression testing machine having a 1500 kN capacity. A load cell having 100 kN capacity and two 20 mm linear variable displacement transducers (LVDT) were used to measure the load and the deflection of the prisms at the mid-span. The data was monitored recorded using a data acquisition system.

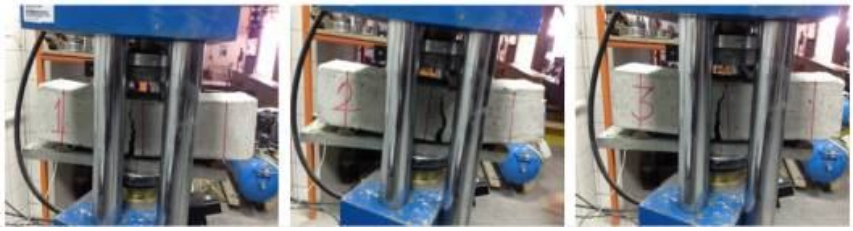

Figure 3-18 – Flexural strength tests (four-point bending)

3.4.4.3 Impact Behavior Tests

The beam specimens having 60×60×500, 100×100×500, and 150×150×500 mm dimensions were tested under impact loading using a drop-hammer testing apparatus. This apparatus consists of a steel hammer falling from a specific height on the specimen freely under the gravitational acceleration. Many researchers used similar devices to apply impact loading on specimens. However, Kishi et al. (2002) and Barr and Baghli (1988) stated that there was no confirmed standards or systems for impact loading testing up to nowadays' studies. According to Siewert et al. (1999), ASTM E23 regulations improved the test set-up implementation safely and assigned good beginning points for the borders of impacts experiments.

3.4.4.3.1 Construction of Drop-Hammer Testing Apparatus

Based on the results of the literature review, a drop-hammer testing apparatus having the following aspects was intended to be constructed:

- Very simple and lightweight.
- Moderate weight hammer to be used easily by an operator.
- Easy to construct, re-fix and transfer to any place as required.
- Changeable dropping heights up to 3 m height.
- Easy release system for the hammer.

Based on these ideas, the drop-hammer testing apparatus constructed in this research consisted of a steel hammer and a steel I-beam carrying a 3 m plastic pipe having 75 mm diameter perpendicularly. The beam specimens were simply supported under the plastic tube for the impact testing. The total length of the beams was 500 mm and the

gage length between the pin and roller supports were 420 mm (Figure 3-1). A white board marked with lines at every 5 cm horizontal distances were used to monitor and measure the velocity of the hammer and beam specimens.

The load was applied using a 5.96 kgf steel hammer falling freely from predetermined height. A pulley at the top of the assembly was used to move the hammer in vertical direction. A long steel wire was connected to top of the hammer and this wire was passing through the pulley. This wire was pulled down to move the hammer up till the necessary height is reached for each specimen. The wire was released to start the test and hammer started to move freely downwards. A schematic view of the drop-hammer testing apparatus constructed in the scope of this research is shown in Figure 3-19. Photographs related to the construction process are shown in Figure 3-20. A closer view of the hammer used in this research is shown in Figure 3-21.

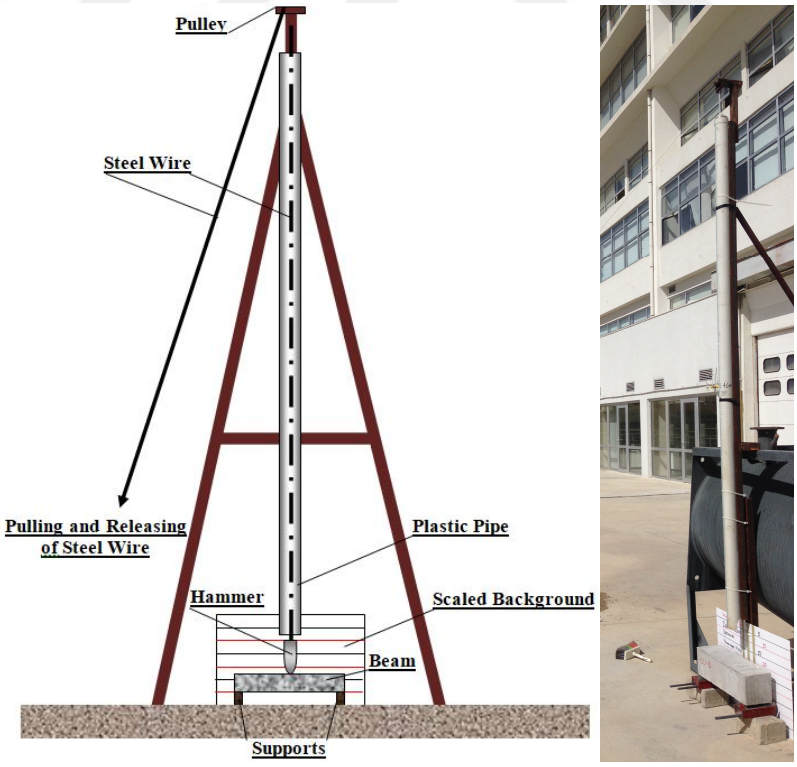

Figure 3-19 – Schematic view of the drop-hammer testing apparatus used in this research

Figure 3-20 – Construction process of the drop-hammer testing apparatus

Figure 3-21 – Steel hammer used in this research

3.4.4.3.2 Trial Tests, Video Recording, and Analysis

After the construction of the drop-hammer testing apparatus, numerous trial tests were performed. The initial trial tests were conducted using beams made of any material (such as wood, concrete, steel, etc.). The weight was dropped on these beams and the video images were recorded using various camera including Sony HDR-CX240 HD Camcorder, iPhone 5, iPhone 7, and Canon D60 having various frame rates per second (fps) as shown in Figure 3-22. When the recorded videos using light projectors were analyzed, it was discovered that the indoor lightings for the recordings were not enough to capture the desired motion quality. Therefore, the drop-hammer testing apparatus was moved outdoors as shown in Figure 3-23 and the trial tests were continued under sunlight. However, the desired number of fps for a better slow motion video was still not achieved. A more powerful camera (Photron FASTCAM MC2.1-10K) was supplied from Atılım University Mechatronics Engineering Department. Using this advanced high-speed camera, the slow motion videos having up to 2000 fps could be achieved, which was good enough for the requirements of this research. A photograph of the recording of an outdoor test is shown in Figure 3-24. Specifications related to Photron FASTCAM MC2.1-10K advanced high-speed camera is given in the Appendices.

Figure 3-22 – Cameras used in trial tests

Figure 3-23 – Drop-hammer testing apparatus at different locations (indoors and outdoors)

Figure 3-24 – Recording of test videos using high-speed camera

The video recordings obtained by the high-speed camera were analyzed using TEMA Motion Software as shown in Figure 3-25.

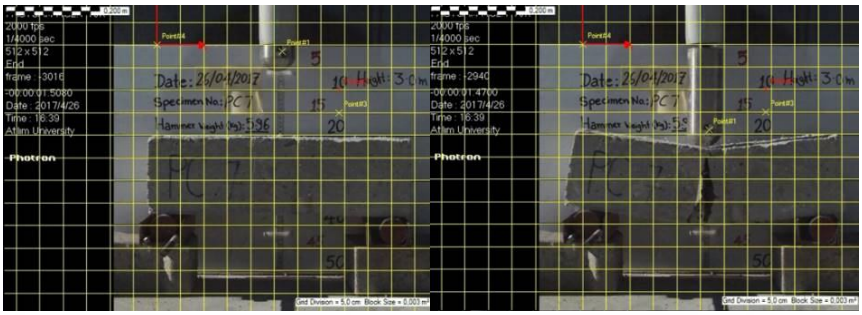

Figure 3-25 – Analysis of test videos using TEMA Motion Software

3.4.4.3.3 Dropping Heights Calculations

The maximum energy of the constructed drop-hammer testing apparatus used in this research was calculated based on the maximum usable dropping height, which was equal to 2.95 m. The potential energy (PE) of the hammer was calculated using the following equation:

$$PE = m \times g \times h \qquad \text{Equation 3-1}$$

where PE is the potential energy in J., m is hammer mass in kg, g is the gravitational acceleration (9.81 m/s^2), and h is dropping height in m. The maximum potential energy of the hammer was calculated as 17.85 J. and this was applied to the specimen having the largest cross-sectional dimensions (150×150×500 mm). The energies for other specimens (60×60×500 and 100×100×500 mm) were calculated based on the ratio of the cross-section dimension to the largest specimen (150×150×500 mm). The energies for other specimens were determined as 7.03 and 11.72 J. for 60×60×500 and 100×100×500 mm specimens, respectively.

The dropping heights of the hammer for various specimen groups are shown in Table 3-1 and Table 3-2, and in Figure 2-8.

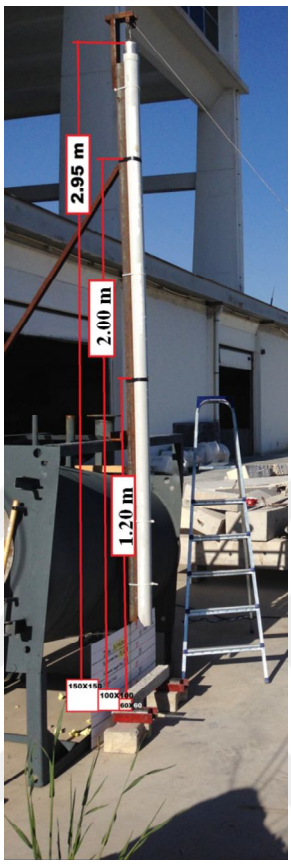

Figure 3-26 – Dropping heights for various specimens

3.4.4.3.4 Impact Testing Procedure

The first requirement for impact testing was related to the weather conditions, since the video recordings shall be performed in a sunny and not windy weather. The pulley must be greased to minimize friction. The specimen was placed on top of the supports under the drop-hammer testing apparatus. The white board marked with horizontal lines was located at the back of the specimen. The hammer is marked with test marker to follow the motion using the high-speed camera.

The high-speed camera and the computer shall be checked. A plexiglass must be placed between the camera and the test specimens to avoid any damage of the camera due to fragments of concrete moving with high speeds after impact.

The test was conducted by two people; one controlling the camera and computer, other pulling and releasing the hammer. When the camera became ready, the person

responsible from the camera and computer started the test. The hammer was moved up and the wire was released for impact loading. After the specimen was hit by the hammer, the test and recording of the camera was stopped. All the steps are repeated for each specimen.

Specimens cast using Batch 1, 2, and 3 were impact tested on 26/04/2017, 20/09/2017, and 21/09/2017, respectively. Related photos of impact testing are shown in Figure 3-27 to Figure 3-29.

Figure 3-27 – Impact behavior tests - Batch 1

Figure 3-28 – Impact behavior tests - Batch 2

Figure 3-29 – Impact behavior tests - Batch 3

4. RESULTS AND DISCUSSIONS

4.1 General

In this chapter, test results obtained from 150×300 mm cylinders under compression, 150×150×600 mm prismatic beams under flexure, and 60×60×500, 100×100×500, and 150×150×500 mm beams with and without reinforcement under impact loading are presented in tabular and graphical forms. Comments were made based on visual observations during the testing. Comparisons and discussions were performed based on these results.

4.2 Compressive Strength Test Results

According to the visual observations during compressive strength tests on 150×300 mm cylinders, CC cylinders showed a brittle and sudden failure mode of directly after reaching the maximum strength values. The failure mode of specimens having NSC was sudden and more brittle than that of specimens having LSC. SFRC specimens sustained a considerable amount of compressive load for a longer period of time. Typical failure modes of CC and SFRC cylinders are shown in Figure 4-1 and Figure 4-2.

Figure 4-1 – Typical failure mode of CC cylinders under compression

Figure 4-2 – Typical failure mode of SFRC cylinders under compression

The load and time values were recorded during the tests. Strength values were calculated by dividing the ultimate load values to the area of the specimens. The strength values obtained from compression tests of all the batches are shown in Table 4-1. The concrete compressive strengths of Batch 1, 2, and 3 were 11.929, 25.987, and 34.940 MPa, respectively.

Table 4-1 – Average measured concrete compressive strengths of batches

Batch No	Average Measured Compressive Strength (MPa)
1 (LSC-CC)	11.969
2 (NSC-CC)	25.987
3 (SFRC)	34.948

4.3 Flexural Tensile Strength Test Results

According to the visual observations during flexural tensile strength tests on 150×150×600 mm prisms, CC specimens showed a brittle and sudden failure mode with two pieces directly after cracking of concrete. However, specimens having SFRC did not break into two when the first crack appeared. The failure mode was ductile. Typical failure modes of CC and SFRC prisms are shown in Figure 4-3 to Figure 4-5.

Figure 4-3 – Typical failure mode of CC prisms under flexure 1

Figure 4-4 – Typical failure mode of CC prisms under flexure 2

Figure 4-5 – Typical failure mode of SFRC prisms under flexure

The load and displacement at mid-span values were recorded during the tests. The flexural tensile strength values obtained from flexural tests of all the batches are shown in Table 4-2. The concrete flexural tensile strengths of Batch 1, 2, and 3 were 1.985, 2.954, and 3.543 MPa, respectively.

Table 4-2 – Average measured concrete flexural tensile strengths of batches

Batch No	Average Measured Flexural Tensile Strength (MPa)
1 (LSC-CC)	1.985
2 (NSC-CC)	2.954
3 (SFRC)	3.543

4.4 Impact Behavior Test Results

For the same batch, all the cylinders were tested under compression and all the prisms were tested under flexural tension on the same day or a day before the beam specimens were tested under impact loading.

During testing, concrete beam was hit by steel hammer with its maximum impact velocity while the concrete beam was in static condition with zero velocity. Immediately after the impact moment, the velocity of hammer decreased significantly due to the transfer of energy to the beam. At this moment, the velocity of the beam increased significantly from zero to a velocity greater than the velocity of the hammer resulting in a disconnection of beam and hammer.

The failure modes of all the specimens are shown in Figure 4-6, Figure 4-7, and, Figure 4-8 for unreinforced CC 12 MPa specimens, CC 26 MPa specimens, and, SFRC 12 MPa specimens, respectively, and in Figure 4-9, Figure 4-10 and Figure 4-11 for reinforced CC 12 MPa specimens, CC 26 MPa specimens, and, SFRC 12 MPa specimens, respectively.

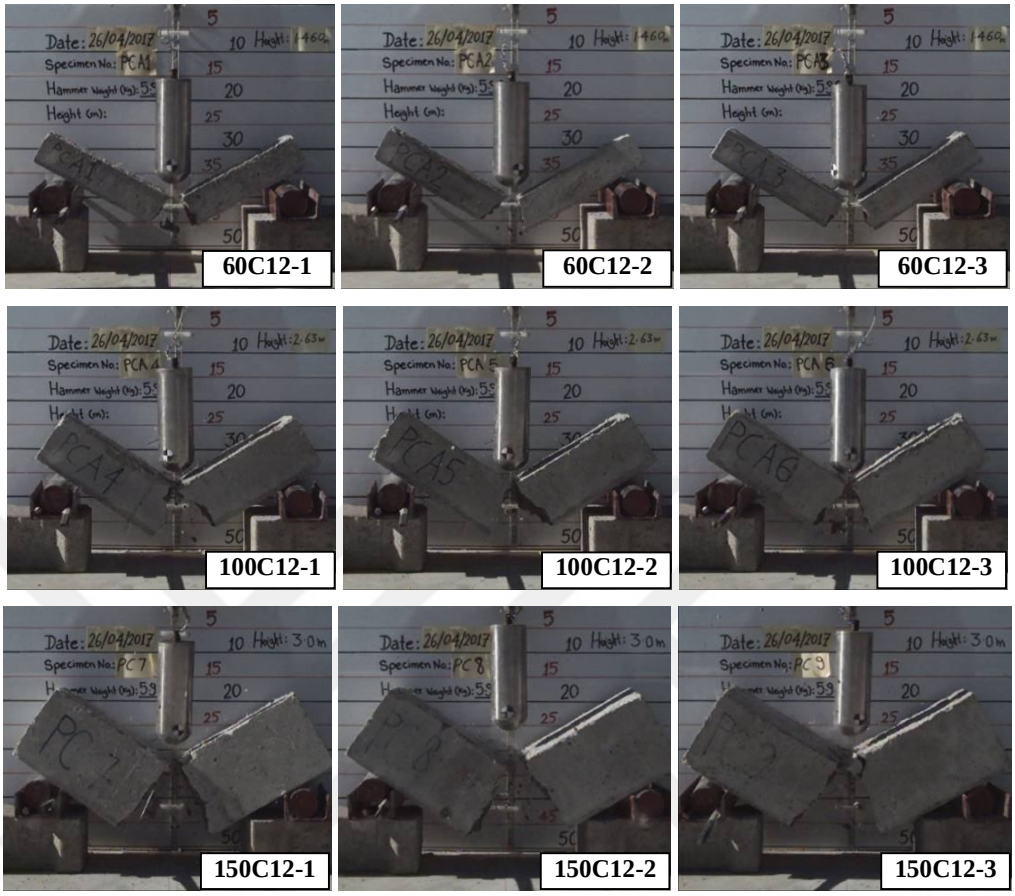

Figure 4-6 – Failure modes of Batch 1 LSC unreinforced specimens (Groups 1, 3, and 5)

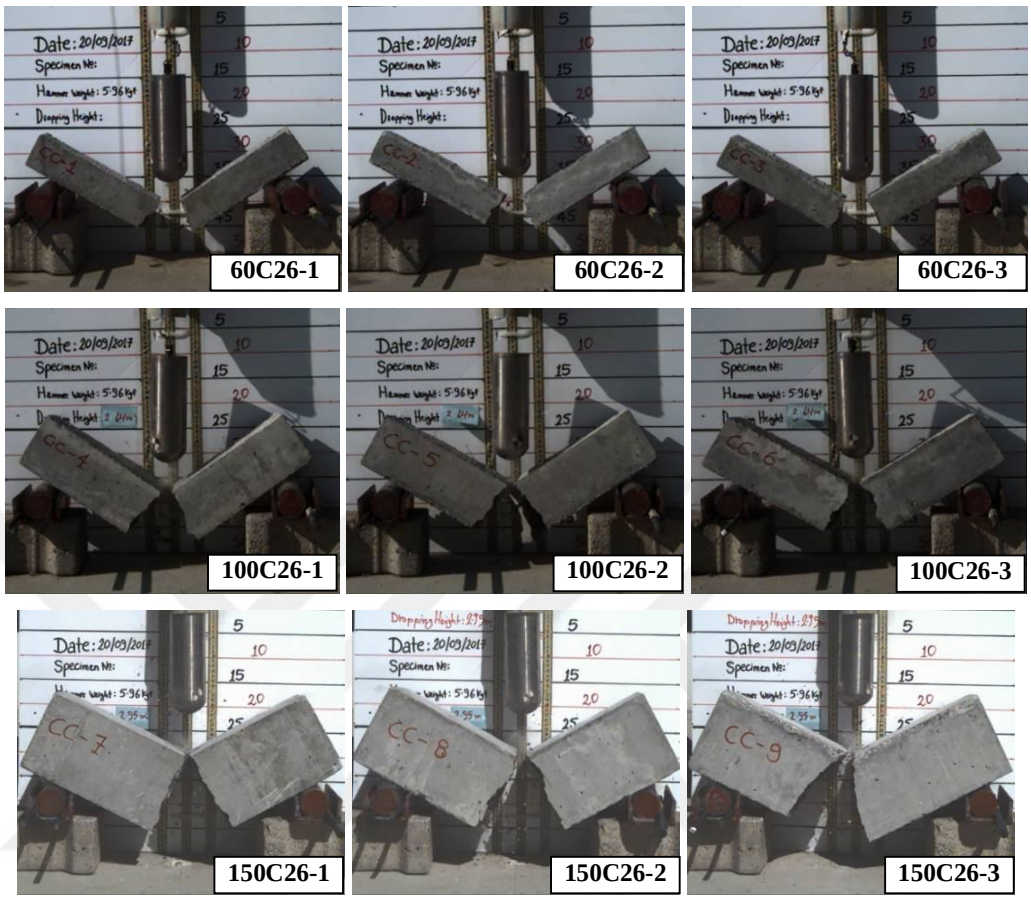

Figure 4-7 – Failure modes of Batch 2 NSC unreinforced specimens (Groups 2, 4, and 6)

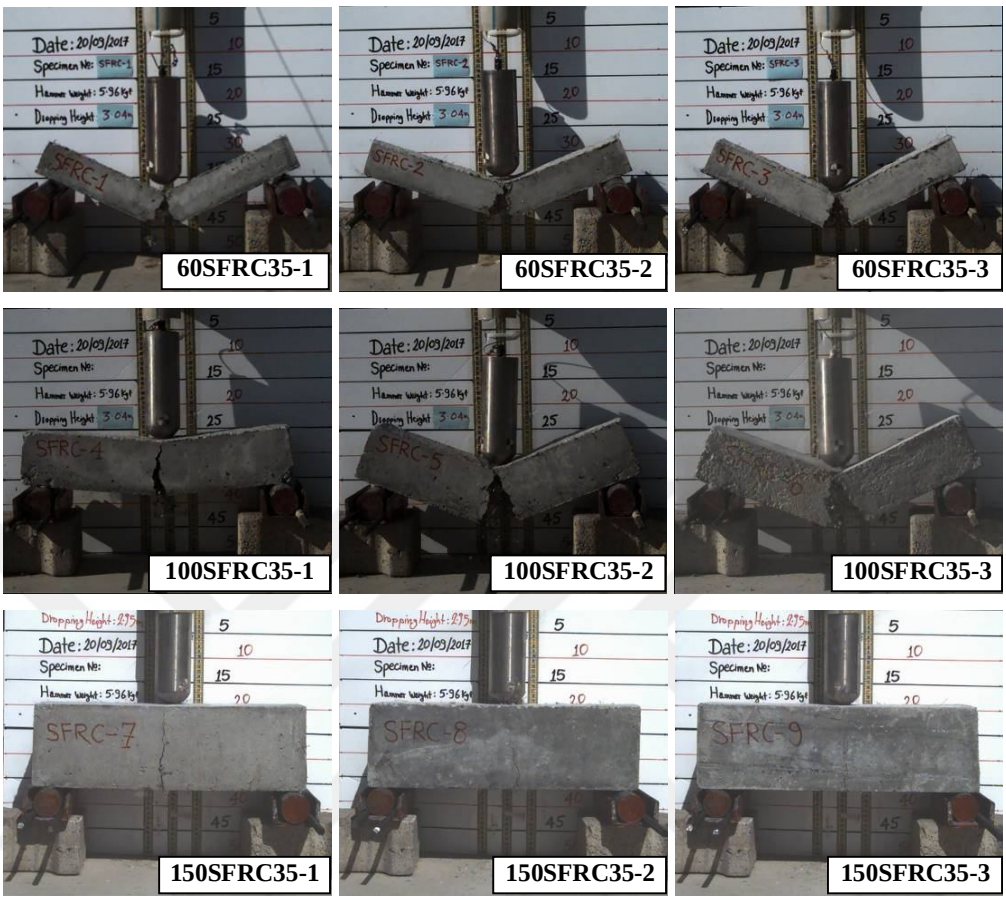

Figure 4-8 – Failure modes of Batch 3 SFRC unreinforced specimens (Groups 13, 15, and 17)

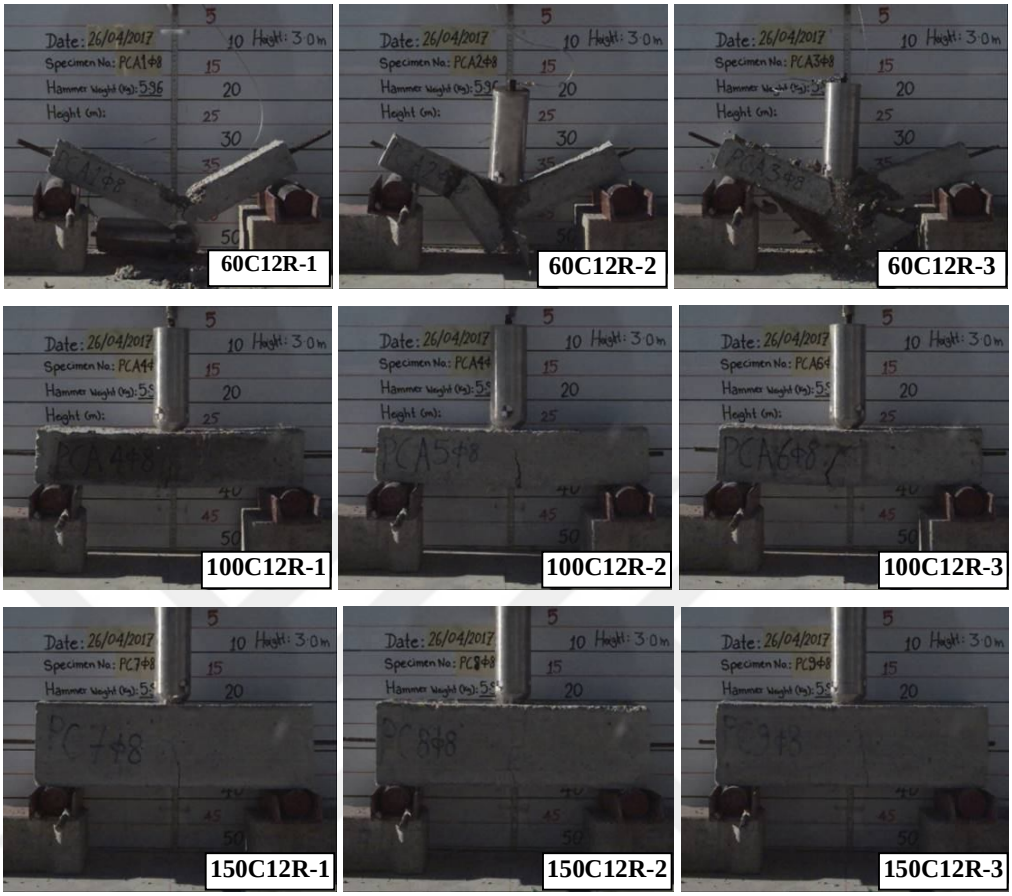

Figure 4-9 – Failure modes of Batch 1 LSC reinforced specimens (Groups 7, 9, and 11)

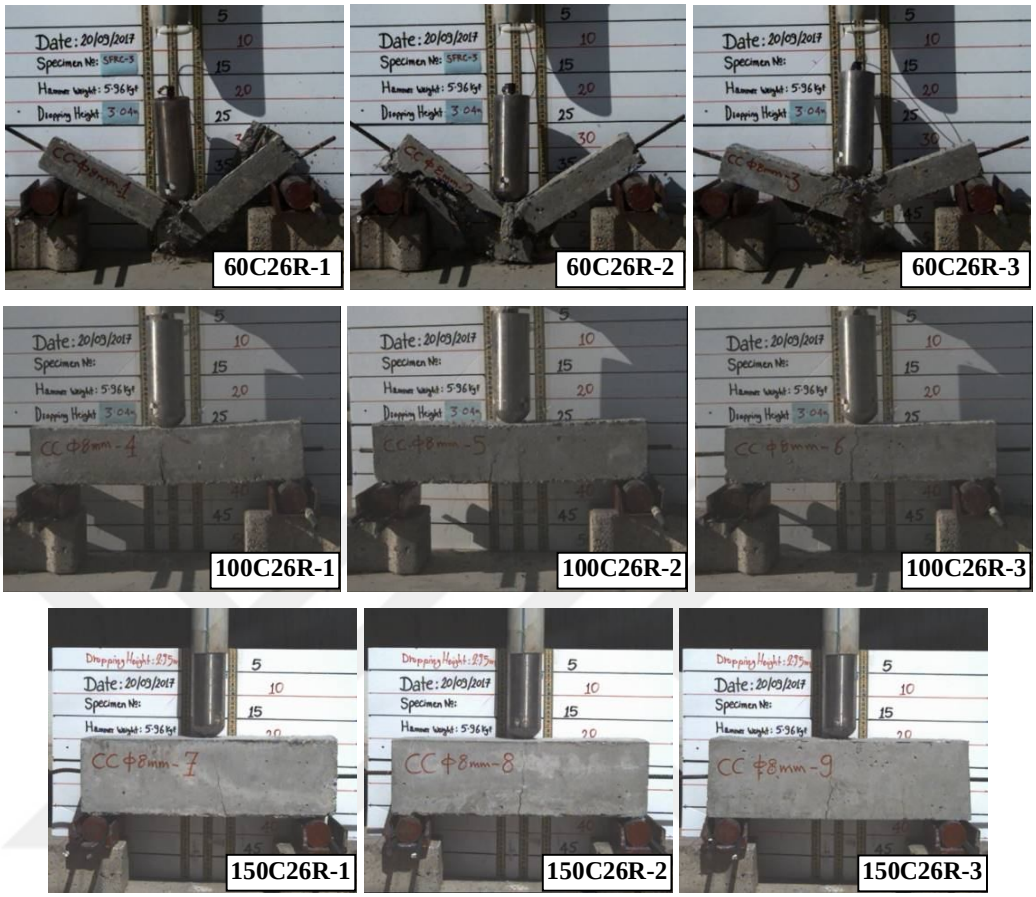

Figure 4-10 – Failure modes of Batch 2 NSC reinforced specimens (Groups 8, 10, and 12)

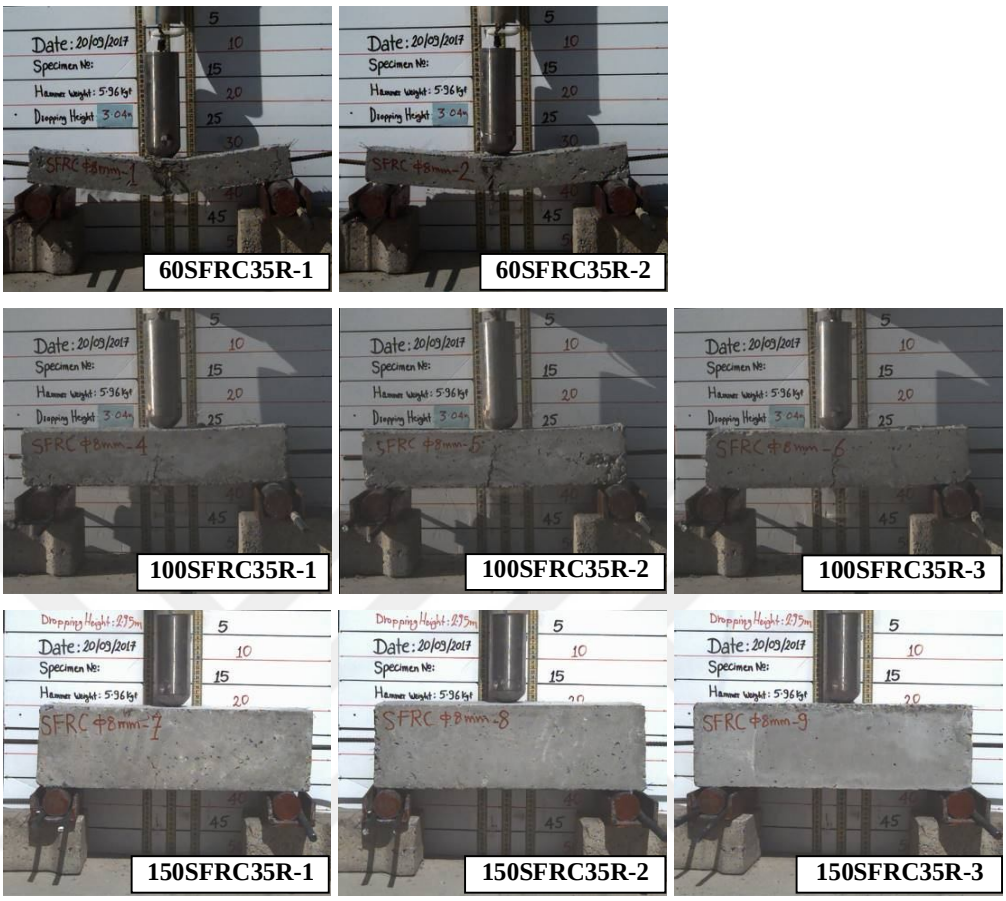

Figure 4-11 – Failure modes of Batch 3 SFRC reinforced specimens (Groups 14, 16, and 18)

The specimens of unreinforced Groups 1 to 6 (LSC and NSC) split into two pieces, both pieces having different motions due to different support conditions (pin at one end and roller at the other).

For SFRC unreinforced specimens, Group 13 (60×60×500 mm) specimens split into two pieces. For Group 15 (100×100×500 mm) specimens, 2/3 of the specimens split into two pieces, while 1/3 of the specimens had cracks propagated from beam mid-span up to 80 mm.

When the unreinforced CC specimens are compared, the velocities of the hammer after the impact were highest for Group 1 and 2 specimens (60×60×500 mm LSC and NSC unreinforced) and lowest for Group 5 and 6 specimens (150×150×500 mm LSC and NSC unreinforced). The impact test results for unreinforced specimens showed

that flexural cracks propagated from bottom to top at the center of all the specimens. All beam specimens ended up in two pieces at the mid-span.

When the reinforced CC specimens are compared, the velocities of the hammer after the impact were highest for Group 7 and 8 specimens (60×60×500 mm LSC and NSC reinforced) and lowest for Group 11 and 12 specimens (150×150×500 mm LSC and NSC reinforced). All beam specimens were bent at the mid-span. The flexural bending was highest for Group 7 and 8 specimens (60×60×500 mm LSC and NSC reinforced) and lowest for Group 11 and 12 specimens (150×150×500 mm LSC and NSC reinforced).

The velocities of the hammer after the impact for unreinforced SFRC beams were highest for Group 13-a and 13-b specimens (60×60×500 mm SFRC unreinforced) and lowest for Group 17 specimens (150×150×500 mm SFRC unreinforced).

The velocities of the hammer after the impact for reinforced SFRC specimens were highest for Group 14 specimens (60×60×500 mm SFRC reinforced) and lowest for Group 18 specimens (150×150×500 mm SFRC reinforced). The impact test results showed that flexural cracks propagated from bottom to top at the center of all the specimens. All reinforced beam specimens were bent at the mid-span. The flexural bending was highest for Group 14 specimens (60×60×500 mm SFRC reinforced) and lowest for Group 18 specimens (150×150×500 mm SFRC reinforced). For unreinforced beam specimens, all Group 13-a, 13-b specimens (60×60×500 mm SFRC unreinforced) and Group 15 specimens (100×100×500 mm SFRC unreinforced) ended up in two pieces at the mid-span. For Group 17 specimens (150×150×500 mm SFRC unreinforced), the cracks propagated from bottom to top at the mid-span.

The experimental velocity-time relationships for LSC, NSC, and SFRC specimens are shown in Figure 4-12 to Figure 4-29.

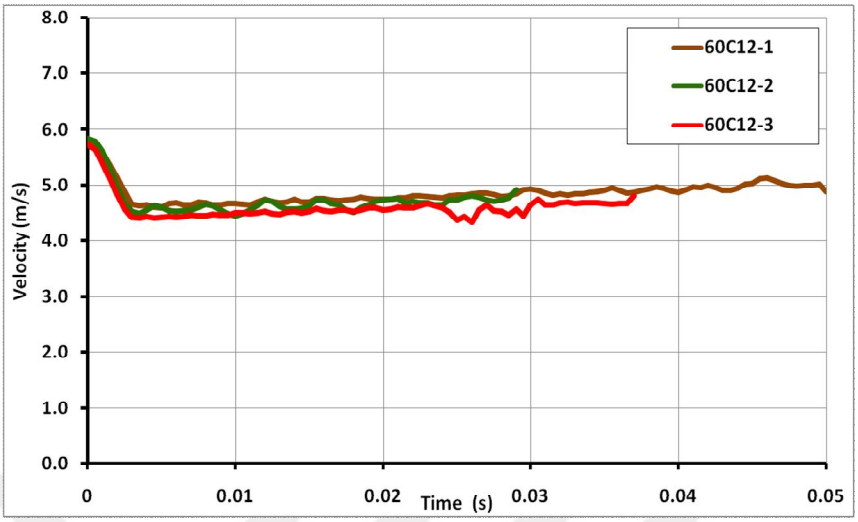

Figure 4-12 – Experimental velocity-time relationships of hammer for 60×60×500 mm unreinforced LSC specimens

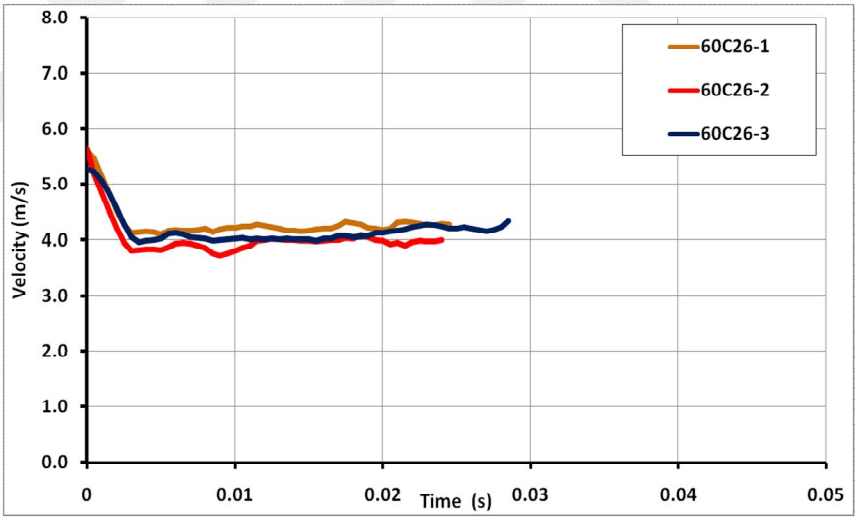

Figure 4-13 – Experimental velocity-time relationships of hammer for 60×60×500 mm unreinforced NSC specimens

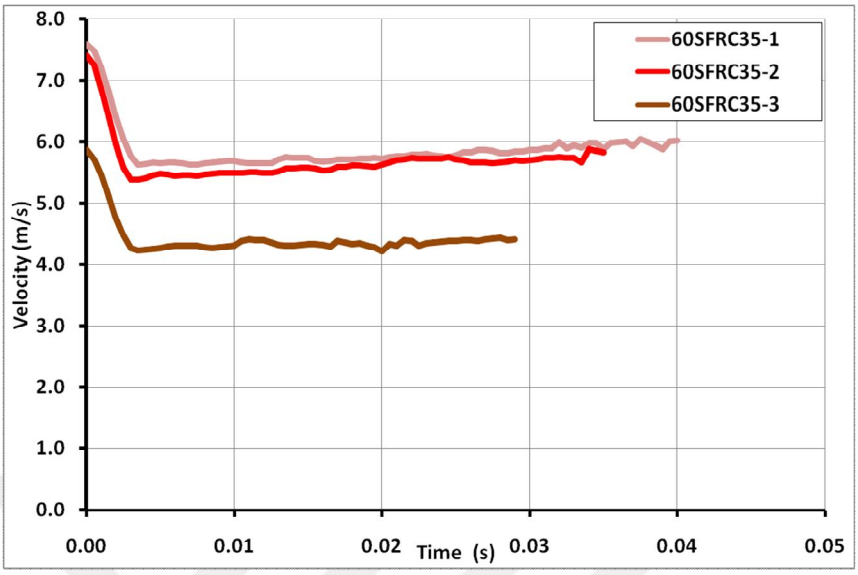

Figure 4-14 – Experimental velocity-time relationships of hammer for 60×60×500 mm unreinforced SFRC specimens

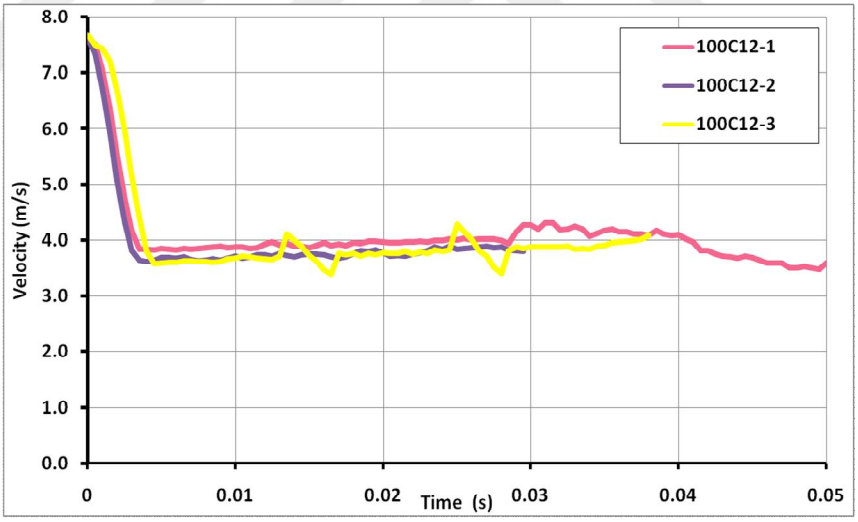

Figure 4-15 – Experimental velocity-time relationships of hammer for 100×100×500 mm unreinforced LSC specimens

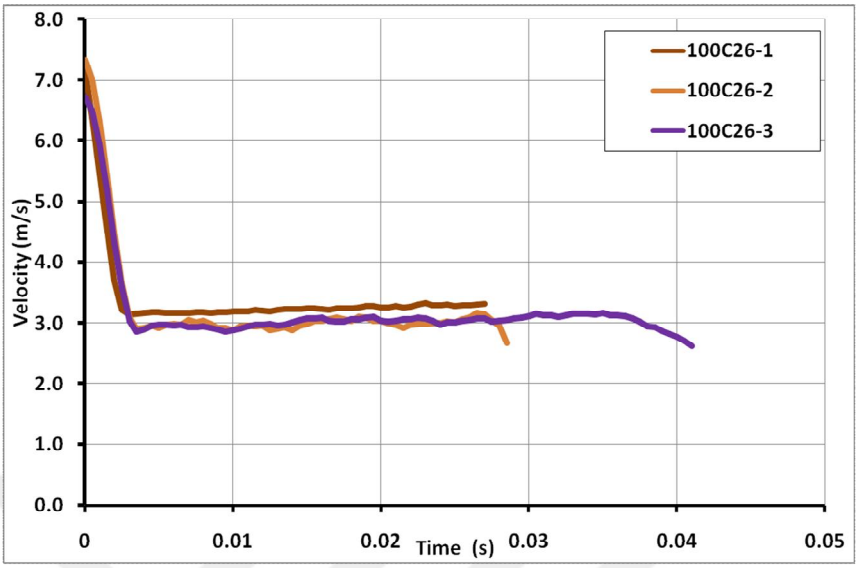

Figure 4-16 – Experimental velocity-time relationships of hammer for 100×100×500 mm unreinforced NSC specimens

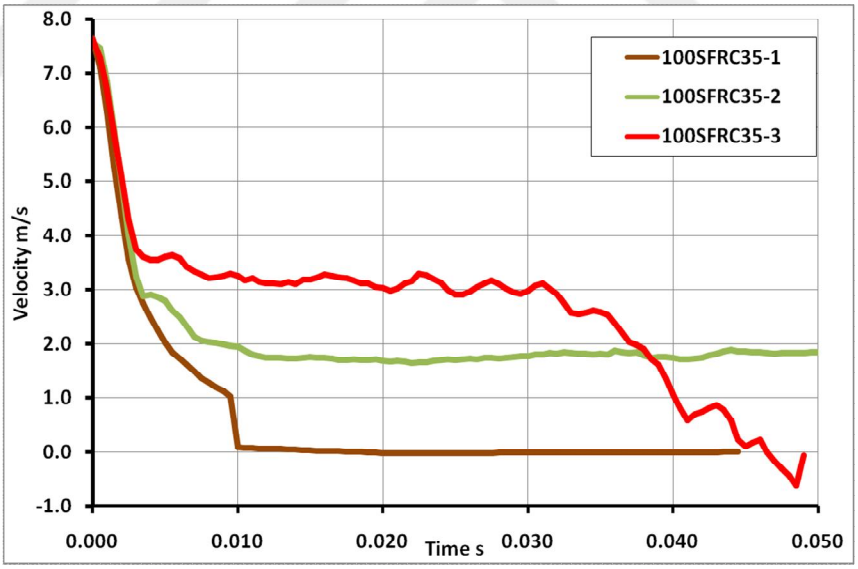

Figure 4-17 – Experimental velocity-time relationships of hammer for 100×100×500 mm unreinforced SFRC specimens

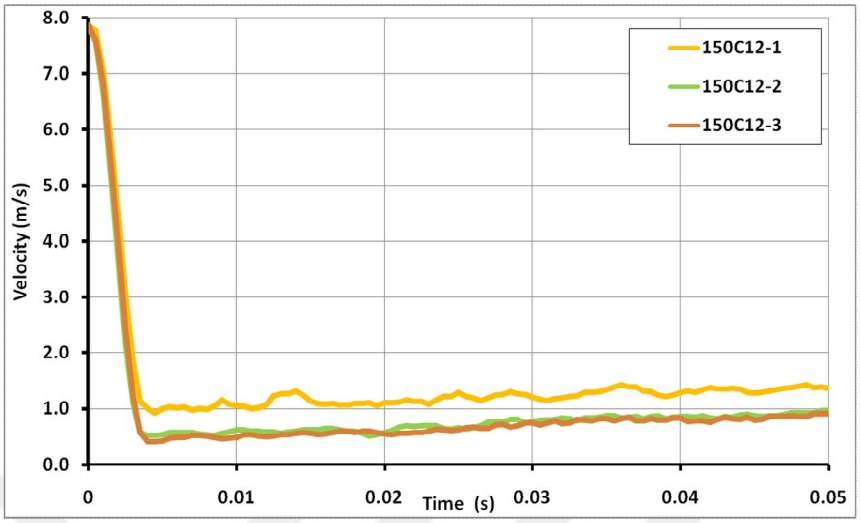

Figure 4-18 – Experimental velocity-time relationships of hammer for 150×150×500 mm unreinforced LSC specimens

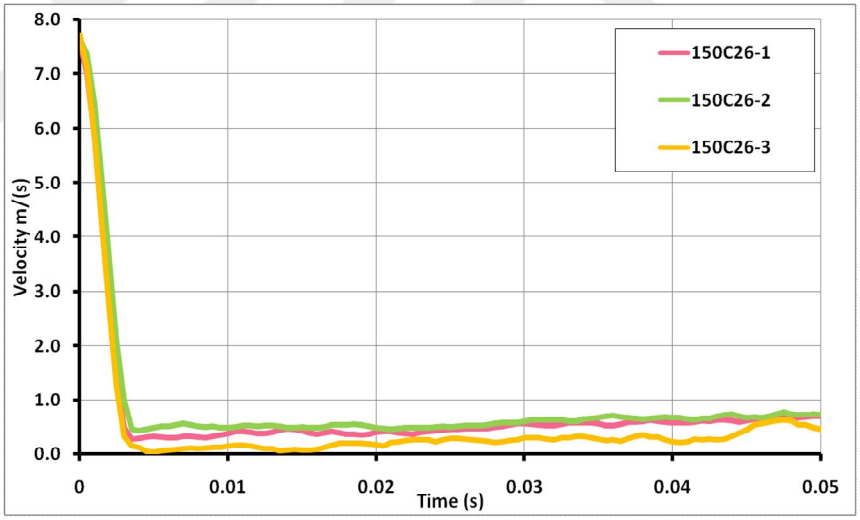

Figure 4-19 – Experimental velocity-time relationships of hammer for 150×150×500 mm unreinforced NSC specimens

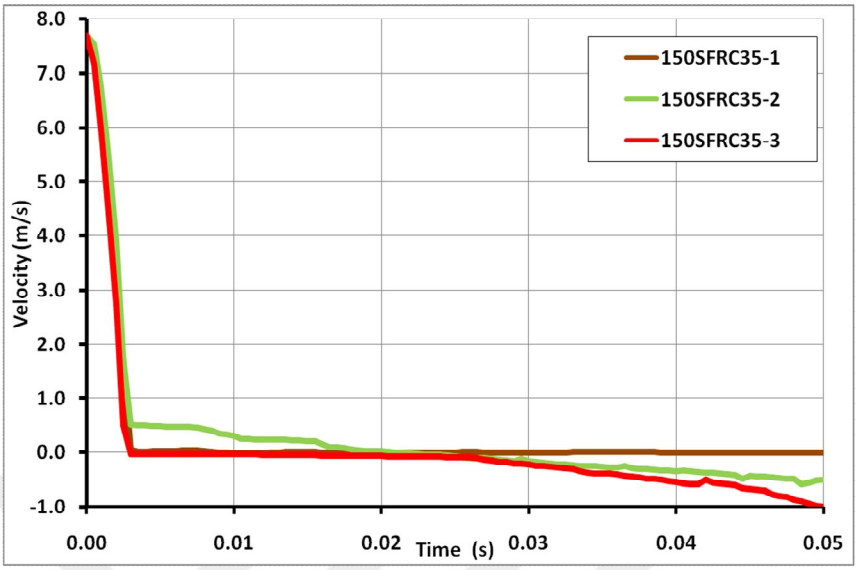

Figure 4-20 – Experimental velocity-time relationships of hammer for 150×150×500 mm unreinforced SFRC specimens

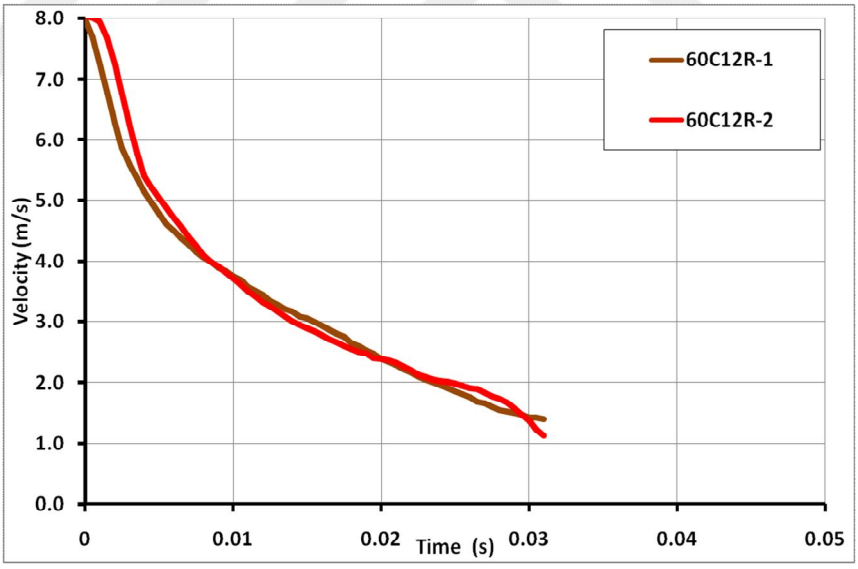

Figure 4-21 – Experimental velocity-time relationships of hammer for 60×60×500 mm reinforced LSC specimens

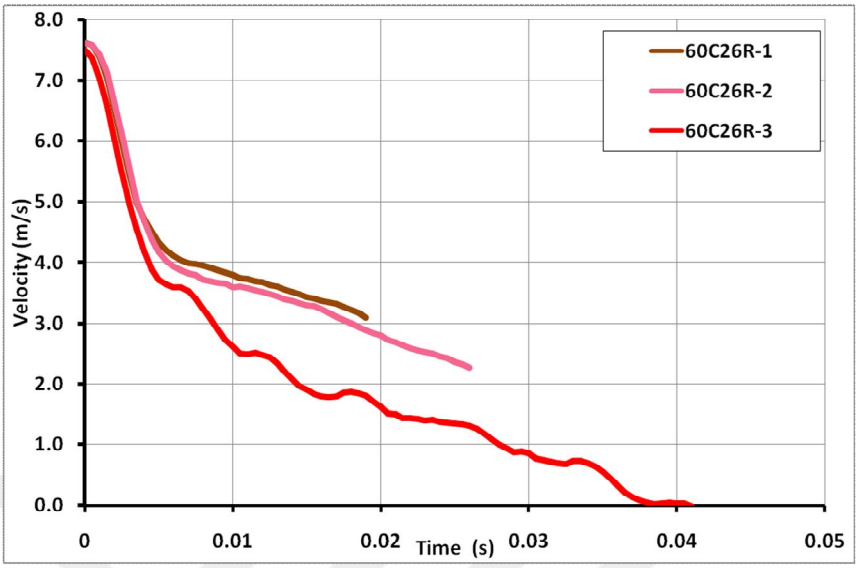

Figure 4-22 – Experimental velocity-time relationships of hammer for 60×60×500 mm reinforced NSC specimens

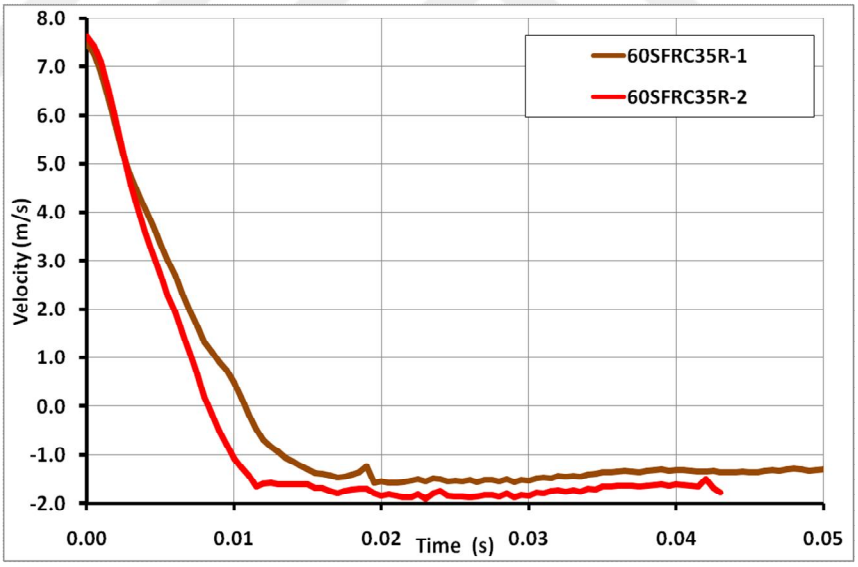

Figure 4-23 – Experimental velocity-time relationships of hammer for 60×60×500 mm reinforced SFRC specimens

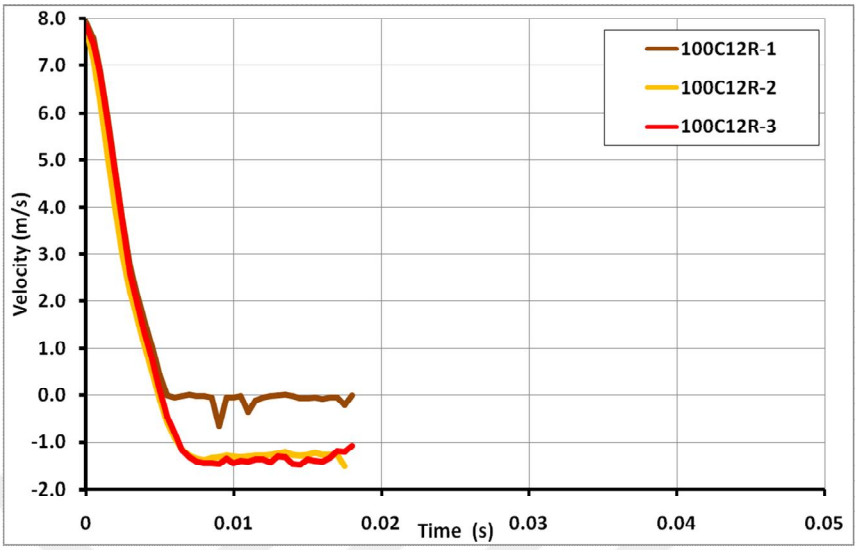

Figure 4-24 – Experimental velocity-time relationships of hammer for 100×100×500 mm reinforced LSC specimens

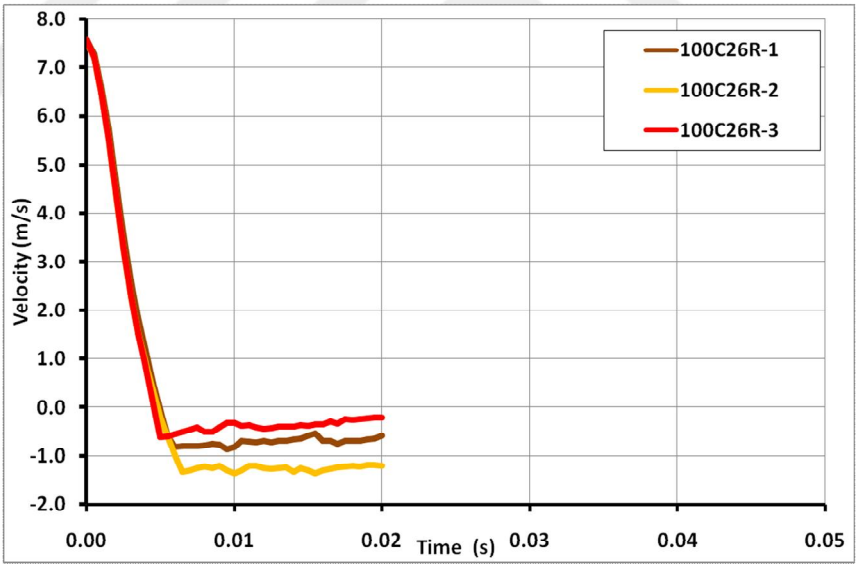

Figure 4-25 – Experimental velocity-time relationships of hammer for 100×100×500 mm reinforced NSC specimens

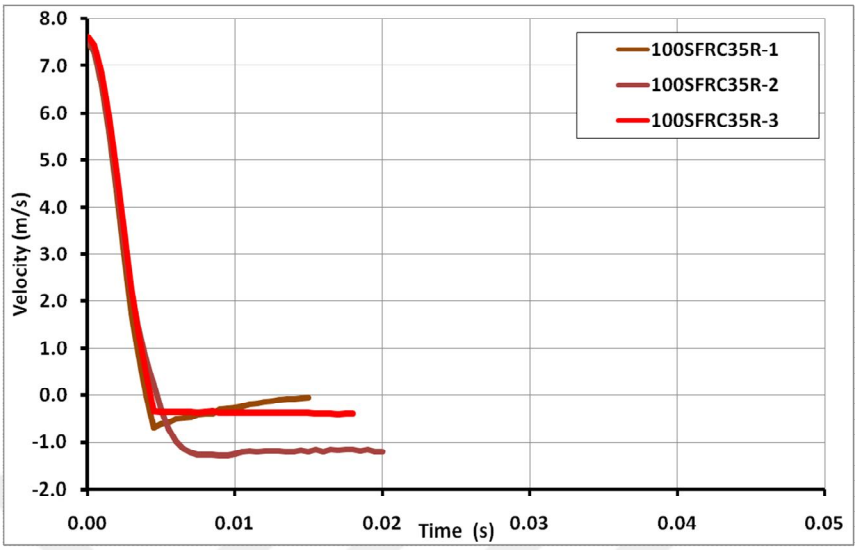

Figure 4-26 – Experimental velocity-time relationships of hammer for 100×100×500 mm reinforced SFRC specimens

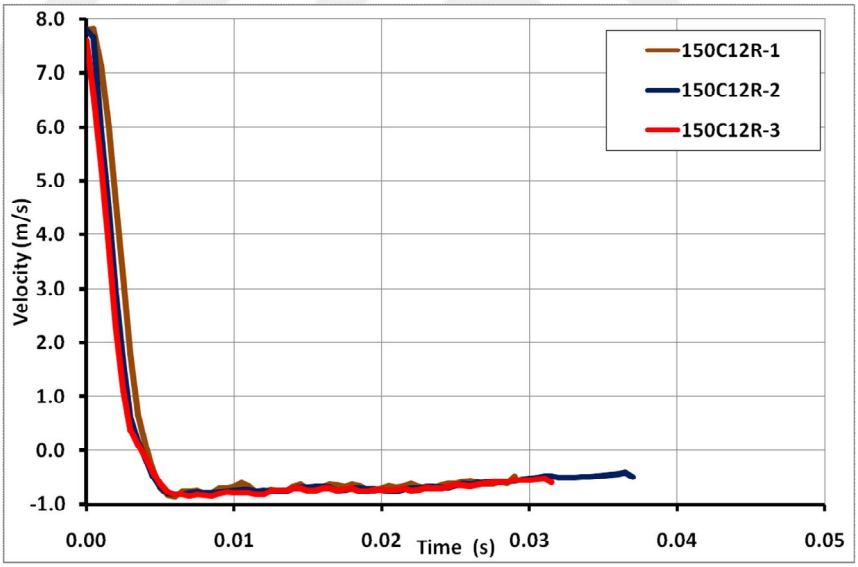

Figure 4-27 – Experimental velocity-time relationships of hammer for 150×150×500 mm reinforced LSC specimens

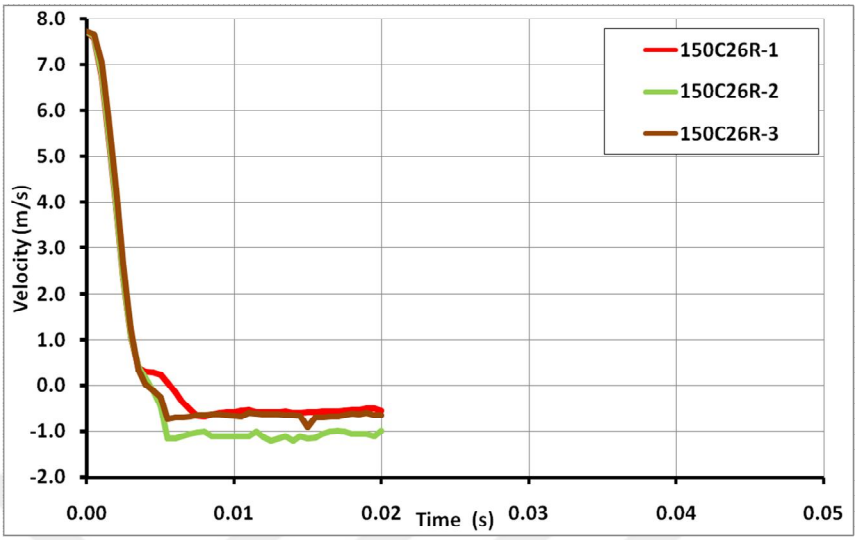

Figure 4-28 – Experimental velocity-time relationships of hammer for 150×150×500 mm reinforced NSC specimens

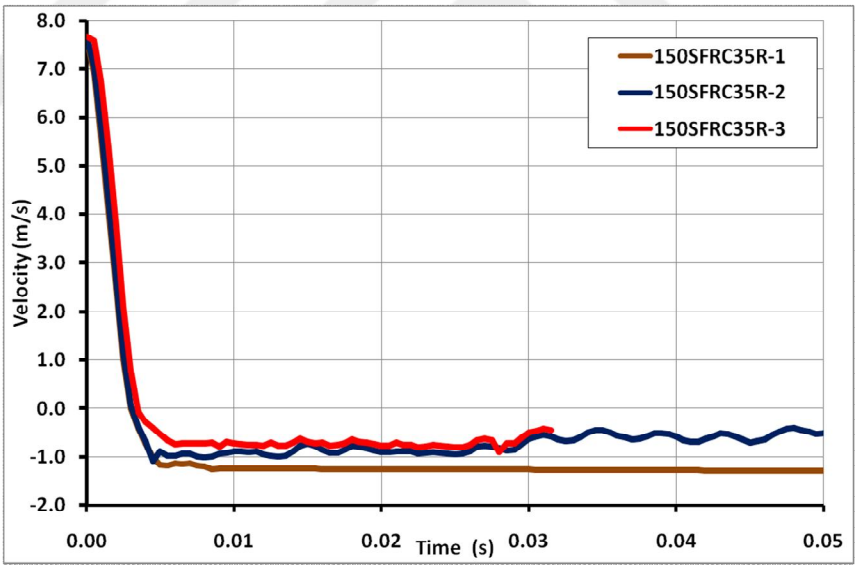

Figure 4-29 – Experimental velocity-time relationships of hammer for 150×150×500 mm reinforced SFRC specimens

5. ANALYTICAL WORK

5.1 General

Modeling and analysis using finite element method (FEM) became very common for the researchers and research centers. A huge number of software packages is available in market conducting FEM based analysis. ANSYS Finite Element Software is considered to be one of the most well-known programs used by many researchers worldwide. In this study, ANSYS Workbench Version 15.0 was used based on the findings of the literature review. Other software packages such as ABAQUS had more difficulties and complexities in modeling than that of ANSYS. Kantar et al. (2011) stated that ABAQUS FEM Software had critical assumptions. Due to the uncertainties and complexities of ABAQUS FEM Software, the modeling became very hard.

5.1.1 Finite Element Modeling

The modeling using ANSYS Finite Element Software included defining the testing environment similar to experimental details such as material properties (steel hammer, steel supports, steel reinforcement bar, and concrete), dimensions, and hammer velocities. Based on the literature review, it was concluded that the impact loading can best be simulated when ANSYS Explicit Dynamics Method (EDM) was used. Therefore, the information related to testing was defined as dynamic explicit in ANSYS software environment. Detailed parametric studies were performed for all the parameters of modeling explained in this section.

5.1.2 Geometry

Beam, hammer, support 1, and support 2 were modeled in the ANSYS Finite Element Software. General view of the model is shown in Figure 5-1. Details related to modeling parameters of each of these elements are shown in Table 5-1, Table 5-2, and Table 5-3.

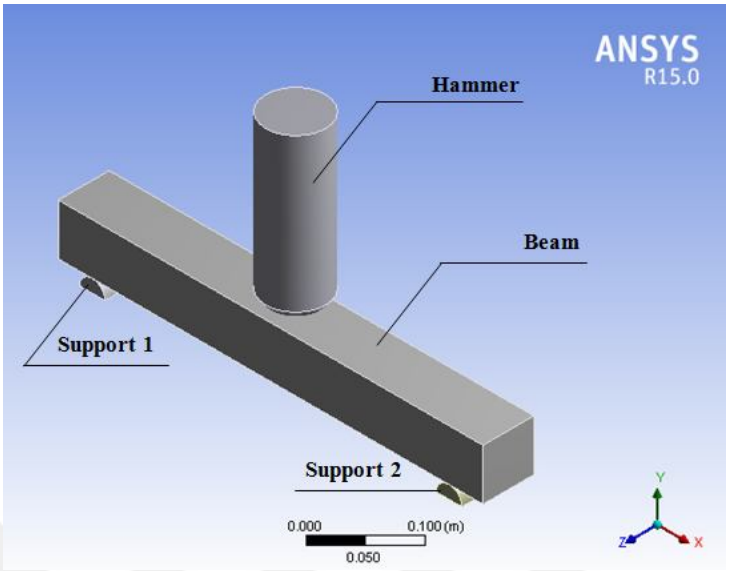

Figure 5-1 – General view of model

Table 5-1 – Details related to modeling of beams

Cross-Section (mm)	60×60	100×100	150×150
Material	Concrete		
X-Length (m)	0.5		
Y-Length(m)	0.06	0.10	0.15
Z-Length(m)	0.06	0.10	0.15
X-Centroid (m)	0		
Y-Centroid (m)	0.03	0.05	0.075
Z-Centroid (m)	0.03	0.05	0.075
# of Nodes	2499	2240	2106
# of Elements	1800	1666	1600

Table 5-2 – Details related to modeling of hammer

Cross-Section(mm)	60×60	100×100	150×150
Material	Steel		
X-Length (m)	0.0700		
Y-Length (m)	0.2000		
Z-Length(m)	0.0700		
X-Centroid (m)	-0.000441		
Y-Centroid (m)	0.16442	0.20442	0.25442
Z-Centroid (m)	0.03	0.05	0.075
# of Nodes	1960	616	308
# of Elements	1634	455	210

Table 5-3 – Details related to modeling of supports

	Support 1			Support 2		
Cross-Section(mm)	60×60	100×100	150×150	60×60	100×100	150×150
Material	Steel					
X-Length (m)	0.03					
Y-Length (m)	0.015					
Z-Length(m)	0.06	0.10	0.15	0.06	0.10	0.15
X-Centroid (m)	-0.210			0.210		
Y-Centroid (m)	-0.009			-0.009		
Z-Centroid (m)	0.03	0.05	0.075	0.03	0.05	0.075
# of Nodes	84	132	192	84	132	192
# of Elements	42	72	105	42	72	105

5.1.3 Material Properties

The materials used in modeling were concrete for beam specimens and steel for hammer and supports. ANSYS Explicit Dynamics modeling includes of a number of material models for concrete and steel. Based on the literature review, the RHT concrete model developed by Riedel et al. (1999) was the most appropriate model to simulate the concrete behavior under impact loading. The RHT model was also readily available in the library of ANSYS AUTODYN Explicit Dynamic. Therefore, the RHT concrete model was used to model the concrete beams in this research.

In RHT model, the concrete strength was defined as concrete compressive strength of a cube specimen. Therefore the cylinder strengths obtained in the scope of this research were converted to cube strength by dividing the cylinder strengths to 0.85. The default variables for material properties of concrete and steel defined in modeling are shown in Table 5-4 and Table 5-5, respectively.

Table 5-4 – Material properties of concrete defined in modeling (RHT Concrete model)

Property	Units	Value
RHT Concrete Model		
Density	kgf/m^3	2328
Compressive Strength, f_c (strength of cube)	MPa	14.1 (LSC) or 30.6 (NSC)
Tensile to Compressive Strength, f_t/f_c	None	0.08
Shear to Compressive Strength, f_s/f_c	None	0.18 (default)
Intact failure surface constant, A_{FAIL}	None	1.6 (default)
Intact failure surface exponent, N_{FAIL}	None	0.61 (default)
Tens./Comp. Meridian ratio, $Q_{2.0}$	None	0.6805 (default)
Brittle to Ductile Transition, BQ	None	0.0105 (default)
Hardening Slope	None	2 (default)
Elastic Strength/f_t	None	0.7 (default)
Elastic Strength/f_c	None	0.53 (default)
Fracture Strength Constant, B	None	1.6 (default)
Fracture Strength Exponent, m	None	0.61 (default)
Compressive strain rate exponent, α	None	0.032 (default)
Tensile strain rate exponent, δ	None	0.036 (default)
Maximum fracture strength ratio, *SFMAXSFMAX*	None	1E+20 (default)
Use cap on elastic surface	None	Yes (default)
Damage constant, D_1	None	0.04 (default)
Damage constant, D_2	None	1 (default)
Minimum strain to failure	None	0.01 (default)
Residual Shear modulus fraction	None	0.13 (default)
Shear Modulus	MPa	16,700 (default)
Use CAP on elastic surface?	None	Yes (default)
Polynomial EOS		
Parameter A1	MPa	35,270 (default)
Parameter A2	MPa	39,580 (default)
Parameter A3	MPa	9,040 (default)
Parameter B0	None	1.22 (default)
Parameter B1	None	1.22 (default)
Parameter T1	MPa	35,270 (default)
Parameter T2	MPa	0 (default)
P-alpha EOS		
Solid Density	kgf/m^3	2,750 (default)
Porous Soundspeed	m/s	2,920 (default)
Initial Compaction Pressure, P_e	MPa	23.3 (default)
Solid Compaction Pressure, P_s	MPa	6000 (default)
Compaction Exponent, n	None	3 (default)

Table 5-5 – Material properties of steel defined in modeling

Property	Units	Value
Density	kgf/m^3	7850 (default)
Young's Modulus	GPa	200 (default)
Poisson's Ratio, ν	None	0.3 (default)
Bulk Modulus	GPa	166.67 (calculated by ANSYS)
Shear Modulus	GPa	76.923 (calculated by ANSYS)
Tensile Yield Strength f_y	MPa	443
Elastic Modulus, E_{el}	GPa	200 (default)
Tangent Modulus, E_t	GPa	19 (default)

The steel hammer, steel support 1, and support 2 were modeled as rigid bodies with a density of 7850 kgf/m^3 with an elastic modulus of 210 GPa, and Poission's ratio of 0.30. The steel reinforcing bar was modeled the same above mentioned steel input parameter values with bilinear isotropic hardening parameters within the Engineering Data Library of the software using default values.

5.1.4 Analysis Settings

5.1.4.1 Erosion

Erosion option in ANSYS Analysis Settings is used to automatically delete highly distorted elements from the analysis. This technique is a necessity to solve impact penetration problems. Several options are available to initiate erosion. ANSYS Explicit Dynamics Analysis Guide (2015) recommended the values of geometric strain limit for erosion to be in the range of 0.75 and 3.0 with a default value of 1.5. After a detailed parametric study, the value of geometric strain limit was used as 1.5 in this research. The settings for erosion option are shown in Table 5-6.

Table 5-6 – Erosion option settings

Property	**Value**
On geometric strain limit	Yes
Geometric Strain limit	1.5 (default)
On material Failure	Yes
On minimum element Time Step	No
Retain inertia of Eroded Material	Yes

5.1.4.2 Meshing

Free meshing method, readily available in ANSYS Software, was used for meshing the modeled elements initially. However, the number of elements used in this meshing was so high that one analysis took more than 6 hours. Later a convergence study was conducted on the concrete elements. This study included comparison of the mid-point deflection of various sizes of meshing. As an example, unreinforced specimen having 60×60×500 mm dimensions was meshed with increasing element numbers such as 555, 3048, 3439, 3492, 3798, 4082, 4152, and 4302 elements as

shown in Figure 5-2, and reinforced specimen having 60×60×500 mm dimensions was meshed with increasing element numbers such as 475, 1053, 2736, 3010, 3323, 3568, 5023, and 6244 elements as shown in Figure 5-3. After each meshing the mid-point deflection was calculated by the software. The model became unstable after maximum element numbers for meshing (4302 elements for 60×60×500 mm unreinforced specimens and 6244 elements for 60×60×500 mm reinforced specimens) was reached. The analysis did not continue based on the capability of the software package. The results showed that the calculated deflection value for unreinforced specimen was constant (deflection value of 0.019 m) for 3492, 3518, 4082, and 4158 elements, and for reinforced specimen the calculated deflection value was constant (deflection value of 0.007 m) for 3010, 3323, 3568, and 5023 elements. The mid-point deflections were not affected with the fineness of the meshing in these ranges as shown in Figure 5-4 and Figure 5-5. Therefore, meshing with 3518 elements (including beam, hammer and supports) was selected for unreinforced specimen having 60×60×500 mm dimensions. For reinforced specimen having 60×60×500 mm dimensions, 3568 elements (including beam, hammer, supports and reinforcement steel bar) was selected. The final meshed model for unreinforced and reinforced specimen having 60×60×500 mm dimensions are shown in Figure 5-6 and Figure 5-7, respectively. This convergence study was performed for each specimen and meshing was selected accordingly. Based on the results of convergence study, the number of beam elements for beam size 60×60×500 mm is 1800 elements with a mesh size of 10 mm. For beam sizes of 100×100×500 mm and 150×150×500 mm, 1666 elements with a mesh size of 15 mm and 1600 elements with a mesh size of 20 mm were used in the analysis as shown in Figure 5-8.

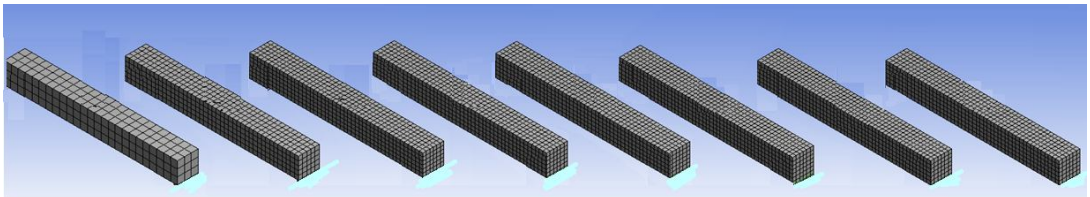

Figure 5-2 – Number of elements used for convergence study for unreinforced specimen having 60×60×500 mm dimensions

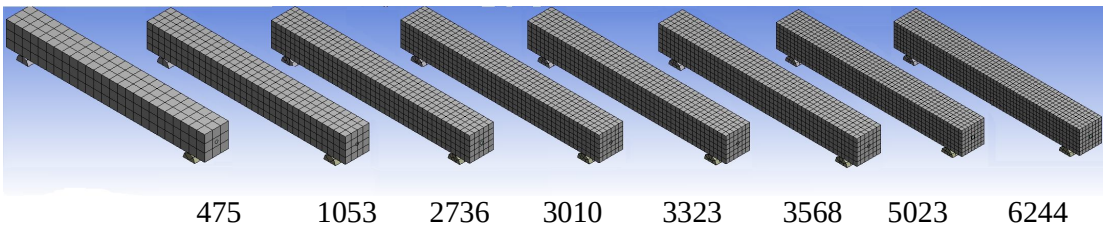

Figure 5-3 – Number of elements used for convergence study for reinforced specimen having 60×60×500 mm dimensions

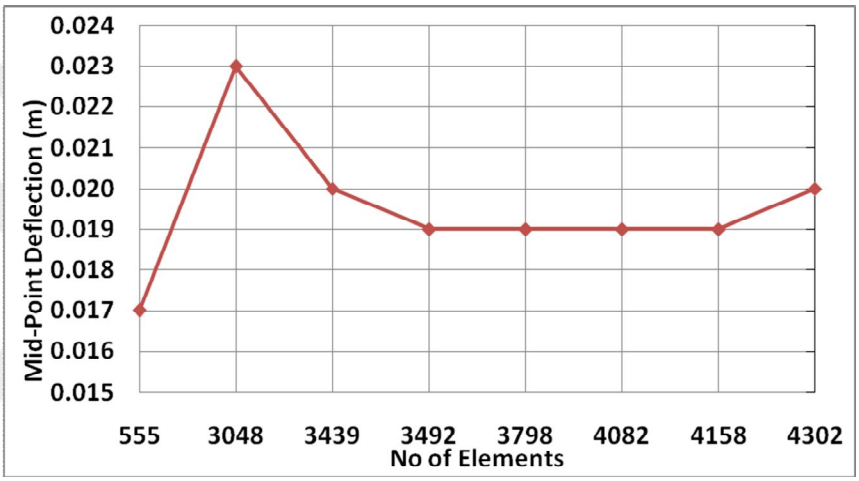

Figure 5-4 – Results of the convergence study for unreinforced specimen having 60×60×500 mm dimensions

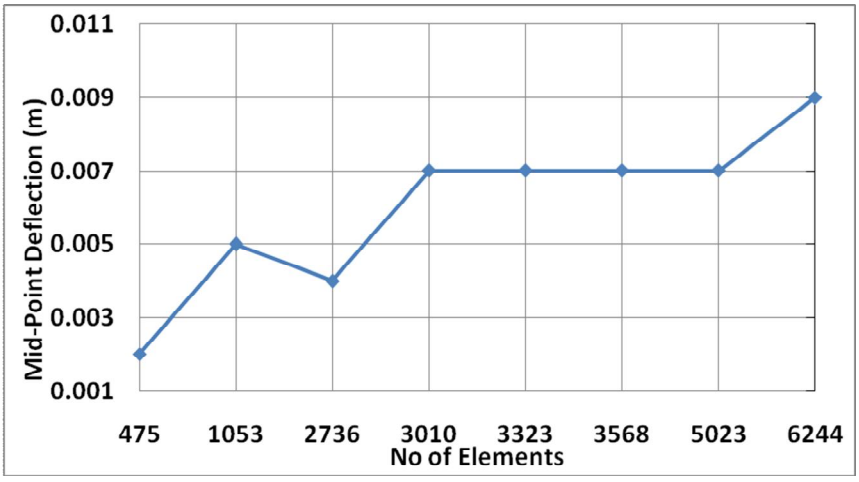

Figure 5-5 – Results of the convergence study for reinforced specimen having 60×60×500 mm dimensions

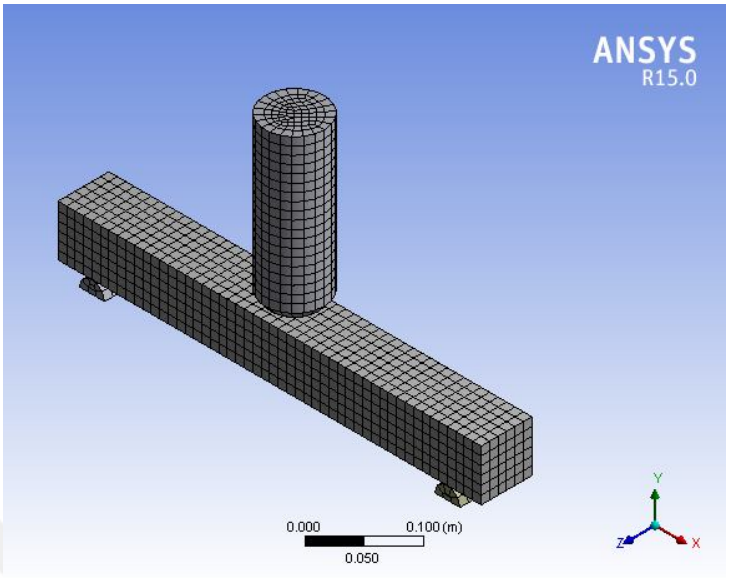

Figure 5-6 – Final meshed model for unreinforced specimen having 60×60×500 mm dimensions

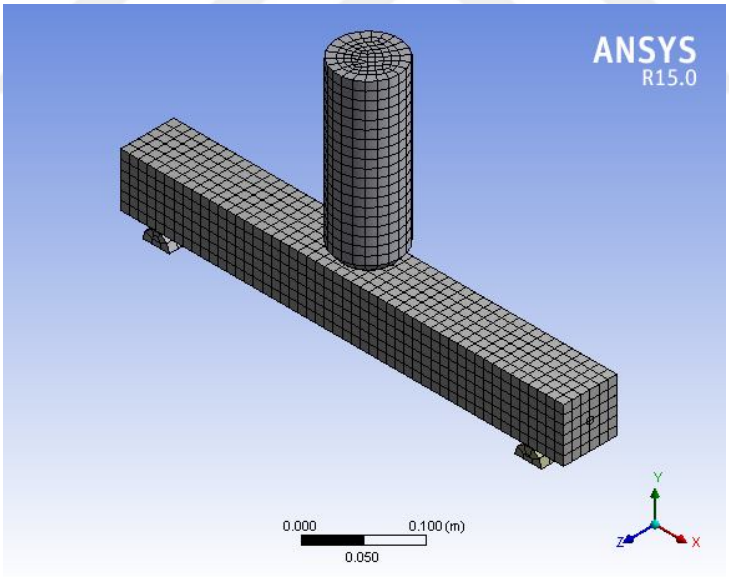

Figure 5-7 – Final meshed model for reinforced specimen having 60×60×500 mm dimensions

Table 5-7 – Determination of mesh size according to convergence study

Specimen Dimension	Number of Nodes				Final Number of Nodes	Final Mesh Size
	Mesh Size (m)					
	0.005	**0.010**	**0.015**	**0.020**		
60×60×500	14400	**1800**	533	225	**1800**	**0.010**
100×100×500	40000	5000	**1481**	625	**1666**	**0.015**
150×150×500	90000	11250	3333	**1406**	**1600**	**0.020**

5.1.4.3 Initial Contact Velocity

As explicit dynamic modeling, the initial conditions shall be determined before running the solution. In this study, the velocity of steel hammer at the time of impact was calculated using the recorded impact videos and the TEMA Motion Analysis Software. Experimental impact velocity values for each test obtained from the TEMA Motion Analysis Software are shown in Table 5-8. The average velocity for each group was used to define the initial contact velocity of the hammer in ANSYS Dynamic Explicit Modeling as shown in Figure 5-8.

Table 5-8 – Experimental and ANSYS impact velocities

Group No	Specimen ID	Experimental Impact Velocity (m/s) (TEMA Motion)	ANSYS Impact Velocity (m/s)
1	60C12-1	5.837	5.798
	60C12-2	5.837	
	60C12-3	5.720	
2	60C26-1	5.609	5.505
	60C26-2	5.630	
	60C26-3	5.277	
3	100C12-1	7.610	7.649
	100C12-2	7.639	
	100C12-3	7.697	
4	100C26-1	7.145	7.067
	100C26-2	7.335	
	100C26-3	6.722	
5	150C12-1	7.855	7.864
	150C12-2	7.867	
	150C12-3	7.871	
6	150C26-1	7.601	7.654
	150C26-2	7.642	
	150C26-3	7.718	
7	60C12R-1	Video could not captured.	8.009
	60C12 R -2	7.979	
	60C12 R -3	8.039	
8	60C26 R -1	7.618	7.574
	60C26 R -2	7.606	
	60C26 R -3	7.499	
9	100C12 R -1	7.920	7.818
	100C12 R -2	7.788	

Group No	Specimen ID	Experimental Impact Velocity (m/s) (TEMA Motion)	ANSYS Impact Velocity (m/s)
	100C12 R -3	7.848	
10	100C26 R -1	7.569	7.558
	100C26 R -2	7.335	
	100C26 R -3	7.570	
11	150C12 R -1	7.803	7.738
	150C12 R -2	7.809	
	150C12 R -3	7.603	
12	150C26 R -1	7.715	7.711
	150C26 R -2	7.701	
	150C26 R -3	7.717	
13-a	60SFRC35-1	7.602	7.505
	60SFRC35-2	7.408	
13-b	60SFRC35-3	5.867	7.867
14	60SFRC35R-1	7.497	7.567
	60SFRC35R-2	7.636	
15	100SFRC35-1	7.639	7.616
	100SFRC35-2	7.575	
	100SFRC35-3	7.634	
16	100SFRC35R-1	7.527	7.601
	100SFRC35R-2	7.563	
	100SFRC35R-3	7.638	
17	150SFRC35-1	7.671	7.694
	150SFRC35-2	7.702	
	150SFRC35-3	7.708	
18	150SFRC35R-1	7.659	7.670
	150SFRC35R-2	7.673	
	150SFRC35R-3	7.678	

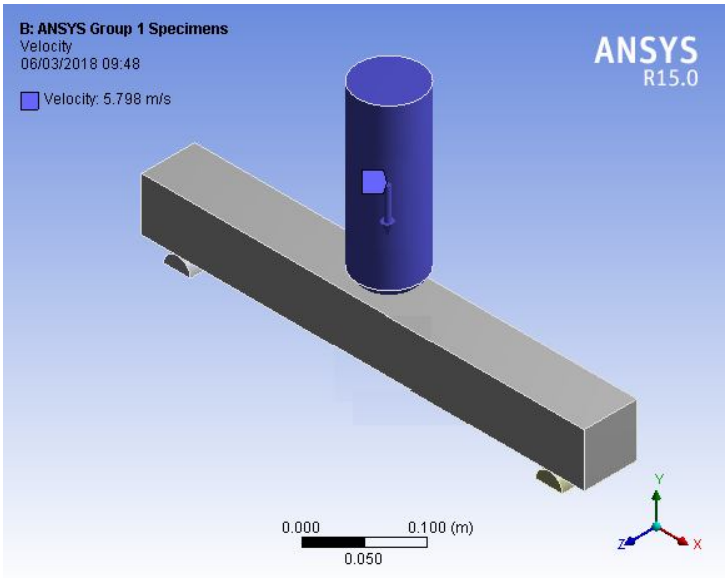

Figure 5-8 – Average velocity of hammer used in ANSYS modeling for Group 1 specimens

5.2 Modifications to RHT Concrete Model

Computationally long and detailed parametric studies were performed for all the parameters of modeling explained in this section. RHT model that used in ANSYS dynamic Explicit AUTODYN solver was studied and compared to the experimental studies performed on CC and SFRC. Based on these studies, the settings and values of the parameters were determined and stress strain parameters were modified.

The following modified values for LSC, NSC, and SFRC shown in Table 5-9 to Table 5-11 were used in the analysis. The details of these modifications are explained in the next sections.

Table 5-9 – Modified analysis parameters of RHT Concrete Model for LSC (Batch 1)

Property	Units	Value	
RHT Concrete Model			
		Modified RHT	Default RHT
Density	kgf/m^3	2294	2314(default)
Compressive Strength, f_c (cube strength)	MPa	14.1	14.1
Tensile to Compressive Strength, f_t/f_c	None	0.14	0.1(default)
Shear to Compressive Strength, f_s/f_c	None	0.11	0.18 (default)
Intact failure surface constant, A_{FAIL}	None	1.6 (default)	1.6 (default)
Intact failure surface exponent, N_{FAIL}	None	0.61 (default)	0.61 (default)
Tens./Comp. Meridian ratio, $Q_{2.0}$	None	0.6805 (default)	0.6805 (default)
Brittle to Ductile Transition, *BQ*	None	0.0105 (default)	0.0105 (default)
Hardening Slope	None	2 (default)	2 (default)
Elastic Strength/f_t	None	0.7 (default)	0.7 (default)
Elastic Strength/f_c	None	0.53 (default)	0.53 (default)
Fracture Strength Constant, *B*	None	1.6 (default)	1.6 (default)
Fracture Strength Exponent, *m*	None	0.61 (default)	0.61 (default)
Compressive strain rate exponent, α	None	0.064	0.032 (default)
Tensile strain rate exponent, δ	None	0.059	0.036 (default)
Maximum fracture strength ratio, *SFMAX*	None	1E+20 (default)	1E+20 (default)
Use cap on elastic surface	None	Yes (default)	Yes (default)
Damage constant, D_1	None	0.06	0.04 (default)
Damage constant, D_2	None	1 (default)	1 (default)
Minimum strain to failure	None	0.01 (default)	0.01 (default)
Residual Shear modulus fraction	None	0.13 (default)	0.13 (default)
Shear Modulus	MPa	16,700 (default)	16,700 (default)
Use CAP on elastic surface?	None	Yes (default)	Yes (default)
Polynomial EOS			
Parameter A1	MPa	35,270 (default)	35,270 (default)
Parameter A2	MPa	39,580 (default)	39,580 (default)
Parameter A3	MPa	9,040 (default)	9,040 (default)
Parameter B0	None	1.22 (default)	1.22 (default)
Parameter B1	None	1.22 (default)	1.22 (default)
Parameter T1	MPa	35,270 (default)	35,270 (default)
Parameter T2	MPa	0 (default)	0 (default)
P-alpha EOS			
Solid Density	kgf/m^3	2,750 (default)	2,750 (default)
Porous Soundspeed	m/s	2,920 (default)	2,920 (default)
Initial Compaction Pressure, P_e	MPa	23.3 (default)	23.3 (default)
Solid Compaction Pressure, P_s	MPa	6000 (default)	6000 (default)
Compaction Exponent, *n*	None	3 (default)	3 (default)

Table 5-10 – Modified analysis parameters of RHT Concrete Model for NSC (Batch 2)

Property	Units	Value	
RHT Concrete Model			
		Modified RHT	Default RHT
Density	kgf/m^3	2334	2314(default)
Compressive Strength, f_c (cube strength)	MPa	30.6	30.6
Tensile to Compressive Strength, f_t/f_c	None	0.10 (default)	0.1(default)
Shear to Compressive Strength, f_s/f_c	None	0.17	0.18 (default)
Intact failure surface constant, A_{FAIL}	None	1.6 (default)	1.6 (default)
Intact failure surface exponent, N_{FAIL}	None	0.61 (default)	0.61 (default)
Tens./Comp. Meridian ratio, $Q_{2.0}$	None	0.6805 (default)	0.6805 (default)
Brittle to Ductile Transition, *BQ*	None	0.0105 (default)	0.0105 (default)
Hardening Slope	None	2 (default)	2 (default)
Elastic Strength/f_t	None	0.7 (default)	0.7 (default)
Elastic Strength/f_c	None	0.53 (default)	0.53 (default)
Fracture Strength Constant, *B*	None	1.6 (default)	1.6 (default)
Fracture Strength Exponent, *m*	None	0.61 (default)	0.61 (default)
Compressive strain rate exponent, α	None	0.036	0.032 (default)
Tensile strain rate exponent, δ	None	0.044	0.036 (default)
Maximum fracture strength ratio, *SFMAX*	None	1E+20 (default)	1E+20 (default)
Use cap on elastic surface	None	Yes (default)	Yes (default)
Damage constant, D_1	None	0.013	0.04 (default)
Damage constant, D_2	None	1 (default)	1 (default)
Minimum strain to failure	None	0.01 (default)	0.01 (default)
Residual Shear modulus fraction	None	0.13 (default)	0.13 (default)
Shear Modulus	MPa	16,700 (default)	16,700 (default)
Use CAP on elastic surface?	None	Yes (default)	Yes (default)
Polynomial EOS			
Parameter A1	MPa	35,270 (default)	35,270 (default)
Parameter A2	MPa	39,580 (default)	39,580 (default)
Parameter A3	MPa	9,040 (default)	9,040 (default)
Parameter B0	None	1.22 (default)	1.22 (default)
Parameter B1	None	1.22 (default)	1.22 (default)
Parameter T1	MPa	35,270 (default)	35,270 (default)
Parameter T2	MPa	0 (default)	0 (default)
P-alpha EOS			
Solid Density	kgf/m^3	2,750 (default)	2,750 (default)
Porous Soundspeed	m/s	2,920 (default)	2,920 (default)
Initial Compaction Pressure, P_e	MPa	23.3 (default)	23.3 (default)
Solid Compaction Pressure, P_s	MPa	6000 (default)	6000 (default)
Compaction Exponent, *n*	None	3 (default)	3 (default)

Table 5-11 – Modified analysis parameters of RHT Concrete Model for SFRC (Batch 3)

Property	Units	Value	
RHT Concrete Model			
		Modified RHT	Default RHT
Density	kgf/m^3	2379	2314(default)
Compressive Strength, f_c (cube strength)	MPa	41.1	41.1
Tensile to Compressive Strength, f_t/f_c	None	0.09	0.1(default)
Shear to Compressive Strength, f_s/f_c	None	0.19	0.18 (default)
Intact failure surface constant, A_{FAIL}	None	1.6 (default)	1.6 (default)
Intact failure surface exponent, N_{FAIL}	None	0.61 (default)	0.61 (default)
Tens./Comp. Meridian ratio, $Q_{2.0}$	None	0.6805 (default)	0.6805 (default)
Brittle to Ductile Transition, *BQ*	None	0.0105 (default)	0.0105 (default)
Hardening Slope	None	2 (default)	2 (default)
Elastic Strength/f_t	None	0.7 (default)	0.7 (default)
Elastic Strength/f_c	None	0.53 (default)	0.53 (default)
Fracture Strength Constant, *B*	None	1.6 (default)	1.6 (default)
Fracture Strength Exponent, *m*	None	0.61 (default)	0.61 (default)
Compressive strain rate exponent, α	None	0.028	0.032 (default)
Tensile strain rate exponent, δ	None	0.033	0.036 (default)
Maximum fracture strength ratio, *SFMAX*	None	1E+20 (default)	1E+20 (default)
Use cap on elastic surface	None	Yes (default)	Yes (default)
Damage constant, D_1	None	0.028	0.04 (default)
Damage constant, D_2	None	1 (default)	1 (default)
Minimum strain to failure	None	0.01 (default)	0.01 (default)
Residual Shear modulus fraction	None	0.13 (default)	0.13 (default)
Shear Modulus	MPa	16,700 (default)	16,700 (default)
Use CAP on elastic surface?	None	Yes (default)	Yes (default)
Polynomial EOS			
Parameter A1	MPa	35,270 (default)	35,270 (default)
Parameter A2	MPa	39,580 (default)	39,580 (default)
Parameter A3	MPa	9,040 (default)	9,040 (default)
Parameter B0	None	1.22 (default)	1.22 (default)
Parameter B1	None	1.22 (default)	1.22 (default)
Parameter T1	MPa	35,270 (default)	35,270 (default)
Parameter T2	MPa	0 (default)	0 (default)
P-alpha EOS			
Solid Density	kgf/m^3	2,750 (default)	2,750 (default)
Porous Soundspeed	m/s	2,920 (default)	2,920 (default)
Initial Compaction Pressure, P_e	MPa	23.3 (default)	23.3 (default)
Solid Compaction Pressure, P_s	MPa	6000 (default)	6000 (default)
Compaction Exponent, *n*	None	3 (default)	3 (default)
Failure		**Modified**	**Default**
Principle Strength Failure			
Maximum Tensile Stress	MPa	3.58	1E+20
Maximum Shear Stress	MPa	21.783	1E+20
Principle Strain Failure			
Maximum Tensile Strain		0.000118	1+E20
Maximum Shear Strain		0.0023	1E+20
Crack Softening Failure			
Flow Role		No Bulking (default)	No Bulking (default)
Fracture Energy, G_f	J/m^2	1515, 3029 and 4544	0

5.2.1 Density (Unit Weight)

Unit weight is defined as the initial mass per unit volume of a material at initial time. In RHT Concrete model the default value of unit weight is 2314 kgf/m^3. The unit weights of the types of concrete used in this research were determined by measuring the weight of each specimen and dividing the weight by the volume. A photograph of weighing the specimens is shown in Figure 5-9. For LSC, NSC, and SFRC, the average unit weights were determined as 2294, 2334, and 2379 kgf/m^3, respectively. Details related to all the specimens are shown in Table 5-12.

Figure 5-9 – Measurement of specimens weight at laboratory to determine its density

Table 5-12 – Details of calculation of unit weights of specimens

Group No	Specimen ID	Weight (kgf)	Unit Weight (kgf/m^3)	Average Unit Weight (kgf/m^3)
1	60C12-1	4.16	2311	2294 for LSC 2334 for NSC
	60C12-2	4.16	2311	
	60C12-3	4.36	2422	
2	60C26-1	4.25	2361	
	60C26-2	4.35	2417	
	60C26-3	4.42	2456	
3	100C12-1	11.30	2260	
	100C12-2	11.78	2356	
	100C12-3	11.26	2252	
4	100C26-1	11.45	2290	
	100C26-2	11.67	2334	
	100C26-3	11.88	2376	
5	150C12-1	24.94	2217	
	150C12-2	25.56	2272	
	150C12-3	25.22	2242	
6	150C26-1	25.25	2244	
	150C26-2	25.60	2276	
	150C26-3	25.34	2252	
13-a	60SFRC35-1	4.36	2422	2379 For SFRC
	60SFRC35-2	4.42	2456	
13-b	60SFRC35-3	4.40	2444	
15	100SFRC35-1	11.78	2356	
	100SFRC35-2	12.08	2416	
	100SFRC35-3	12.06	2412	
17	150SFRC35-1	26.01	2312	
	150SFRC35-2	26.11	2321	
	150SFRC35-3	25.59	2275	

5.2.2 Compressive Strength

According to ANSYS Explicit Dynamics Analysis Guide (2015), RHT model formulated such that the input compressive strength value shall be in terms of cube strength. The users may convert their cylinder strength values to cube strength values before entering the concrete strength parameter. In this research, a conversion factor of 0.85 was used to convert the cylinder strength to cube strength by dividing the cylinder strength values to this conversion factor.

The material library of ANSYS Finite Element Software includes RHT Concrete Model data for cube concrete strengths of 35 MPa and 140 MPa with default values. Cylinder concrete compressive strength values for LSC, NSC, and SFRC obtained in this research were converted to cube strength values of 14.1, 30.6, and 41.1 MPa,

respectively. These values were used in ANSYS Finite Element Software as shown in Table 5-9 to Table 5-11, respectively.

5.2.3 Tensile Strength

The ratio between tensile strength and compressive strength, f_t/f_c, is defined in RHT Model Library as tensile strength. As default for C35, the material library uses 0.1 for f_t/f_c. In this study, the measured tensile strengths were divided by the measured compressive strengths and 0.14, 0.10, and 0.09 was used as the input data for LSC, NSC, and SFRC, respectively. These values were used in ANSYS Finite Element Software as shown in Table 5-9, Table 5-10 and, Table 5-11, respectively.

5.2.4 Stress-Strain Relationship

The RHT concrete model in compression consists of three parts: elastic, failure, and residual softening part. The elastic part depends on elastic modulus. The linear curve for elastic part starts from the origin and continues up to stress of 53% of ultimate concrete strength which is a property of RHT Concrete Model. The strain at this point is calculated using this value of stress and elastic modulus. The failure part is another linear line between the 53 and 100% of ultimate concrete strength. The equations related to these parts are shown in Equation 2-13 and Equation 2-14. The residual part starts from the ultimate concrete strength and ends at a point that is defined by the user using Equation 2-25. A typical stress-strain relationship of RHT concrete model in compression is shown in Figure 5-10.

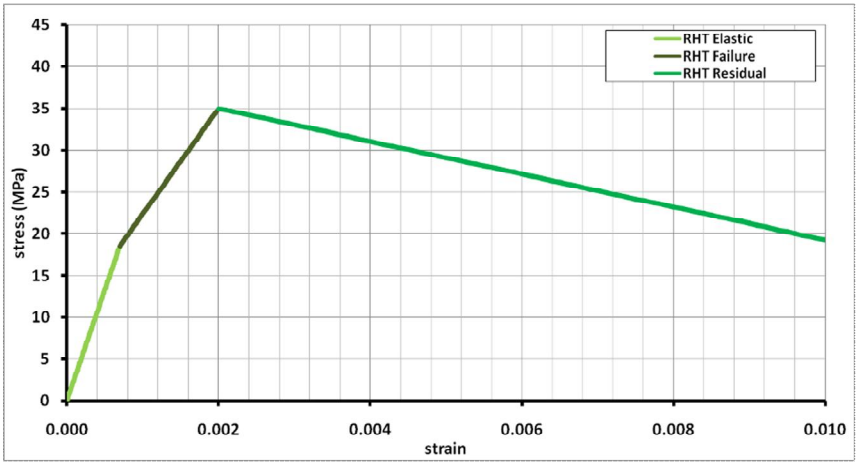

Figure 5-10 – Typical elastic, failure, and residual branches of stress–strain relationship of RHT concrete model in compression

The residual part includes two parameters called damage parameters. Tu and Lu (2008) stated that the determination of damage parameters, D_1, D_2, and plastic strain was very crucial to obtain a reasonable stress-strain relationship in softening region. In this study, modification of the parameter D_1 was performed while the value of the parameter D_2 was kept unchanged.

5.2.4.1 CC in Compression

The RHT model is modified for CC in compression based on the model proposed by Popovics (1973). The default value for the concrete strength of RHT Concrete Model was 35 MPa. As an example, the Popovics (1973) concrete model and RHT Concrete Model were drawn on the same graph for the same strength and the parameters related to RHT Concrete Model were modified to match the stress-strain relationship proposed by Popovics (1973) for that concrete strength. Corresponding stress-strain relationship is shown in Figure 5-11. The elastic parts for both the RHT Concrete Models were the same. The default RHT had a greater strain at ultimate stress and a less steep descending branch compared to Popovics (1973) Concrete Model. The modified RHT Concrete Model was matching better since the strain at maximum stress and the descending branches of the relationship was fitted to the Popovics (1973) Concrete Model. Related values of the parameters are shown in the same graph.

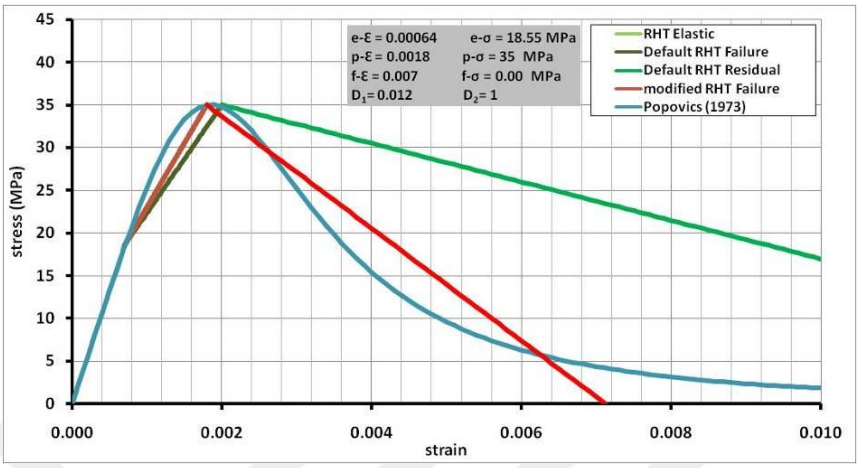

Figure 5-11 – Comparison of default and modified RHT Concrete Models to Popovics (1973) Concrete Model for 35 MPa concrete compressive strength

In this study, two types of CC were used, LSC having 12 MPa and NSC having 26 MPa cylinder concrete compressive strength. The RHT Concrete Model uses the cubic strength values in construction of the stress-strain relationship. Therefore, the cylinder concrete strengths were converted to cubic strength values as explained previously. Therefore LSC having 14.1 MPa and NSC having 30.6 MPa was used in construction of stress-strain relationships CC. Comparison of default and modified RHT Concrete Models to Popovics (1973) CC Model for 14.1 and 30.6 MPa concrete compressive strength is shown in Figure 5-12 and Figure 5-13. Related values of the parameters are also shown in the same graphs.

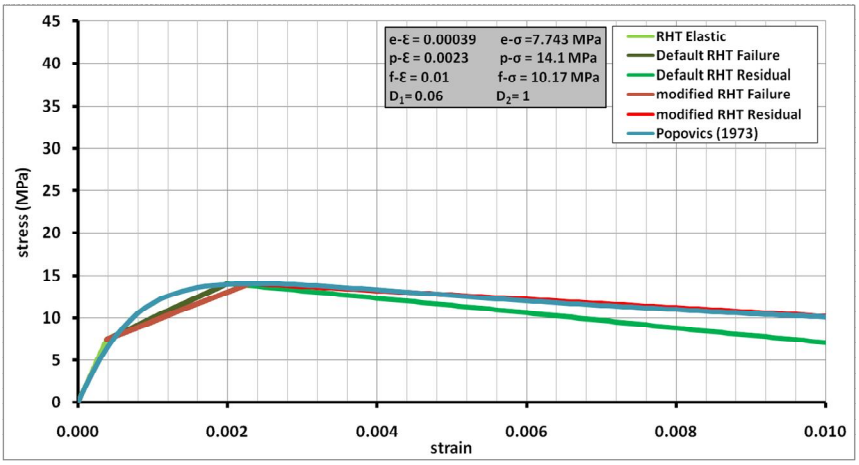

Figure 5-12 – Comparison of default and modified RHT Concrete Models to Popovics (1973) CC Model for 14.1 MPa concrete compressive strength

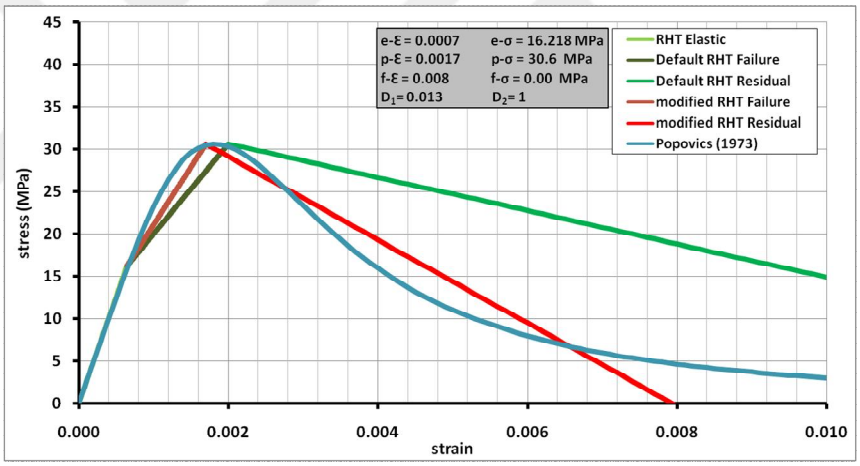

Figure 5-13 – Comparison of default and modified RHT Concrete Models to Popovics (1973) CC Model for 30.6 MPa concrete compressive strength

5.2.4.2 SFRC in Compression

The RHT model is modified for SFRC in compression based on the model proposed by Ezeldin and Balaguru (1990). In this study, one type of SFRC having 35 MPa cylinder concrete compressive strength was used. The cylinder concrete strength was converted to cubic strength value as explained previously. Therefore SFRC having 41.1 MPa was used in construction of stress-strain relationships of SFRC. Comparison of default and modified RHT Concrete Models to Ezeldin and Balaguru

(1990) SFRC Model for 41.1 MPa concrete compressive strength is shown in Figure 5-14.

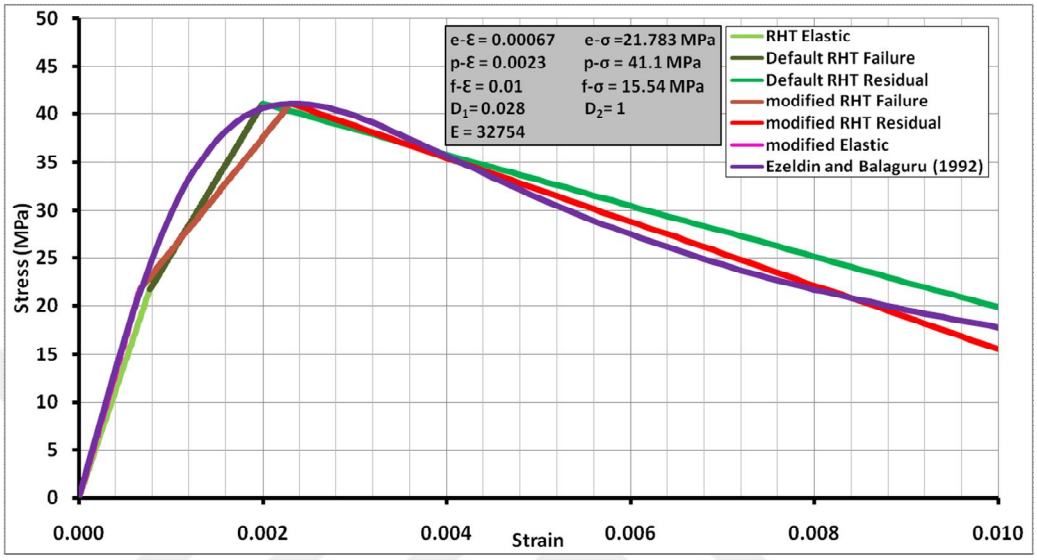

Figure 5-14 – Comparison of default and modified RHT Concrete Models to Ezeldin and Balaguru (1990) SFRC Model for 41.1 MPa concrete compressive strength

5.2.4.3 SFRC in Tension

The RHT model is modified for SFRC in tension based on the model proposed Soranakom et al. (2008). In this study, the average flexural tensile strength for SFRC was measured as 3.543 MPa. The tensile stress-strain relationships for SFRC proposed by Soranakom et al. (2008) for 3.543 MPa tensile strength and various μ values (0.25, 0.5, and 0.75) are shown in Figure 5-15.

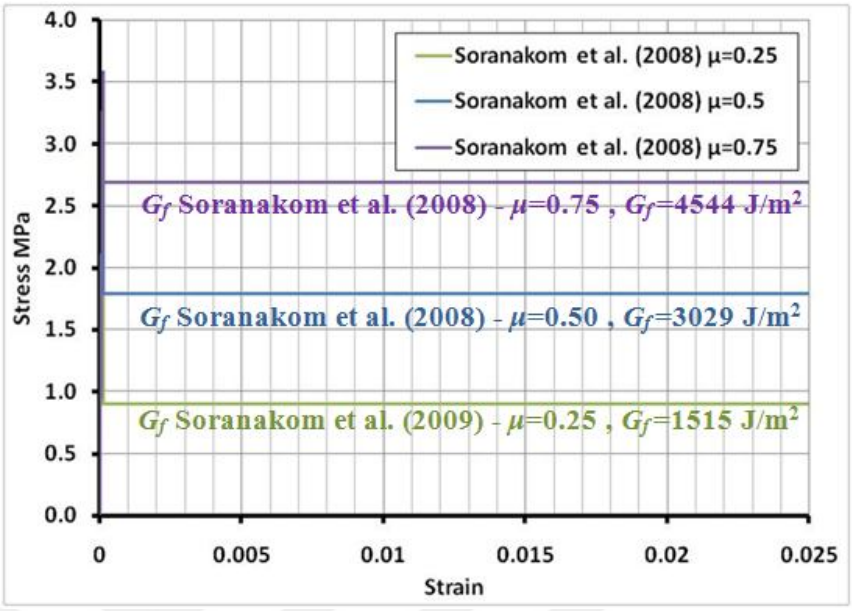

Figure 5-15 – Tensile stress-strain relationships for SFRC proposed by Soranakom et al. (2008) for 3.543 MPa tensile strength and various μ values (0.25, 0.5, and 0.75)

RHT Concrete Model uses the fracture energy methodology for the effect of tension stiffening which requires the calculation of fracture energy of the tension behavior of the material. Abdelatif et al. (2015) studied and modeled concrete in tension as linear-elastic until tensile strength is reached. The researchers implemented the post-cracking behavior based on the cracking concept proposed by Hillerborg et al. (1976). They assumed a linearly decreasing tension softening behavior based on the findings by Phillips and Binsheng (1993) as shown in Figure 5-16.

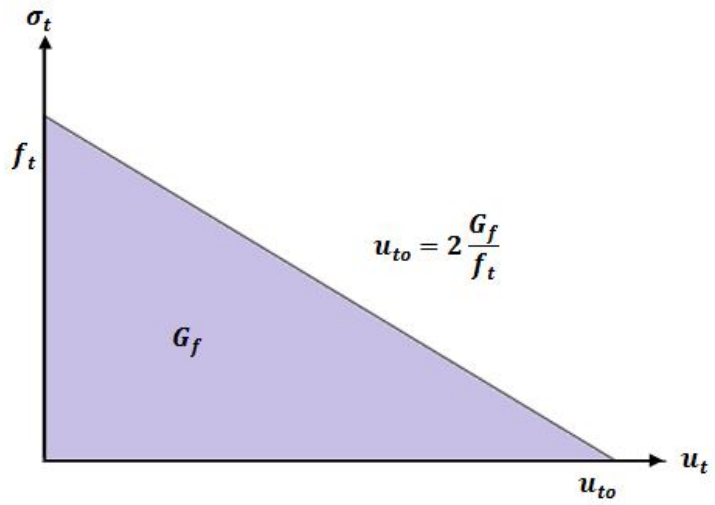

Figure 5-16 – Post-failure stress–fracture energy curve applied in the non- linear model

The fracture energy required to create a crack per unit area, G_f, is the area under the stress-strain relationship in tension. It is calculated using the following equation:

$$G_f = 0.5 * f_t * U_{to} * L_c \qquad \text{Equation 5-1}$$

where f_t is concrete tensile strength in MPa, U_{to} is the ultimate tensile strain, L_c is the characteristic length.

Based on Bazant and Oh (1983), the characteristic length can be determined by the following equation:

$$L_c = 2.7 * d_a \qquad \text{Equation 5-2}$$

where d_a is the maximum aggregate size.

Based on this methodology and tensile behavior of SFRC proposed by Soranakom et al. (2008) (Figure 5-15), G_f values were calculated as 1515, 3029, and 4544 J/m^2 for μ was equal to 0.25, 0.5, and 0.75, respectively. These values were used in ANSYS Finite Element Software for G_f.

5.2.5 Compressive Strain Rate Exponent

Based on Riedel et al. (2009), compressive strain rate exponent, α, was calculated using the following expression:

$$\alpha = \frac{1}{(5+\frac{3}{4}f_c)} \qquad \text{Equation 5-3}$$

where f_c is the concrete compressive strength.

In RHT Concrete model, the default value of compressive strain rate exponent is defined as 0.032. Using the above equation, the compressive strain rate exponents for LSC, NSC, and SFRC were calculated as 0.064, 0.036, and 0.028, respectively. These values were used in ANSYS Finite Element Software as shown in Table 5-9, Table 5-10 and, Table 5-11, respectively.

5.2.6 Tensile Strain Rate Exponent δ input variables

Based on Riedel et al. (2009), tensile strain rate exponent, δ, was calculated using the following expression:

$$\delta = \frac{1}{(10+\frac{1}{2}f_c)} \qquad \text{Equation 5-4}$$

where f_c is the concrete compressive strength.

In RHT Concrete model, the default value of tensile strain rate exponent is defined as 0.036. Using the above equation, the tensile strain rate exponents for LSC, NSC, and SFRC were calculated as 0.059, 0.044, and 0.033, respectively. These values were used in ANSYS Finite Element Software as shown in Table 5-9, Table 5-10 and, Table 5-11, respectively.

5.3 Steel Model

No modifications was performed for the input parameters of steel. These parameters are shown in Table 5-13.

Table 5-13 – Material properties of steel

Property	Units	Value
Density	kgf/m^3	7850 (default)
Young's Modulus	GPa	200 (default)
Poisson's Ratio, ν	None	0.3 (default)
Bulk Modulus	GPa	166.67 (calculated by ANSYS)
Shear Modulus	GPa	76.923 (calculated by ANSYS)
Tensile Yield Strength, f_y	MPa	443
Elastic Modulus, E_{el}	GPa	200 (default)
Tangent Modulus, E_t	GPa	19 (default)

5.4 Analysis Results and Comparisons

5.4.1 General

The model of the impact testing was produced based on the explanations and modifications given in the previous sections. Based on the results of the analysis, typical failure modes of various specimens are shown in Figure 5-17. The comparisons of the motions for various times after impact (impact time is marked as zero seconds) obtained from the impact tests and the analyzed model for CC and SFRC specimens are shown in Figure 5-18, Figure 5-19, Figure 5-20, Figure 5-21, Figure 5-22, Figure 5-23, Figure 5-24, Figure 5-25, and Figure 5-26. The results indicated that the motions of tested beam specimens and hammer obtained from the analyzed videos showed very good agreement with that of analyzed model for the specimens.

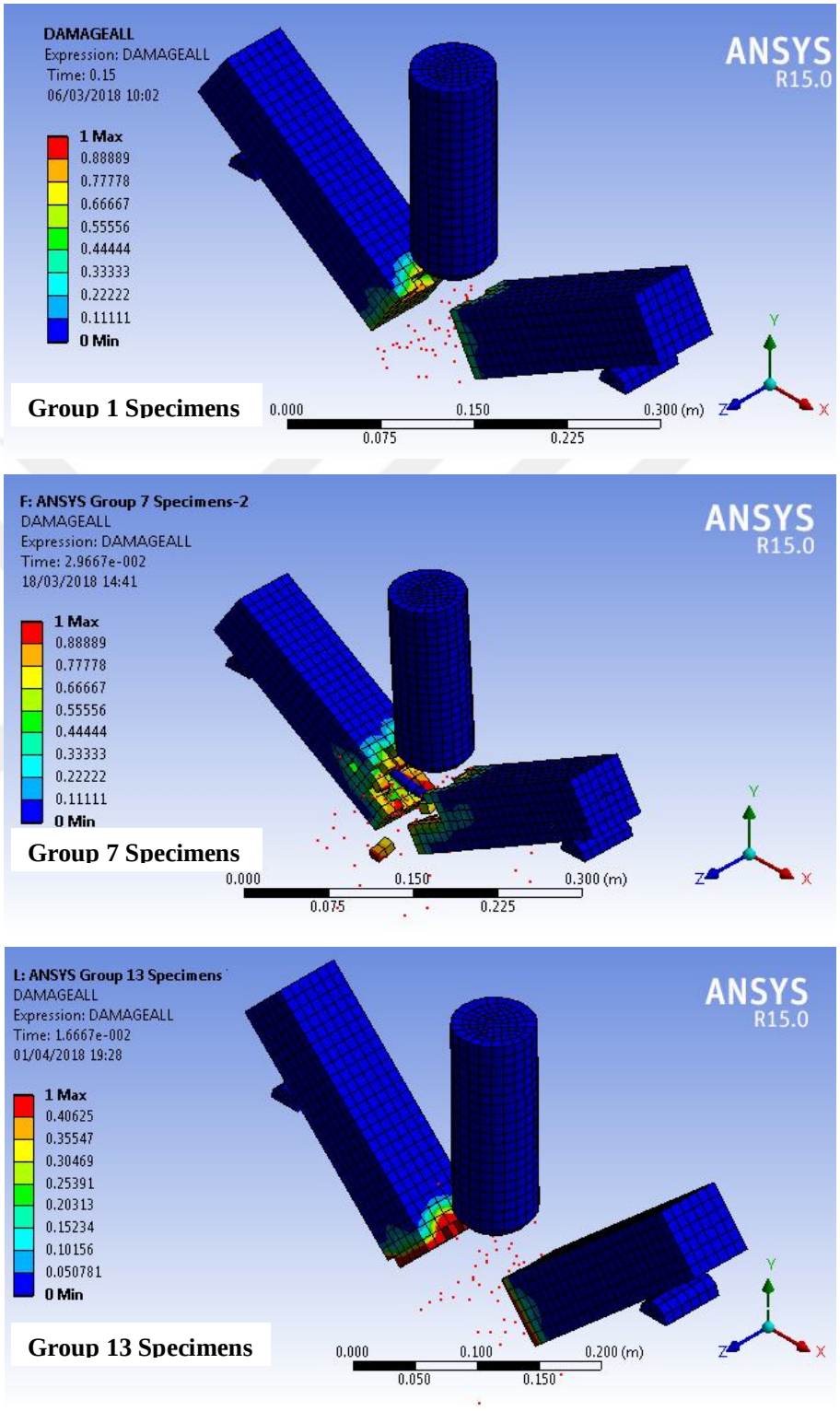

Figure 5-17 – Typical failure modes of various specimens

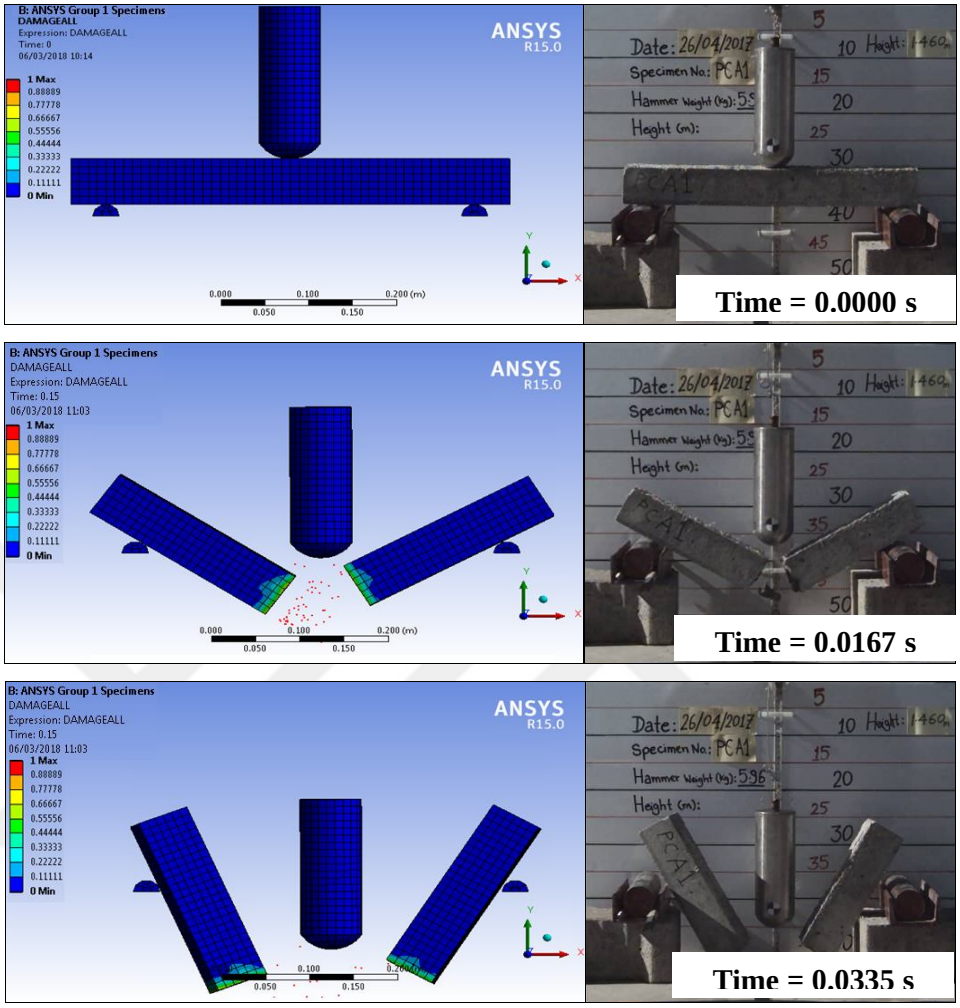

Figure 5-18 – Comparison of the motions for various times after impact obtained from the impact tests and the analyzed model for 60C12-1

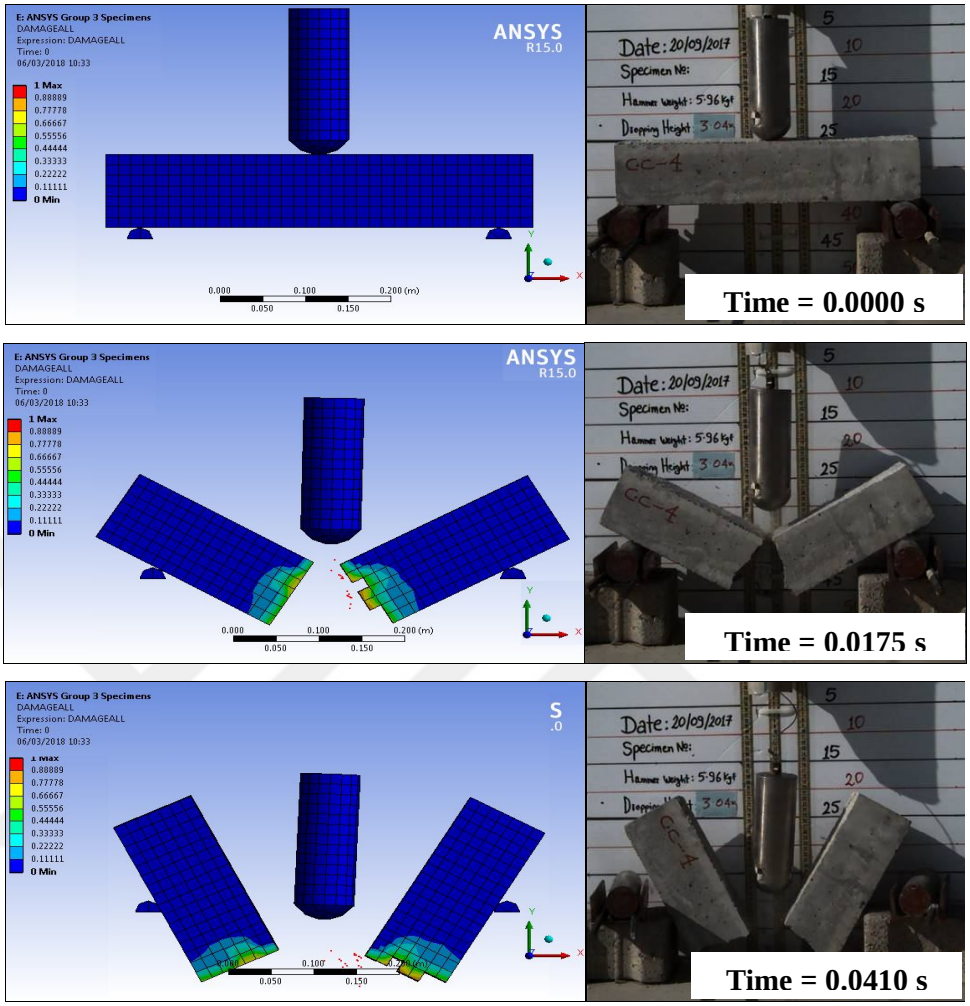

Figure 5-19 – Comparison of the motions for various times after impact obtained from the impact tests and the analyzed model for 100C26-1

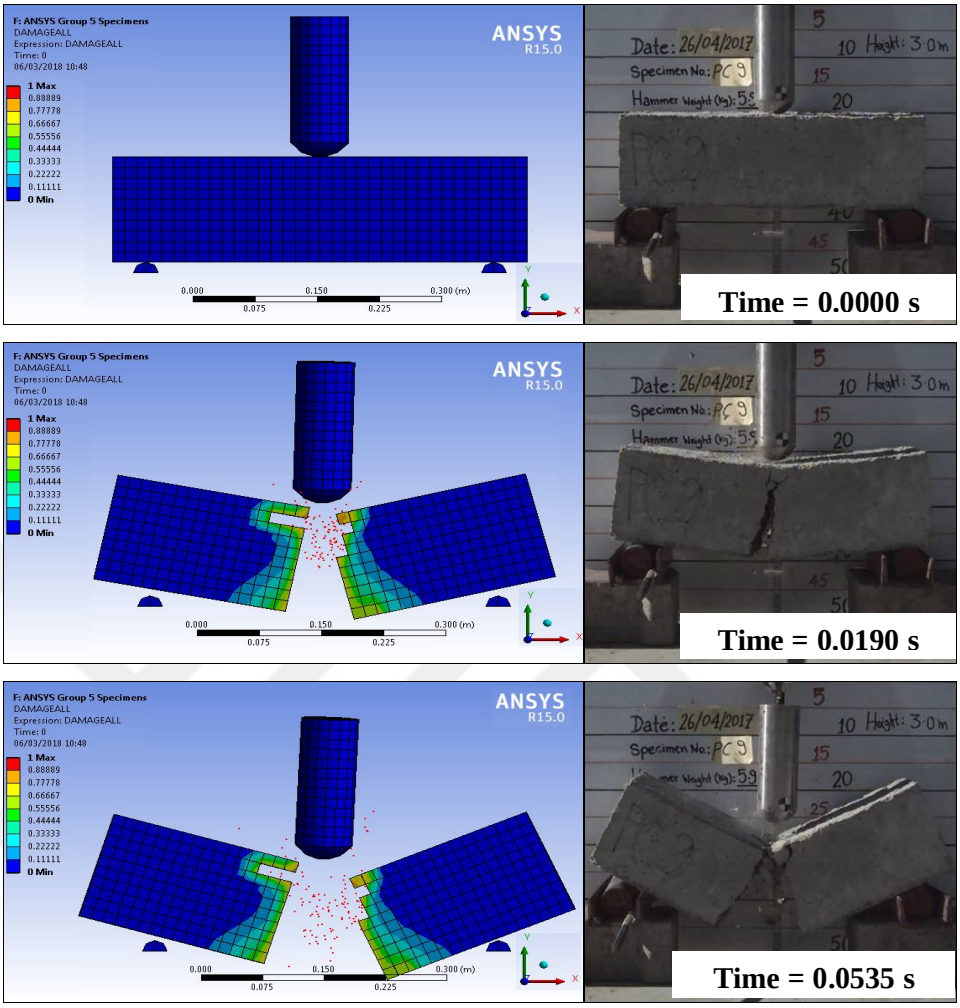

Figure 5-20 – Comparison of the motions for various times after impact obtained from the impact tests and the analyzed model for 150C12-3

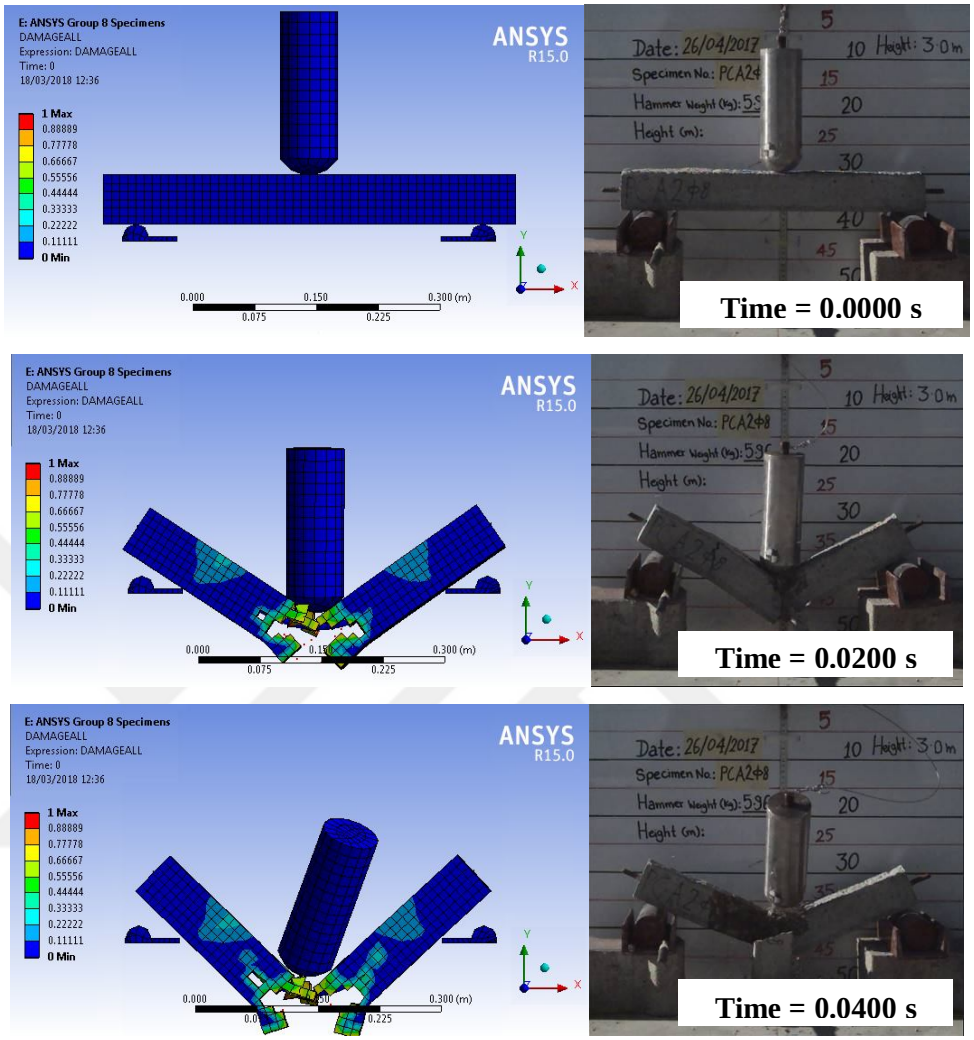

Figure 5-21 – Comparison of the motions for various times after impact obtained from the impact tests and the analyzed model for 60C12R-2

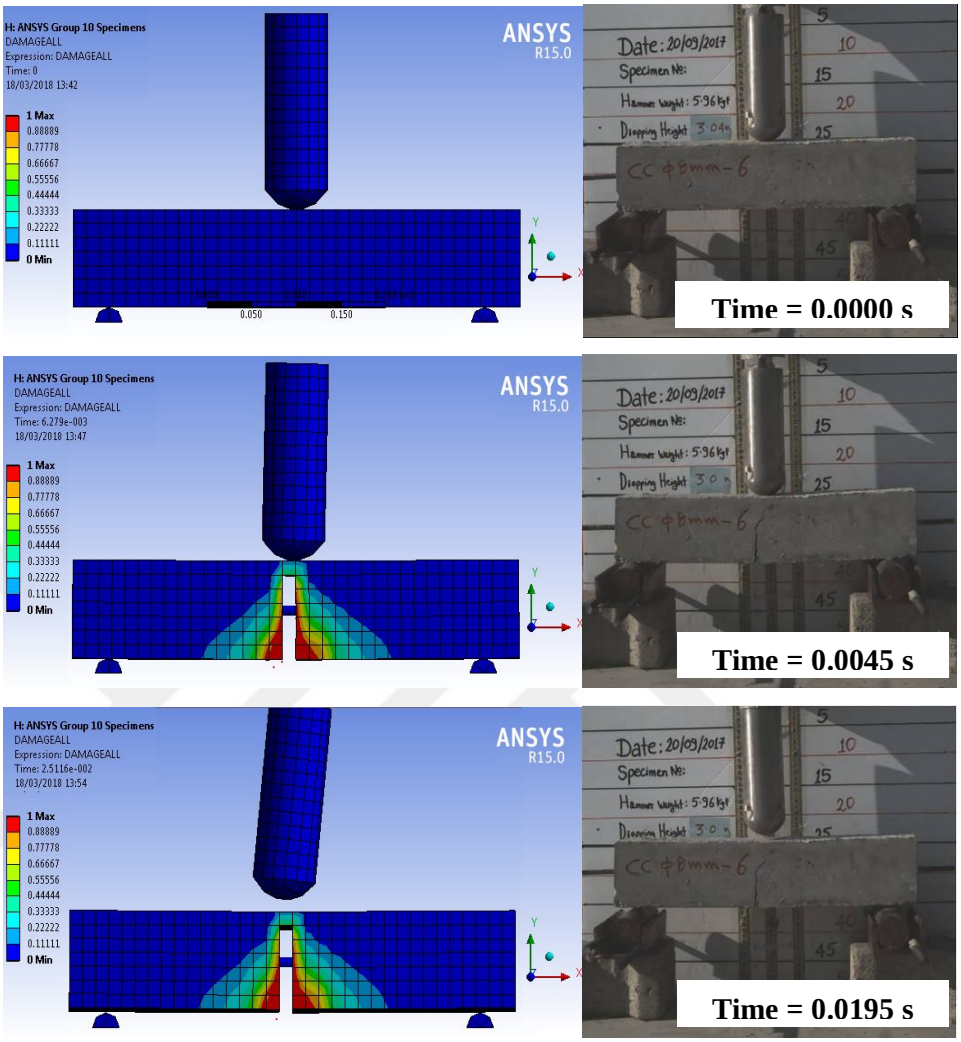

Figure 5-22 – Comparison of the motions for various times after impact obtained from the impact tests and the analyzed model for 100C26R-3

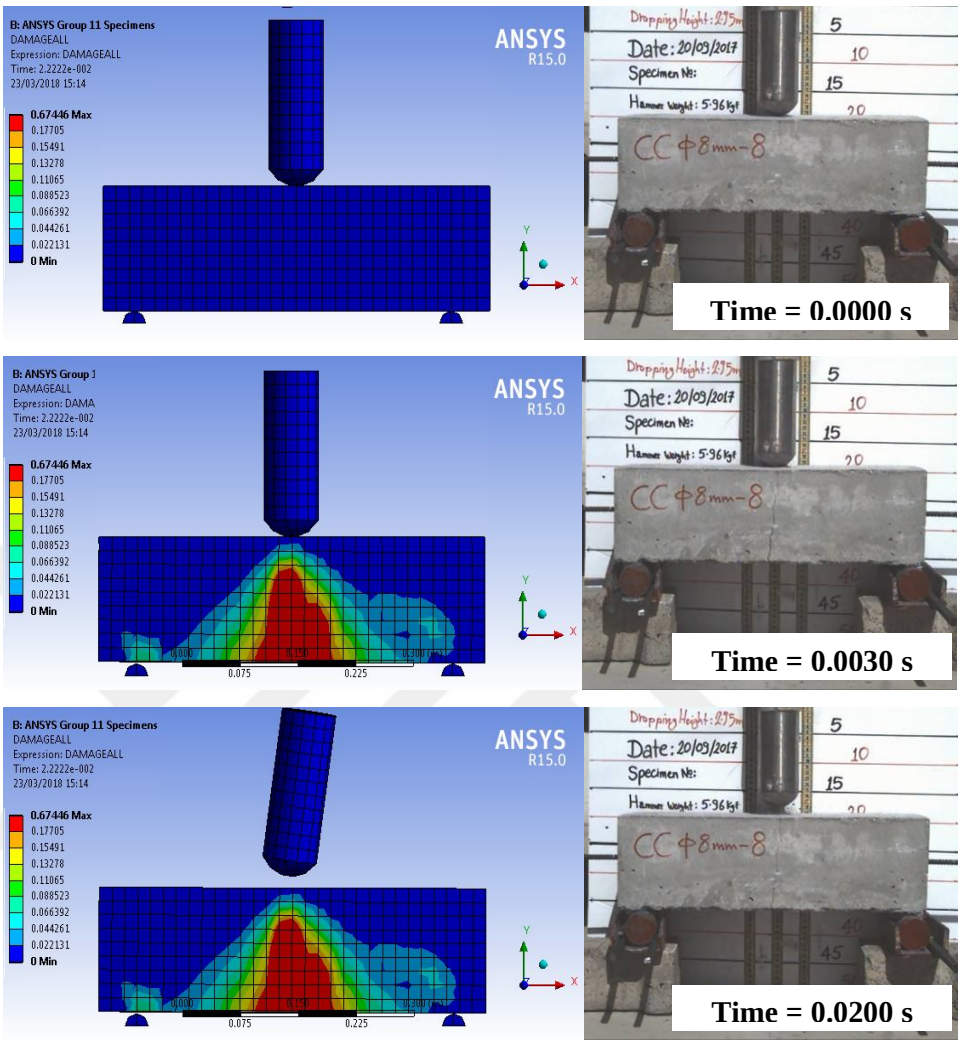

Figure 5-23 – Comparison of the motions for various times after impact obtained from the impact tests and the analyzed model for 150C12R-2

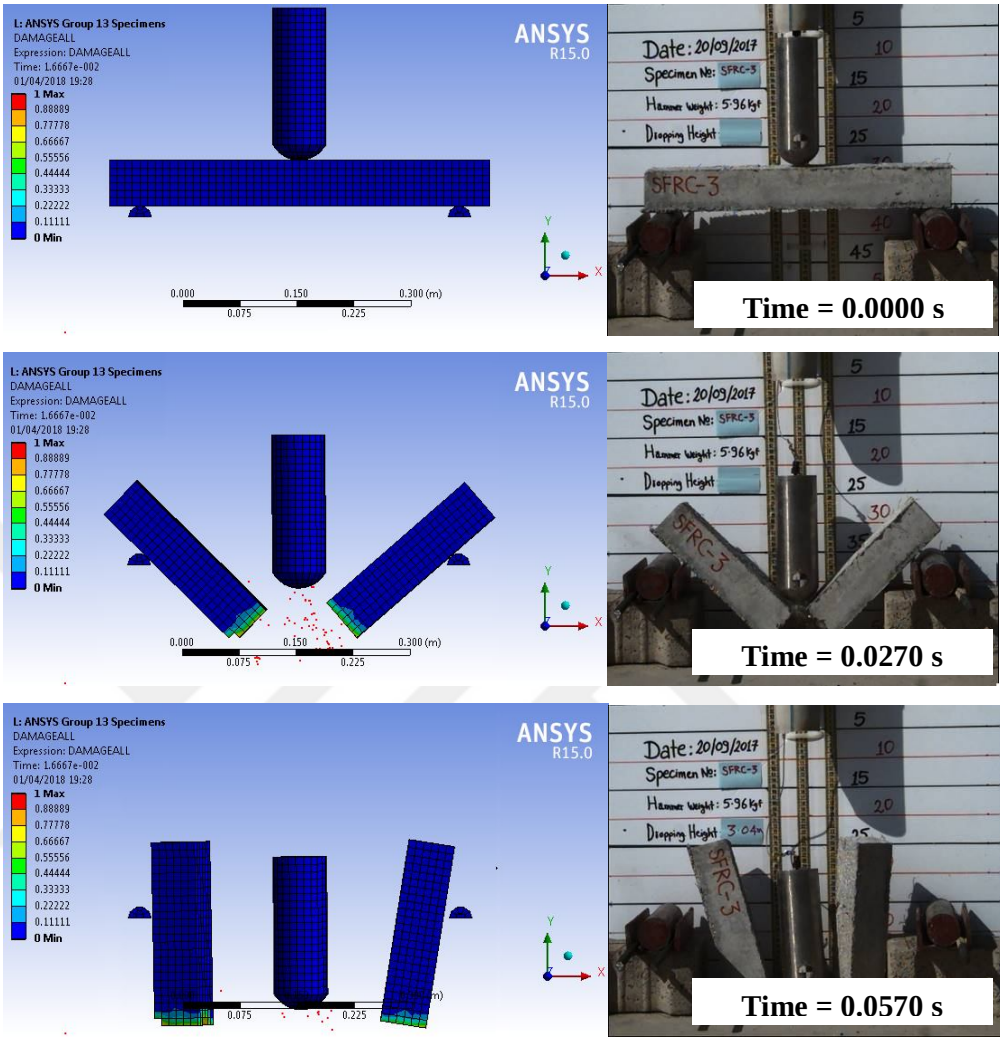

Figure 5-24 – Comparison of the motions for various times after impact obtained from the impact tests and the analyzed model for 60SFRC35-3

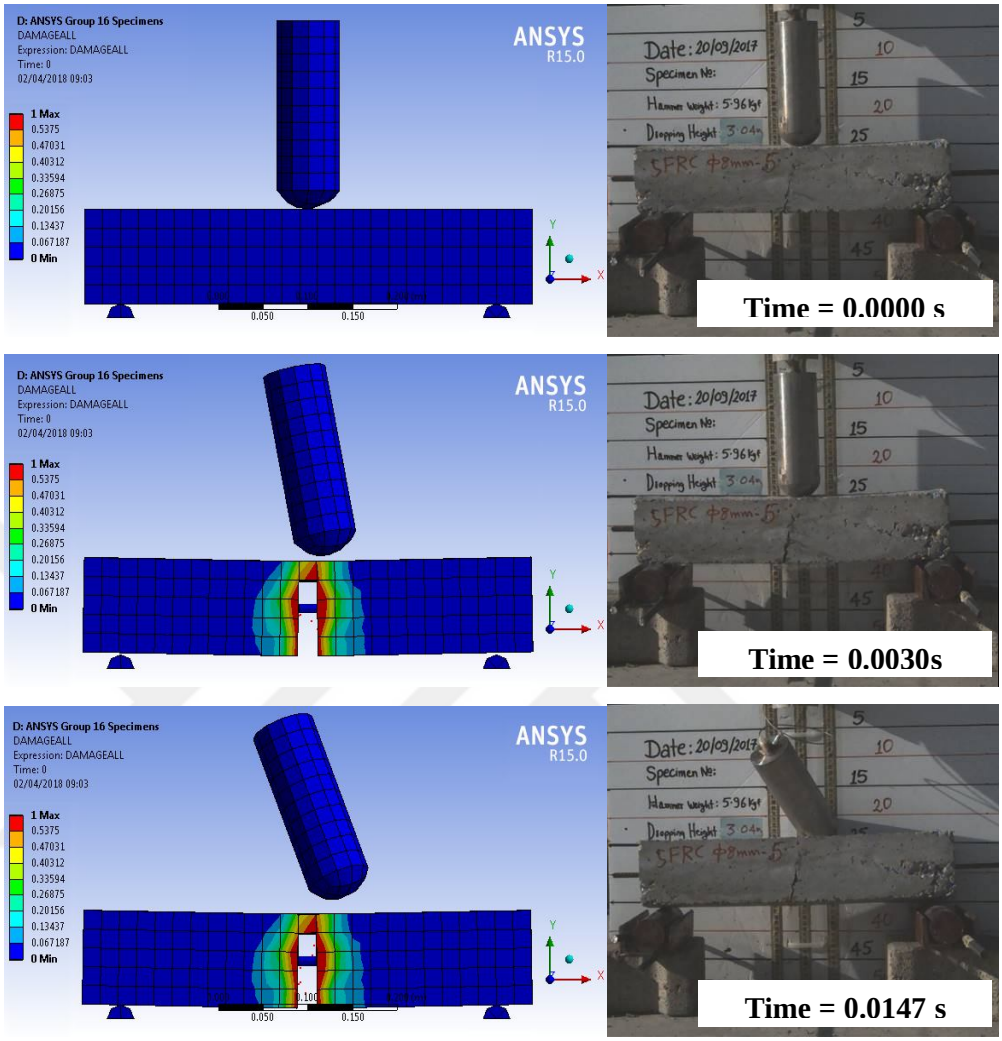

Figure 5-25 – Comparison of the motions for various times after impact obtained from the impact tests and the analyzed model for 100SFRC35R-1

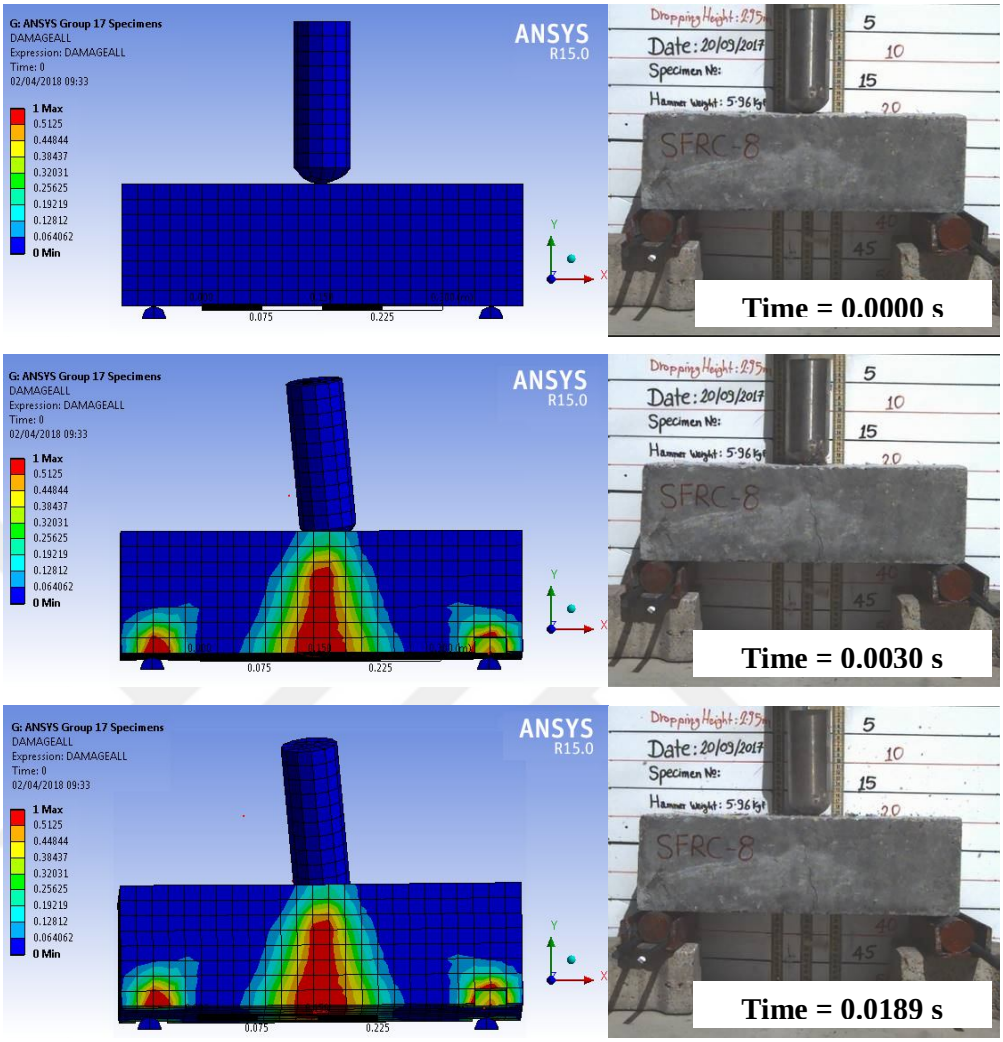

Figure 5-26 – Comparison of the motions for various times after impact obtained from the impact tests and the analyzed model for 150SFRC35-2

5.5 Comparison of Velocity-Time Relationships of Hammer using Default and Modified RHT Concrete Model for LSC and NSC Specimens

The most important difference of this research compared to the studies in the literature was that the material properties of concrete and analysis options in modeling were determined based on the motion of the steel hammer. The parametric studies performed in the scope of this research indicated that any modification related to the properties of CC and SFRC analysis options in modeling changed the motion of steel hammer after impact. Therefore, best parameters for concrete model

and analysis options were modified and determined based on the material properties and velocity-time relationships of the hammer.

Experimental velocity-time relationships for hammer (named as specimens ID's in the graphs) were obtained by analyzing of recorded impact videos using the TEMA Motion Analysis Software (target marker analysis). Velocity-time curves were also obtained from the analysis of the model (named as ANSYS and group number of the specimens in the graphs) for default and modified RHT parameters. The comparisons of the experimental, default, and modified RHT ANSYS velocity-time relationships for LSC and NSC specimens are shown in Figure 5-27 to Figure 5-38.

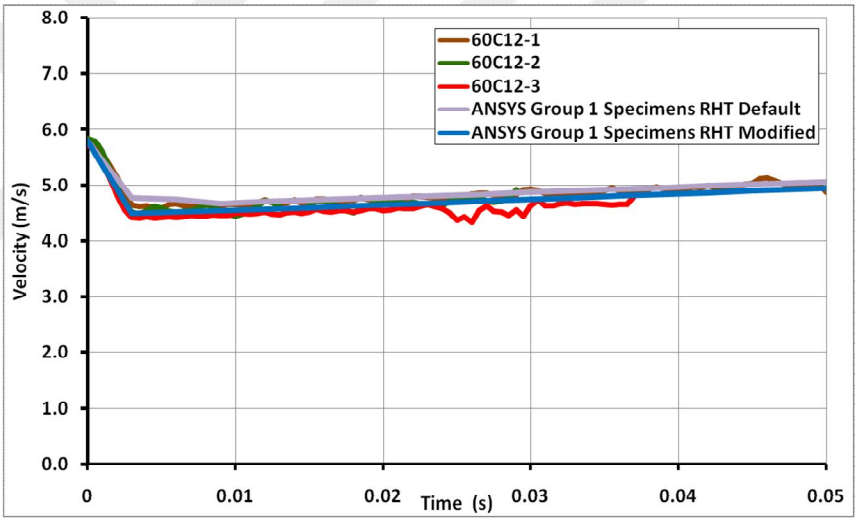

Figure 5-27 – Experimental and analytical velocity-time relationships of hammer using default and modified RHT Concrete Model for Group 1 specimens

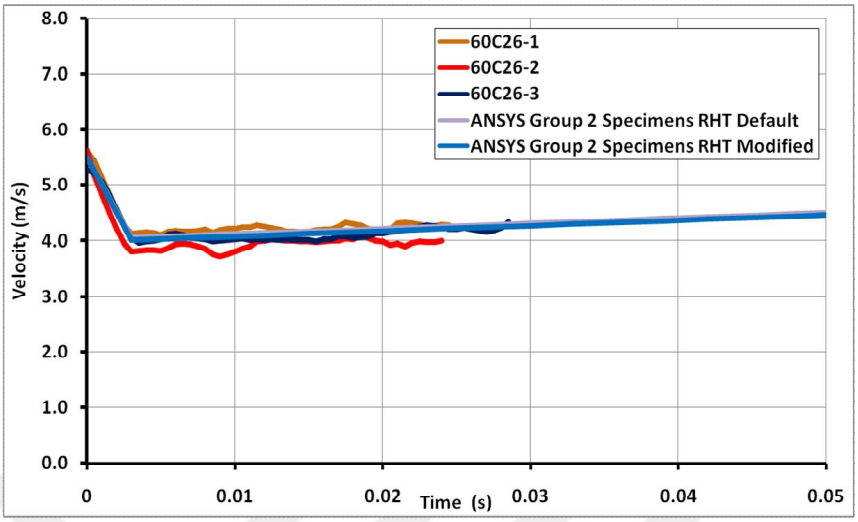

Figure 5-28 – Experimental and analytical velocity-time relationships of hammer using default and modified RHT Concrete Model for Group 2 specimens

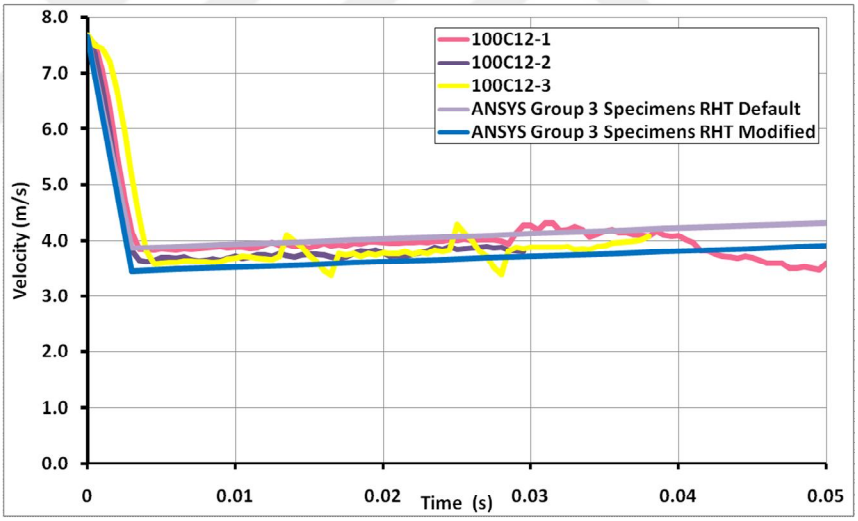

Figure 5-29 – Experimental and analytical velocity-time relationships of hammer using default and modified RHT Concrete Model for Group 3 specimens

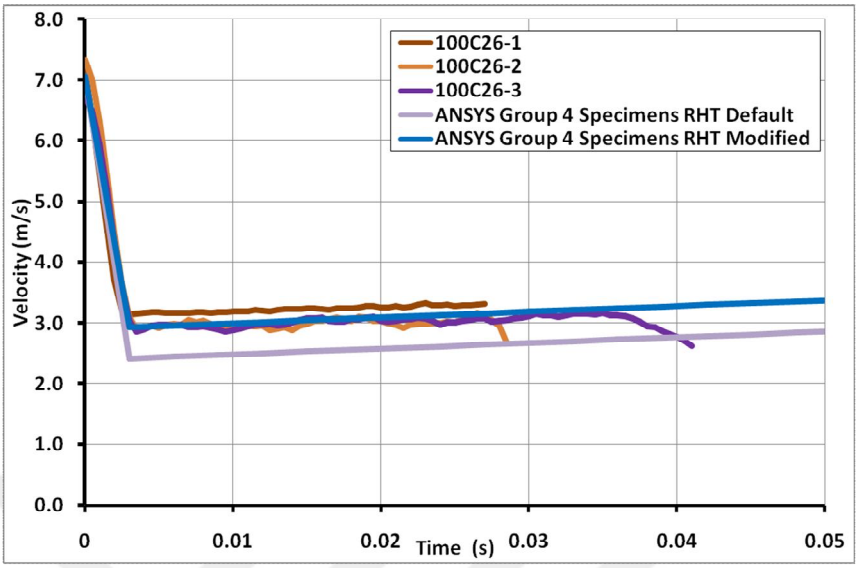

Figure 5-30 – Experimental and analytical velocity-time relationships of hammer using default and modified RHT Concrete Model for Group 4 specimens

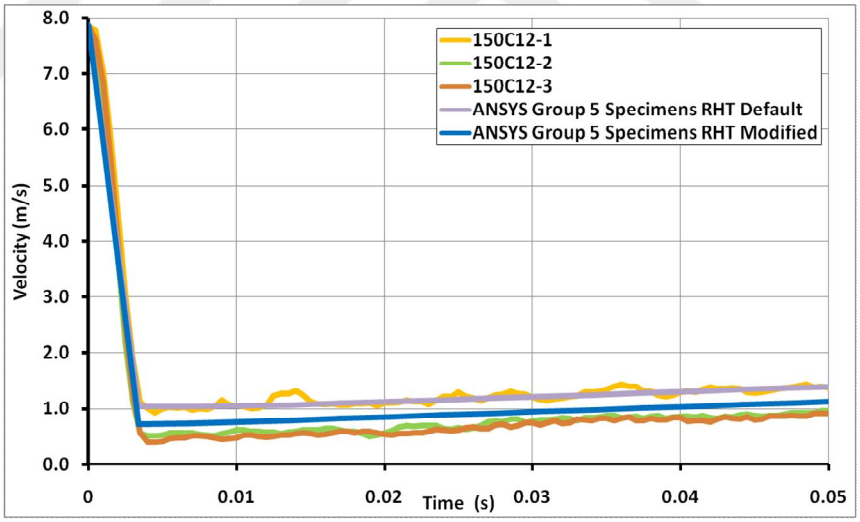

Figure 5-31 – Experimental and analytical velocity-time relationships of hammer using default and modified RHT Concrete Model for Group 5 specimens

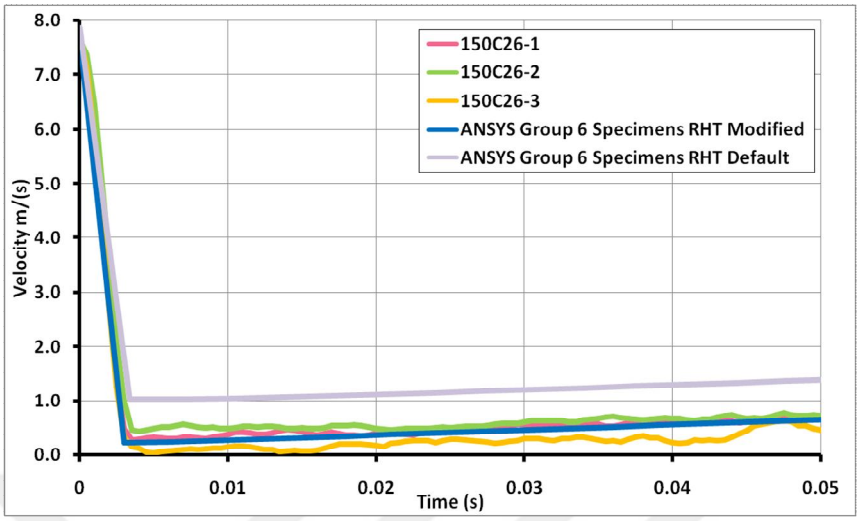

Figure 5-32 – Experimental and analytical velocity-time relationships of hammer using default and modified RHT Concrete Model for Group 6 specimens

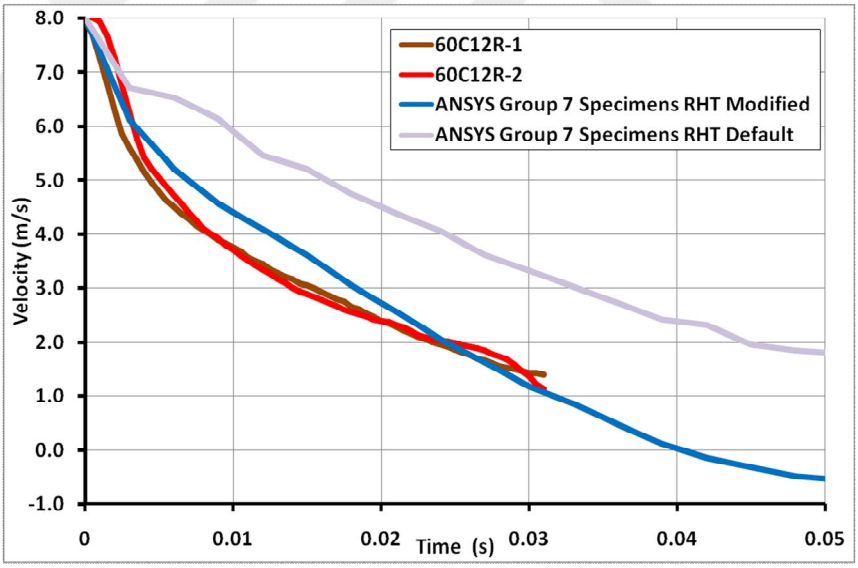

Figure 5-33 – Experimental and analytical velocity-time relationships of hammer using default and modified RHT Concrete Model for Group 7 specimens

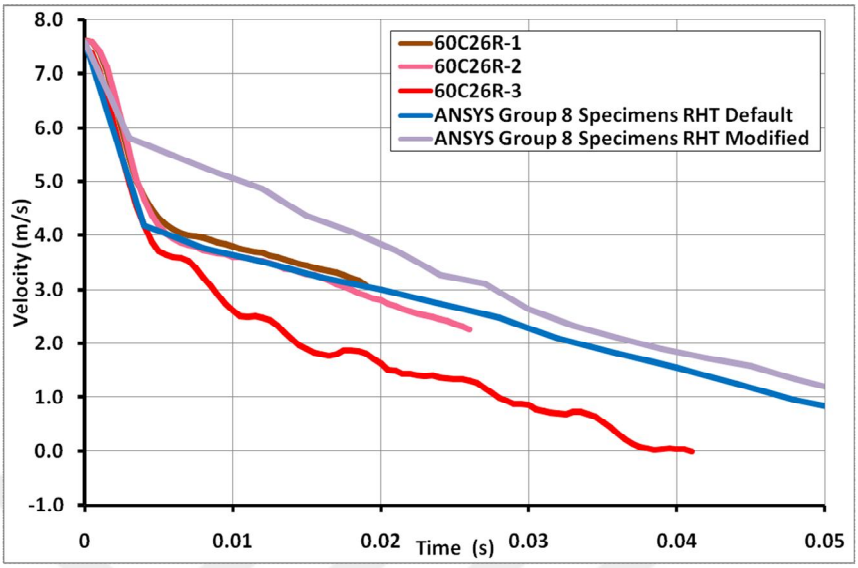

Figure 5-34 – Experimental and analytical velocity-time relationships of hammer using default and modified RHT Concrete Model for Group 8 specimens

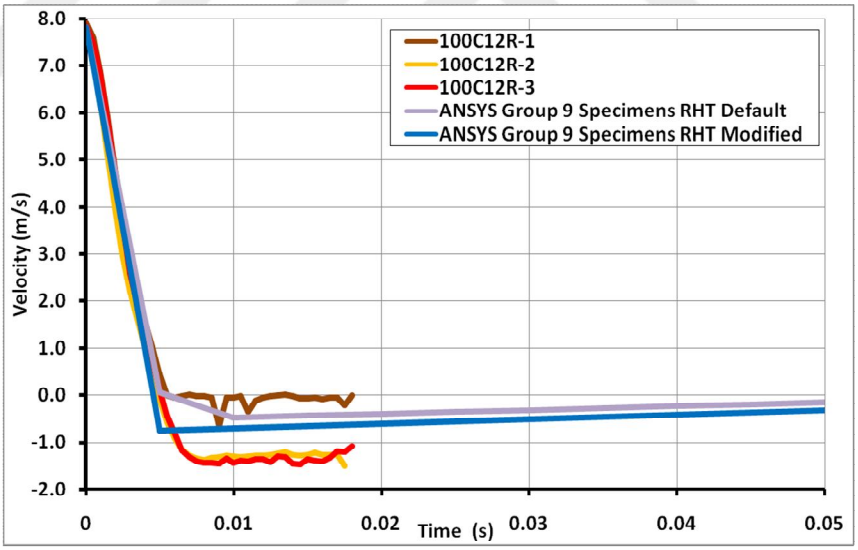

Figure 5-35 – Experimental and analytical velocity-time relationships of hammer using default and modified RHT Concrete Model for Group 9 specimens

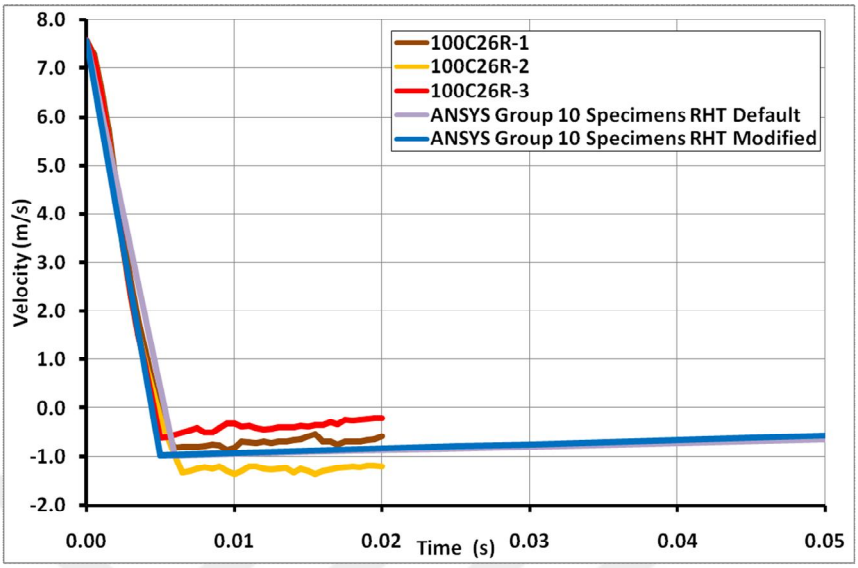

Figure 5-36 – Experimental and analytical velocity-time relationships of hammer using default and modified RHT Concrete Model for Group 10 specimens

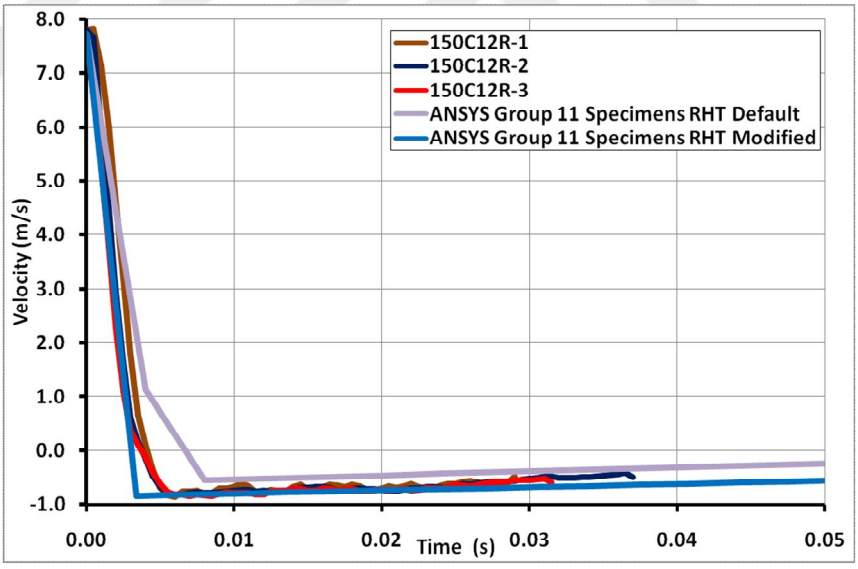

Figure 5-37 – Experimental and analytical velocity-time relationships of hammer using default and modified RHT Concrete Model for Group 11 specimens

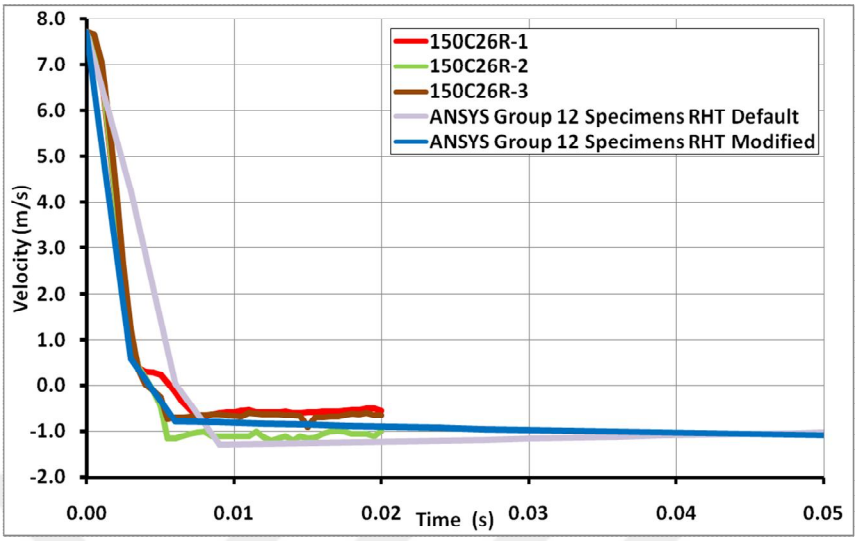

Figure 5-38 – Experimental and analytical velocity-time relationships of hammer using default and modified RHT Concrete Model for Group 12 specimens

These figures indicated that experimental velocity-time relationships of hammer can be predicted well enough when the modified RHT parameters for concrete model and analysis options defined in this research were used no matter which concrete type (LSC and NSC) and cross-section (60×60, 100×100, and 150×150 mm) were used.

For comparisons of default and modified RHT Concrete Model results for unreinforced CC specimens, the figures indicated the following:

- For Group 1 (LSC) and 2 (NSC) specimens having 60×60×500 mm dimensions, the analytical velocity-time analytical relationships of hammer for both the default and modified RHT Concrete Model fit well with the experimental relationships
- For specimen size of 100×100×500 mm, the analytical velocity-time relationships of hammer using modified RHT Concrete Model for Group 3 (LSC) and 4 (NSC) specimens estimated the experimental results better than the default model.
- For specimen size of 150×150×500 mm, the analytical velocity-time relationships of hammer using modified RHT Concrete Model for Group 5 (LSC) and 6 (NSC) specimens estimated the experimental results better than the default model.
- For Group 3 specimens (LSC - 100×100×500 mm), Group 5 specimens (LSC - 150×150×500 mm), and Group 6 specimens (NSC - 150×150×500 mm), the

analytical velocity-time relationships of hammer using default RHT Concrete Model resulted in a higher velocity after impact than the modified one.

- For Group 4 specimens (NSC - 100×100×500 mm), the analytical velocity-time relationships of hammer using default RHT Concrete Model resulted in a much lower velocity after impact.

For comparisons of default and modified RHT Concrete Model results for reinforced CC specimens, the figures indicated the following:

- For Group 7 (LSC) and 8 (NSC) specimens having 60×60×500 mm dimensions, the analytical velocity-time analytical relationships of hammer for both the default and modified RHT Concrete Model fit well with the experimental relationships
- For specimen size of 100×100×500 mm, the analytical velocity-time relationships of hammer using modified RHT Concrete Model for Group 9 (LSC) and 10 (NSC) specimens estimated the experimental results better than the default model.
- For specimen size of 150×150×500 mm, the analytical velocity-time relationships of hammer using modified RHT Concrete Model for Group 11 (LSC) and 12 (NSC) specimens estimated the experimental results better than the default model.

Generally, the ANSYS model results becomes fit to the experimental results after applying modified RHT model for all specimens sizes, strengths and concrete mixture that consist CC.

5.6 Comparison of Velocity-Time Relationships of Hammer using Default and Modified RHT Concrete Model for SFRC Specimens

The comparisons of the experimental, default, and modified RHT ANSYS velocity-time relationships for SFRC specimens are shown in Figure 5-39 to Figure 5-45.

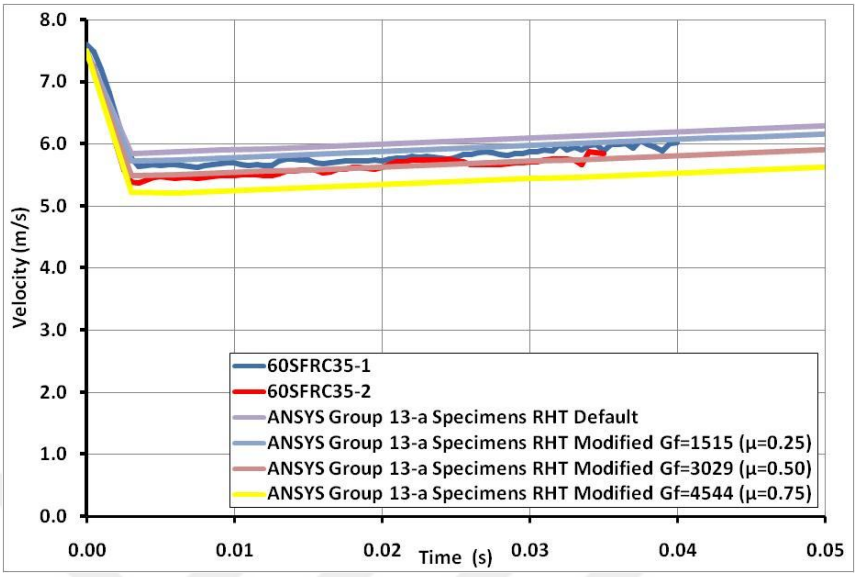

Figure 5-39 – Experimental and analytical velocity-time relationships of hammer using default and modified RHT Concrete Model for Group 13-a specimens for various G_f

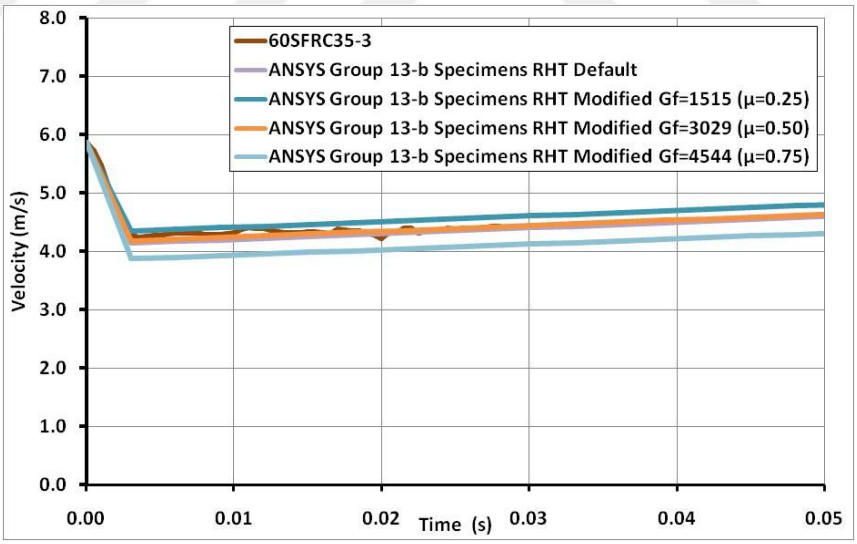

Figure 5-40 – Experimental and analytical velocity-time relationships of hammer using default and modified RHT Concrete Model for Group 13-b specimens for various G_f

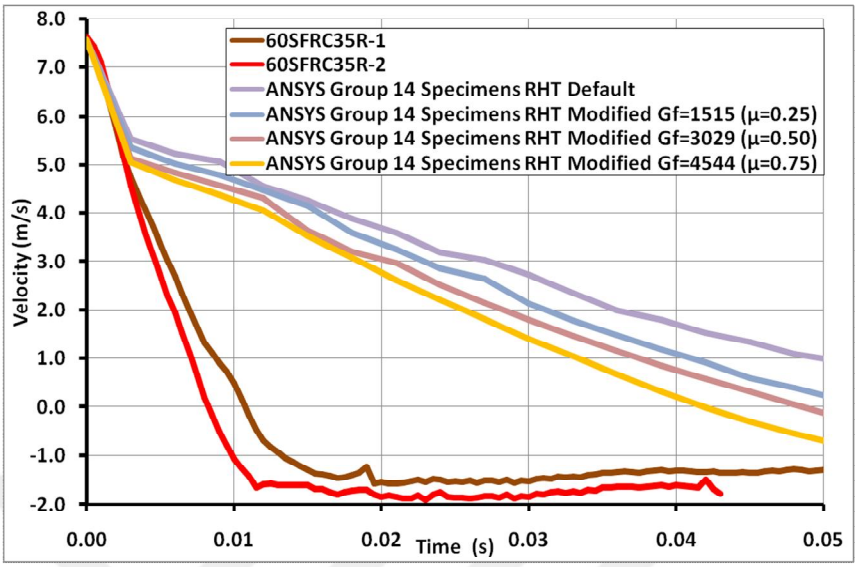

Figure 5-41 – Experimental and analytical velocity-time relationships of hammer using default and modified RHT Concrete Model for Group 14 specimens for various G_f

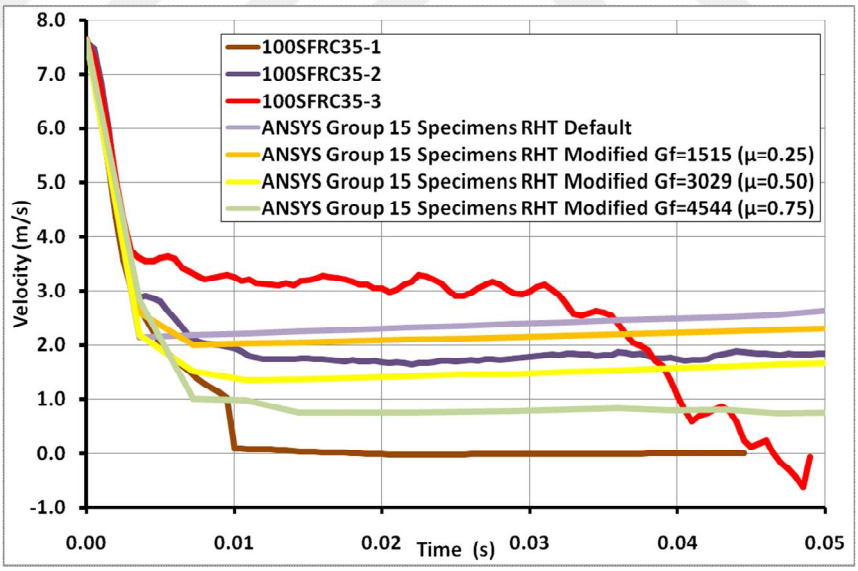

Figure 5-42 – Experimental and analytical velocity-time relationships of hammer using default and modified RHT Concrete Model for Group 15 specimens for various G_f

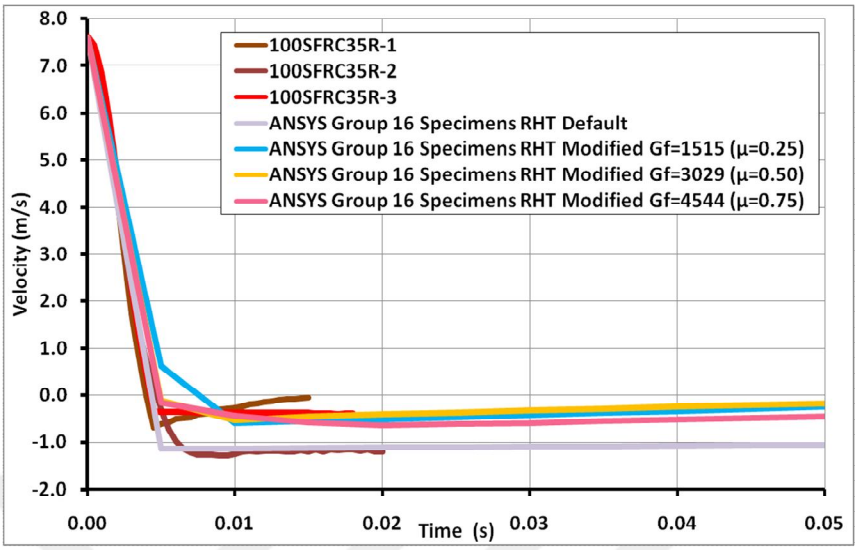

Figure 5-43 – Experimental and analytical velocity-time relationships of hammer using default and modified RHT Concrete Model for Group 16 specimens for various G_f

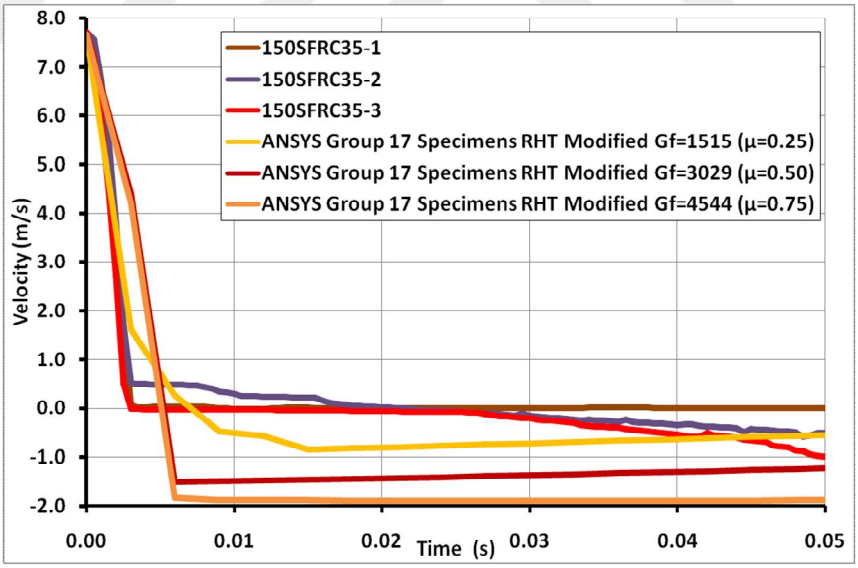

Figure 5-44 – Experimental and analytical velocity-time relationships of hammer using default and modified RHT Concrete Model for Group 17 specimens for various G_f

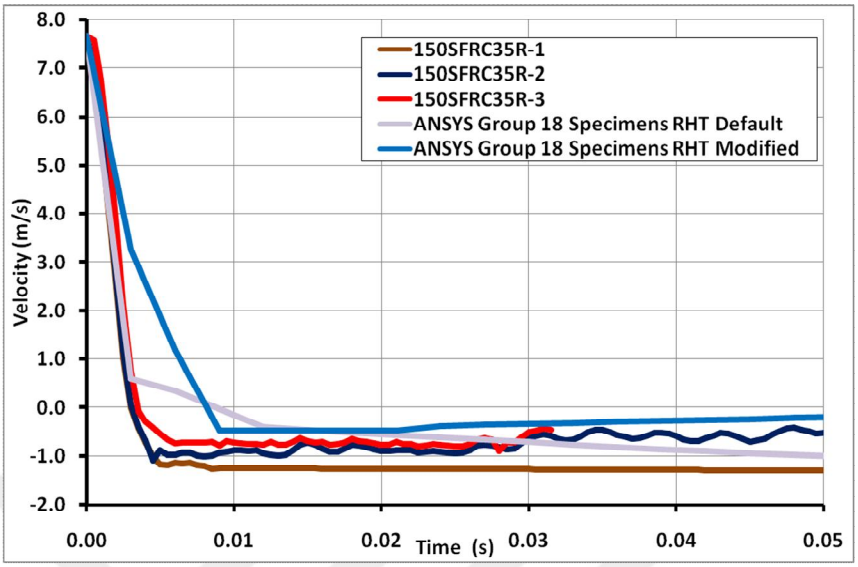

Figure 5-45 – Experimental and analytical velocity-time relationships of hammer using default and modified RHT Concrete Model for Group 18 specimens for various G_f

These figures indicated that experimental velocity-time relationships of hammer can be predicted well enough when the modified RHT parameters for concrete model and analysis options defined in this research were used for SFRC specimens having 60×60×500, 100×100×500, and 150×150×500 mm dimensions.

For comparisons of default and modified RHT Concrete Model results for unreinforced SFRC specimens, the figures indicated the following:

- For Group 13-a and 13-b specimens having 60×60×500 mm dimensions, the analytical velocity-time analytical relationships of hammer for both the default and modified RHT Concrete Model with μ=0.5 fit well with the experimental relationships
- For specimen size of 100×100×500 mm, the analytical velocity-time relationships of hammer using modified RHT Concrete Model with μ=0.5 for Group 15 specimens estimated the experimental results better than the default model.
- For specimen size of 150×150×500 mm, the analytical velocity-time relationships of hammer using modified RHT Concrete Model with μ=0.5 for Group 17 specimens estimated the experimental results better than the default model.

For comparisons of default and modified RHT Concrete Model results for reinforced SFRC specimens, the figures indicated the following:

- For Group 14 specimens having 60×60×500 mm dimensions, there was significant variation between the experimental and analytical results, since the hammer became tilted after the impact for these specimens.
- For specimen size of 100×100×500 mm, the analytical velocity-time relationships of hammer using modified RHT Concrete Model with μ=0.5 for Group 16 specimens estimated the experimental results better than the default model.
- For specimen size of 150×150×500 mm, the analytical velocity-time relationships of hammer using modified RHT Concrete Model with μ=0.5 for Group 18 specimens estimated the experimental results better than the default model.

5.7 Comparison of Predicted Velocity-Time Relationships

5.7.1 Effect of Specimen Size

To evaluate the effect of specimen sizes, the predicted velocity-time relationships were compared for CC and SFRC specimens as shown in Figure 5-46 to Figure 5-51. It can be concluded that for unreinforced specimens as the size of the specimen increased, the velocity of the hammer decreased significantly no matter what the concrete strength was. For reinforced specimens, the change in velocity of the hammer was approximately equal for 100×100 and 150×150 mm specimens since the hammer stopped and deflected up for these group specimens. However, the specimens having 60×60 mm dimensions, the reinforcement did not have similar effect like larger specimens. This specimen failed and the reinforcement was bent at the end of the test.

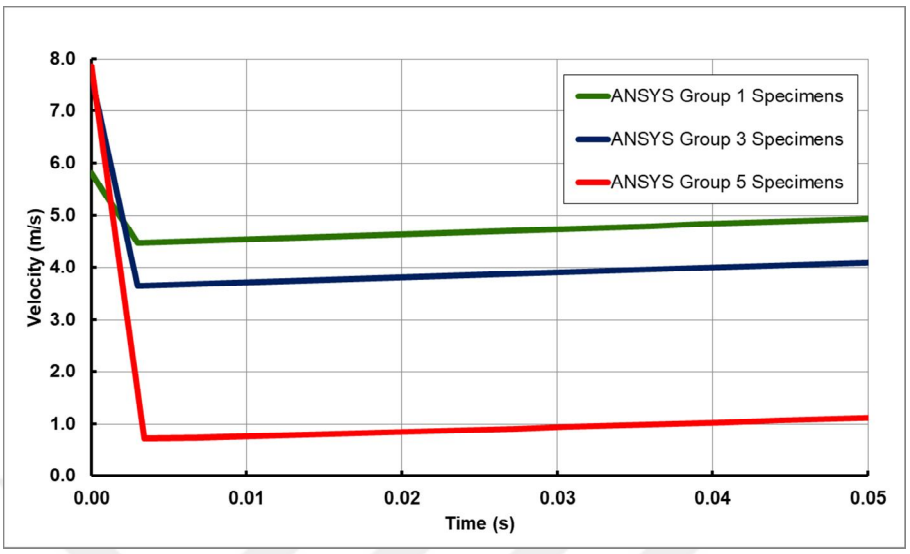

Figure 5-46 – Predicted velocity-time relationships for LSC unreinforced specimens (Group 1: 60×60 mm, Group 3: 100×100 mm, and Group 5: 150×150 mm)

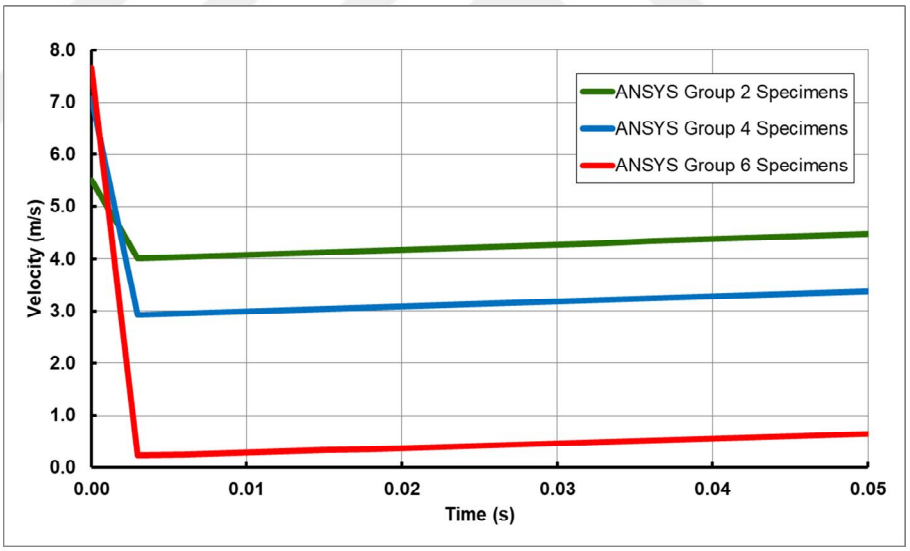

Figure 5-47 – Predicted velocity-time relationships for NSC unreinforced specimens (Group 2: 60×60 mm, Group 4: 100×100 mm, and Group 6: 150×150 mm)

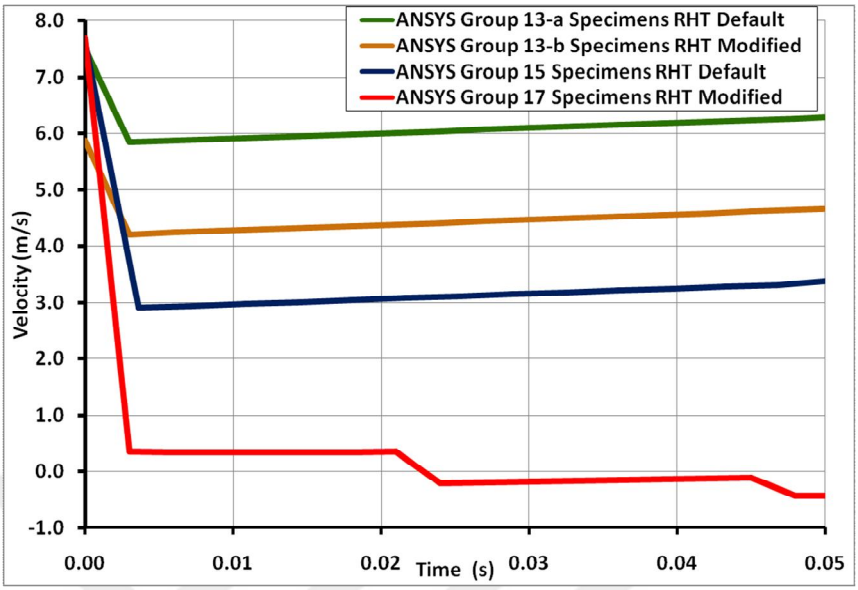

Figure 5-48 – Predicted velocity-time relationships for SFRC unreinforced specimens (Group 13: 60×60 mm, Group 15: 100×100 mm, and Group 17: 150×150 mm)

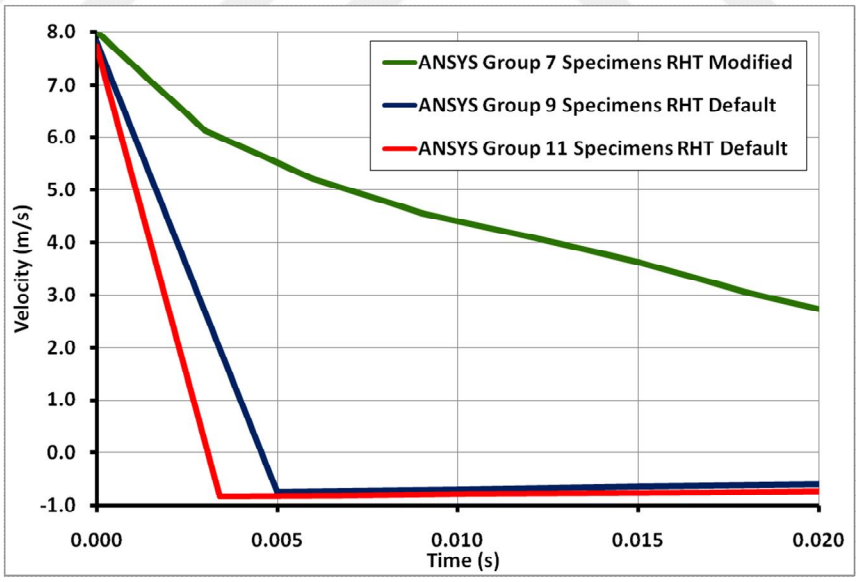

Figure 5-49 – Predicted velocity-time relationships for LSC reinforced specimens (Group 7: 60×60 mm, Group 9: 100×100 mm, and Group 11: 150×150 mm)

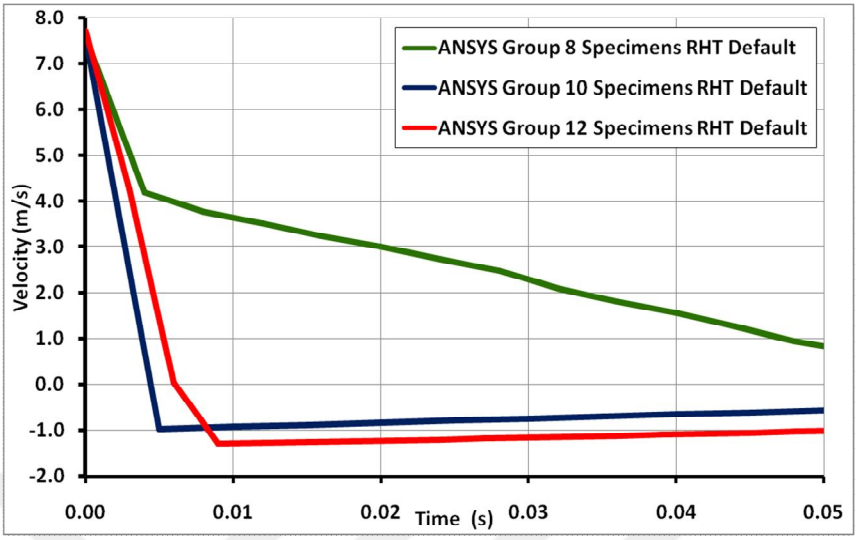

Figure 5-50 – Predicted velocity-time relationships for NSC reinforced specimens (Group 8: 60×60 mm, Group 10: 100×100 mm, and Group 12: 150×150 mm)

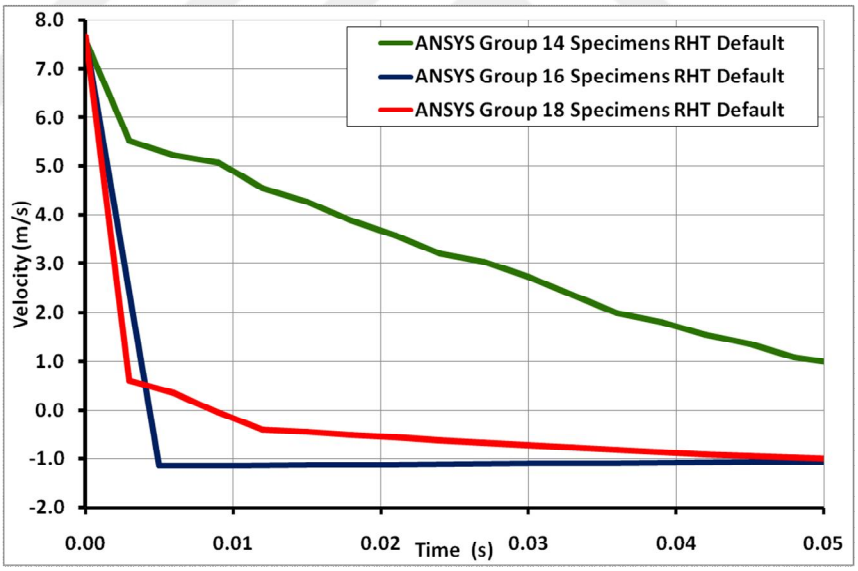

Figure 5-51 – Predicted velocity-time relationships for SFRC reinforced specimens (Group 14: 60×60 mm, Group 16: 100×100 mm, and Group 18: 150×150 mm)

5.7.2 Effect of Concrete Strength

To evaluate the effect of concrete strength, the predicted velocity-time relationships were compared for CC and SFRC specimens as shown in Figure 5-52 to Figure 5-57. It can be concluded that for unreinforced specimens as the concrete strength

increased, the velocity of the hammer decreased. For the reinforced specimens, the concrete strength did not have any significant effect on the behavior.

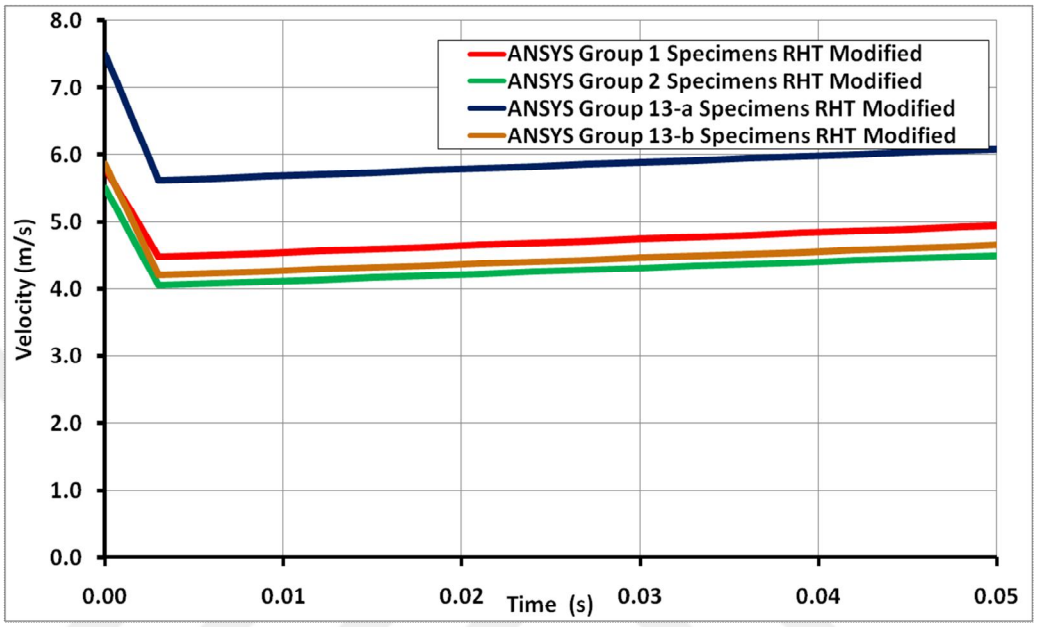

Figure 5-52 – Predicted velocity-time relationships for 60×60 mm unreinforced specimens (Group 1: LSC, Group 2: NSC, and Group 13a, 13b: SFRC)

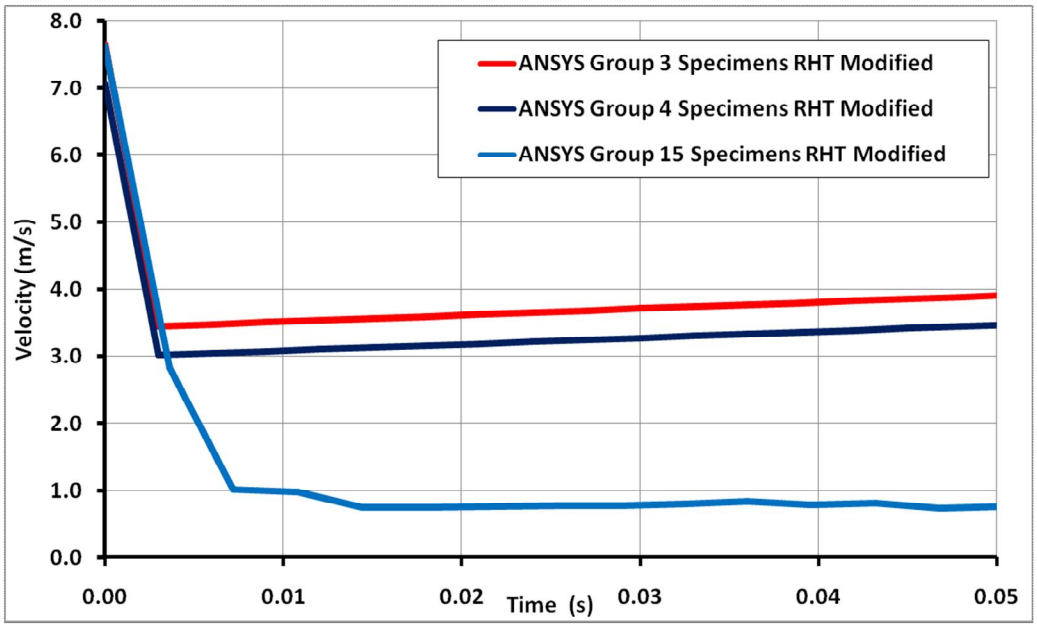

Figure 5-53 – Predicted velocity-time relationships for 100×100 mm unreinforced specimens (Group 3: LSC, Group 4: NSC, and Group 15: SFRC)

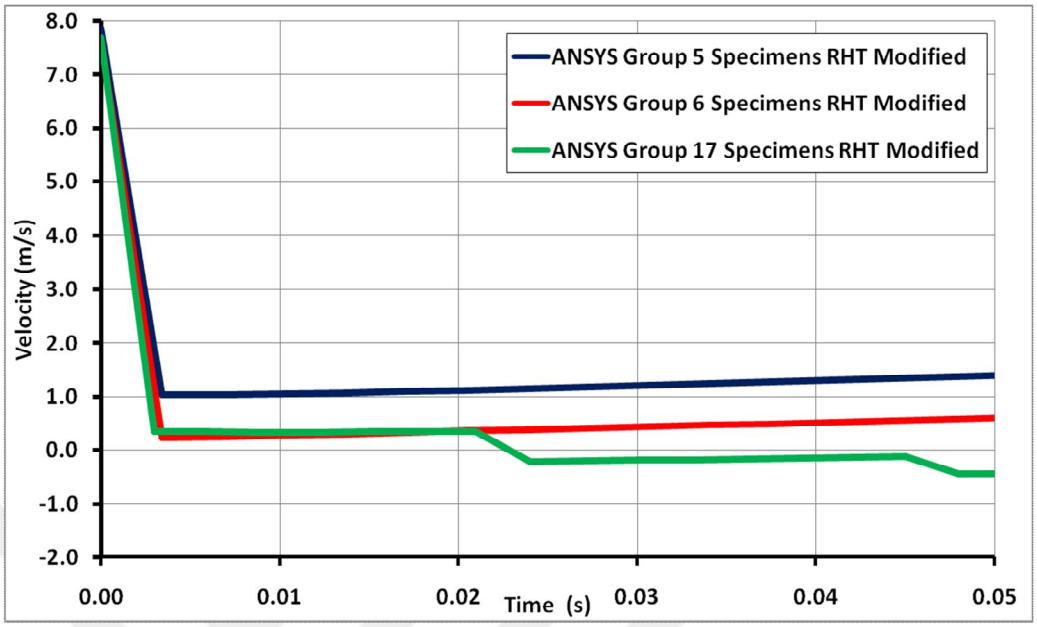

Figure 5-54 – Predicted velocity-time relationships for 150×150 mm unreinforced specimens (Group 5: LSC, Group 6: NSC, and Group 17: SFRC)

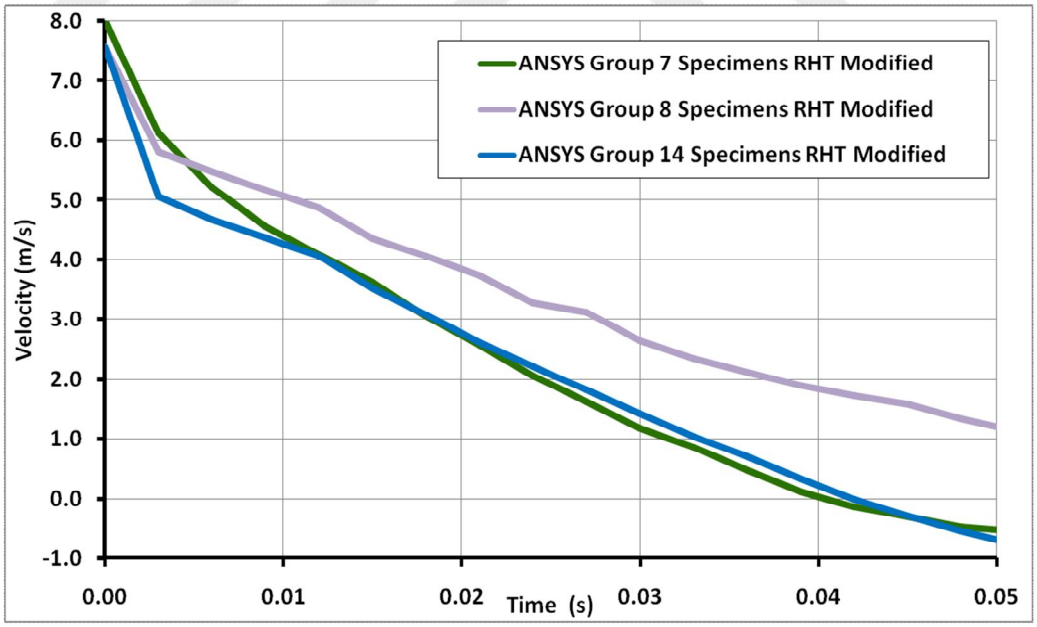

Figure 5-55 – Predicted velocity-time relationships for 60×60 mm reinforced specimens (Group 7: LSC, Group 8: NSC, and Group 14: SFRC)

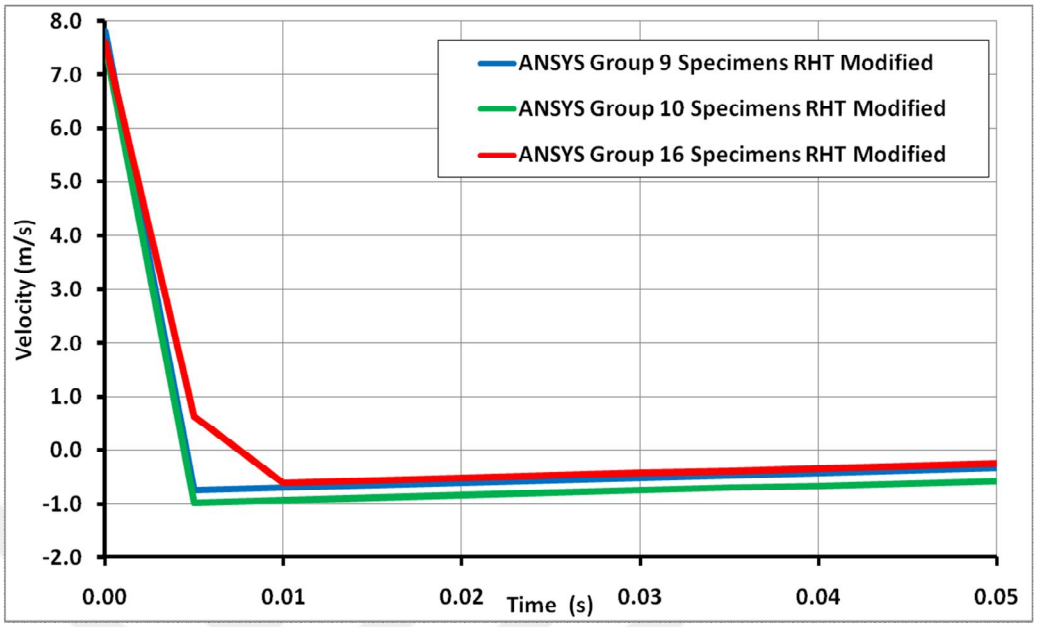

Figure 5-56 – Predicted velocity-time relationships for 100×100 mm reinforced specimens (Group 9: LSC, Group 10: NSC, and Group 16: SFRC)

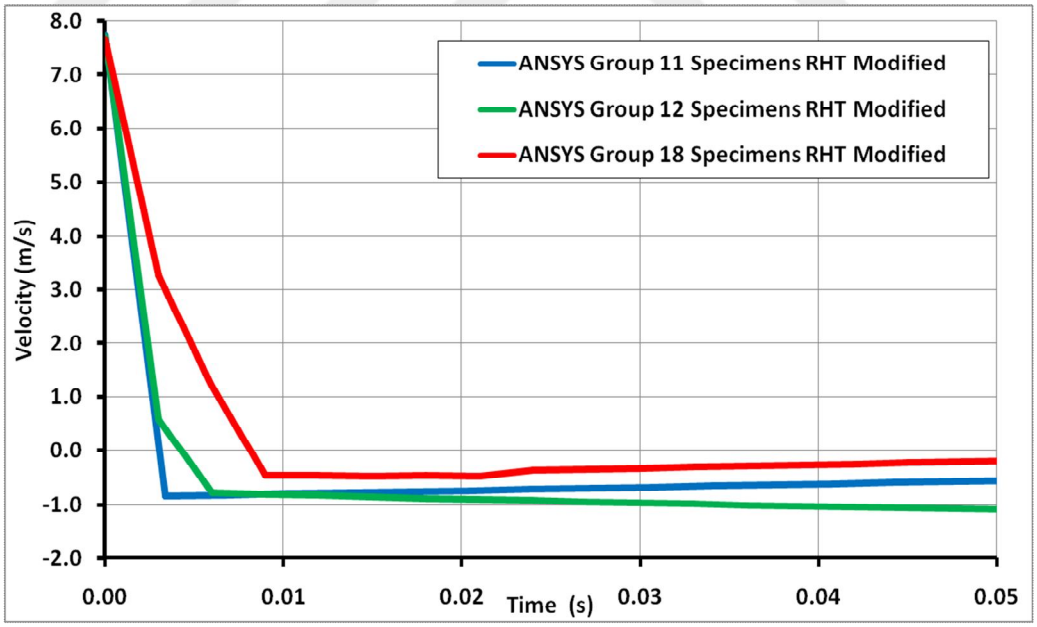

Figure 5-57 – Predicted velocity-time relationships for 150×150 mm reinforced specimens (Group 11: LSC, Group 12: NSC, and Group 18: SFRC)

5.7.3 Effect of Reinforcement

To evaluate the effect of reinforcement, the predicted velocity-time relationships were compared for CC and SFRC specimens as shown in Figure 5-58 to Figure 5-66. For smaller sized specimens, the effect of reinforcement is much larger. The velocity of the hammer decreased more for smaller sized specimens. For larger sized specimens, the difference of the velocity of the hammer between the unreinforced and reinforced specimens was smaller.

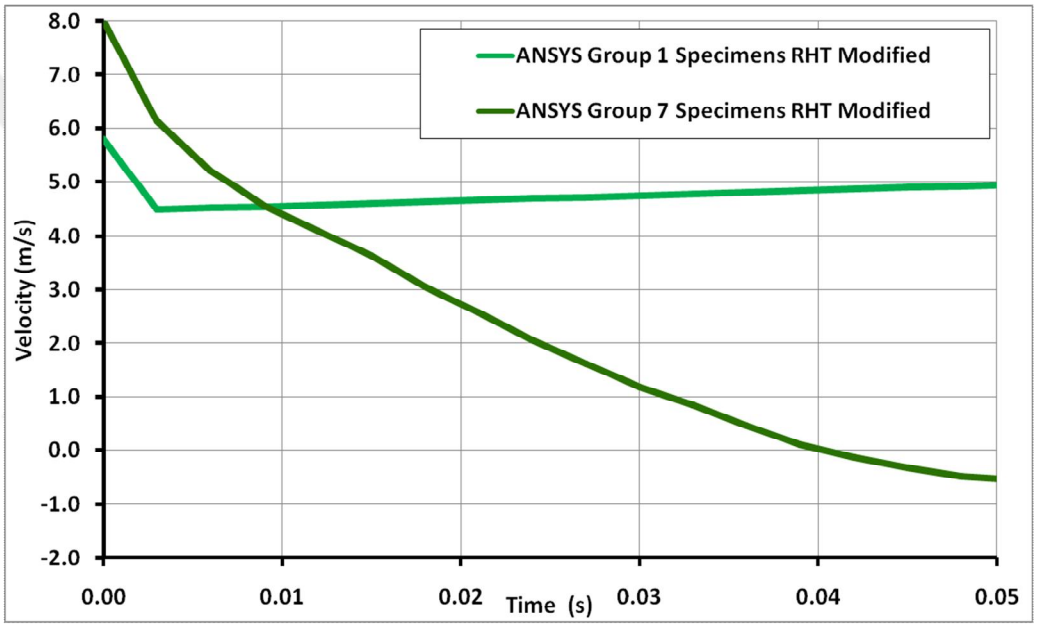

Figure 5-58 – Predicted velocity-time relationships for 60×60 mm LSC specimens (Group 1: unreinforced and Group 7: reinforced)

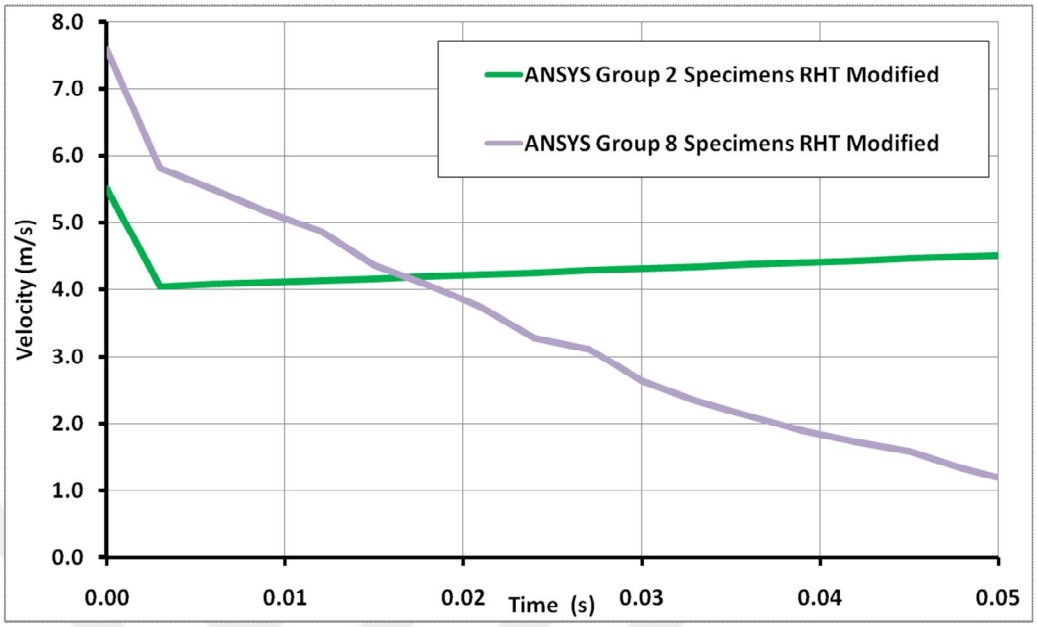

Figure 5-59 – Predicted velocity-time relationships for 60×60 mm NSC specimens (Group 2: unreinforced and Group 8: reinforced)

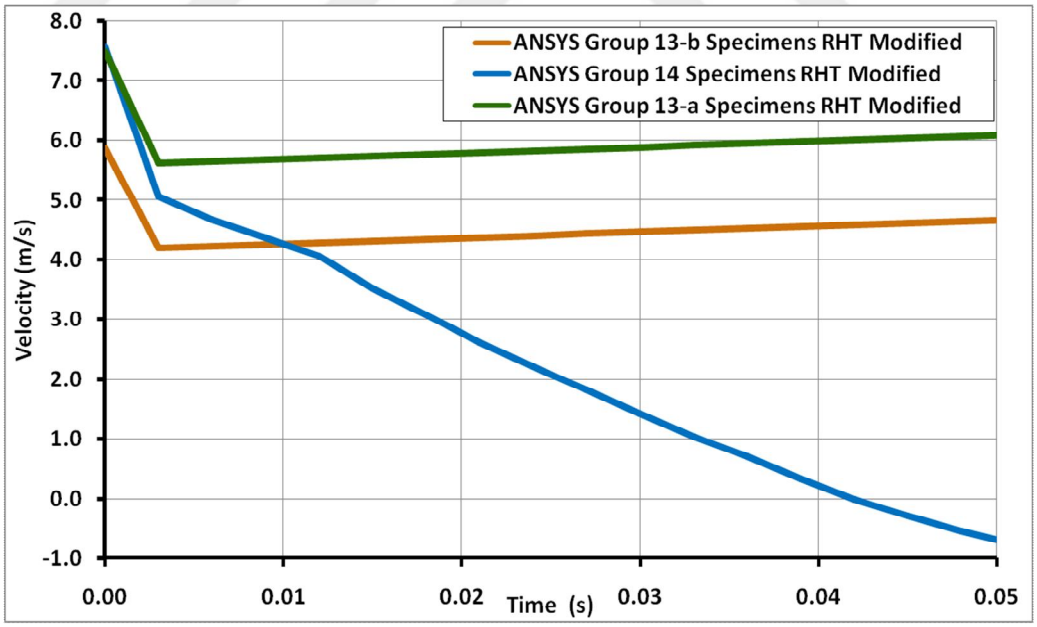

Figure 5-60 – Predicted velocity-time relationships for 60×60 mm SFRC specimens (Group 13a, 13b: unreinforced and Group 14: reinforced)

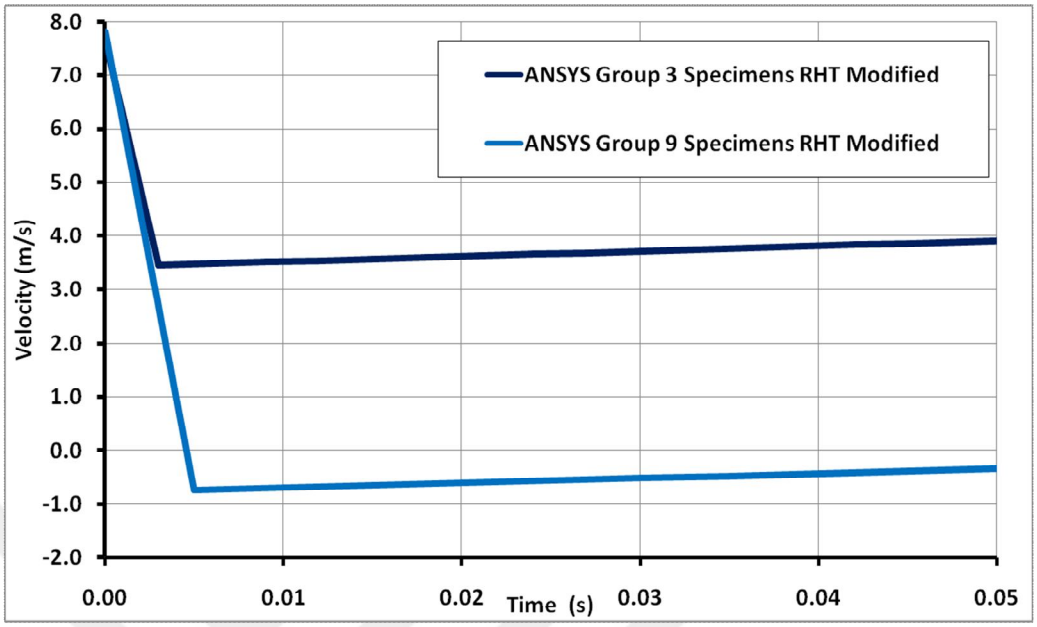

Figure 5-61 – Predicted velocity-time relationships for 100×100 mm LSC specimens (Group 3: unreinforced and Group 9: reinforced)

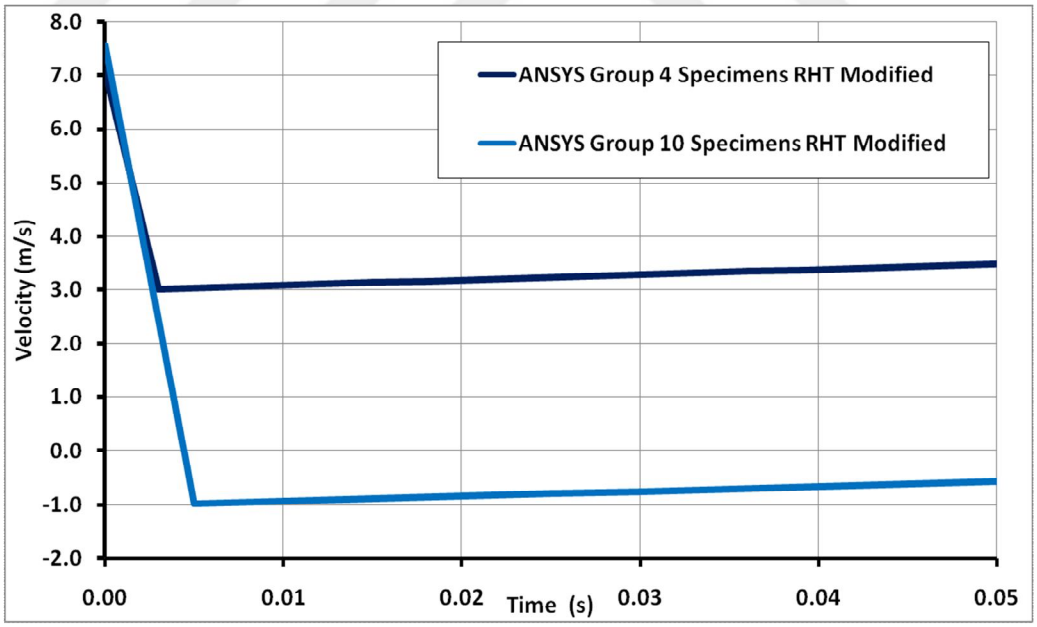

Figure 5-62 – Predicted velocity-time relationships for 100×100 mm NSC specimens (Group 4: unreinforced and Group 10: reinforced)

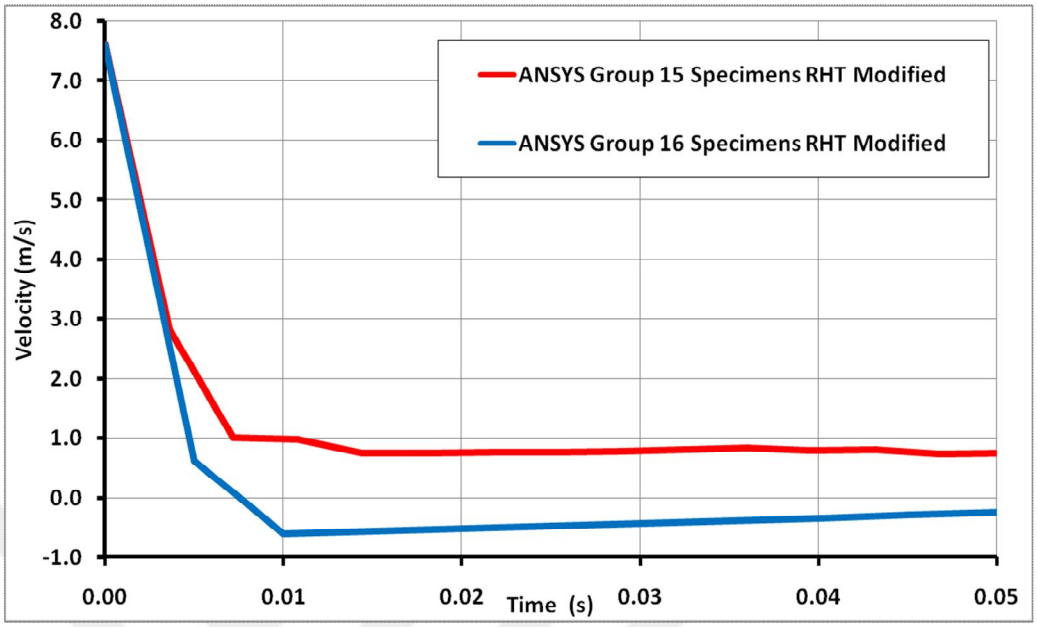

Figure 5-63 – Predicted velocity-time relationships for 100×100 mm SFRC specimens (Group 15: unreinforced and Group 16: reinforced)

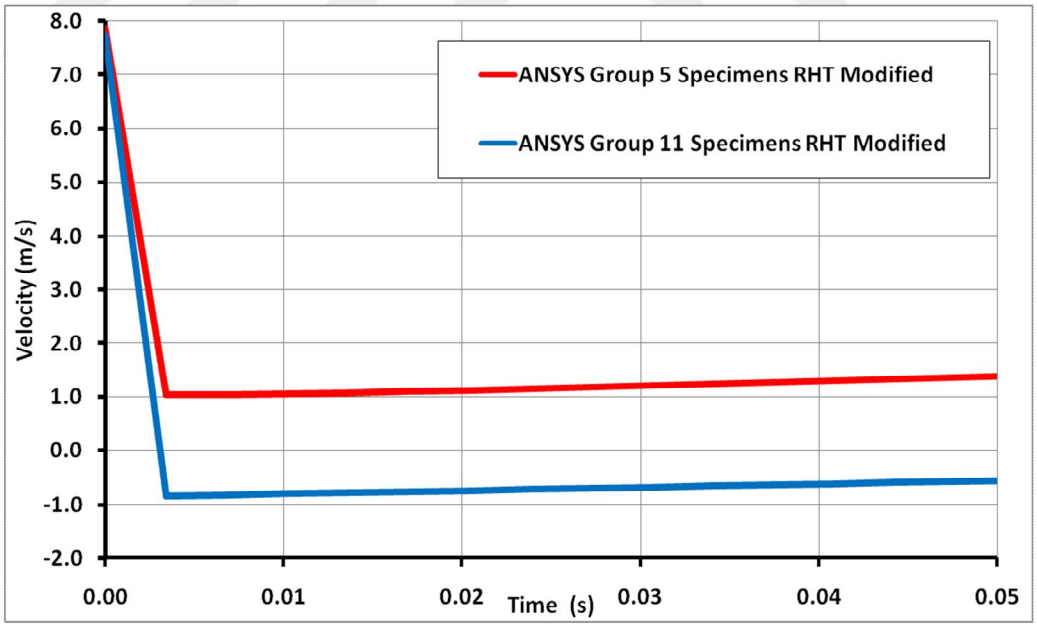

Figure 5-64 – Predicted velocity-time relationships for 150×150 mm LSC specimens (Group 5: unreinforced and Group 11: reinforced)

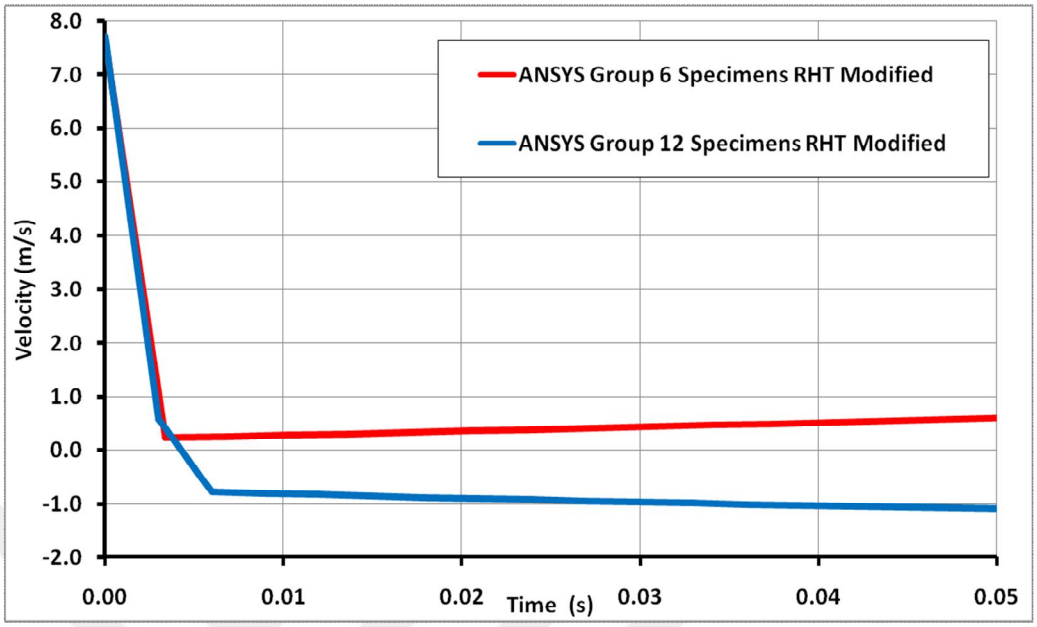

Figure 5-65 – Predicted velocity-time relationships for 150×150 mm NSC specimens (Group 6: unreinforced and Group 12: reinforced)

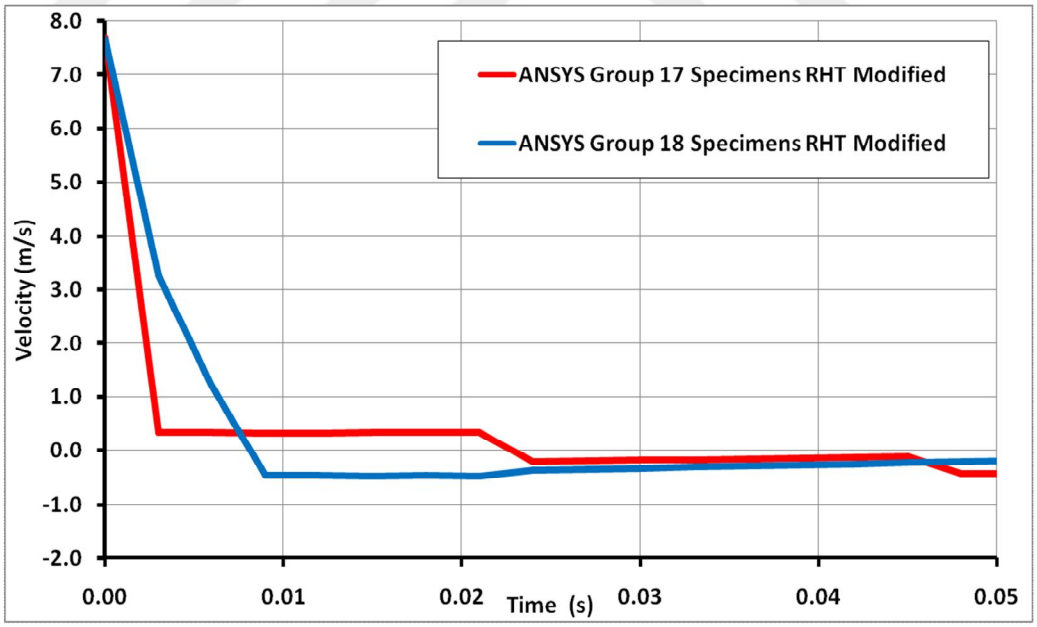

Figure 5-66 – Predicted velocity-time relationships for 150×150 mm SFRC specimens (Group 17: unreinforced and Group 18: reinforced)

5.7.4 Energy Absorption Capacity

The energy before and after impact were calculated for all CC and SFRC unreinforced specimens base on the hammer velocities before and after impact. An effort was made to predict the absorbed energy of the reinforced specimens; however the calculations related to crack energy were very complex. Therefore, no results were shown for the energy absorption of the reinforced specimens. The kinetic energy (KE) of the hammer was calculated using the following equation:

$$KE = 0.5\ m \times v^2 \qquad \text{Equation 5-5}$$

where KE is the kinetic energy in Joules, m is hammer mass in kg, and v is the hammer velocity before or after impact in m/s.

Energy absorbed by crack, G_c, was calculated based on fracture energy concept of CC and SFRC (G_f = 100 J/m^2 for CC and 3029 for SFRC), crack length L_c that observed experimentally and specimen width (crack area width) w_c as shown in Figure 5-67 using the following equation:

$$G_c = G_f \times L_c \times w_c \qquad \text{Equation 5-6}$$

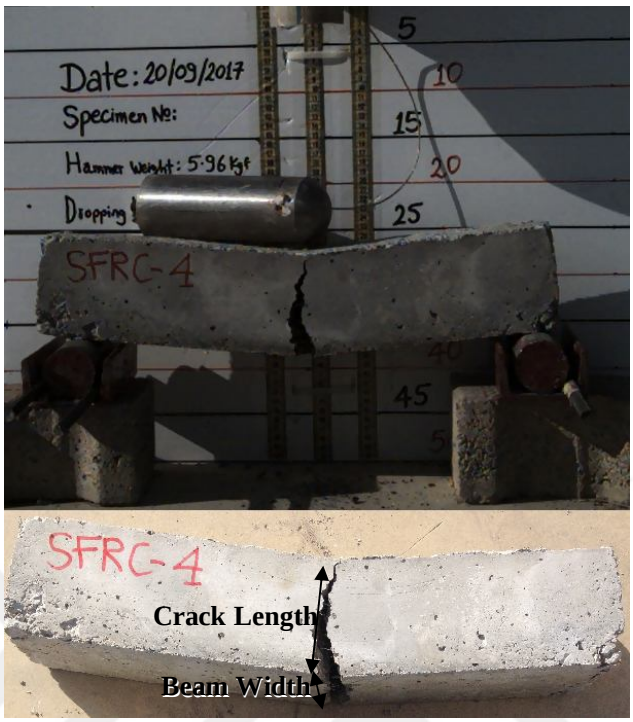

Figure 5-67 – Definitions for crack length and beam width

The energy absorbed by other means such as supports, beam translation, beam rotation, etc. was calculated by subtracting the energy absorbed by crack from the KE difference of the hammer before and after impact.

Table 5-14 shows the velocities and calculated energies obtained from the predicted velocity-time relationships. The result shows that energy absorbed by cracks increases with increase in dimensions of specimen size.

Table 5-14 – Velocities and calculated energies obtained from the predicted velocity-time relationships

Group No	Velocity before Impact (m/s)	Velocity after Impact (m/s)	Energy before Impact (J)	Energy after Impact (J)	Energy Absorbed by Crack (J)	Energy Absorbed by Other Means (J)
1	5.798	4.530	100.2	61.2	0.4	38.7
2	5.505	3.996	90.3	47.6	0.4	42.4
3	7.649	4.371	174.4	56.9	1.0	116.4
4	7.067	3.087	148.8	28.4	1.0	119.4
5	7.864	1.403	184.3	5.9	2.3	176.2
6	7.654	0.602	174.6	1.1	2.3	171.2
13-a	7.505	5.577	167.8	92.7	10.9	64.3
13-b	5.867	4.277	102.6	54.5	10.9	37.2
15	5.616	3.340	94.0	33.2	29.4	31.4
17	7.694	-0.109	176.4	0.04	51.3	125.0

This table indicated that the energy absorption capacity of concrete was greater as the cross-section of concrete got larger. No correlation was observed when predicted absorbed energy of the LSC and NSC specimens were compared. It can be concluded that the change in the concrete strength from 12 to 26 MPa did not have any significant effects on the energy absorption capacity of beams under impact loading.

5.8 Parametric Study on Reinforcement

The specimens were reinforced using one 8 mm diameter steel reinforcement fixed at center of specimen cross section in this research. A parametric study was conducted to evaluate the variation of the behavior for various diameters of the reinforcement. The parametric study was performed for Group 9, 10, and 16. All of these groups had 100×100×500 mm dimensions and had one 8 mm diameter reinforcement. Group 9 specimens were cast from LSC, Group 10 specimens were cast from NSC, and Group 16 specimens were cast from SFRC. The reinforcement for these specimen groups were varied from ϕ8 to ϕ20. The velocity-time relationships of beams having various reinforcement diameters were obtained from ANSYS Analysis Software Package. The results of this parametric study are shown in Figure 5-68 to Figure 5-70.

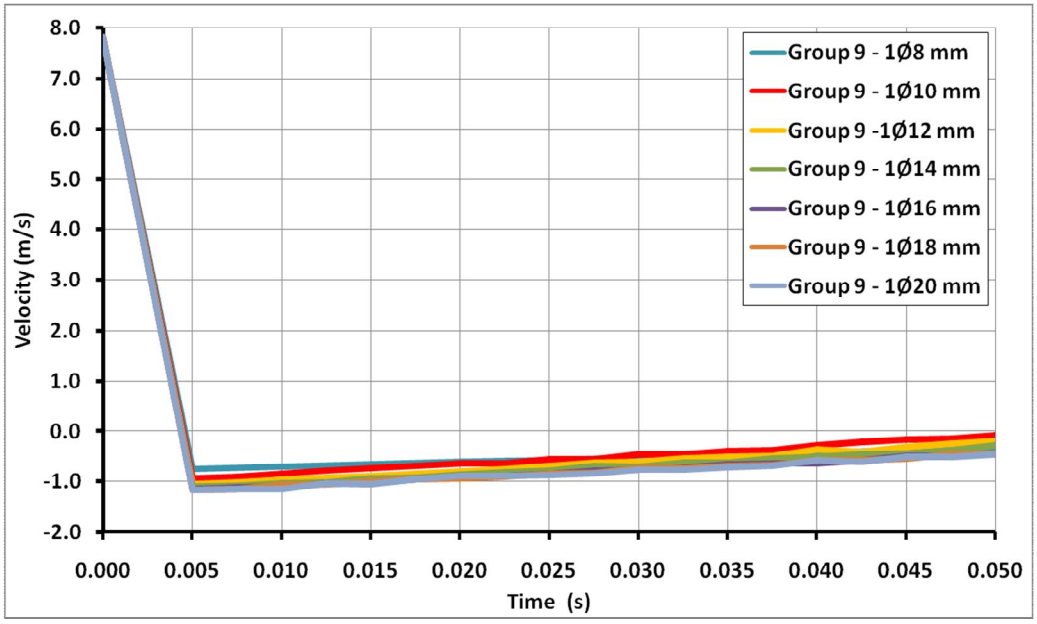

Figure 5-68 – Velocity-time relationships of hammer obtained from ANSYS for various reinforcement diameters for LSC specimens (Group 9 specimens)

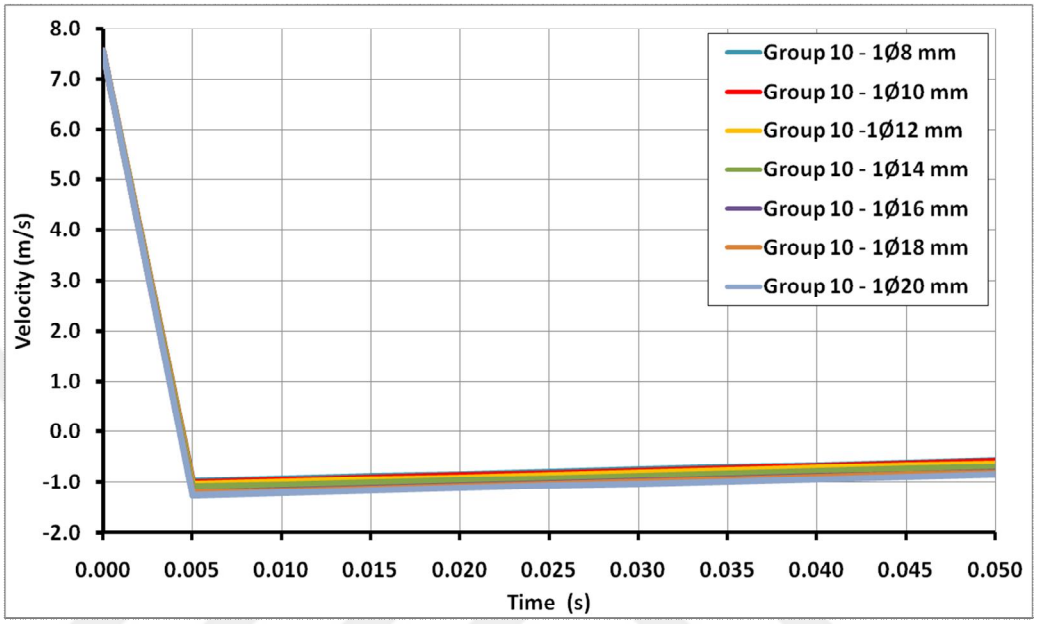

Figure 5-69 – Velocity-time relationships of hammer obtained from ANSYS for various reinforcement diameters for NSC specimens (Group 10 specimens)

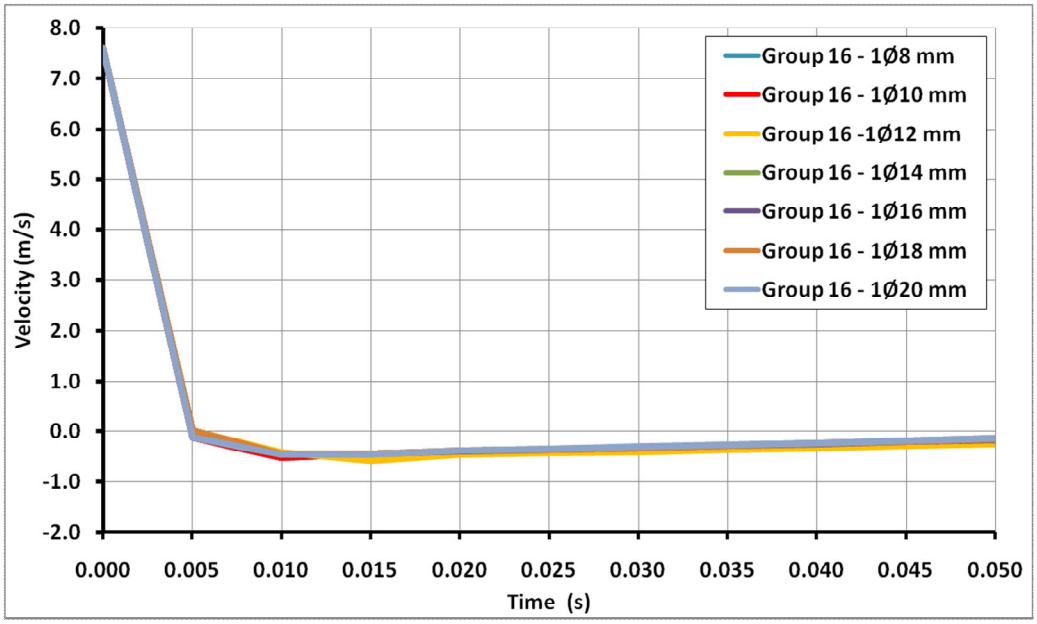

Figure 5-70 – Velocity-time relationships of hammer obtained from ANSYS for various reinforcement diameters for SFRC specimens (Group 16 specimens)

The results indicated that as reinforcement diameter increased, the velocity of the hammer decreased and the absorbed energy by the system increased. The difference and variation between hammer velocities were greater for LSC specimens than that of NSC specimen. This variation and difference were not significantly different for SFRC specimens.

6. SUMMARY, CONCLUSIONS, AND RECOMMENDATIONS

6.1 Summary

This research investigated the experimental and analytical behavior of unreinforced and reinforced concrete beams cast using conventional concrete (CC) and steel fiber reinforced concrete (SFRC) under impact loading. Dramix ZP-305 type steel fibers were used for SFRC. Half of the beam specimens were unreinforced and the others were reinforced using one 8 mm diameter steel reinforcement fixed at center of specimen cross section. Cylinder concrete compressive strengths used in this study were 12 and 26 MPa for CC specimens and 35 MPa for SFRC specimens. Beam specimens had 60×60×500, 100×100×500, and 150×150×500 mm dimensions. The specimens were tested under impact loading using a drop-hammer testing apparatus having a weight of 58.5 N. This weight was dropped from various heights (1.20, 2.00, and 2.95 m for unreinforced specimens and 2.95, 3.00, and 3.04 m for reinforced specimens) based on specimen sizes. The slow motion videos of the tested specimens were recorded using a high-speed camera having a frame rate of 2000 fps. Experimental velocity-time relationships for hammer were obtained by analyzing of recorded impact videos using the TEMA Motion Analysis Software. Beams, hammer, and supports were modeled in ANSYS Finite Element Analysis Program and parameters related to modeling were calibrated based on the test results. Riedel, Hiermaier, and Thoma (RHT) Concrete Model was used in ANSYS Dynamic Explicit AUTODYN solver. The results were compared to the experimental studies on CC and SFRC in this research and input parameters of the model were modified.

6.2 Conclusions

The following conclusions were derived based on the findings of this research.

Based on the results of the comparisons of default and modified RHT Concrete Model results for unreinforced CC specimens:

- For Group 1 (LSC) and 2 (NSC) specimens having 60×60×500 mm dimensions, the analytical velocity-time analytical relationships of hammer for both the default and modified RHT Concrete Model fit well with the experimental relationships
- For specimen size of 100×100×500 mm, the analytical velocity-time relationships of hammer using modified RHT Concrete Model for Group 3 (LSC) and 4 (NSC) specimens estimated the experimental results better than the default model.
- For specimen size of 150×150×500 mm, the analytical velocity-time relationships of hammer using modified RHT Concrete Model for Group 5 (LSC) and 6 (NSC) specimens estimated the experimental results better than the default model.
- For Group 3 specimens (LSC - 100×100×500 mm), Group 5 specimens (LSC - 150×150×500 mm), and Group 6 specimens (NSC - 150×150×500 mm), the analytical velocity-time relationships of hammer using default RHT Concrete Model resulted in a higher velocity after impact than the modified one.
- For Group 4 specimens (NSC - 100×100×500 mm), the analytical velocity-time relationships of hammer using default RHT Concrete Model resulted in a much lower velocity after impact.

Based on the results of the comparisons of default and modified RHT Concrete Model results for reinforced CC specimens:

- For Group 7 (LSC) and 8 (NSC) specimens having 60×60×500 mm dimensions, the analytical velocity-time analytical relationships of hammer for both the default and modified RHT Concrete Model fit well with the experimental relationships
- For specimen size of 100×100×500 mm, the analytical velocity-time relationships of hammer using modified RHT Concrete Model for Group 9 (LSC) and 10 (NSC) specimens estimated the experimental results better than the default model.
- For specimen size of 150×150×500 mm, the analytical velocity-time relationships of hammer using modified RHT Concrete Model for Group 11 (LSC) and 12 (NSC) specimens estimated the experimental results better than the default model.

Based on the results of the comparisons of default and modified RHT Concrete Model results for unreinforced SFRC specimens:

- For Group 13-a and 13-b specimens having 60×60×500 mm dimensions, the analytical velocity-time analytical relationships of hammer for both the default and modified RHT Concrete Model with μ=0.5 fit well with the experimental relationships
- For specimen size of 100×100×500 mm, the analytical velocity-time relationships of hammer using modified RHT Concrete Model with μ=0.5 for Group 15 specimens estimated the experimental results better than the default model.
- For specimen size of 150×150×500 mm, the analytical velocity-time relationships of hammer using modified RHT Concrete Model with μ=0.5 for Group 17 specimens estimated the experimental results better than the default model.

Based on the results of the comparisons of default and modified RHT Concrete Model results for reinforced SFRC specimens:

- For Group 14 specimens having 60×60×500 mm dimensions, there was significant variation between the experimental and analytical results, since the hammer became tilted after the impact for these specimens.
- For specimen size of 100×100×500 mm, the analytical velocity-time relationships of hammer using modified RHT Concrete Model with μ=0.5 for Group 16 specimens estimated the experimental results better than the default model.
- For specimen size of 150×150×500 mm, the analytical velocity-time relationships of hammer using modified RHT Concrete Model with μ=0.5 for Group 18 specimens estimated the experimental results better than the default model.

Based on the results of the comparisons of the predicted velocity-time relationships:

- For unreinforced specimens as the size of the specimen increased, the velocity of the hammer decreased significantly no matter what the concrete strength was. For reinforced specimens, the change in velocity of the hammer was approximately equal for 100×100 and 150×150 mm specimens since the hammer stopped and

deflected up for these group specimens. However, the specimens having 60×60 mm dimensions, the reinforcement did not have similar effect like larger specimens. This specimen failed and the reinforcement was bent at the end of the test.

- For unreinforced specimens as the concrete strength increased, the velocity of the hammer decreased. For the reinforced specimens, the concrete strength did not have any significant effect on the behavior.
- For smaller sized specimens, the effect of reinforcement is much larger. The velocity of the hammer decreased more for smaller sized specimens. For larger sized specimens, the difference of the velocity of the hammer between the unreinforced and reinforced specimens was smaller.

Based on the results of the comparisons of the energy absorption capacity of the unreinforced specimens:

- The energy absorption capacity of concrete was greater as the cross-section of concrete got larger. No correlation was observed when predicted absorbed energy of the LSC and NSC specimens were compared. It can be concluded that the change in the concrete strength from 12 to 26 MPa did not have any significant effects on the energy absorption capacity of beams under impact loading.

Based on the results of the parametric study:

- As reinforcement diameter increased, the velocity of the hammer decreased and the absorbed energy by the system increased. The difference and variation between hammer velocities were greater for LSC specimens than that of NSC specimen. This variation and difference were not significantly different for SFRC specimens.

6.3 Recommendations

The following recommendations may be suggested:

- The dropping heights for the specimens may be kept same for better comparisons of the results.

- The concrete may be marked suing test marker at various locations to evaluate the motion of concrete better.
- Sensitive force transducers may be located at the support to evaluate the force of the hammer.
- Various diameters of the reinforcement may be used in future studies.
- Higher concrete strengths may be used with larger reinforcement sizes in future studies.

7. REFERENCES

Abdelatif, A. O., Owen, J. S., and Hussein, M. F. M., "Modelling the prestress transfer in pre-tensioned concrete elements," Finite Elements in Analysis and Design, Vol. 94, 2015, pp. 47-63.

Abdelmola, S., "Fatigue behavior of prestressed steel fiber reinforced concrete beams," M.S. Thesis, Civil Engineering Department, Atılım University, 2018, 79 p.

Abdussalam, A. A. G. A., "Compressive and tensile behaviors of steel fiber reinforced concrete," M.S. Thesis, Civil Engineering Department, Atılım University, 2015, 113 p.

ACI Committee 318, "Building code requirements for structural concrete and commentary (ACI 318mM-05)," Structural Building Code, 2004.

ACI Committee 544, "Measurement of properties of fiber reinforced concrete," ACI Materials Journal, No. 85, 1988, pp. 583-93.

ANSYS Inc., "ANSYS explicit dynamics analysis guide," www.ansys.com, 2015, 250 p.

Arıoglu, N., Girgin, Z. C., and Arıoglu, E., "Evaluation of ratio between splitting tensile strength and compressive strength for concretes up to 120 MPa and its application in strength criterion," ACI Materials Journal, Vol. 103, No. 1, 2006, pp. 18-24.

ASTM C39, "Standard test method for compressive strength of cylindrical concrete specimens," American Society for Testing and Materials, Annual Book, 2008.

ASTM C78, “Standard test method for flexural strength of concrete (using simple beam with third-point loading),” American Society for Testing and Materials, Annual Book, 2002.

ASTM A820, “Standard specification for steel fibers for fiber-reinforced concrete,” American Society for Testing and Materials, Annual Book, 2006.

ASTM C143 / C143M-15a, “standard test method for slump of hydraulic-cement concrete,” ASTM International, West Conshohocken, PA, 2015.

ASTM C192 / C192M-16a, “Standard Practice for Making and Curing Concrete Test Specimens in the Laboratory,” ASTM International, West Conshohocken, PA, 2016.

ASTM E23, “Standard test methods for notched bar impact testing of metallic materials,” American Society for Testing and Materials, Annual Book, 2007.

Azeez, H. A., “Modeling of shear strength in rectangular reinforced concrete beams,” Engineering and Technology Journal,Vol. 27, No. 12, 2009, pp. 2352-2366.

Badiger, N. S. and Malipatil, K. M., “Parametric study on reinforced concrete beam using ANSYS,” IISTE Knowledge Sharing Partners, Civil and Environmental Research, Vol. 6, No. 8, 2014, pp. 88-94.

Balaguru, P. N. and Shah, S. P., “Fiber reinforced cement composites,” Mc Graw Hill International Editions, 1992.

Banthia, N., Mindess, S., Bentur, A., and Pigeon, M., “Impact testing of concrete using a drop-weight impact machine,” Experimental Mechanics, 1989, pp. 63-69.

Barr, B. and Baghli, A., “A repeated drop-weight impact testing apparatus for concrete,” Magazine of Concrete Research, Vol. 40, No. 144, 1988, pp.167-76.

Bazant, Z. P. and Oh, B. H., “Crack band theory for fracture of concrete,” Materials and Structures, RILEM, Paris, France, Vol. 16, 1983, pp. 155-177.

Bello, H. J., “Flexural behavior of lightly and heavily reinforced steel fiber concrete beams,” M.S. Thesis, Civil Engineering Department, Atılım University, 2014, 113 p.

Bindhu, K. R. and Jaya, K. P., “Strength and behavior of exterior beam column joints with diagonal cross bracing bars,” Asian Journal of Civil Engineering (Building and Housing), Vol. 11, No. 3, 2010, pp. 397-410.

Bindiganavile, V. S., “Dynamic fracture toughness of fiber reinforced concrete,” Ph. D. Thesis, Department of Civil Engineering, The University of British Columbia, 2003, 231 p.

Bortolotti, L., “First cracking load of concrete subjected to direct tension,” ACI Materials Journal, Vol. 88, No. 1, 1991, pp. 70-73.

Bortolotti, L., “Influence of concrete tensile ductility on compressive strength of confined columns,” Journal of Materials in Civil Engineering, ASCE, Vol. 6, No. 4, 1994, pp. 542-563.

Brown, M. D., Bayrak, O., and Jirsa, J. O., “Design for shear based on loading conditions,” ACI Structural Journal, Vol. 103, No. 4, 2006.

Carreira, D. J. and Chu, K. M., “Stress-strain relationship for plain concrete in compression,” ACI Journal, Vol. 82, No. 6, 1985, pp. 797-804.

Chanh, N. V., “Steel fibre reinforced concrete,” Faculty of Civil Engineering, Ho Chi Minh City University of Technology, pp.108-116.

CEB (Comite Euro-International de Beton), “Concrete structures under impact and impulsive loading,” Synthesis Report, Bulletin d’Information, 2008.

Craig, R. J., “Structural applications of reinforced steel fibrous concrete,” Concrete International Design and Construction, 1984.

Endgington, J., Hannant, D. J., and Williams, R. I. T., “Steel fiber reinforced concrete,” Building research establishment Garston Watford, CP 69/74, 1974.

Ezeldin, A. S. and Balaguru, P. N., “Normal high-strength fiber reinforced concrete under compression,” Journal of Materials in Civil Engineering, Vol. 4, No.4, 1992, pp. 415-427.

Faeq, M. N. F., “Flexural behavior of reinforced concrete beams having various layers of conventional and steel fiber reinforced concrete,” M.S. Thesis, Civil Engineering Department, Atılım University, 2015, 73 p.

Galuta, E. and Regig, W., “Numerical simulations of RC panels subjected to high speed projectile - erosion selection in AUTODYN-code,” International Journal of Innovative Science, Engineering & Technology, Vol. 4, No. 8, 2017, pp. 25-30.

Griffiths, G. and Thom, N., “Concrete pavement design guidance notes,” Taylor and Francis, New York, 2007, NY, USA.

Haido, J. H. and Musa, I. H., “Cracking strength of steel fiber reinforced concrete shallow beams under impact actions,” International Journal of Scientific and Engineering Research, Vol. 4, No. 4, 2013, pp. 464-472.

Henager, C. H., “Steel fibrous shotcrete: A summary of the state of the art,” Concrete International Design and Construction, Vol. 3, No. 1, 1981, pp. 50-58.

Hillerborg, A., Modéer, N., and, Petersson, P. E., “Analysis of crack formation and crack growth in concrete by means of fracture mechanics and finite elements,” Cement and Concrete Research, Vol. 6, No. 6, 1976, pp. 773-781.

IS 1893, “Indian standard code on criteria for earthquake resistant design of structures,” Bureau of Indian Standards, 2002, New Delhi, India.

Jeon, S., Kim, T. H., and You, K. H., “Characteristics of crater formation due to explosives blasting in rock mass,” Geomechanics and Engineering, Vol. 9, No. 3, 2015, pp. 329-344.

Johnston, C. D., “Definition and measurement of flexural toughness parameters for fiber reinforced concrete,” Cement and Concrete Aggregates, Vol. 4, No. 2, 1982, pp. 53-60.

Kantar, E., Erdem, R. T., and Anıl, Ö., “Nonlinear finite element analysis of impact behavior of concrete beam,” Mathematical and Computational Applications, Vol. 16, No. 1, 2011, pp. 183-193.

Karlovšek, J., Wagner, N., and Scheuermann, A., “Frequency-dependant dielectric parameters of steel fiber reinforced concrete,” 14th International Conference on Ground Penetrating Radar (GPR), Shanghai, China, 2012, pp. 510-516.

Kim, H. S., Ahn, J. G., and Ahn, H. S., “Numerical simulation of progressive collapse for a reinforced concrete building,” World Academy of Science, Engineering and Technology, International Journal of Civil, Environmental, Structural, Construction and Architectural Engineering, Vol. 7, No. 4, 2013.

Kim, D. J., Naaman, A. E., and El-Tawil, S., “High performance fiber reinforced cement composites with innovative slip hardending twisted steel fibers,” International Journal of Concrete Structures and Materials, Vol. 3, No. 2, 2009, pp. 119-126.

Kishi, N., Konno, H., Ikeda, K., and Matsuoka, K. G., “Prototype impact tests on ultimate impact resistance of PC rocksheds,” International Journal of Impact Enginering, Vol. 27, No. 9, 2002, pp. 969-85.

Leppänen, J., "Concrete subjected to projectile and fragment impacts: Modelling of crack softening and strain rate dependency in tension," International Journal of Impact Engineering, Vol. 32, No. 11, 2006, pp. 1828-1841.

Li, T., "Shear strengthening of unreinforced masonry (URM) walls with FRP composites," Ph. D. Dissertation, University of Missouri-Rolla, 2004.

Löfgren, I. A., "Fibre-reinforced concrete for industrial construction: A fracture mechanics approach to material testing and structural analysis," Ph. D. Thesis, Chalmers Tekniska Hogskola, Sweden, 2005.

Majeed, S. A., "Finite element analysis of strengthened reinforced concrete beams," Al Rafidain Engineering, Vol. 21, No. 1, 2013, pp. 135-145.

Mohammadi, Y., Carkon-Azad, R., Singh, S.P., and Kaushik, S.K., "Impact resistance of steel fibrous concrete containing fibres of mixed aspect," Construction and Building Materials, Vol. 23, No. 1, 2009, pp. 183-189.

Naaman, A. E., "Engineered steel fibers with optimal properties for reinforcement of cement composites," Journal of Advanced Concrete Technology, Vol. 1, 2003, pp. 241-252.

Naaman, A., E. and Reinhardt, H., W., "Characterization of high performance fiber reinforced cement composites," HPFRCC-2, 1996, pp. 1-24.

Nyström, U. and Gylltoft, K, "Comparative numerical studies of projectile impacts on plain and steel-fibre reinforced concrete," International Journal of Impact Engineering, Vol. 38, No. 2-3, 2011, pp. 95-105.

Palmstrom, A. and Nilsen, B., "Engineering geology and rock engineering," Handbook No. 2, Norwegian Group for Rock Mechanics, Oslo, Norway, 2000.

Park, D., Jeon, B., and Jeon, S., “A numerical study on the screening of blast-induced waves for reducing ground vibration,” Rock Mechanics and Rock Engineering, Vol. 42, No. 3, 2009, pp. 449-473.

Park, D. and Jeon, S., “Reduction of blast-induced vibration in the direction of tunneling using an air-deck at the bottom of a blasthole,” International Journal of Rock Mechanics and Mining Sciences, Vol. 47, No. 5, 2010, pp. 725-761.

Phillips, D. and Binsheng, Z, “Direct tension tests on notched and un-notched plain concrete specimens,” Magazine of Concrete Research, Vol. 45, No. 162, 1993, pp. 25-35.

Popovics, S., “A review of stress-strain relationship for concrete,” ACI Journal, Vol. 67, No. 3, 1970.

Rai, A. and Joshi, Y. P., “Applications and properties of fibre reinforced concrete,” Journal of Engineering Research and Applications, Vol. 4, Issue 5, 2014, pp.123-131.

Rao, M. C., Bhattacharyya, S. K., and Barai, S. V., “Behavior of recycled aggregate concrete under drop weight impact load,” Construction and Building Materials, Vol. 25, No. 1, 2011, pp. 69-80.

Ravindrarajah, R. S. and Lyte, M. C., “Energy absorbing concrete for impact loading,” Centre for Built Infrastructure Research, University of Technology, Sydney, Broadway, NSW, Australia, 2007.

Reeta, Manoj, Karandeep, and Singhal, A., “Fiber reinforced concrete,” International Journal of All Research Education and Scientific Methods (IJARESM), Vol. 4, No. 7, 2016, pp. 155-160.

Riedel, W., Kawai, N., and Kondo K., "Numerical assessment for impact strength measurements in concrete materials," International Journal of Impact Engineering, Vol. 36, 2009, pp. 283-293.

Riedel, W., Thoma, K., Hiermaier, S., and Schmolinske E., "Penetration of reinforced concrete by BETA-B-500, numerical analysis using a new macroscopic concrete model for hydrocodes," Proceedings of Internationales Symposium on Interaction of the Effects of Munitions with Structures, Berlin, Germany, 1999, pp. 315-322.

Shende, A. M., Pande, A. M., and Pathan, M. G., "Experimental study on steel fiber reinforced concrete for M-40 grade," International Refereed Journal of Engineering and Science (IRJES), Vol. 1, No. 1, 2012, pp. 43-48.

Siewert, T. A., Manahan, M. P., McCowan, M. P., Holt, J. M., Marsh, F. J., and Ruth, E. A., "The history and importance of impact testing," ASTM, 1999.

Soranakom, C., Yekani-Fard, M., and Mobasher, B., "Development of design guidelines for strain softening fiber reinforced concrete," 7th I0nternational Symposium of Fiber Reinforced Concrete: Design and Applications BEFIB2008, 2008, pp. 513-523.

Strauss, A., Zimmermann, T., Lehký, D., Novák, D., and Keršner, Z., "Stochastic fracture-mechanical parameters for the performance-based design of concrete structures," Structural Concrete, Vol. 15, No. 3, 2014, pp. 380-394.

Subramani, T., Devi, K. B., Saravanan, M. S., and Thomas, S., "Analysis of RC structures subject to vibration by using ANSYS," International Journal of Engineering Research and Applications, Vol. 4, No. 12, 2014, pp. 45-54.

Tu, T. and Lu, Y., "Evaluation of typical concrete material models used in hydrocodes for high dynamic response simulations," International Journal of Impact Engineering, Vol. 36, No. 1, 2009, pp. 132-146.

Vaiciunas, J., Dorosevas, V., and Ivanauskas, E., “The estimation of test analysis the interaction of reinforced concrete slabs under impact load,” Proceedings of 16th International Conference, Mechanika, 2011, pp. 317-320.

Vasudevan, G., Kothandaraman, S., and Azhagarsamy, S., “Study on non-linear flexural behavior of reinforced concrete beams using ANSYS by discrete reinforcement modeling,” Strength of Materials, Vol. 45, No. 2, 2013, pp. 231-241.

Vidhya, K., Palanisamy, T., and Selvan, R. T., “An experimental study on behaviour of steel fibre reinforced concrete beams,” International Journal of Advanced Research Methodology in Engineering and Technology, Vol. 1, No. 2, 2017, pp. 178-183.

Wang, H. T. and Wang, L. C., “Experimental study on static and dynamic mechanical properties of steel fiber reinforced lightweight aggregate concrete,” Construction and Building Materials, Vol. 38, 2013, pp. 1146-1151.

Weidner, A. M., Pantelides, C. P., Richins, W. D., Larson, T. K., and Blakeley, J. E., “Drop-hammer test on concrete cylinders considering fiber reinforcement and elevated temperature,” INL/EXT-13-28118, Idaho National Laboratory, Idaho Falls, Idaho, 2012, 93 p.

Yilmaz, M. C., Anıl, Ö., Alyavuz, B., and Kantar, E., “Load displacement behavior of concrete beam under monotonic static and low velocity impact load,” International Journal of Civil Engineering, Transaction A: Civil Engineering, Vol. 12, No. 4, 2014, pp. 488-503.

Zhang, X. X., Ruiz, G., and Yu, Rena C., “A new drop weight impact machine for studying fracture process in structural concrete,” Anales de Mecánica de la Fractura, Vol. 25, No. 2, 2008, pp. 655-659.

Ziara, M. M., "Behavior of beams strengthened with steel fiber RC overlays," Journal of Advanced Concrete Technology, Vol. 7, No. 1, 2009, pp. 111-121.

8. APPENDICES

Figure A-1 – Specifications of high-speed camera 1

FASTCAM MC2

HIGH PERFORMANCE VIDEO SYSTEM

Specifications

MODEL	FRAME RATE (fps)	MAX RESOLUTION Horizontal	MAX RESOLUTION Vertical	RECORD DURATION TIME (Sec.) 1GB	TIME (Sec.) 2GB	TIME (Sec.) 4GB	FRAMES 1GB	FRAMES 2GB	FRAMES 4GB
10K / 2K / 500	250	512	512	16.37	32.75	65.52	4,092	8,188	16,380
	500	512	512	8.18	16.38	32.76	4,092	8,188	16,380
	1,000	512	512	4.09	8.19	16.38	4,092	8,188	16,380
	2,000	512	512	2.05	4.09	8.19	4,092	8,188	16,380
	3,000	512	352	1.98	3.97	7.94	5,952	11,909	23,825
	4,000	512	256	2.05	4.09	8.19	8,184	16,376	32,760
	8,000	512	128	2.05	4.09	8.19	16,368	32,752	65,520
	10,000	512	96	2.18	4.37	8.74	21,824	43,669	87,360

Sensor	CMOS (Bayer system color, single sensor) with 10µm pixel
Shutter	Global electronic shutter from 20ms to 6µs
Saved Image Formats	JPEG, AVI, TIFF, BMP, RAW, PNG, MOV, and FTIF. Images can be saved with or without image or comment data
Phase Lock	Enables cameras to be synchronized precisely together to a master camera or external source
Triggering	Selectable positive or negative TTL 5Vp-p, or switch closure
Lens Mount	Cube Cam: C-mount Pencil Cam: NF-mount
Data Display	Frame Rate, Shutter Speed, Trigger Mode, Date or Time (can be switched), Status (Playback/Record), Real Time, Frame Count and Resolution
Video Output	NTSC or PAL. Live video during recording. Ability to zoom, pan and scroll within image via keypad
Recording Modes	Start, End, Center, Manual, Random
Camera Control	Through a Gigabit Ethernet PC interface and optional RS-422 keypad
Camera Cable Length	7 meters (23')
Dimensions and Weight	Processor: 195mm (7.68")H x 159mm (6.26")W x 130mm (5.12")D *excluding protrusions Weight: 5 kg (11 lbs) Cube Cam: 35mm (1.38")H x 35mm (1.38")W x 33.3 mm (1.31")D *excluding protrusions Weight: 90g (0.2 lbs) Pencil Cam: 23mm (0.91")H x 23.2mm (0.91")W x 77.1mm (3.04")D *excluding protrusions Weight: 145g (0.3 lbs)
Power Requirements	DC operation 18 - 36 VDC, 45VA, 100V - 240V AC, 50 - 60Hz power supply provided
Video Output	NTSC, PAL RS170 video output

Specifications subject to change without notice

PHOTRON USA, INC.
9520 Padgett Street, Suite 110
San Diego, CA 92126-4446
USA
Tel: 858.684.3555 or 800.585.2129
Fax: 858.684.3558
Email: image@photron.com
www.photron.com

PHOTRON (EUROPE) LIMITED
The Barn, Bottom Road
West Wycombe, Bucks, HP14 4BS
United Kingdom
Tel: +44 (0) 1494 481011
Fax: +44 (0) 1494 487011
Email: image@photron.com
www.photron.com

PHOTRON LIMITED
Fujimi 1-1-8
Chiyoda-Ku, Tokyo 102-0071
Japan
Tel: +81 (0) 3 3238 2107
Fax: +81 (0) 3 3238 2109
Email: image@photron.co.jp
www.photron.co.jp

Photron

SLOW MOTION IMAGING SOLUTIONS

Figure A-2 – Specifications of high-speed camera 2

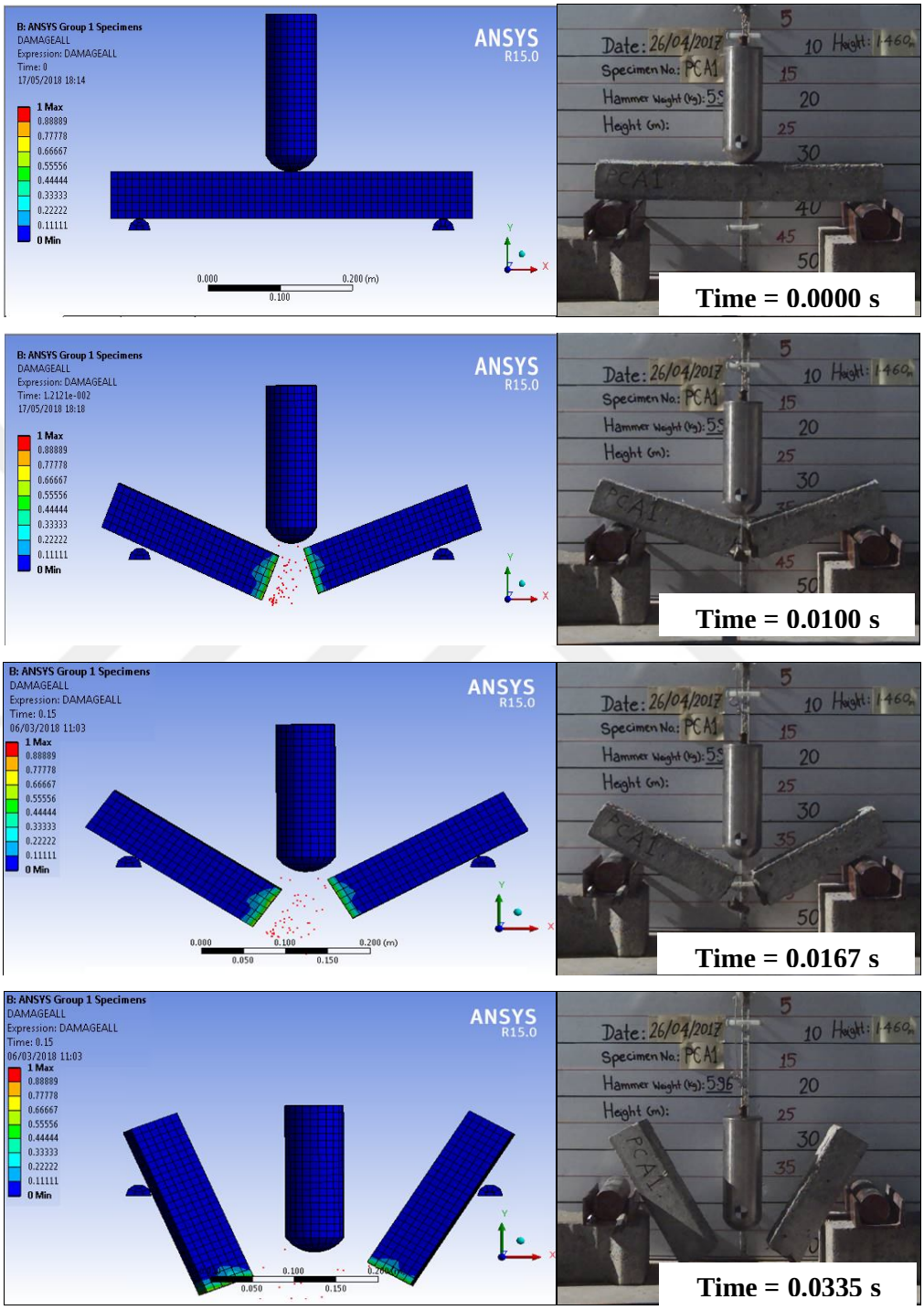

Figure A-3 – Comparison of the motions for various times after impact obtained from the impact tests and the analyzed model for 60C12-1

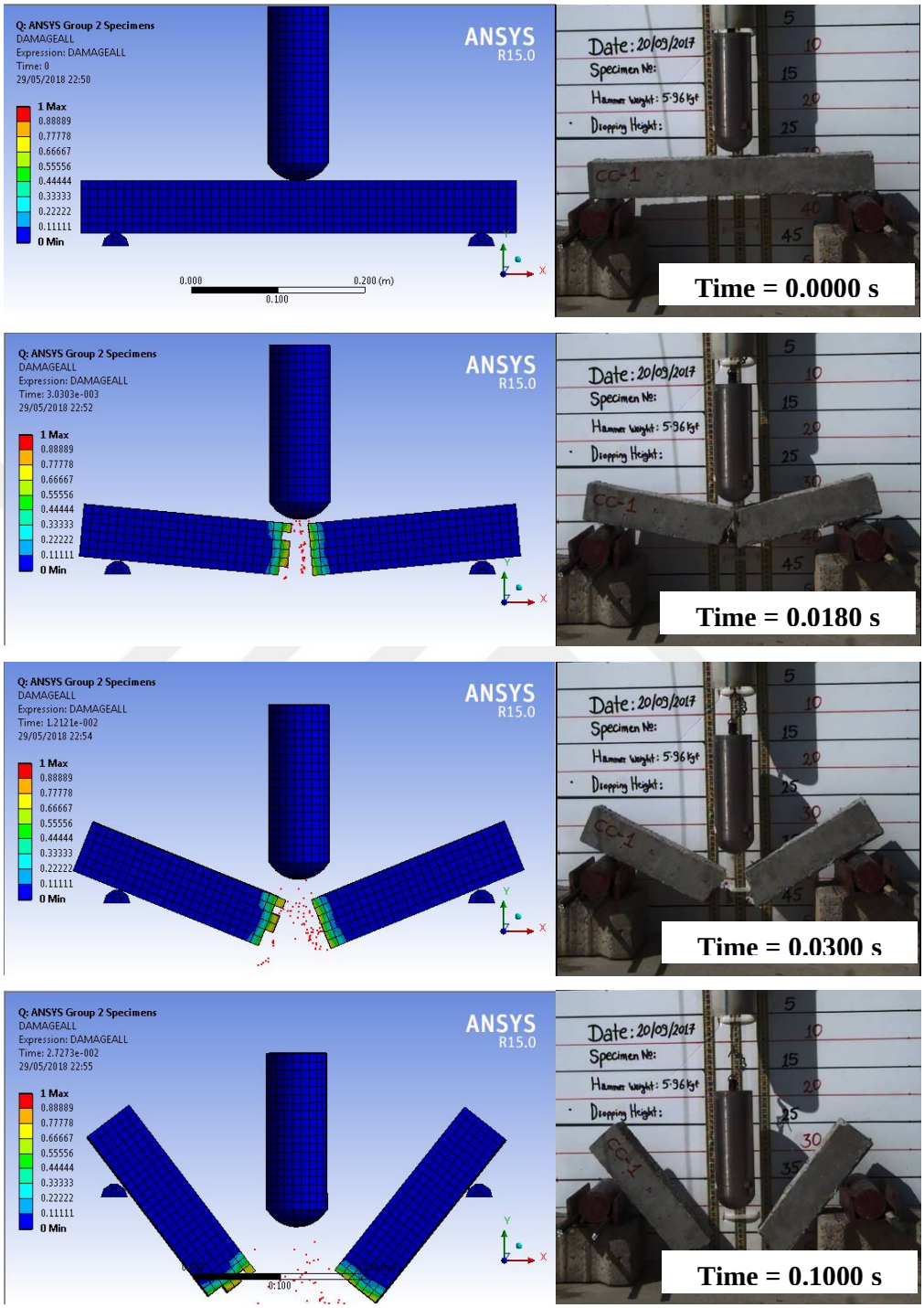

Figure A-4 – Comparison of the motions for various times after impact obtained from the impact tests and the analyzed model for 60C26-1

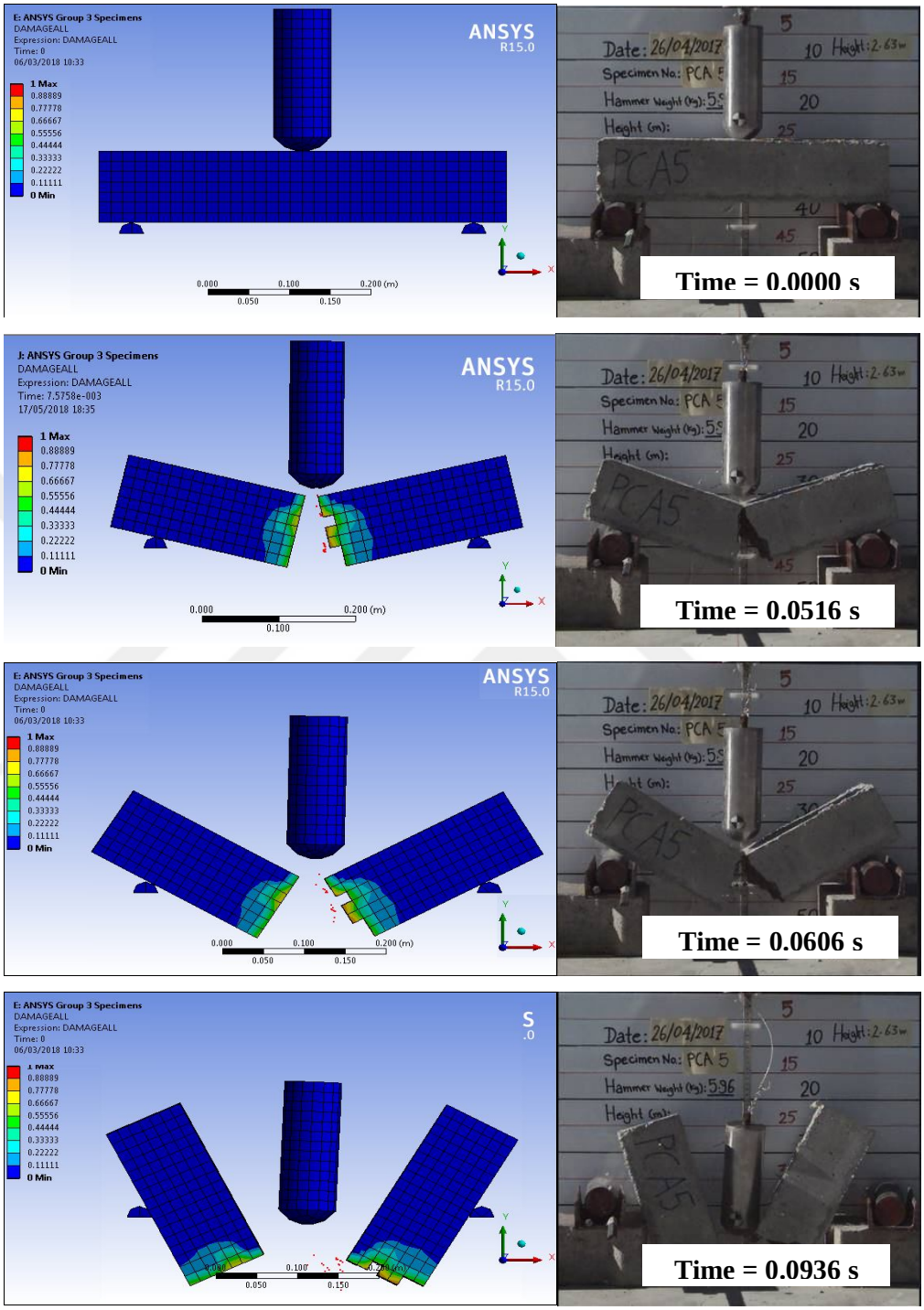

Figure A-5– Comparison of the motions for various times after impact obtained from the impact tests and the analyzed model for 100C12-2

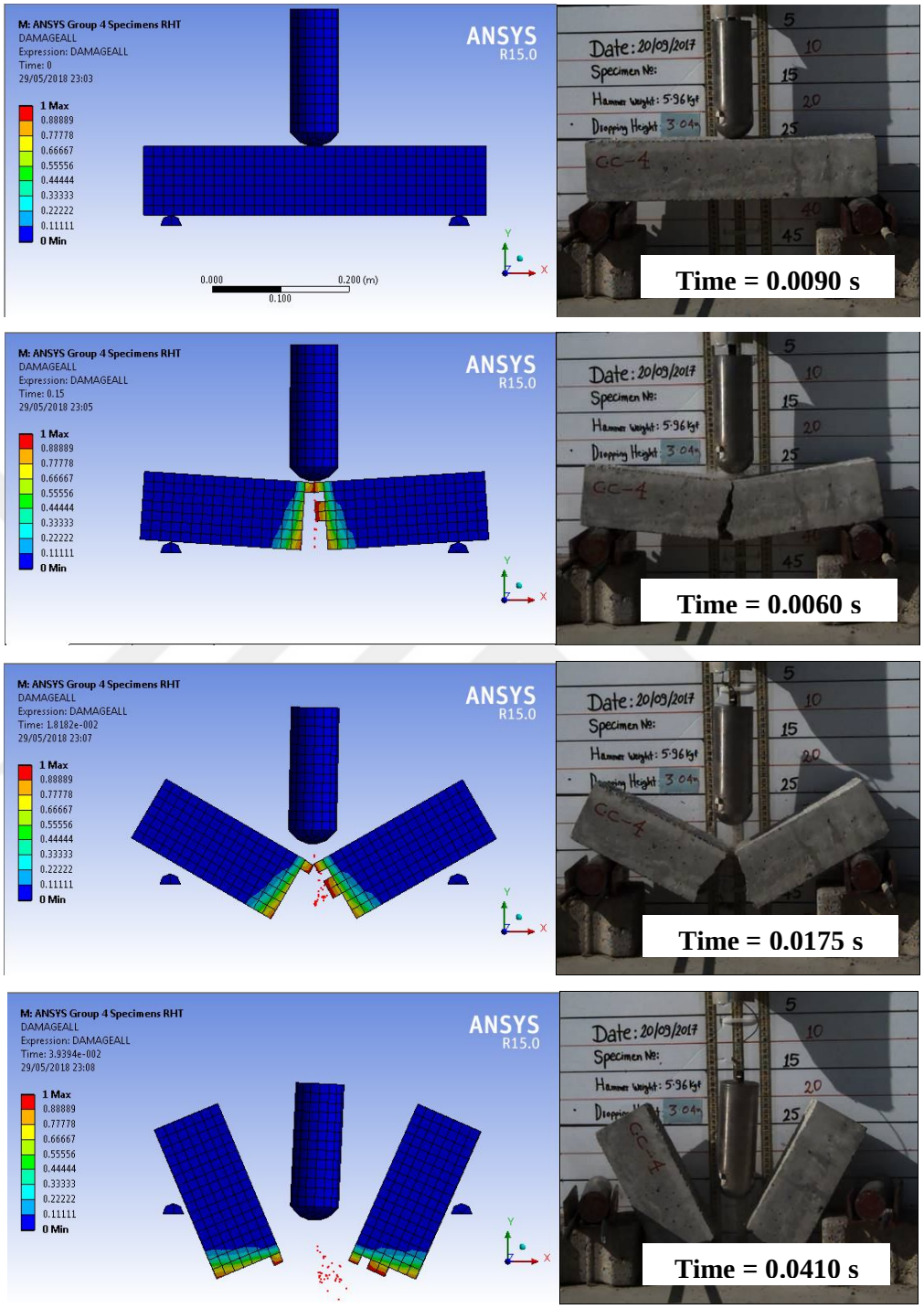

Figure A-6– Comparison of the motions for various times after impact obtained from the impact tests and the analyzed model for 100C26-1

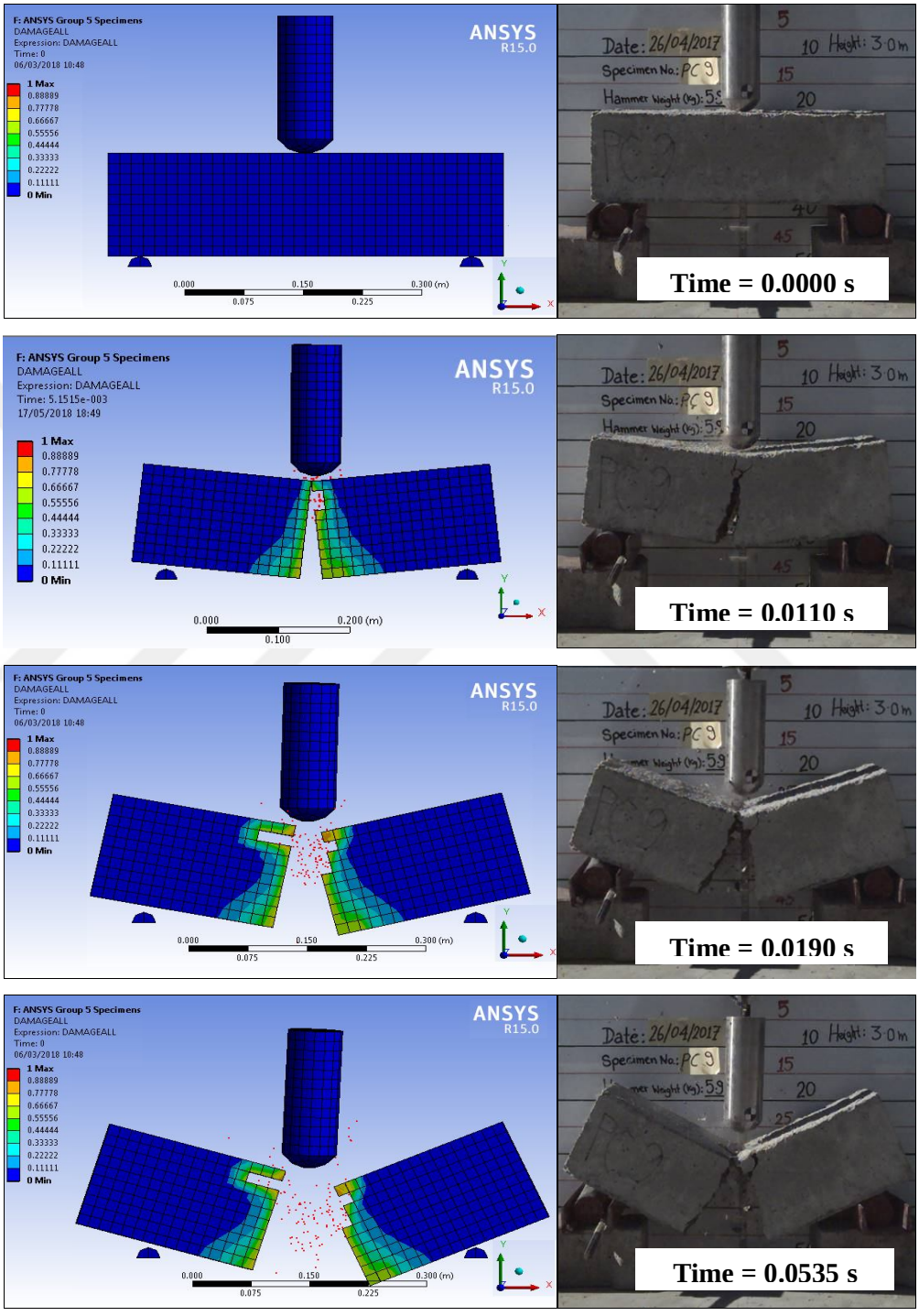

Figure A-7– Comparison of the motions for various times after impact obtained from the impact tests and the analyzed model for 150C12-3

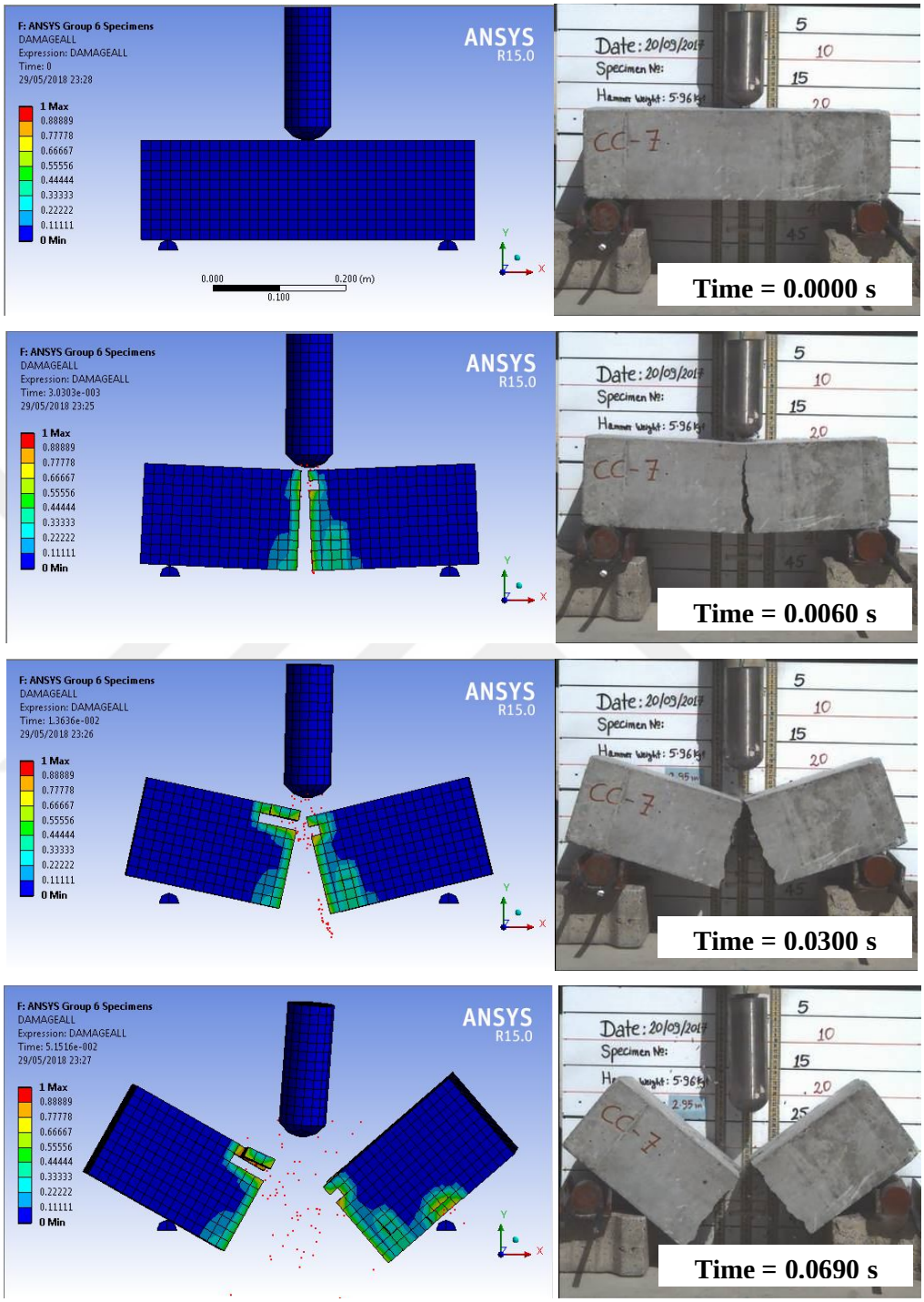

Figure A-8– Comparison of the motions for various times after impact obtained from the impact tests and the analyzed model for 150C26-1

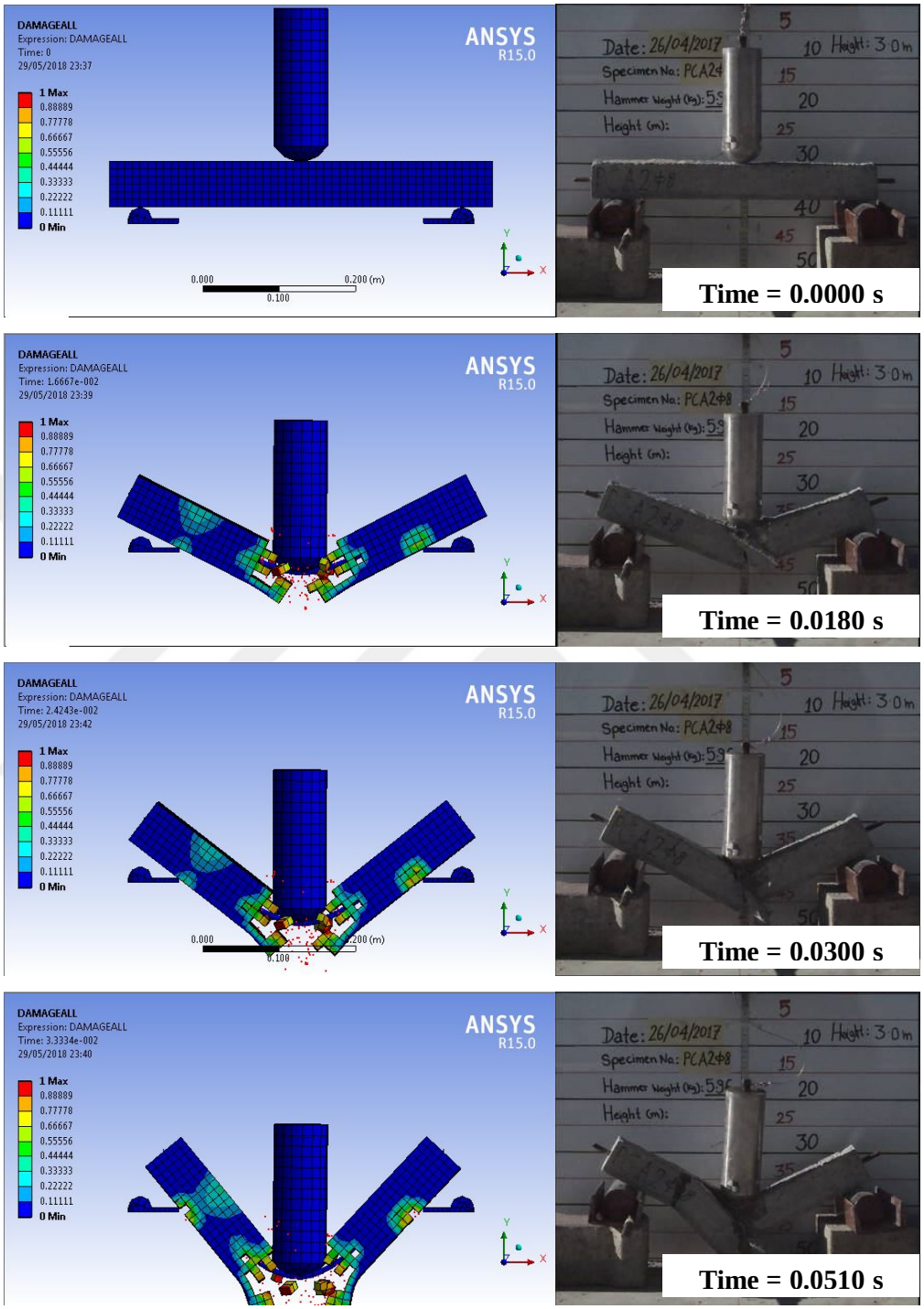

Figure A-9– Comparison of the motions for various times after impact obtained from the impact tests and the analyzed model for 60C12R-2

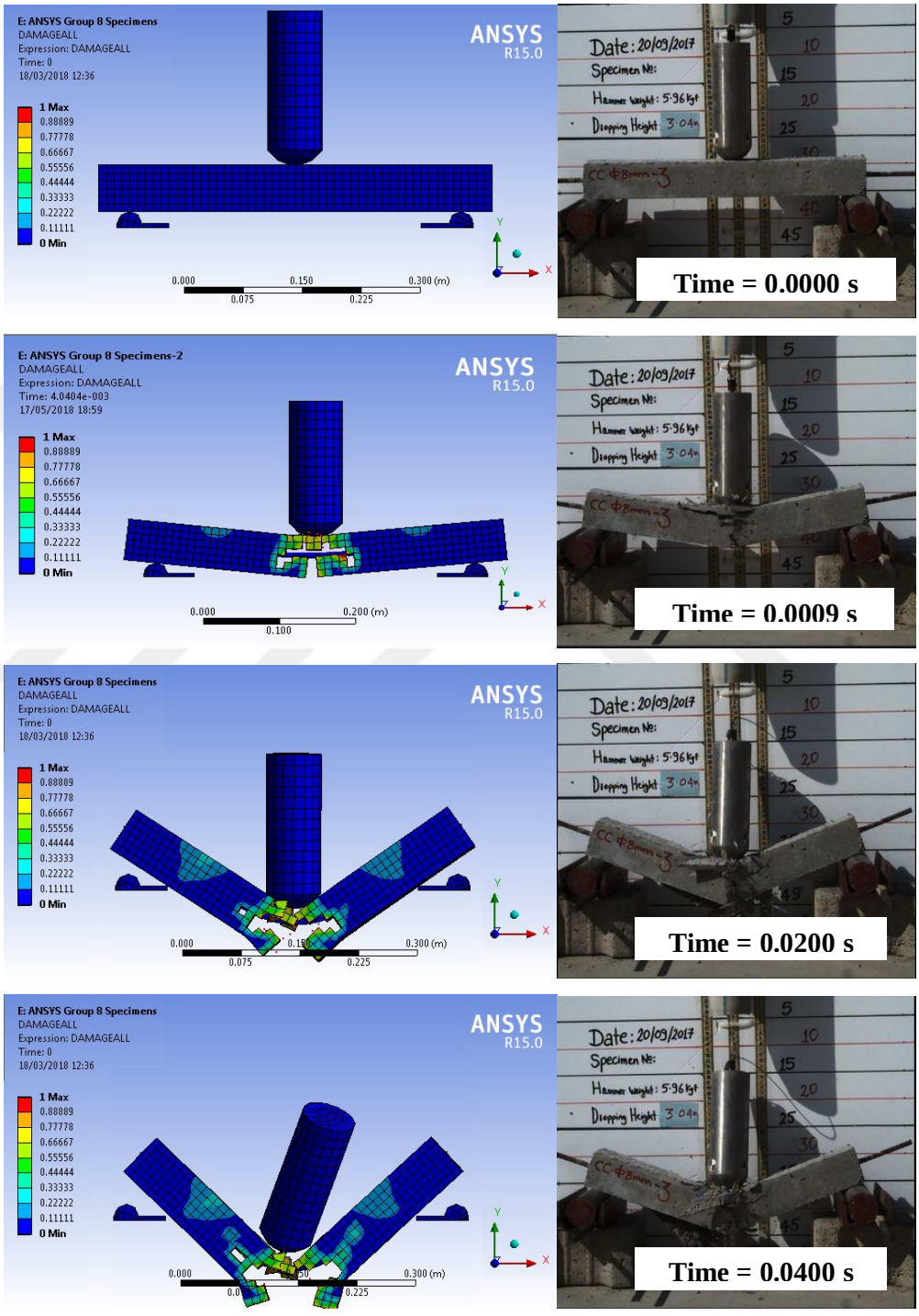

Figure A-10– Comparison of the motions for various times after impact obtained from the impact tests and the analyzed model for 60C26R-2

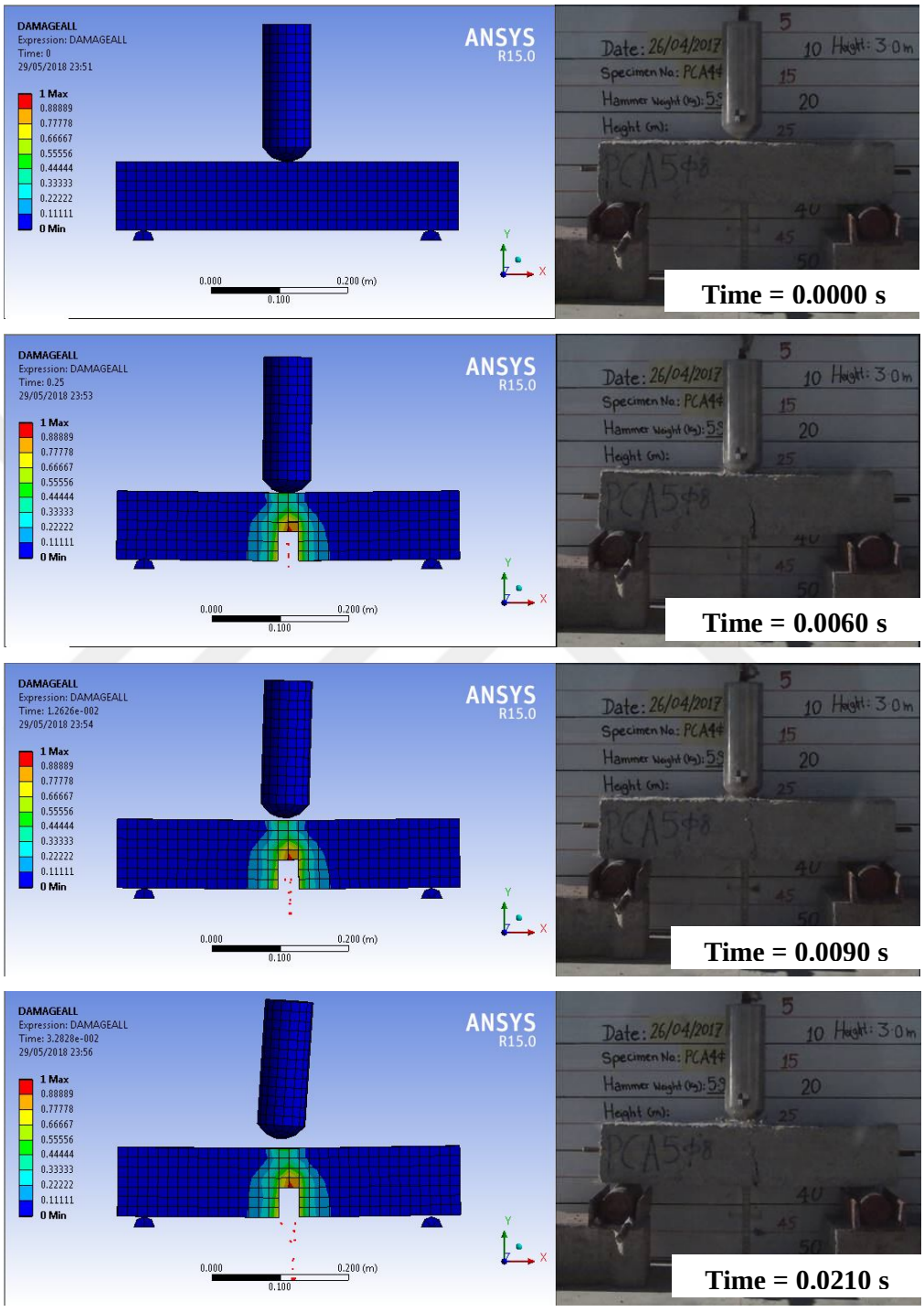

Figure A-11– Comparison of the motions for various times after impact obtained from the impact tests and the analyzed model for 100C12R-2

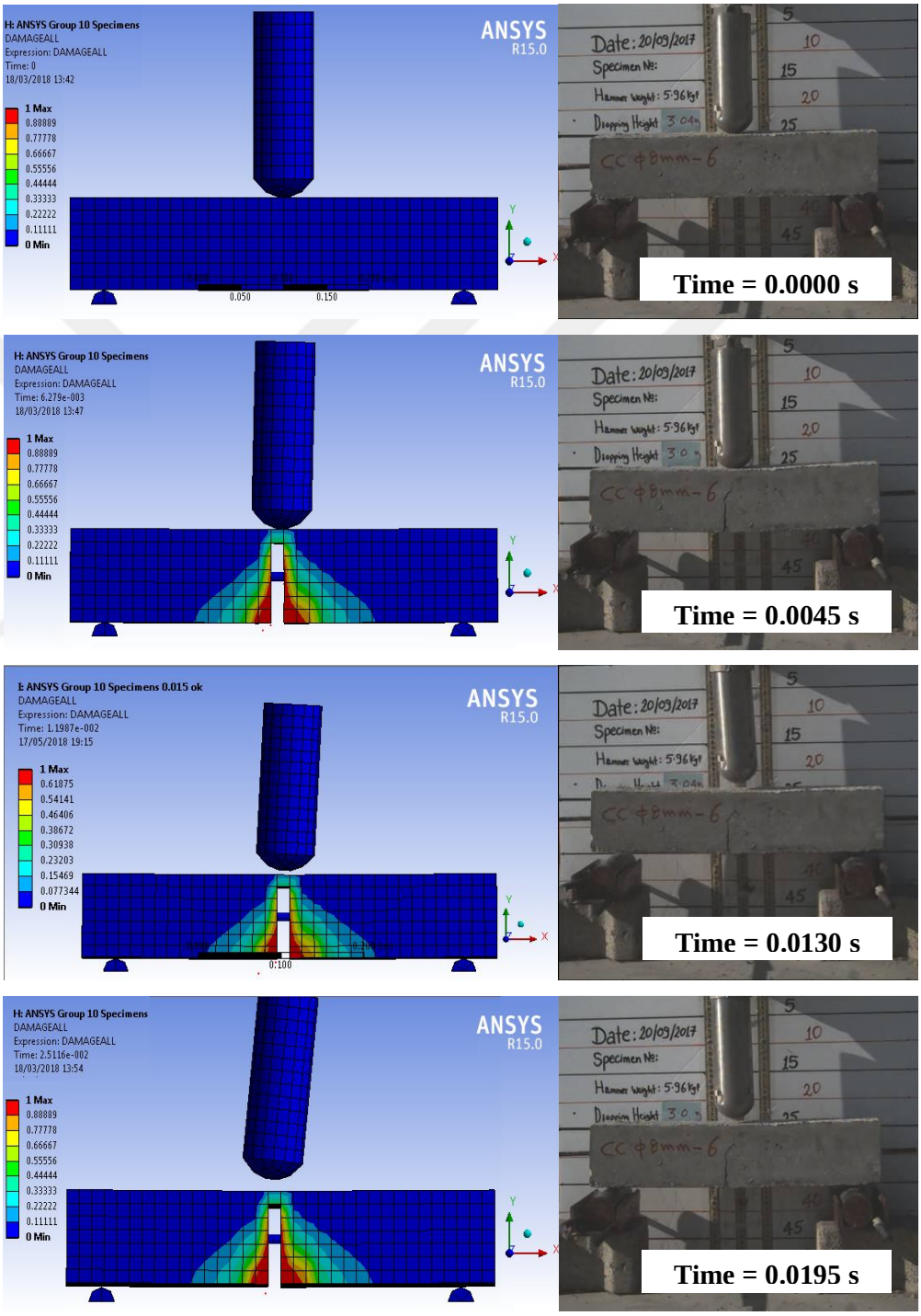

Figure A-12– Comparison of the motions for various times after impact obtained from the impact tests and the analyzed model for 100C26R-3

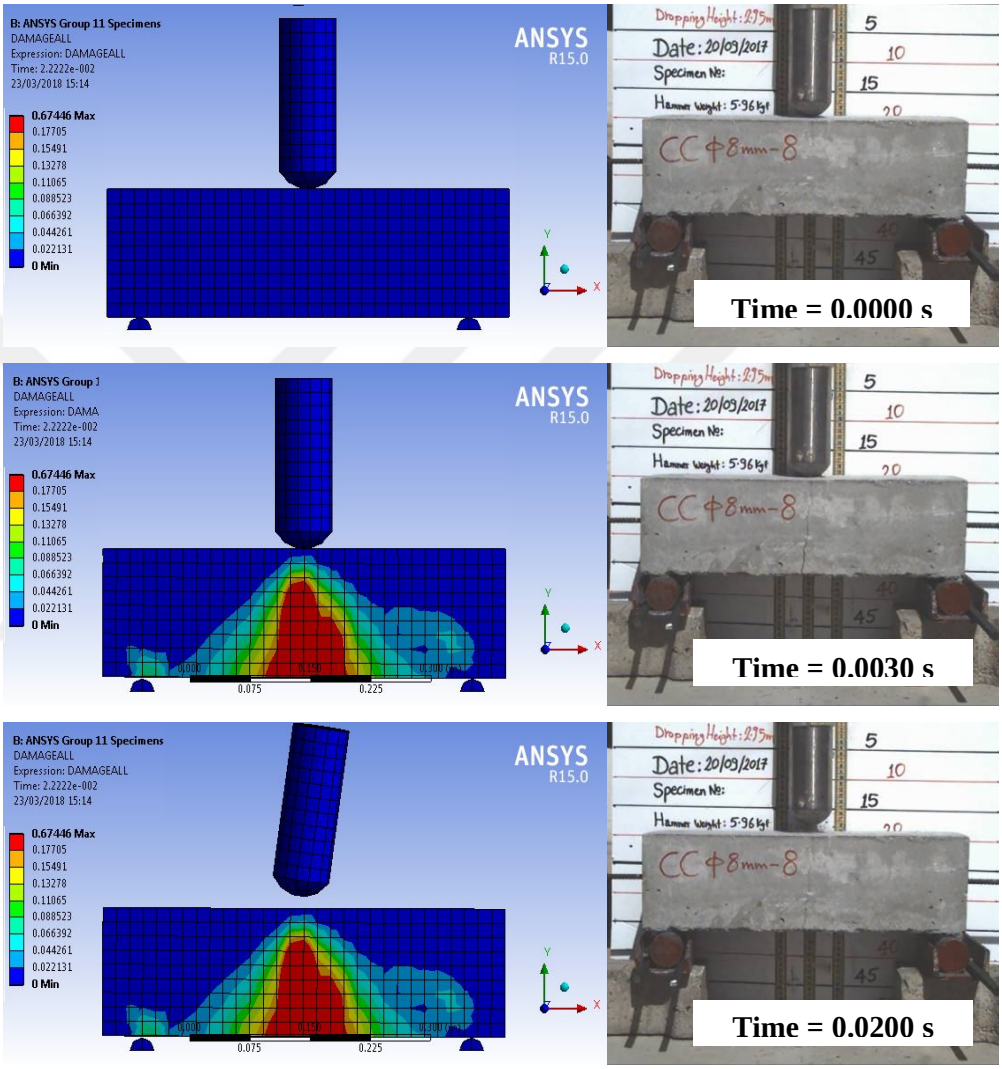

Figure A-13– Comparison of the motions for various times after impact obtained from the impact tests and the analyzed model for 150C12R-2

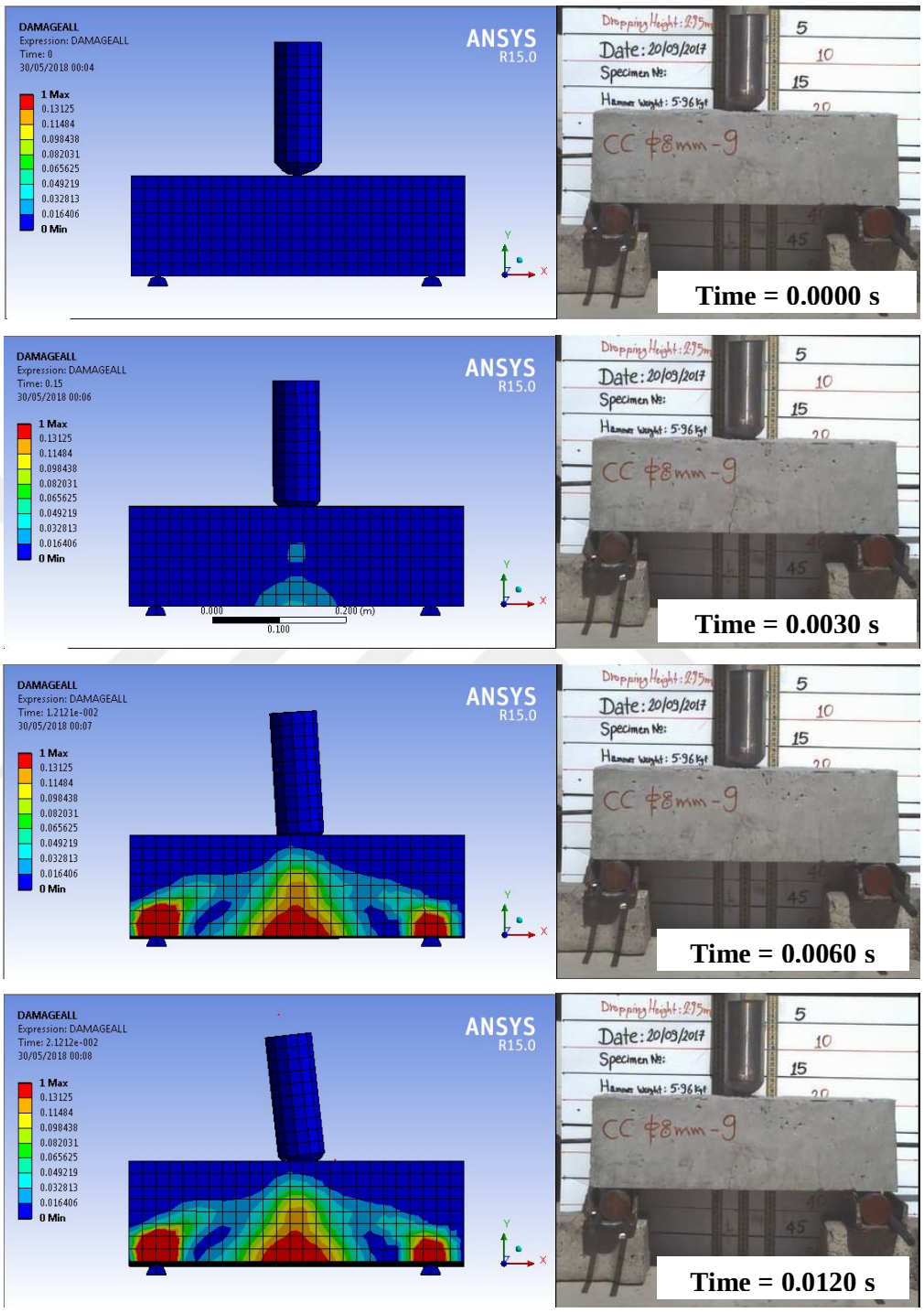

Figure A-14– Comparison of the motions for various times after impact obtained from the impact tests and the analyzed model for 150C26R-3

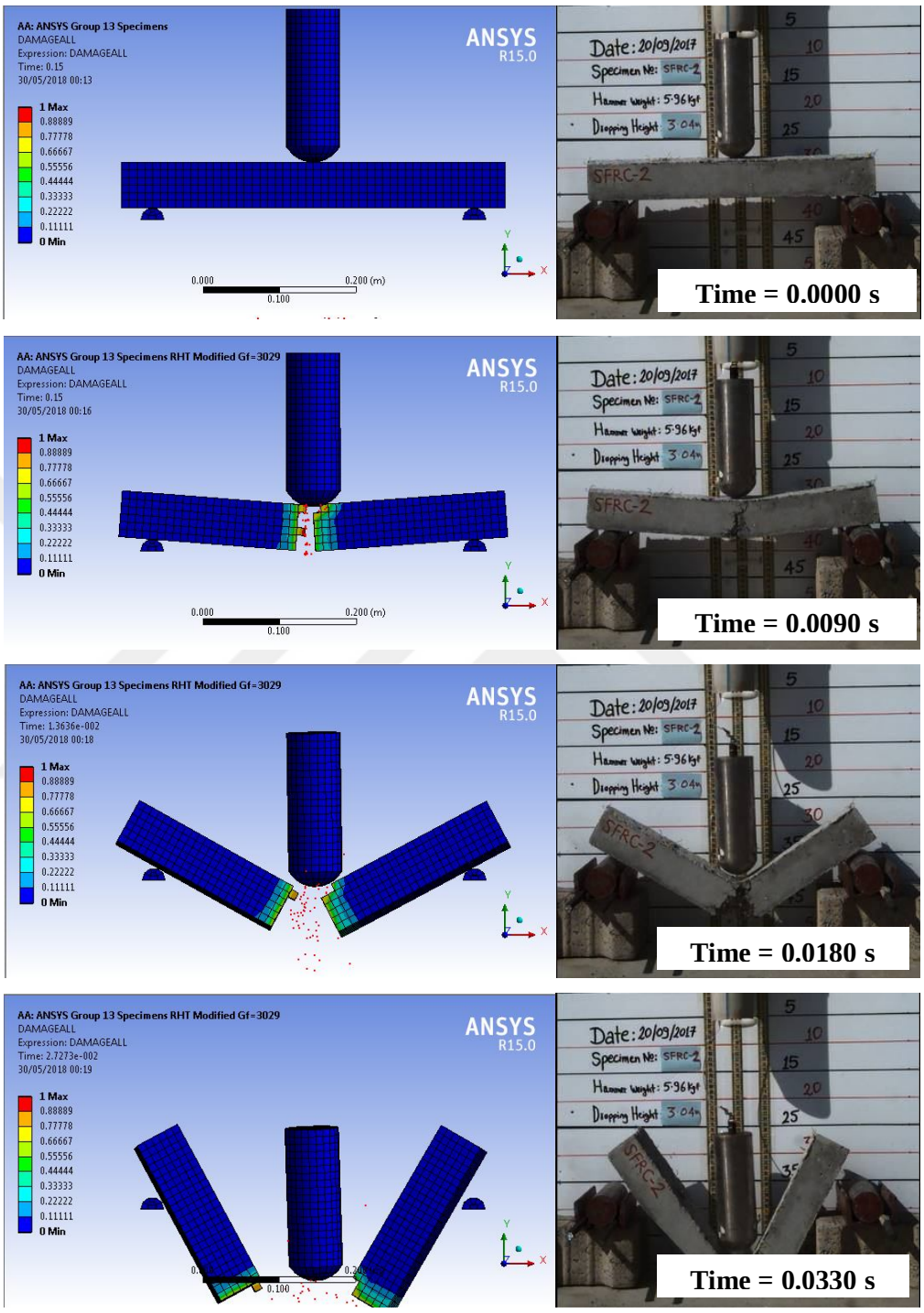

Figure A-15– Comparison of the motions for various times after impact obtained from the impact tests and the analyzed model for 60SFRC35-1

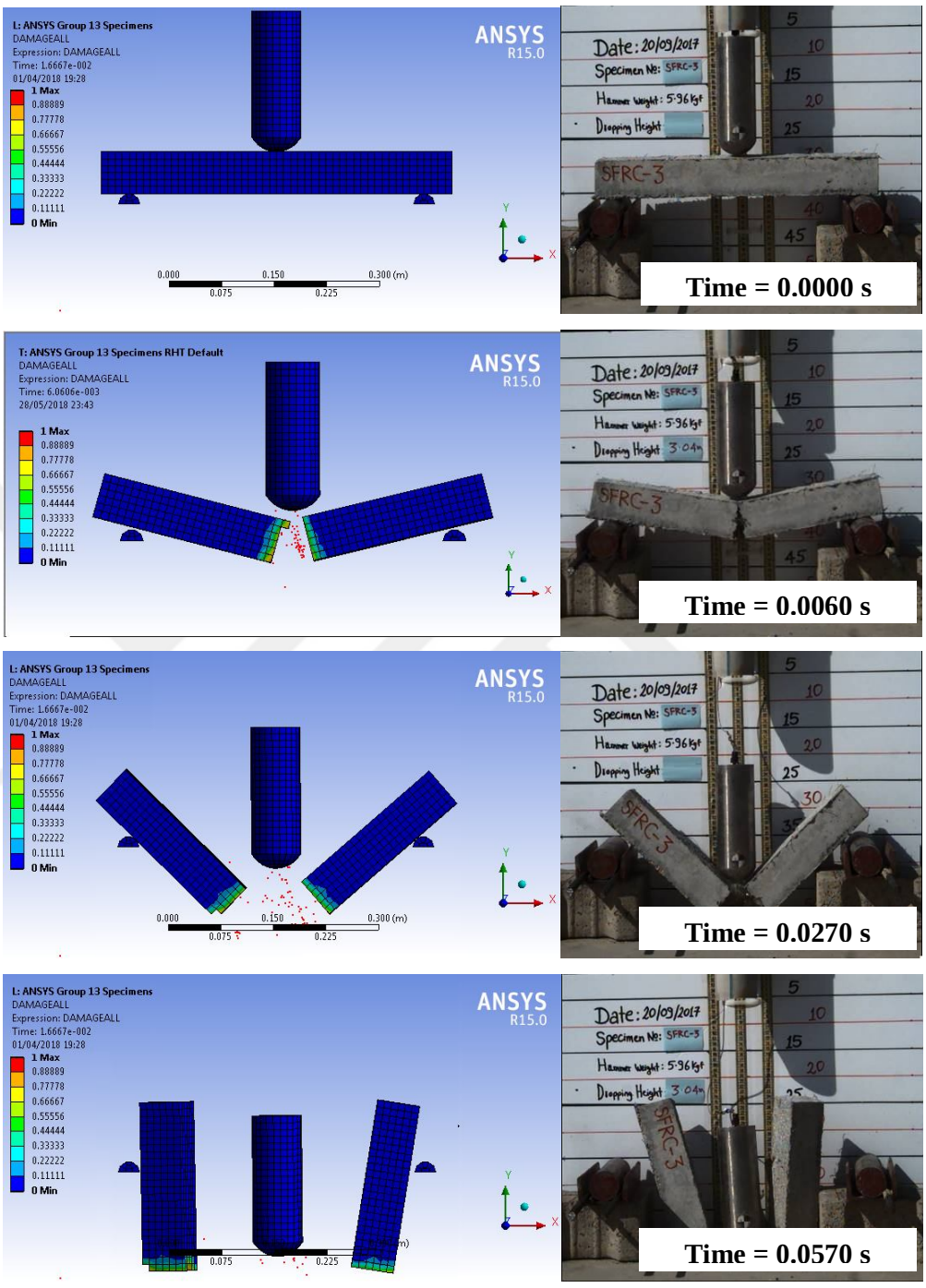

Figure A-16– Comparison of the motions for various times after impact obtained from the impact tests and the analyzed model for 60SFRC35-3

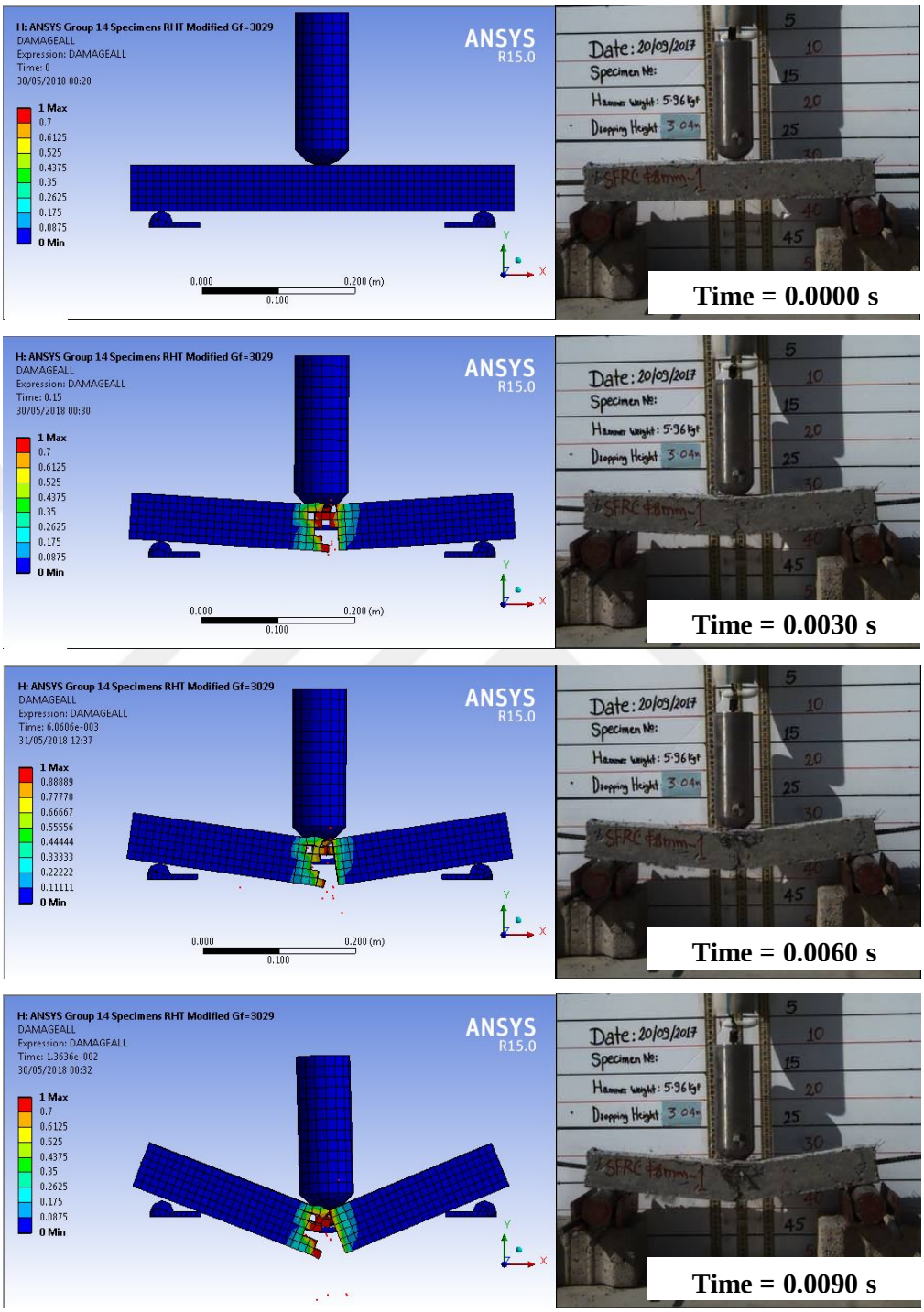

Figure A-17– Comparison of the motions for various times after impact obtained from the impact tests and the analyzed model for 60SFRC35R-1

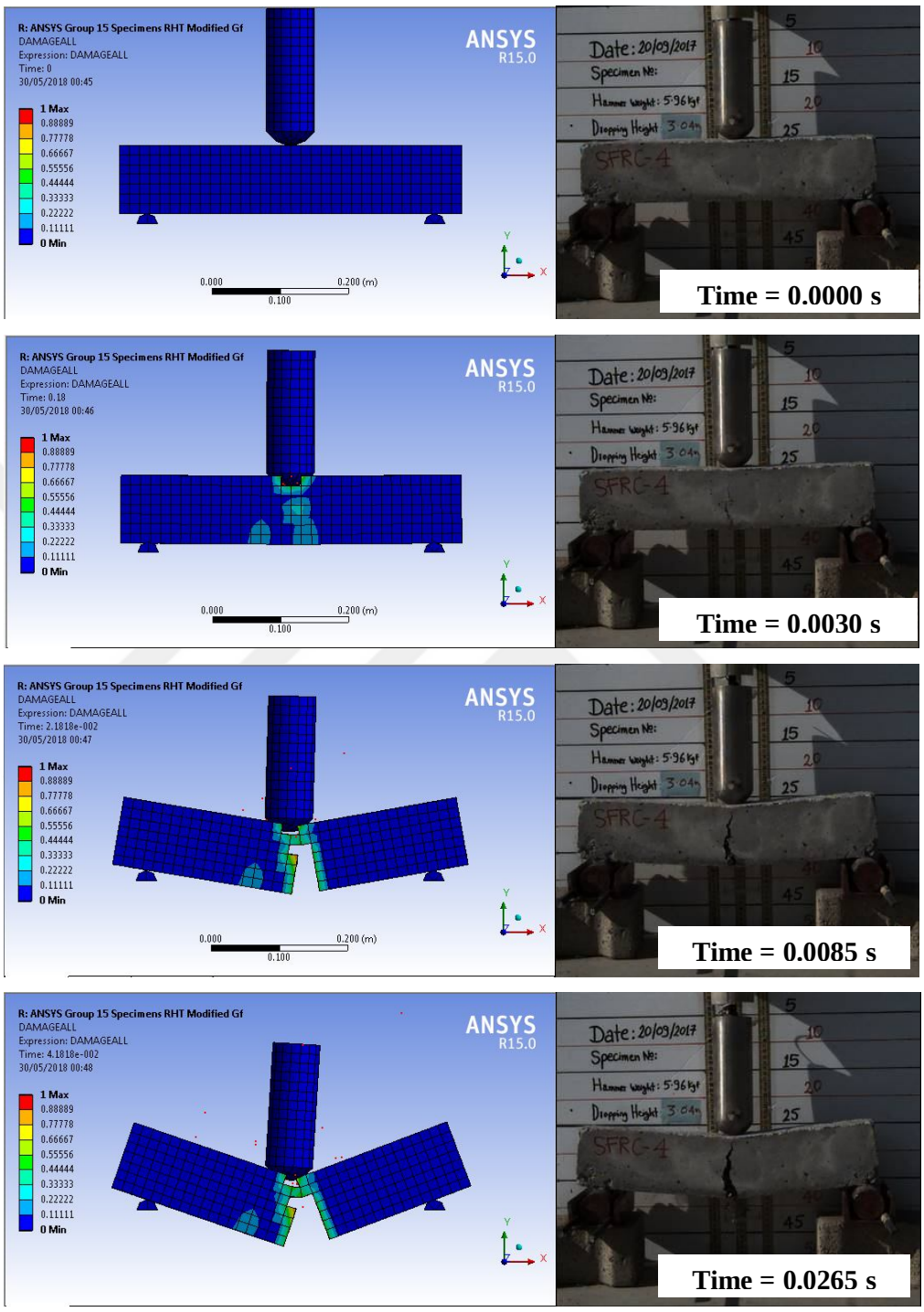

Figure A-18– Comparison of the motions for various times after impact obtained from the impact tests and the analyzed model for 100SFRC35-1

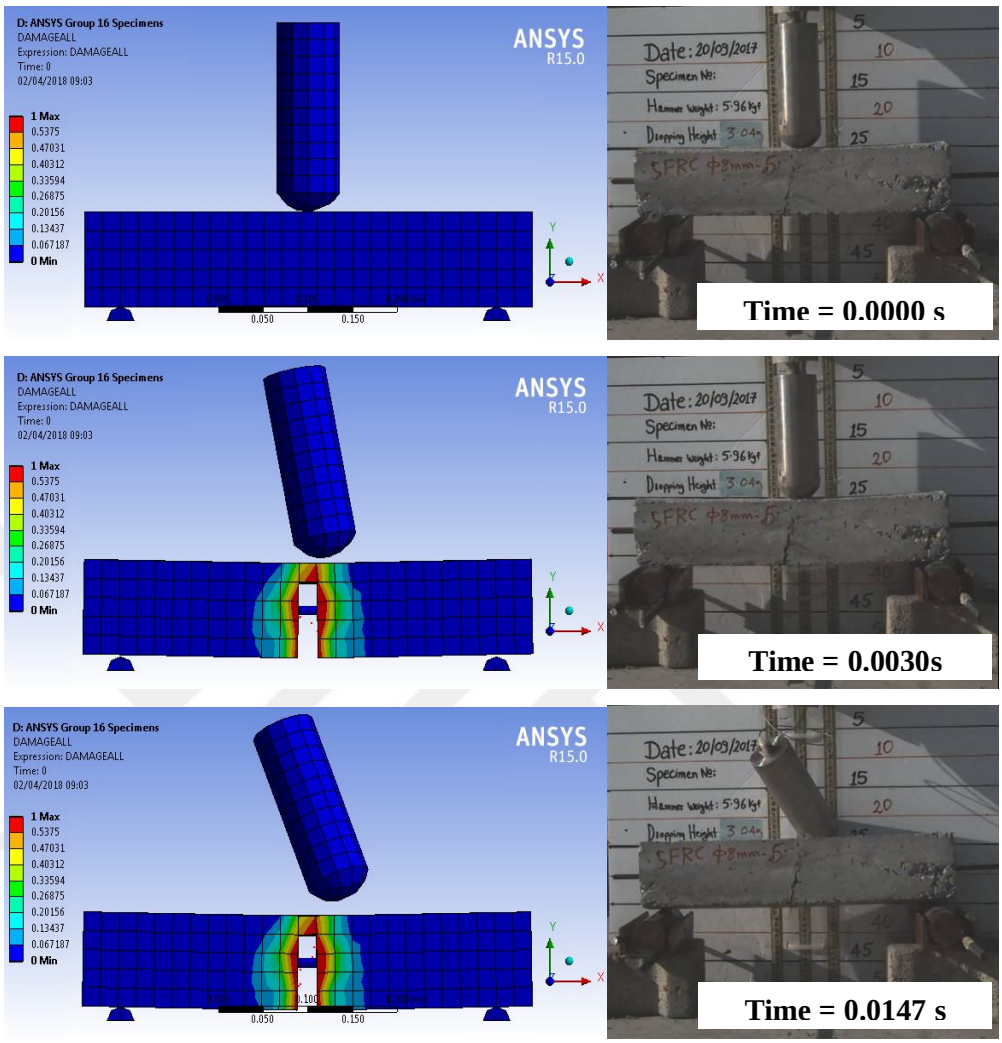

Figure A-19– Comparison of the motions for various times after impact obtained from the impact tests and the analyzed model for 100SFRC35R-1

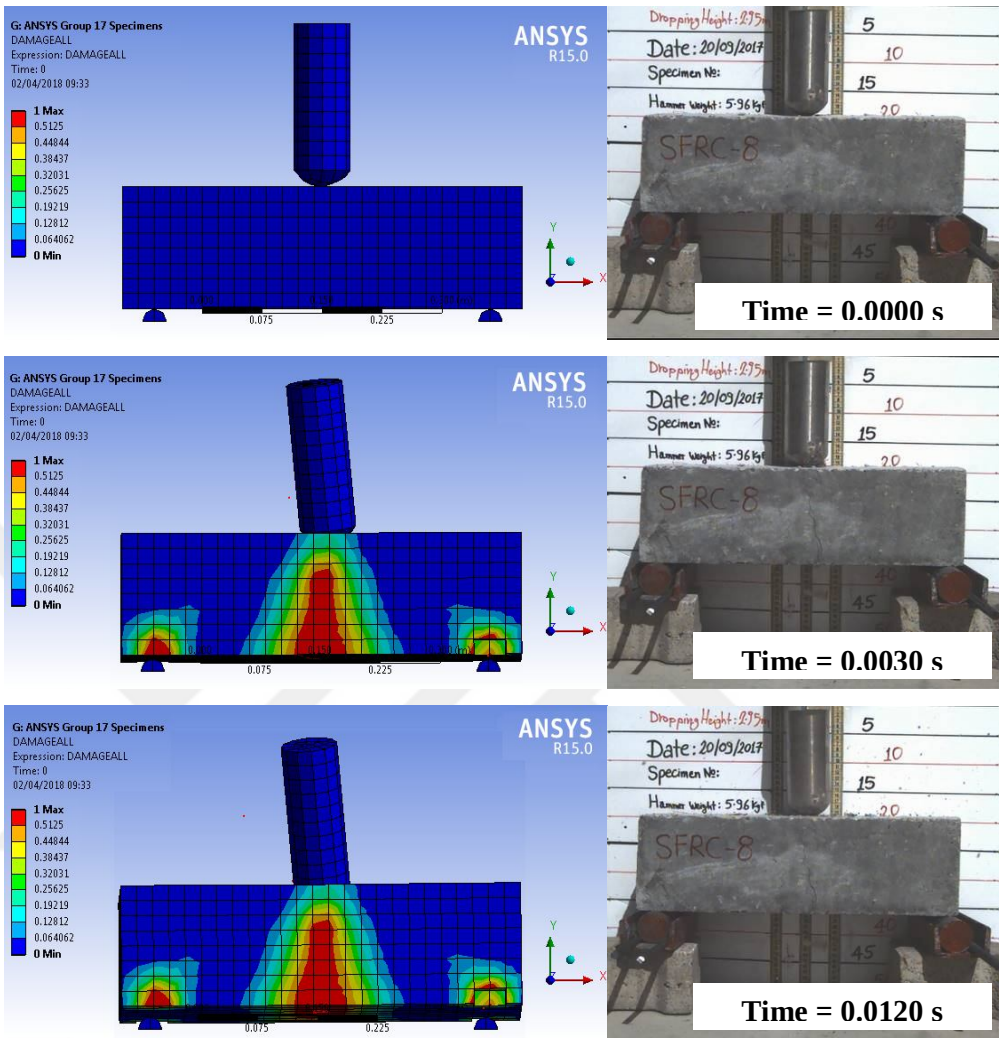

Figure A-20– Comparison of the motions for various times after impact obtained from the impact tests and the analyzed model for 150SFRC35-2

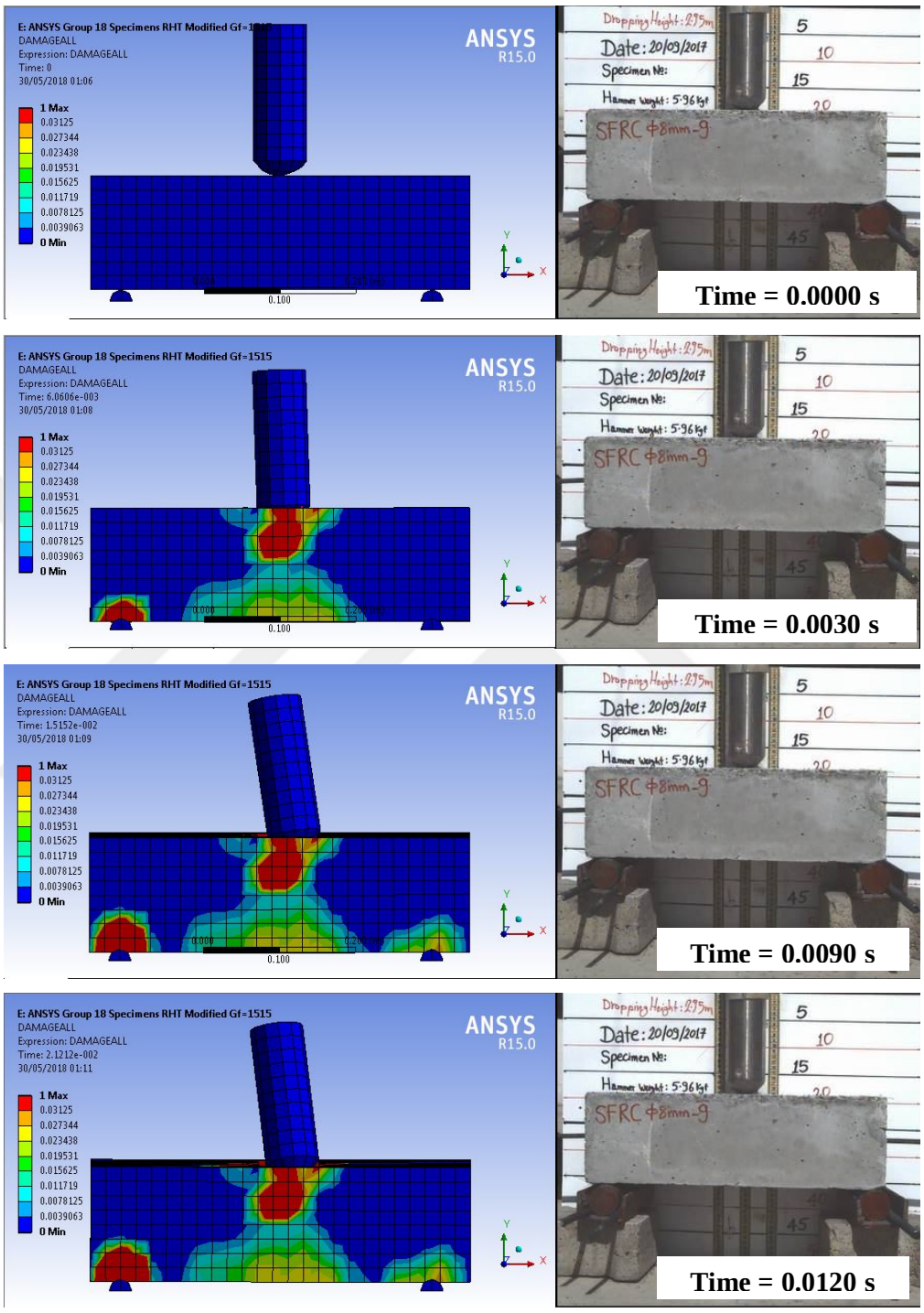

Figure A-21– Comparison of the motions for various times after impact obtained from the impact tests and the analyzed model for 150SFRC35R-3